

Geochemical interaction between projectile and target in hypervelocity cratering experiments.

by

Dipl. Geowiss. Matthias Ebert

*Dissertation submitted to obtain the academic degree
Doctor rerum naturalium (Dr. rer. nat.)
presented at the Department of Geosciences,
Freie Universität Berlin*

Berlin, July 2014

Hiermit versichere ich, dass ich die vorliegende Arbeit selbstständig verfasst und keine anderen als die angegebenen Hilfsmittel benutzt habe. Die Stellen der Arbeit, die anderen Werken wörtlich oder inhaltlich entnommen sind, wurden durch entsprechende Angaben der Quellen kenntlich gemacht.

Diese Arbeit hat in gleicher oder ähnlicher Form noch keiner anderen Prüfungsbehörde vorgelegen.

Matthias Ebert, Berlin, den 04.07.2014

Day of defense: 22.08.2014

Referees:

1. **Prof. Dr. Harry Becker**

Freie Universität Berlin
Fachbereich Geowissenschaften
Malteserstr. 74-100
12249 Berlin

2. **PD. Dr. Lutz Hecht** (Supervisor)

Museum für Naturkunde
Leibniz-Institut für Evolutions- und Biodiversitätsforschung
Forschungsbereich: Evolution und Geoprozesse
Invalidenstraße 43
10115 Berlin

3. **Prof. Dr. Alexander Deutsch** (Supervisor)

Westfälische Wilhelms-Universität Münster
Institut für Planetologie
Wilhelm-Klemm-Str. 10
48149 Münster

I Acknowledgments

First and foremost, I would like to express my sincere gratitude to my supervisor **PD. Dr. Lutz Hecht** for his supervision and helpful advices throughout the study, as well as his permanent desire to explain and, not at least, his everlasting good mood are a few characteristics, which are of great value for a PhD student. He is always happy to discuss new ideas, and has a wonderful ability of pointing out the important and interesting aspects of a scientific work.

Most deeply, I would like to acknowledge the help from my co-advisor, **Prof. Dr. Alex Deutsch**. In particular, I would like to mention his extensive scientific support as well as his very critical reading of the manuscripts, during my time as PhD student in the MEMIN group.

The opportunity to work in the MEMIN group has been an honor, privilege, positive experience and a lot of fun. I am very grateful to **Thomas Kenkmann, Kai Wünnemann, Wolf Uwe Reimold, Michael Peolchau, Dorothee Moser, Elmar Buhl, Tobias Hoerth, Frank Sommer** and **Anja Dufresne** for discussions, technical and theoretical advice as well as comments on drafts.

I would also like to thank **Astrid Kowitz, Nicole Güldemeister, Dirk Elbeshausen, Michael Bierhaus, Christopher Hamann, Jörg Fritz, Patrice Zaag, Ulli Raschke** and **all my colleagues** within the Museum für Naturkunde Berlin who have helped to make the past years so enjoyable.

I thank **Peter Czaja** for help with the microprobe analyses, **Kirsten Born** for the support at the scanning electron microscope, **Ralf Thomas Schmitt** for the whole rock XRF analysis, and **Hans Knöfler** for the skillful sample preparation.

I also thank the Deutsche Forschungsgemeinschaft (**DFG**) for the financial support of my PhD study in the framework of the MEMIN project.

A special "thank you" must be given to my friends **Hanne, Lutz, Kevin** and **Roman**, who always support me, give me good advice and make my life colorful.

My deepest gratitude goes to **Dani** and **my family** for their love, support, encouragement and understanding. Without them, none of this would have been possible.

II Preface - The MEMIN program



"Impact cratering is a fundamental geologic process throughout the solar system. Understanding this process requires multi- and interdisciplinary research that includes studies of natural craters, laboratory experiments, and numerical simulations. In this general context a **Multidisciplinary Experimental and Modeling Impact Research Network (MEMIN)** was established as a DFG financed Research Unit (Forschergruppe, FOR 887) comprising geologist, mineralogists, physicists, and engineers. Central to MEMIN were two-stage light gas accelerators capable of producing craters in the decimeter-range in solid rocks, a size previously not achieved at the laboratory scale that enables detailed spatial analysis. The hypervelocity impact experiments (HIE) on silica-rich targets comprised parametric studies of the role of water, porosity, target layering, and impact velocity on cratering mechanics, shock effects, and projectile distribution during cratering."(www.memin.de) The following PhD thesis was conducted within the framework of MEMIN, especially in a sub-project named *"On the fate of the projectile in impact cratering experiments"*. The major goal of this sub-project and thus the goal of this dissertation was to reach an improved knowledge of the physicochemical conditions during projectile emplacement, modes of target-projectile mixing, and associated chemical fractionation processes. The parameters that affect the dissemination of projectile material into impact derived materials are not well constrained. It is of great importance for our knowledge of impact cratering to quantify to which extent impact energy, water-saturation and porosity of the target control the fate of the projectile. The majority of the question could be answered. However, like so many times before in natural sciences new question have arisen...it remains an exciting and fascinating topic.

museum für
naturkunde
berlin



Museum für
Naturkunde
Berlin

Institut für
Planetologie
Westfälische-
Wilhelms-
Universität
Münster



Institut für
Geowissenschaften
Albert-
Ludwigs-
Universität
Freiburg

Fraunhofer
EMI

Fraunhofer
Ernst-Mach-Institut
Für Kurzzeiddynamik

GFZ
Helmholtz-Zentrum
POTSDAM

Deutsches
GeoForschungsZentrum
Potsdam

DFG

Deutsche
Forschungs-
Gemeinschaft

III Abstract

Geochemical projectile-target interaction was studied by means of 6 hypervelocity impact experiments and 4 laser-induced melting experiments, using sandstone and quartzite targets and projectiles (steel and iron meteorite) rich in siderophile (Ni, Co, Mo, W) and some lithophile tracer elements (Cr, V). The high chemical contrast between target and projectile facilitated tracing of very small projectile material within the target. During the cratering process ejecta fragments were formed showing shock-metamorphic features such as planar deformation features (PDF) in quartz, the onset to complete transformation of quartz to lechatelierite, partial melting of the sandstone (quartzite), and partially molten projectile, mixed mechanically and chemically with target melts. These highly shocked projectile-rich fragments are mainly ejected in a steep angle ($\sim 70^\circ$ - $\sim 80^\circ$) compared to the impact angle, which is in accordance with previous impact experiments. The laser experiments provided an additional control on the melting behavior and chemical mixing of projectile and target materials. This was especially important to constrain the heterogeneity of projectile and target melts prior to their mixing. During mixing of projectile and target melts, whether impact or laser experiments, Fe, Cr and V of the projectiles are preferentially partitioned into target melts compared to Ni, Co, Mo and W, yielding inter-element ratios in the sandstone or quartzite melt which completely differ from the element ratios of the projectiles. Due to the loss of the more lithophile elements (e.g., Cr, V) the projectile droplets are enriched in the siderophile elements (e.g., Co, Ni, Mo, W). This inter-element fractionation results from differences in the reactivity of the respective elements with oxygen during incorporation of metal melt into silicate melt. Data from Meteor Crater (Arizona, USA) and the Wabar craters (Saudi Arabia) show trends similar to those observed in the mesoscale laboratory craters of the MEMIN project.

Melting of projectile requires temperatures higher than expected from the calculation of maximum shock pressures. Three mechanisms for enhanced thermal input are suggested: 1) friction and deformation (i.e., plastic work) of the projectile, 2) more effective transfer of kinetic energy to porous material (in case of the sandstone) including the local increase of shock pressure due to pore collapse, and 3) heat transfer from shock compressed air during projectile flight (projectile pre-heating). The results indicate that the principles of projectile-target interaction and associated fractionation do not depend on impact energies (at least for the selected experimental conditions) and water saturation of the target. Partitioning of the projectile tracer elements is intensified in experiments with non-porous quartzite compared to the porous sandstone target. This is mainly the result of higher shock pressure and the related higher shock and post-shock temperatures including a longer time-span with physical conditions sufficient to partition of elements between projectile and target melt. The intensified partitioning processes in impact experiments with quartzite as target material led to the formation of an Fe enrichment zone surrounding projectile droplets. During quenching of the ejecta the Fe enrichment zone experiences a phase separation into an Fe-rich liquid (*L_{Fe}*) and a Si-rich liquid (*L_{Si}*). This liquid immiscibility occurs between melts with strong chemical differences and forms conspicuous emulsions textures. The incorporation of steel and Fe meteorite matter into sandstone melt of the laser experiments is also accompanied by phase separation of iron rich and silica rich melts. In addition, this feature was recently described in the impact glass of the Wabar crater.

IV Kurzfassung

Projektilfragmente sind nur unter speziellen Bedingungen nach einem Hochgeschwindigkeitseinschlag erhalten. Meist findet man das Projektil als chemische Spuren im Kraterboden oder im Fernauswurf (Ejekta). Die physikalisch-chemischen Bedingungen bei der Projektilplatznahme, der Mischung zwischen Projektil und Target und die Ursachen für dabei auftretende Inter-Elementfraktionierungen sind bislang kaum bekannt. Weiterhin gibt es nur wenige Annahmen inwieweit Impaktenergie, sowie Wassersättigung und Porosität des Targets, die Verteilung des Projektils kontrollieren. Die vorliegende experimentelle Studie befasst sich, als Teil des MEMIN Forschungsprojektes (FOR 887), mit der geochemischen Interaktion zwischen Projektil und Target. Hierfür wurden, unter Verwendung von Quarz-reichen Targets (Sandstein und Quarzit) und Eisenmeteorit- bzw. Stahlprojektilen (reich an siderophilen - Co, Ni, Mo, W und lithophilen - Cr, V Elementen), verschiedene Hochgeschwindigkeits- Impaktexperimente und sogenannte Laserschmelzexperimente durchgeführt. Die extremen chemischen Unterschiede zwischen Target und Projektil ermöglichten hierbei zum einen eine genaue Identifikation kleinster Projektil-Partikel und zum anderen die Bestimmung relativer Projektil-/Target-Anteile in Mischungen. Während des Kraterbildungsprozesses bildeten sich Ejektafragmente die Schock-metamorphe Phänomene, wie planare Deformationslamellen in Quarz (PDF), Bildung von Lechetalierite (Quartzglas) und Teilaufschmelzen des Targets sowie des Projektils, aufweisen. Projektil- und Targetschmelzen wurden hierbei mechanisch und chemisch miteinander vermischt. Diese hochgeschockte Ejekta, die ca. 10-30 % Projektilmaterial (überwiegend Schmelzkügelchen) enthält, wurde, bezogen auf den Einschlagswinkel, in einem sehr steilen Winkel zwischen $\sim 70^\circ$ und $\sim 80^\circ$ ausgeworfen.

Mit Hilfe der Laserexperimente konnten mehr Details über das Schmelz- und Mischverhalten von Projektil und Target in Erfahrung gebracht werden. Man erhielt vor allem einen genaueren Einblick in die chemische Heterogenität unkontaminierter Targetschmelzen. Sowohl in den Impaktexperimenten als auch in den Laserexperimenten ließ sich zeigen, dass während des Vermischens von Projektil- und Targetschmelzen Elementverteilungsvorgänge stattfinden. Fe, Cr, und V fraktionieren bevorzugt; Co, Ni, Mo und W zu einem deutlich geringeren Maße in die Targetschmelzen. Die Elementverhältnisse der Projektiltracer innerhalb der Targetschmelzen unterscheiden sich somit extrem von den jeweiligen Verhältnissen des Projektils. Diese Fraktionierung ist auf den lithophilen bzw. siderophilen Charakter der Elemente zurückzuführen. Fe, Cr und V bilden bevorzugt Oxide in den silikatischen Schmelzen. Co, Ni, Mo und W besitzen im Vergleich nur eine sehr geringe Reaktivität mit Sauerstoff. Dieses unterschiedliche Elementverhalten wurde bereits in natürlichen Impaktgesteinen des Meteor-Kraters (Arizona, USA) und der Wabar-Krater (Saudi Arabien) beobachtet.

Die aus den berechneten Spitzendrücken der Impaktexperimente abgeleiteten Temperaturen sind generell zu niedrig um die verwendeten Projektilmaterialien aufzuschmelzen. Um dennoch die Vielzahl vorhandener Projektilkügelchen zu erklären, wurden folgende drei Mechanismen angenommen, die für einen Temperaturanstieg verantwortlich sein können: (i) Reibung und Deformation (plastische Arbeit), (ii) die Bildung von lokalen Druckspitzen durch den Kollaps von Poren im Sandstein, (iii) Temperaturanstieg im Frontbereich des Projektils als Folge starker Kompression der verbliebenen Atmosphäre. Aus den Parameterstudien der verschiedenen Impaktexperimente geht hervor, dass die Projektil-Target Interaktionen und die gekoppelten

Elementfraktionierungen weder von der Impaktenergie (Variation der Projektilgröße bei gleicher Geschwindigkeit) noch vom Wassersättigungsgrad des Targets beeinflusst werden. Hingegen zeigt sich ein deutlicher Einfluss der Porosität. In den Quarzitexperimenten (0 % Porosität) fanden verstärkte Fraktionierungsvorgänge statt, verglichen mit den Ergebnissen aus den Experimenten mit Sandstein (~23 % Porosität). Grund dafür ist ein höherer Stoßwellen-Druck und daraus resultierende höhere Post-Schock Temperaturen, die wiederum zu einer längeren Reaktionszeit zwischen geschmolzenem Projektil und Target führen. Die Intensivierung der Fraktionierung innerhalb der Quarzitejekta wurde anhand von Fe-Anreicherungs-zonen bestimmt, die sich als markanter Rand um Projektilkugeln ausbildeten. Während der plötzlichen Abkühlung der Ejekta kam es zu einer Phasentrennung innerhalb der Fe-Anreicherungszone. Aufgrund von extremen chemischen Unterschieden bildeten sich Emulsionstexturen, die durch eine Fe-reiche (*Lfe*) und Si-reiche (*Lsi*) Schmelze definiert sind. Dieses Phänomen tritt ebenfalls bei der Vermischung von geschmolzenem Stahl bzw. geschmolzenem Fe-Meteorit mit Sandsteinschmelze innerhalb der Laserexperimente auf und konnte kürzlich bei der Analyse des Wabar-Impaktglases detailliert beschrieben werden. Die vorliegende Dissertation zeigt, dass kleinmaßstäbige geochemische Prozesse wie (i) Anreicherung von Projektilelementen in Targetschmelzen, (ii) die damit gekoppelte Phasentrennung in *Lfe* und *Lsi* und (iii) die signifikante Veränderung der Verhältnisse der Projektilelemente innerhalb der Targetschmelze, gängige Prozesse sind, die während der Mischungsvorgänge zwischen Projektil- und Targetschmelze in der Natur stattfinden.

V Abbreviations and units

<i>Units</i>	
a	Years
°C	Degree Celsius
μm	Micrometer
GPa	Giga pascal
kJ	Kilojoule
kV	Kilovolt
km×s ⁻¹	Kilometer per second
nA	Nanoampere
nm	Nanometer
ppm	Parts per million
vol.%	Volume percent
wt.%	Weight percent

<i>Abbreviations</i>	
b.d.l.	Below detection limit
CDC	Campo del Cielo meteorite
D ^X _{met/sil}	Metal-silicate partitioning coefficient of element X
D.L.	Detection limit
ΔG	Gibbs free energy
EDX	Energy-dispersive X-ray spectroscopy
EMP	Electron microprobe
EMI	Fraunhofer Ernst-Mach-Institut Freiburg
FIB	Focused ion beam
f _{O₂}	Oxygen fugacity
GFZ	Deutsches GeoForschungsZentrum Potsdam
HAADF	High-angle annular dark-field imaging
HIE	Hypervelocity impact experiments
LA-ICP-MS	Laser ablation inductively coupled plasma mass spectrometry
LE	Laser-induced melting experiments
<i>Lfe</i>	Iron-rich liquid
<i>Lsi</i>	Silica-rich liquid
MfN	Museum für Naturkunde Berlin
Micro-CT	X-ray micro computer tomography
n.a.	Not analyzed
P	Pressure
PD	Projectile droplet
PDF	Planar deformation features
QE	Experiments with quartzite targets
Qtz	Quartz
SE	Experiments with sandstone targets
SEM	Scanning electron microscope
T	Temperature
TEM	Transmission electron microscope
WWU	Westfälische Wilhelms-Universität Münster
WR	Whole rock
XRF	X-ray fluorescence spectroscopy

Contents

I Acknowledgments	i
II Preface - The MEMIN program	iii
III Abstract	iv
IV Kurzfassung	v
V Abbreviations and units	vii
1 Introduction	1
1.1 Impact cratering	1
1.2 Projectile material and its identification at terrestrial impact structures	1
1.3 Experimental impact studies - fate and dissemination of the projectile	5
1.4 The MEMIN hypervelocity impact experiments	6
1.5 Laser-induced melting experiments	7
1.6 Structure of the thesis	7
1.7 Contribution of the author and co-authors to the individual manuscripts and additional chapters	8
2 Chemical modification of projectile residues and target material in a MEMIN cratering experiment.	10
2.1 Abstract	10
2.2 Introduction	10
2.3 Experimental and analytical methods	12
2.3.1 Experimental setup	12
2.3.2 Analytical techniques	12
2.4 Results	13
2.4.1 Composition of target and projectile	13
2.4.1.1 Target (Seeberger Sandstein)	13
2.4.1.2 Projectile (Campo del Cielo meteorite)	14
2.4.2 Ejecta types	15
2.4.3 Chemical modification of the sandstone	17
2.4.4 Chemical modification of the Fe-meteorite projectile	20
2.5 Discussion	21
2.5.1 Chemical interaction between projectile and sandstone target	21
2.5.2 P-T-conditions during the impact	25
2.6 Conclusions	27
2.A Tables of chapter 2.	29
3 Geochemical processes between steel projectiles and silica-rich targets in hypervelocity impact experiments.	32
3.1 Abstract	32

3.2	Introduction	32
3.3	Experimental and analytical methods	34
3.4	Results	35
3.4.1	Composition and microstructure of projectile and target	35
3.4.1.1	Seeberger Sandstein (target lithology)	35
3.4.1.2	Taunus quartzite (target lithology)	35
3.4.1.3	D290-1 steel (projectile material)	36
3.4.2	Impact-induced features and modes of projectile-target mixing	36
3.4.2.1	Highly shocked and projectile rich ejecta	36
3.4.2.2	Projectile within the highly shocked ejecta	41
3.4.3	Chemical modification of projectile and target material	41
3.4.3.1	Chemical modification of the sandstone targets	41
3.4.3.2	Chemical modifications of the quartzite targets	43
3.4.3.3	Chemical modifications of the steel projectile	46
3.5	Discussion	48
3.5.1	Origin of the highly shocked and projectile rich ejecta	48
3.5.2	Inter-element fractionation processes	52
3.5.3	Effects of experimental conditions	54
3.5.3.1	Impact energy	54
3.5.3.2	Water-saturation of the sandstone targets	55
3.5.3.3	Porosity of the target	55
3.6	Conclusions	56
3.A	Tables of chapter 3.	57
4	Distribution of the highly shocked and projectile rich ejecta	61
5	Are laser-induced melting experiments suitable to simulate meteorite impact processes?	65
5.1	Abstract	65
5.2	Introduction	65
5.3	Experimental and analytical methods	67
5.3.1	Laser-induced melting technique	67
5.3.2	Samples and analytical methods	68
5.4	Results	69
5.4.1	Target and projectile material	69
5.4.2	Modes of melting and mixing	69
5.4.2.1	Pure sandstone	69
5.4.2.2	Projectile	72
5.4.2.3	Mixing of target and projectile melts	75
5.4.3	Compositional variations of pure sandstone melt and projectile melts . . .	78
5.4.3.1	Sandstone melt	78
5.4.3.2	D290-1 steel	78
5.4.3.3	Campo del Cielo Meteorite	80

5.4.4	Element partitioning between projectile and target melt	81
5.4.4.1	Iron	81
5.4.4.2	Chromium and vanadium	81
5.4.4.3	Cobalt, nickel, molybdenum and tungsten	82
5.4.4.4	<i>Lfe</i> and <i>Lsi</i>	83
5.5	Discussion	84
5.5.1	Partitioning behavior of projectile tracer elements	84
5.5.2	Comparison with impactites from nature and impact experiments	85
5.5.2.1	Melting, mixing and phase formation processes	85
5.5.2.2	Chemical signature of the projectile	86
5.6	Conclusions	87
5.A	Tables of chapter 5.	88
6	Application to natural impactites	91
6.1	Projectile-target interaction	91
6.2	Application of experimental results to nature	94
7	Summary and general conclusions	97
8	Outlook and open questions	100
	References	103
A	List of figures	113
B	List of tables	119

1 Introduction

1.1 Impact cratering

The collision of solid bodies has been and still is one of the fundamental geological processes in our solar system (Shoemaker, 1977; French, 1998). The exploration of the solar system has shown that all planetary objects with solid surface are affected by impact cratering. Not only the heavily cratered lunar surface emphasizes that hypervelocity impacts have played an important role in the evolution of Moon and Earth: The Moon itself was most probably formed by a giant impact of an Mars-sized object less than 40 Ma after formation of the Earth (Canup & Asphaug, 2001). Impacts of extraterrestrial objects on the Earth, once regarded as an minor astronomical process, have been recognized as a major factor in the geological and biological history of the Earth (French, 1998). It is widely accepted that impacts of comets and carbonaceous chondrites have delivered water and probably organic molecules (Morbidelli *et al.*, 2000; Studier *et al.*, 1968), and large impacts have probably caused re-cycling of the early crust (Grieve, 1980). In addition to the geological disturbances involved, impact events have produced several geological structures with an important economic value, e.g. the nickel-copper sulfide deposits at Sudbury crater, Canada (Farrow & Watkinson, 1997), iron and uranium ores at the Ternovka structure, Ukraine (Grieve, 2005) or impact diamonds at the Popigai impact structure in Siberia (Masaitis, 1998). Finally, at least one large impact, the Chicxulub impact event, about 65 Ma ago, caused a major redirected biological evolution on Earth by producing a mass extinction that now marks the Cretaceous-Paleogene (K/Pg) boundary (e.g., Alvarez *et al.*, 1980). Constant reshaping of the Earth's surface by plate tectonics and erosion processes, however, has erased most of the evidence of the cratering record on Earth. Nevertheless, 184 impact structures have been identified on Earth by 2014 and this number is growing continuously ([http://www.unb.ca/passc/ImpactDatabase/-Earth Impact Database](http://www.unb.ca/passc/ImpactDatabase/-Earth%20Impact%20Database)); in addition, a small number of ejecta layers is known - again, the K/Pg boundary is the most famous example. Only under rare circumstances natural impacts are observed directly, e.g., the impact at Sikhote-Alin, Russia (Krinov & Fesenkov, 1959), the Carancas event, Peru (Kenkmann *et al.*, 2009), the collision of Shoemaker-Levy 9 with Jupiter (Weaver *et al.*, 1995), or the recently observed air burst of the Chelyabinsk meteorite in Russia (Fig. 1.1). Especially the air burst of the Chelyabinsk meteorite in Russia (February 2013) showed quite plainly the persistent timeliness of meteorite impacts. All these aspects document the importance and necessity of studying the formation and all associated processes of impact craters. The reconstruction of the terrestrial impact crater record is a major issue in the field of impact research. Studying this aspect requires a profound knowledge of the **physical and chemical processes acting during projectile-target interaction** (e.g., Grieve, 1991; Grieve & Shoemaker, 1994; Koeberl *et al.*, 2012); which is the basic issue of this PhD-thesis.

1.2 Projectile material and its identification at terrestrial impact structures

Abundant extraterrestrial material has been delivered to Earth throughout its history via impact events. Projectiles that cause impact events can be preserved in the form of fragmental residues or geochemical traces. For instance, small and young craters that are formed by the impact of

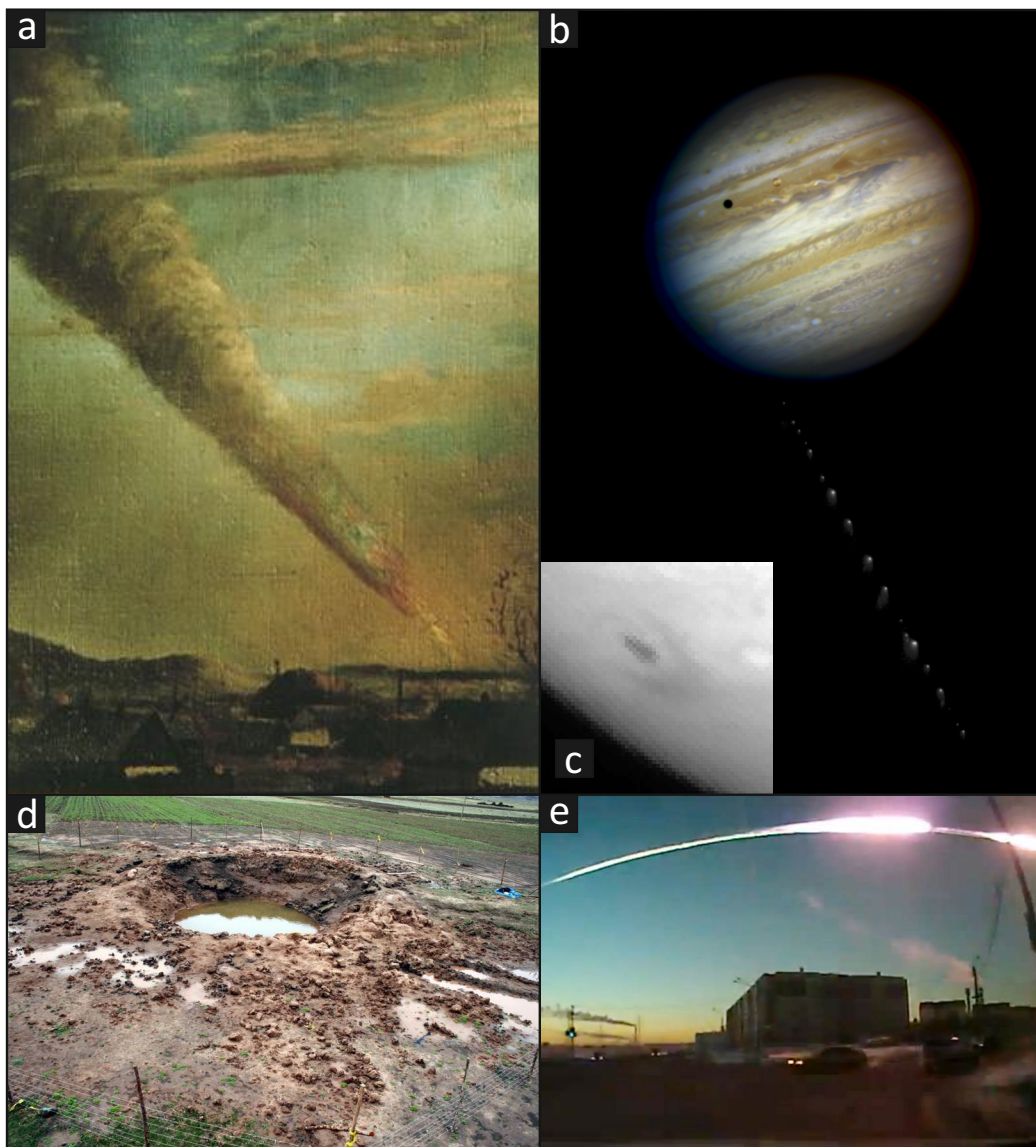


Figure 1.1: (a) Painting: "Fall of the Sikhote Alin meteorite" by A. A. Medvedev, who observed the impact from the roof of his house in February 1947; (b) Hubble image of the 21 fragments of the Shoemaker-Levy 9 comet prior impacting on Jupiter (May, 1994; source: www.hubblesite.org); (c) Jupiter's cloud-tops shortly after the impact of the first fragment-A of comet Shoemaker-Levy 9 (July 16, 1994; source: www.hubblesite.org); (d) Carancas crater, Peru (Kenkmann *et al.*, 2009). (e) A meteorite flashes across the sky over Chelyabinsk, Russia, image taken from a dashboard camera.

iron meteorites like the Kamil crater (Egypt; D'Orazio *et al.*, 2011), Wabar craters (Saudi Arabia; Mittlefehldt *et al.*, 1992), and even the Meteor Crater 1.2 km in diameter (Arizona, USA; Mittlefehldt *et al.*, 2005) each contain, or lie amidst impact debris containing strong deformed fragments of projectiles (shrapnels) as well as melted, disseminated residues in impactites. At larger craters, a certain amount of projectile matter (< 1 wt.%) can be incorporated into impact melt rocks and breccias, fractures in the crater floor, or the ejecta (e.g., Goderis *et al.*, 2012; Koeberl *et al.*, 2012). The chemical composition of these materials is dominated by the

composition of the penetrated target rocks. The identification of meteoritic matter in impact melt rocks relies predominantly on the study of siderophile elements and specifically platinum group elements in impactites (e.g., Morgan *et al.*, 1975; Palme *et al.*, 1981; Evans *et al.*, 1994; McDonald *et al.*, 2001; Koeberl *et al.*, 2012), which are fingerprints reflecting the composition of the impacted bolides. The siderophile character describes the chemical affinity of these elements to partition into metal phases. Siderophile elements e.g., Co, Ni and platinum group elements (PGEs - e.g., Pt, Pd, Os, Ru, Rh, Ir) are enriched by several orders of magnitude in meteorites compared to crustal target rocks (Dressler & Reimold, 2001). Chondrites, primitive achondrites, iron and stony-iron meteorites possess a distinctive detectable elemental or isotopic ratio. This allows a clear differentiation between terrestrial and meteoritic component. Often Cr, Co, Ni and PGE as well as inter-element ratios are used (e.g., Fig. 1.2) to differentiate between chondrites, achondrites and iron meteorites (Tagle & Hecht, 2006; Goderis *et al.*, 2012). For example, the identification of the projectiles of the Morokweng, Popigai and Lappajärvi impact structures are shown in Fig. 1.2 (adopted from Tagle & Hecht, 2006). The fields defined by the slope of the different PGE overlap with the fields of discrete ordinary chondrites, allowing a precise identification of the projectile e.g., L or, most likely, LL chondrite for the Morokweng structure, (South Africa; McDonald *et al.*, 2001 an L chondrite for the Popigai crater (Siberia; Tagle & Claeys, 2005) and a LL chondrite for Serenitatis basin (Apollo 17 samples from the Moon; Tagle, 2005).

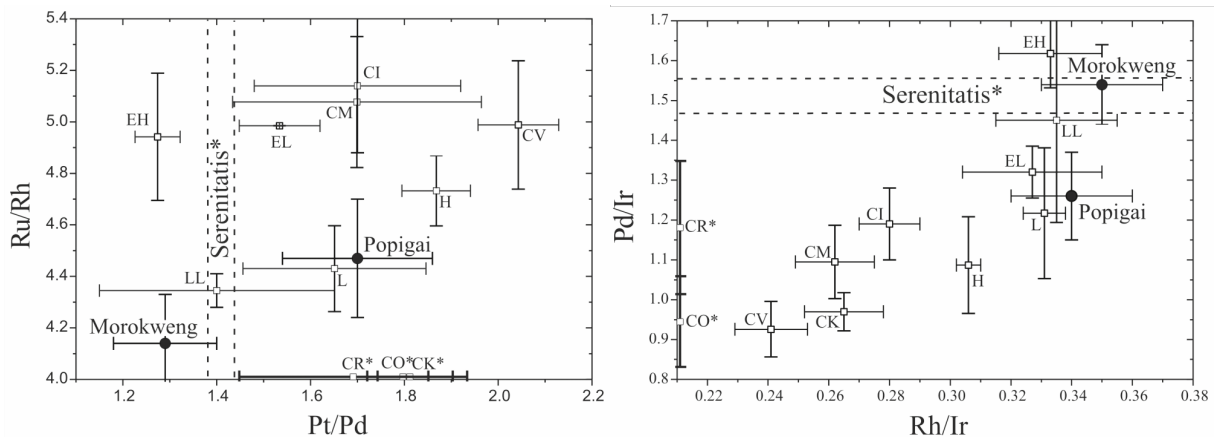


Figure 1.2: Comparison of the PGE projectile elemental ratios determined from the impact melt rocks of Popigai, Morokweng, and Serenitatis with elemental ratios of chondrites (Tagle & Hecht, 2006).

Furthermore, isotope ratios have been shown to complement the identification of projectile matter (e.g., Koeberl, 1998; Tagle & Hecht, 2006; Goderis *et al.*, 2012; Koeberl *et al.*, 2012). Most suitable isotope ratios for determining projectile components in impactites are $^{187}\text{Os}/^{188}\text{Os}$ and $^{53}\text{Cr}/^{52}\text{Cr}$. In most cases, the very high sensitivity of the Os isotope method detects even minute meteoritic contributions in impactites and sediments. Osmium isotopes inter alia ($^{187}\text{Os}/^{188}\text{Os}$) confirmed the meteoritic nature of the PGE anomalies occurring in the K-Pg boundary clay layers (Luck & Turekian, 1983). The measurement of Cr isotopes ratios provide not only an unambiguous detection of meteoritic matter, but also discriminate between different types of

projectiles (Goderis *et al.*, 2012). Data for most meteorite groups show a variable excess of ^{53}Cr relative to terrestrial samples (Koeberl *et al.*, 2012).

The possibility of fractionation processes between these meteoritic tracer elements (see above) during projectile and target mixing may produce problems at the chemical classification of projectile traces in natural impactites. That's why a profound knowledge of the geochemical processes that affect the composition and distribution of projectile matter upon impact is of prime importance (e.g., Grieve, 1991; Grieve & Shoemaker, 1994; Koeberl, 1998) for this classification.

The process(es) of mixing projectile matter into target and impactite materials are far from being understood (e.g., Mittelfehldt *et al.*, 1992; Evans *et al.*, 1994; Koeberl *et al.*, 2012). It could be emplaced in a vapor phase, as melt droplets or as fine-grained solid material. There are several terrestrial craters, e.g., Meteor crater, Kamil crater, Wabar crater field and Henbury crater field (Australia), where intense mixing of target and projectile melts occurred. Impact melt rocks from these craters contain conspicuous metallic spheres, which originated from the impactor (iron meteorites in all the mentioned craters; Gibbons *et al.*, 1976; Hörz *et al.*, 2002; Mittelfehldt *et al.*, 2005; Hamann *et al.*, 2013). These impactites are rarely present in a fresh state; most of them show significant modifications, they are crystallized, hydrated, and oxidized (Hörz *et al.*, 2002). Very pristine and relatively young impact melt of the Wabar craters allowed geochemical analysis of nearly unweathered material. Detailed electron microprobe studies of the Wabar glasses have shown that during the mixing process projectile melt spheres and target melts clearly reveal chemical changes compared to the target and the meteorite. Fe and Ni from the impactor were partitioned in, and became structural part of the silicate melts or of minerals that grew from this melt (Gibbons *et al.*, 1976; Hamann *et al.*, 2013). Especially, the strong iron transfer from the projectile melt spheres into the target melts, which partly leads to phase separations of the silicate melts (Fe-rich (*Lfe*) and Si-rich (*Lsi*) silicate melts; Fig. 1.2), developed as liquid immiscibility emulsions (Hamann *et al.*, 2013), seems to be a unique process occurring in natural impactites.

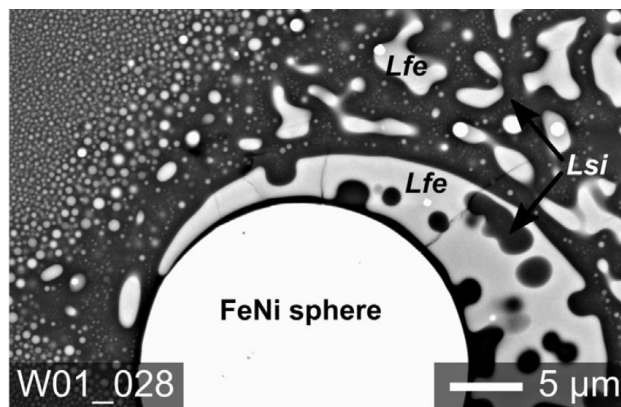


Figure 1.3: Backscattered electron image of emulsion features of Fe-rich (*Lfe*) and Si-rich (*Lsi*) silicate melts in the Wabar impactite. Adopted from Fig. 2d in Hamann *et al.*, 2013.

During the formation of these impact derived materials, different processes, impact conditions as well as element characteristics may lead to fractionation of these siderophile elements: (i) partitioning and diffusion processes of meteoritic matter within the still molten impact-induced melt (Koeberl, 1998), (ii) hydrothermal processes related with high-temperature impact melt (Wallace *et al.*, 1990), and (iii) different vaporization (and condensation) temperatures of the siderophile elements (Gibbons *et al.*, 1976). Quantification of these fractionation processes within impactites requires more sophisticated experiments using meteorite analogues; which is the main subject of the following subsection.

1.3 Experimental impact studies - fate and dissemination of the projectile

Along with the exploration of terrestrial and planetary craters, and numerical modeling of cratering processes, laboratory experiments are the most important tool to study vaporization of projectile and target material, formation of impact melts and possible chemical modifications of projectile and target during these processes. In the past 50 years, numerous studies on hypervelocity impact experiments were carried out, using different setups and different target and projectile materials. Most authors describe crater dimensions, such as size, depth, and shape as a function of projectile size and weight, velocity, and angle of impact (Moore *et al.*, 1963; Shoemaker *et al.*, 1963; Hörz, 1969, 2012; Gault, 1973; Polanskey & Ahrens, 1990; Grey *et al.*, 2002; Schultz, 2003; Cintala & Hörz, 2008). The projectiles were predominantly manufactured of artificial materials like steel, aluminum, lexan and polyethylene, and were accelerated onto basalt, granite, dolomite, sandstone, loose sand, chondritic material, metal (steel, Al, Fe, Mo) blocks and plates as well as onto ice. Projectile material and analytical methods used in previous experiments, however, neither allowed study of complex projectile-target interaction nor fractionation between siderophile elements typically used to identify and characterize a meteoritic component in nature (e.g., Palme *et al.*, 1981; Tagle & Hecht, 2006). While only a few experimental studies have dealt with the physical and chemical dissemination of the projectile during the impact process (e.g., Hörz *et al.*, 1983; Jammes *et al.*, 1983; Evans *et al.*, 1994; Rowan & Hörz, 1995; Wozniakiewicz *et al.*, 2011), the results of these experiments clearly show the importance of melting, vaporization and mixing of projectile and target in the cratering process. Jammes *et al.* (1983) impacted quartz sand targets vertically with aluminum projectiles. In these experiments, a small part of the projectile melt adjacent to the fused sand reacted with silica, but the major part of the projectile neither mixed into the target material nor reacted with it. Evans *et al.* (1994) observed heterogeneous distributions of projectile material among the ejecta. They found that the early high-angle ejecta between 55° and 75° are most projectile rich. Rowan & Hörz (1995) conducted shock recovery experiments using silicate projectiles (e.g., dunite) and diverse metal (e.g., Al and Cu) targets. The authors described physical mixing of projectile- and target melts, but did not observe significant chemical reactions between them. Wozniakiewicz *et al.* (2011) performed hypervelocity impact experiments with pyrrhotite as well as pentlandite projectiles and Al foil targets, as analogue to the Stardust mission. They observed fractionation processes during melting and mixing of molten projectile and target material. The sulfur of the projectiles was partially separated from the Fe and Ni, leaving nearly the original Ni- to Fe-ratio (Wozniakiewicz *et al.*, 2011). Furthermore, Gerasimov *et al.* (2005) performed laser pulse

vaporization experiments in order to simulate impact-induced vaporization. They showed that the vaporization of obsidian and augite (as analogues for Earth's crust chemical composition) starts with the loss of Si, Fe, and alkalis and consequently enrich in Mg, Ca, Al and Ti. The authors found a good possibility to recognize evaporative differentiation trends in natural impact glasses; based on the conservation of the initial Ca/Al ratio and the anti-correlation of Si and Al. The experiments of Gerasimov *et al.* (2005) are only focused on the chemical changes of some major elements of the target (without projectile) and are limited on analyses of condensed vapor.

This reflects the fact that still little is known about:

- 1. the small scale mechanical and geochemical mixing processes of projectile matter and target melts in impactites,**
- 2. the parameters that control inter-element fractionation between siderophile elements of the impactor during penetrating silicate-dominated natural targets**
- 3. the spatial dissemination of projectile material in the ejecta curtain during the excavation of the crater.**

These three points can be considered as the **main objectives** of this experimental work, which was conducted within the framework of the impact research unit MEMIN (**M**ultidisciplinary **E**xperimental and **M**odeling **I**mpact research **N**etwork; Kenkmann *et al.*, 2011, 2013).

1.4 The MEMIN hypervelocity impact experiments

Central to MEMIN were two-stage light gas accelerators (placed at the Fraunhofer Ernst-Mach Institute in Freiburg, Germany) capable of producing craters in the decimeter-range in solid rocks, a size previously not achieved at the laboratory scale that enables detailed spatial analysis. Two-stage light gas gun launchers use highly compressed hydrogen to accelerate projectiles at velocities in excess of $6 \text{ km} \times \text{s}^{-1}$. For more details on the working principle and specifications of the used two-stage light gas gun, see Lexow *et al.* (2013). The hypervelocity impact experiments (HIE) on silica-rich targets comprised parametric studies of the role of water, porosity, target layering, and impact velocity on cratering mechanics, shock effects, and projectile distribution during cratering. An overview of all MEMIN experiments and its experimental setting are compiled in Poelchau *et al.* (2013). This dissertation presents results of 6 different MEMIN hypervelocity cratering experiments using iron meteorite (Campo del Cielo) and steel spheres (D290-1) as projectile and sandstone and quartzite targets. These projectile and target materials were chosen due to their strong chemical difference among each other and their relative homogeneity itself. The use of well-characterized projectile material is mandatory for this project of the MEMIN research unit. The experimental setup enables (i) explicit identification of minute particles or condensates of the projectile, and (ii) determination of mixing and/or fractionation processes between projectile and target matter. Quartzite and sandstone targets were used in order to determine the possible effect of different target porosities ($\sim 0 \%$ vs. $\sim 23 \%$ porosity) and water-saturation (dry or $\sim 50 \%$ wet sandstones) on geochemical processes between projectile and target. The variation of different projectile sizes at constant velocity enables further insights

in the effect of impact energies. Furthermore, the combination of Campo del Cielo iron meteorite and sandstone enables a comparison between experimental results with data from natural craters. This is possible since from 184 known craters, in 41 cases an iron meteorite impacted into silica-rich targets; like the Wabar craters (Saudi Arabia) and Meteor crater (USA), just to mention two of them (Goderis *et al.*, 2012).

1.5 Laser-induced melting experiments

In addition to the MEMIN hypervelocity impact experiments so-called laser-induced melting experiments (LE) were performed at the laser welding facility of the Technical University of Berlin. The aim of these type of experiments was to produce target and projectile melts under more idealized conditions. This method allows (i) separate (partial) melting of target and projectile material to be produced to better constrain "primary" melt heterogeneities before mixing occurs, and (ii) mixing of larger amounts of projectile and target melts to receive better conditions for micro-analytical studies (e.g. to allow larger spot sizes for trace element analysis of glasses). The laser-induced melting technique simulates high-temperature effects of an impact; typical shock effects were not produced with this method.

1.6 Structure of the thesis

The structure of this thesis is divided in three major parts. The first part provides a general introduction into the scientific framework of the thesis (Chapter 1). The second part comprises three manuscripts (see list below) and two further chapters, in which the scientific work and the results carried out in this study are documented and discussed (Chapters 2-6). A detailed comparison between the present experimental study and natural observation is given in chapter 6, which contains extracts from two published papers in which I appeared as co-author during the time as PhD student. An overall conclusion and an outlook (part three) of this thesis can be found in the last chapters 7 and 8, respectively.

Included manuscripts:

Chapter 2: "Ebert M.¹, Hecht L.¹, Deutsch A.³, and Kenkmann T.⁴ (2013) Chemical modification of projectile residues and target material in a MEMIN cratering experiment. *Meteoritics & Planetary Science*, 48: 134-149"

Chapter 3: "Ebert M.^{1, 2}, Hecht L.^{1, 2}, Deutsch A.³, and Kenkmann T.⁴, Wirth R.⁵, Berndt G.³ (2014). Geochemical processes between steel projectiles and silica-rich targets in hypervelocity impact experiments. *Geochimica et Cosmochimica Acta*, 133: 257-279."

Chapter 5: "Ebert M.¹ and Hecht L.^{1,2} (in preparation). Are laser-induced melting experiments suitable to simulate meteorite impact processes?" This chapter is almost ready for submission in *Meteoritics & Planetary Science*.

Affiliations (short form):

- (1) Museum für Berlin - Leibniz-Institut für Evolutions- und Biodiversitätsforschung
- (2) Freie Universität Berlin - Fachbereich Geowissenschaften
- (3) Westfälische Wilhelms-Universität - Fachbereich Planetologie
- (4) Albert-Ludwigs-Universität Freiburg - Fachbereich Geowissenschaften
- (5) GeoForschungsZentrum Potsdam - Sektion: Chemie und Physik der Geomaterialien

1.7 Contribution of the author and co-authors to the individual manuscripts and additional chapters

This thesis is mainly a cumulative dissertation and therefore consists of three individual manuscripts (Chapters 2, 3 and 5). The first two are already published (chapter 2 and 3); the last (chapter 5) is almost ready for submission in an international, peer-reviewed scientific journal. Each author's contribution to the individual manuscripts will be outlined in the following subsection. The manuscripts of chapter 2,3 and 5 were based on a proposal (Research group: The MEMIN-Program (Multidisciplinary Experimental and Modeling Impact Research Network; FOR 887; Sub-project: "On the fate of the projectile in impact cratering experiments; DE 401/23-1 and HE 2893/8-1) by L. Hecht, A. Deutsch and T. Kenkmann; who provided the basic ideas for the research carried out.

M. Ebert entirely wrote preliminary and final versions of all manuscripts and reviewed the relevant literature. All figures and tables in the three manuscripts were prepared by M. Ebert. He collected the investigated samples at the MEMIN campaigns, carried out the major part of the geochemical analytical work and interpreted all data with support from L. Hecht. L. Hecht, who is also the main supervisor of this thesis, did critical reviews and therefore is co-author of all manuscripts. Support during time-consuming hand picking and sorting of relevant sample material was given by students during their internship at MfN

Chapter 2 (manuscript I): Preliminary versions of the manuscript were improved in respect to focus, clarity and readability in discussions and reviews of A. Deutsch and T. Kenkmann. The chapter focuses on the complex chemical and mechanical mixing processes and shock features in ejecta fragments from a hypervelocity impact experiment with a projectile of Campo del Cielo iron meteorite and a sandstone target.

Chapter 3 (manuscript II): Preliminary versions of the manuscript were improved in respect to focus, clarity and readability in discussions and reviews of A. Deutsch and T. Kenkmann. R. Wirth provided laboratory assistance during TEM measurements at the GeoForschungsZentrum Potsdam. He also helped in interpreting some of the TEM data. J. Berndt provided laboratory assistance during an analytical session at the Westfälische Wilhelms-Universität for LA-ICP-

MS measurements of the steel projectile material. The chapter presents results of the MEMIN parameter study in which the influence of impact energy, water-saturation of the target and target porosity on element fractionation was studied. Therefore, different hypervelocity impact experiments with steel (projectile) and sandstone as well as quartzite (target) were investigated.

Chapter 4 (additional chapter): M. Ebert entirely wrote this chapter. C. Hamann (PhD student, intern and former BSc, FU Berlin) helped with sample preparation and created Fig. 4.3 in this chapter. All other figures and tables were prepared by M. Ebert. This chapter deals with the spatial distribution of the highly shocked and projectile rich ejecta during the excavation of the crater.

Chapter 5 (manuscript III): The basic ideas of the third manuscript and the experimental approach in this manuscript were developed in close cooperation with L. Hecht. This manuscript contains results from laser-induced melting experiments which were performed in order to gain an additional control on the melting behavior and chemical mixing of projectile and target materials.

Chapter 6 (additional chapter): M. Ebert entirely wrote the chapter. It is focused on the applicability of the experimental results to nature observations and provides further details of geochemical processes between impactor and target material in natural impactites. Some aspects of this chapter have been published in two papers where I appear as a co-author.:

(I) Kenkmann, T., Trullenque, G., Deutsch, A., Hecht, L., **Ebert, M.**, Salge, T., Schäfer, F., Thoma, K. (2013) Deformation and melting of steel projectiles in hypervelocity cratering experiments. *Meteoritics and Planetary Science* **48**, 150-164.

My contributions (5%) to this publication includes providing of the relevant samples, creating contents for figures and tables, and reviewing the manuscripts.

(II) Hamann, C., Hecht, L., **Ebert, M.**, Wirth, R. (2013) Chemical projectile-target interaction and liquid immiscibility in impact glass from the Wabar craters, Saudi Arabia. *Geochimica et Cosmochimica Acta* **212**, 291-310.

I was involved in the supervision of the BSc student Christopher Hamann, including interpretation of geochemical data and reviewing of manuscripts. My contributions to this paper is about 10%.

2 Chemical modification of projectile residues and target material in a MEMIN cratering experiment.

Matthias Ebert^{1,*}, Lutz Hecht¹, Alexander Deutsch², Thomas Kenkmann³

(published 2013 in *Meteoritics and Planetary Science* **48**, 150-164; DOI: 10.1111/j.1945-5100.2012.1429.x)

⁽¹⁾Museum für Berlin - Leibniz-Institut für Evolutions- und Biodiversitätsforschung, Invalidenstr. 43, D-10115 Berlin, Germany; ⁽²⁾Westfälische Wilhelms-Universität, Institut für Planetologie, Wilhelm-Klemm-Str. 10, D-48149 Münster, Germany; ⁽³⁾Albert-Ludwigs-Universität Freiburg, Institut für Geowissenschaften, Albertstr. 23-B, D-79104 Freiburg, Germany; ^(*)Correspondence author's e-mail address: *matthias.ebert@mfn-berlin.de*

2.1 Abstract

In the context of the MEMIN project, a hypervelocity cratering experiment has been performed using a sphere of the iron meteorite Campo del Cielo as projectile accelerated to $4.56 \text{ km} \times \text{s}^{-1}$, and a block of Seeberger sandstone as target material. The ejecta, collected in a newly designed catcher, are represented by (1) weakly deformed, (2) highly deformed, and (3) highly shocked material. The latter shows shock-metamorphic features such as planar deformation features (PDF) in quartz, formation of diaplectic quartz glass, partial melting of the sandstone, and partially molten projectile, mixed mechanically and chemically with target melt. During mixing of projectile and target melts, the Fe of the projectile is preferentially partitioned into target melt to a greater degree than Ni and Co yielding a Fe/Ni that is generally higher than Fe/Ni in the projectile. This fractionation results from the differing siderophile properties, specifically from differences in reactivity of Fe, Ni and Co with oxygen during projectile-target interaction. Projectile matter was also detected in shocked quartz grains. The average Fe/Ni of quartz with PDF (~ 20) and of silica glasses (~ 24) are in contrast to the average sandstone ratio (~ 422), but resembles the Fe/Ni-ratio of the projectile (~ 14). We briefly discuss possible reasons of projectile melting and vaporization in the experiment, in which the calculated maximum shock pressure does not exceed 55 GPa.

2.2 Introduction

Impact cratering has been, and still is, a major process in the origin and evolution of all the solid bodies of the solar system (French 1998). Only under rare circumstances are natural impacts observed directly, e.g. the impact at Sikhote-Alin, Russia (Krinov and Fesenkov 1959), the Carancas event, Peru (Kenkmann *et al.*, 2009), or the collision of Shoemaker-Levy 9 with Jupiter (Weaver *et al.*, 1995). Projectiles that cause impact events can be preserved in the form of fragmental residues or geochemical traces. For instance, small and young craters that are formed by the impact of iron meteorites like the recently discovered Kamil crater (Egypt; D'Orazio *et al.*, 2011), Wabar crater (Saudi Arabia; Mittlefehldt *et al.*, 1992), and even the 1.2 km diameter Meteor crater (Arizona, USA; Mittlefehldt *et al.*, 2005) each contain, or lie amidst debris containing strong deformed fragments of projectiles (shrapnels) as well as melted, disseminated residues in impact breccias and crater floor fractures. At larger craters, the nature of the impactor can usually be only deciphered by means of geochemical analysis of siderophile

elements in melt-bearing rock types. The process(es) of mixing projectile matter into target and impactite materials are far from being understood (e.g., Evans *et al.*, 1994; Mittlefehldt *et al.*, 1992). It could be emplaced in a vapor phase, as melt droplets or as fine-grained solid material. Along with the exploration of terrestrial and planetary craters, and numerical modeling of cratering processes, laboratory experiments are the most important tool to study impact processes. In the past 50 years, numerous studies on hypervelocity impact experiments were carried out, using different set-ups and different target and projectile materials. Most authors describe crater dimensions, such as size, depth, and shape as a function of projectile size and weight, velocity, and angle of impact (Cintala and Hörz 2008; Gault 1973; Grey *et al.*, 2002; Hörz 1969, 2012; Moore *et al.*, 1963; Polansky and Ahrens 1990; Schultz 2003; Shoemaker *et al.*, 1963). The projectiles were predominantly manufactured of artificial materials like steel, aluminum, lexan and polyethylene, and were accelerated onto basalt, granite, dolomite, sandstone, loose sand, chondritic material, metal (steel, Al, Fe, Mo) blocks and plates as well as onto ice.

Projectile material and analytical methods used in previous experiments, however, neither allowed study of complex projectile-target interaction nor fractionation between siderophile elements typically used to identify and characterize a meteoritic component in nature (e.g., Palme *et al.*, 1981; Tagle and Hecht 2006). The identification of meteoritic matter in impact melt rocks relies on the study of siderophile elements such as Fe, Ni, Co, and Cr and the platinum group elements (PGE), which are significantly enriched in meteorites compared to terrestrial rocks (e.g., Palme *et al.*, 1981). While only a few experimental studies have dealt with the physical and chemical dissemination of the projectile during the impact process (Evans *et al.*, 1994; Hörz *et al.*, 1983; Jammes *et al.*, 1983; Rowan and Hörz 1995; Wozniakiewicz *et al.*, 2011), the results of these experiments clearly show the importance of melting, vaporization and mixing of projectile and target in the cratering process. Jammes *et al.*, (1983) impacted quartz sand targets vertically with aluminum projectiles. In these experiments, only a small part of the projectile melt adjacent to the fused sand reacted with silica but the major part of the projectile neither mixed into the target material nor reacted with it. Evans *et al.*, (1994) observed heterogeneous distributions of projectile material among the ejecta. They found that the early high-angle ejecta between 55° and 75° are most projectile rich. Rowan and Hörz (1995) conducted shock recovery experiments using silicate projectiles (e.g., dunite) and diverse metal (e.g., Al and Cu) targets. The authors described physical mixing of projectile- and target melts, but did not observe significant chemical reactions between them. Wozniakiewicz *et al.*, 2011 performed hypervelocity impact experiments with pyrrhotite as well as pentlandite projectiles and Al foils targets, as analogue to the Stardust mission. They observed fractionation processes during melting and mixing of molten projectile and target material. The sulfur of the projectiles was partially separated from the Fe and Ni, leaving nearly the original Ni to Fe ratio (Wozniakiewicz *et al.*, 2011).

However, little is known about processes that control inter-element fractionation between siderophile elements during cratering on silicate-dominated natural targets. The impact research unit MEMIN (Multidisciplinary Experimental and Numerical Impact research Network) is aimed at a better understanding of impact crater formation by using fully instrumented mesoscale hypervelocity cratering experiments in combination with numerical modeling and a thorough

post-mortem investigation of the crater, the ejecta, and the projectile remnants (Kenkmann *et al.*, 2011; 2012). Here, we present results of one MEMIN hypervelocity cratering experiment using an iron meteorite sphere as projectile and a sandstone target. Sandstone and iron meteorite were chosen due to their strong chemical difference (Table 1). This setup enables (i) explicit identification of minute particles or condensates of the projectile, and (ii) determination of mixing and/or fractionation processes between projectile and target matter. Hence, the use of well-characterized projectile material is mandatory for this project of the MEMIN research unit. This study addresses a fundamental topic in impact cratering, namely the fate of the projectile upon impact, although our experimental impact velocities are lower than most planetary impacts.

2.3 Experimental and analytical methods

2.3.1 Experimental setup

The MEMIN experiment under discussion (D3-3298) was carried out with the extra large two-stage light gas gun (Lexow *et al.*, 2013). For experiment D3-3298 a spherical projectile (\varnothing 10 mm, weight 4.12 g) was manufactured at the EMI machine shop on a lathe from a piece of the iron meteorite Campo del Cielo. The projectile impacted along a horizontal trajectory with a velocity of $\sim 4.56 \text{ km} \times \text{s}^{-1}$ onto a 50 x 50 x 50 cm sized cube of air-dry Seeberger Sandstein, a sandstone from the Thuringian basin in Germany. The impact energy was calculated at $\sim 43 \text{ kJ}$, the estimated peak pressure at the contact between projectile and target is 55 GPa, using the planar impact approximation with Coconino sandstone and steel parameters (Melosh, 1989). The target chamber was evacuated to 0.3 bar during the shot, to reduce deceleration of the projectile in flight and turbulent deflection of the ejecta. Material ejected from the crater was collected with a newly designed catcher system, in which bricks of phenolic foam and tiles of degassed petrolatum were assembled in a modular system (Reiser *et al.*, 2011). The catcher was mounted parallel to the target surface at a distance of 53 cm and had a 12 cm diameter entry hole for the projectile. Impact and ejection processes were recorded with a high-speed camera at 105 frames per seconds. After the shot, the target chamber was flooded with air; loose particles were collected from the bottom of the target chamber. The impacted sandstone block and the catcher assemblage were carefully removed for further investigation. The ejecta fragments analyzed in this study originate from the "inner zone" of the green phenolic foam plates (Sommer *et al.*, 2013). They were recovered from the small green foam pieces with tweezers and brushes. The position of single ejecta pieces was recorded for determination of the ejecta angle. The "inner zone" of the catcher system contains material which was ejected with angles between 70° and 85° to the target surface.

2.3.2 Analytical techniques

The recovered ejecta particles were characterized by optical and scanning electron microscopy (JEOL JSM-6610LV) at the MfN Berlin. Quantitative chemical analyses were performed at the MfN Berlin with the JEOL JXA-8550F electron microprobe, equipped with a field emission gun and 5 wavelength-dispersive spectrometers. Analytical conditions varied, depending on the measured phase. Projectile residues were measured with 15 kV accelerating voltage and 50 nA

beam current; sandstone melt with 15 kV and 30 nA. The sample spot-size varied between 1 μm for metallic components and 3 μm for silicate components. We used pure element standards for Fe, Ni, and Co, and mineral standards for the other elements. The raw data were processed for matrix effects using a conventional ZAF routine in the JEOL series program. Special analytical conditions were applied to trace Fe and Ni at low concentrations in the order of a few 100 ppm (e.g., in shocked quartz). In this case Fe and Ni were analyzed at 15 kV, 60 nA, 60 s counting time on peak and background and adding the counting rates of two spectrometers. The JEOL software enables a detailed consideration of possible peak overlapping between the different emission lines of Fe and Ni (and Co). A detection limit (D.L.) of 100 ppm was achieved for Ni (D.L. of Fe 200 ppm) using the JEOL calculation method:

$$D.L. = \frac{1}{\frac{I_{netSTD}}{mass(\%)_{STD}}} \sqrt{\frac{2 * I_{netSTD}}{t_{back}}}$$

where I_{back} is the average intensity of the background X-rays, t_{back} is the counting time of the background signals in seconds, I_{netSTD} is the intensity of net X-rays of the standard sample, and $mass(\%)_{STD}$ is the mass concentration in the standard sample. The accuracy of the measurements was in the order of 5 to 10 % tested on two NIST glass standards (NIST SRM 610 and 612; Table 2.1). For measurements on the NIST standards the average of 112 measurements performed with a defocused beam (20 μm) was used as Ni is distributed slightly heterogeneously in these materials (Jochum *et al.*, 2011). Therefore, the precision of trace element analysis is most likely better than the values given in Table 2.1, which include the standard heterogeneity. Even at concentrations below the calculated D.L., the standard values were reproduced with a rather high accuracy of 10 % (see Table 2.1). Whole rock geochemical analysis of the target sandstone was carried out using X-ray fluorescence spectroscopy (XRF, Siemens SRS 3000) at the MfN Berlin on glass tablets. In order to get precise values for Ni, Co and Cr, additional measurements were conducted with ICP-MS (ALS Environmental Lab, Vancouver). The proportion of the phyllosilicate-bearing matrix on the sandstone whole rock was determined in two steps on thin sections: First, element-mapping with SEM, and second, calculation with an image analysis program (ImageJ).

2.4 Results

2.4.1 Composition of target and projectile

2.4.1.1 Target (Seeberger Sandstein)

The Seeberger Sandstein, a sandstone of Rhaetian age was chosen as target material. Blocks were cut from the stratigraphic layer 3, which is characterized by fine-grain sizes of 76 - 125 μm , high quartz content, a visible but not dominant layering, and a porosity of 23 ± 1 vol.% of the bulk sandstone volume. The sandstone is comprised of ~ 89 vol.% quartz, ~ 10 vol.% phyllosilicate (evaluated by graphical analysis of EDX element-mapping images), and traces of accessory minerals (rutile, altered ilmenite, zircon, rare iron-oxides/hydroxides). The phyllosilicates, mostly clay minerals and subordinate micas, account for the majority of the sandstone matrix forming coatings around quartz grains and occasional accumulations of fine material within the pore space between the frameworks of quartz grains (Fig. 2.2). Individual phyllosilicate flakes of the matrix are smaller than 10 μm . The rare detrital micas have a grain size on

the order of 100 μm . The composition of the sandstone and its phyllosilicate bearing matrix is given in Table 2.2

2.4.1.2 Projectile (Campo del Cielo meteorite)

The Campo del Cielo (CDC) meteorite was chosen as a material that represents natural "meteorite" impacts. Furthermore, large homogenous Fe-meteorite pieces are available to produce multiple identical projectiles that are also strong enough to resist the stresses that occur during the hypervelocity acceleration. Campo del Cielo is a IAB iron meteorite that belongs to the group of coarse octahedrites (Og) with a Widmannstätten pattern bandwidth of 3.0 ± 0.6 mm (Buchwald, 1975). The Campo del Cielo meteorite has a homogenous kamacite matrix, minor amounts of taenite, plessite, schreibersite, and rhabdite (Fig. 2.1), that are distributed irregularly, as well as some rare silicate-inclusions. The modal composition of the meteorite and the chemical compositions of each phase are listed in Table 2.2. Taenite and plessite appear only as degenerated comb plessite or as pearlitic fields, in sizes smaller than 3×1 mm (Buchwald, 1975). The most elongated taenites vary in composition. They predominantly have Ni-poor (Fe-rich) cores and Ni-rich (Fe-poor) rims. Iron-nickel phosphides $(\text{Fe,Ni})_3\text{P}$ occur in two different textural modes in the Campo del Cielo meteorite: elongate idiomorphic rhabdites of micrometer-scale width (Fig. 2.1b) within coarser kamacite (e.g. Oshtrakh *et al.*, 2011), and coarser blocky schreibersite macro-inclusions ($50 - 200 \mu\text{m}$; Fig. 2.1a). The schreibersite crystals are often fractured, presumably by the same stress that formed the Neumann bands (mechanical deformation twins) in the kamacite matrix (Bunch & Cassidy, 1968). The silicate-inclusions occur as cm-sized lenses and have an average composition of 37.9 vol.% forsterite, 35.3 vol.% chrome-diopside, 18.4 vol.% enstatite and 8.4 vol.% oligoclase (Park *et al.*, 1966). Material with silicate inclusions was avoided during preparation of the meteorite projectiles. Micro-CT scans (EMI) have been carried out to characterize the meteorite projectiles in terms of internal fractures, and distribution of the different mineralogical components.

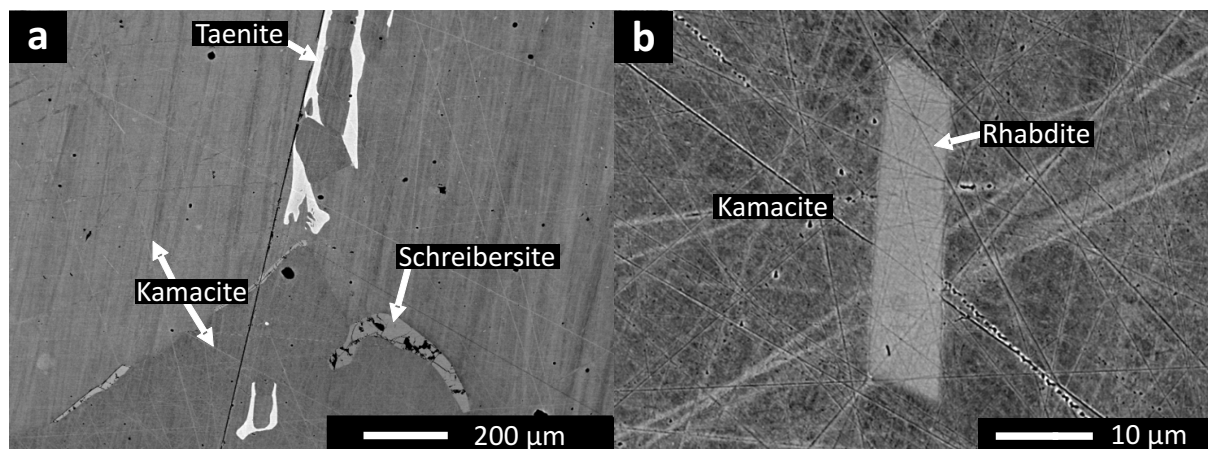


Figure 2.1: (a) Back-scattered electron image (BSE) of the Campo del Cielo meteorite with various phases. (b) Rhombohedral rhabdite in kamacite matrix of the Campo del Cielo meteorite projectile.

2.4.2 Ejecta types

The different ejecta fragments were distinguished according to macro- and microscopic features (Fig. 2.2, 2.3). The ejected material is represented *inter alia* by weakly deformed, highly deformed, and highly shocked ejecta fragments. These three types represent end members of different shock-metamorphic states. Consequently the ejecta contain fragments with intermediate stages between weakly deformed and highly shocked fragments. This study is focused on the geochemical interaction between projectile and target material. Although only the highly shocked ejecta contain projectile material, we also characterize weakly and highly deformed ejecta in order to allow comparison between the unshocked sandstone with its shocked counterparts. Detailed information about grain size distributions of the ejecta are presented in Sommer *et al.* (2013).

The *weakly deformed ejecta* fragments represent almost unstressed μm - to mm-sized sandstone fragments of yellow-beige color, with a completely preserved original pore (Fig. 2.2a). The quartz grains very rarely display cracks and fractures; the phyllosilicate-bearing matrix also lacks evidence for mechanical stress (Fig. 2.2b). The intensity of sandstone deformation in these fragments is comparable with ejecta type 1 of Kenkmann *et al.* (2011).

The *highly deformed ejecta fragments* show a distinctive white color (Fig. 2.2c). They occur as μm - to mm-sized fragments, but are on average smaller than weakly deformed ejecta material. Fracturing in quartz is typical, causing disintegration of the original texture (Fig. 2.2d). This strong fracturing increases the surface area of the quartz, so that the fragment appears macroscopically white. The shock significantly reduced the pore space and compressed and deformed phyllosilicates of the matrix so that individual grains are barely recognizable. Large micas were strongly deformed (Fig. 2.2d). The highly deformed ejecta show no evidence of melting or other shock-metamorphic features, and projectile admixture has not been found. The intensity of deformation, indicated by the micro-structures, is comparable with the type 3 sandstone deformation in Kenkmann *et al.* (2011). Kiefer (1971) described similar features in shocked fragments of the Coconino sandstone in Meteor crater, which are characterized by a "snow white" color.

The *highly shocked ejecta fragments* are represented by white-gray variegated, μm - to mm-sized fragments (Fig. 2.3). In these ejecta fragments, the microstructure of the unshocked sandstone is completely lost. Moreover, the highly shocked ejecta fragments show various shock-metamorphic features including multiple sets of planar deformation features (PDF) in quartz, the onset to complete transformation of quartz to fused silica glass, and partial melting of the sandstone (Figs. 2.4, 2.5). This partial melting of the sandstone mainly comprises the phyllosilicate-bearing matrix but involves quartz, too. The presence of vesicles in the shock-produced melt substantiates the release of volatiles from the phyllosilicates during melting (Figs. 2.4, 2.5b). However, vesicles also exist within partly melted quartz grains where no phyllosilicates were intruded (Fig. 2.4).

Fig. 2.4a illustrates differences in the degree of shock-metamorphic overprint in quartz over a narrow area in one ejecta fragment: in the interior of grain Qtz-A, we see two sets of PDF together with some irregular cracks while onset of melting occurs at the grain margins. Grain Qtz-B shows an even higher degree of melt formation: melting starts at the rim and propagates along cracks and PDF. In this grain, the PDF are slightly expanded compared to the PDF of

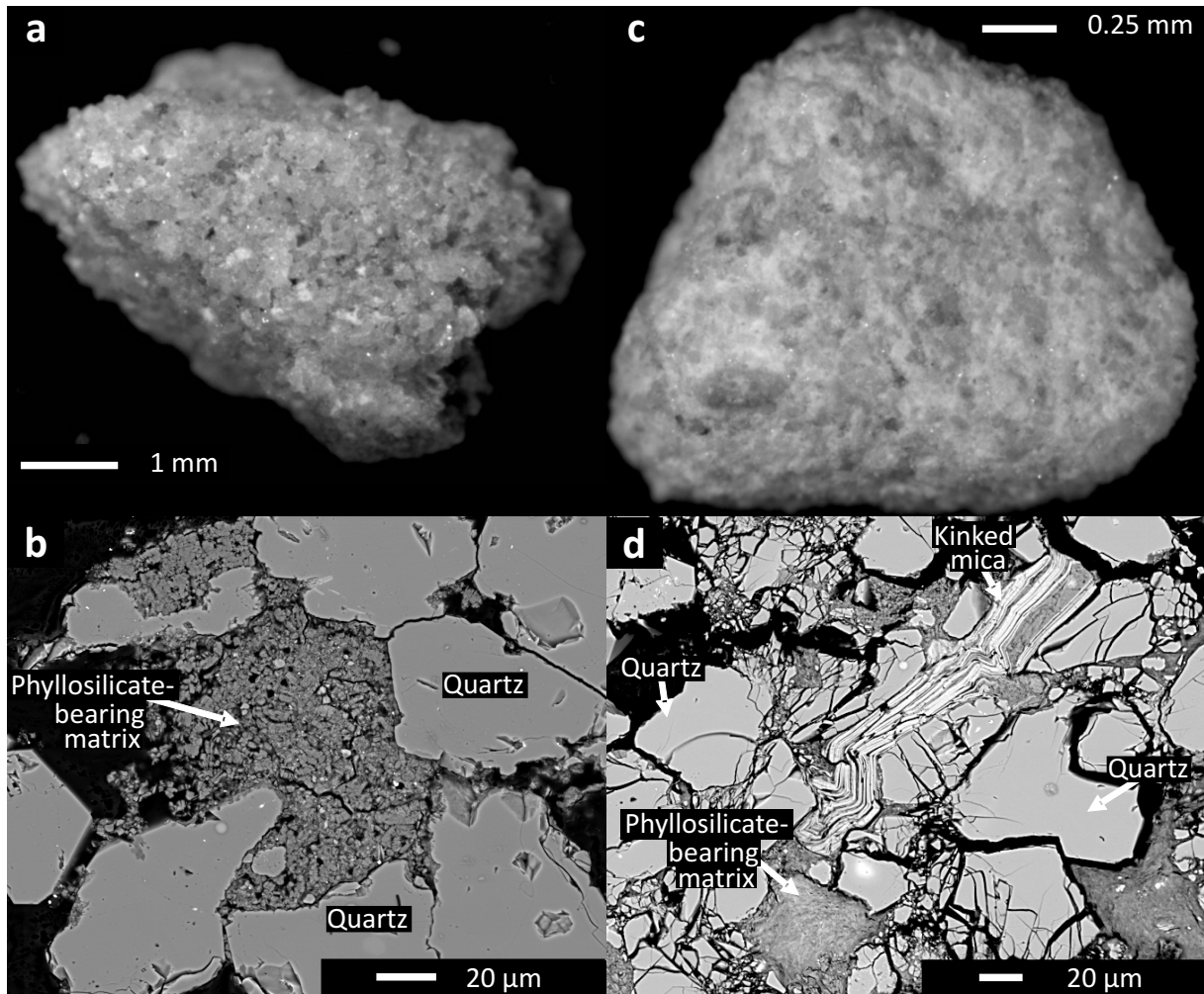


Figure 2.2: (a) Photomicrograph and (b) BSE image of a weakly deformed ejecta fragment; for detailed explanation see text. (c) Photomicrograph and (d) BSE image of a highly deformed ejecta fragment; for detailed explanation see text.

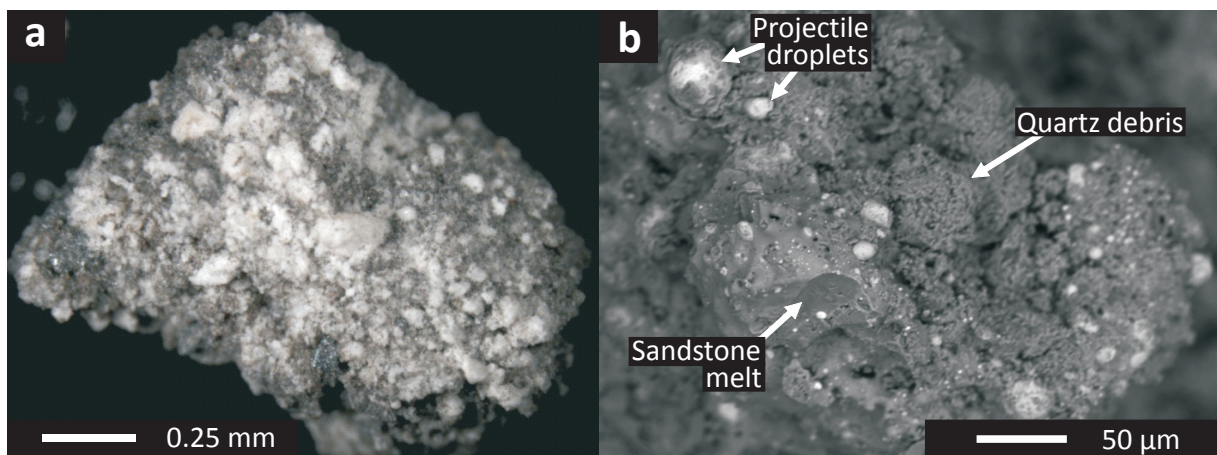


Figure 2.3: Photomicrograph (a) and scanning electron microscope image - BSE mode (b) of a highly shocked ejecta fragment; for detailed explanation see text.

Qtz-A. Qtz-C, however, is almost completely transformed into silica glass. Slightly brighter areas in Qtz-C are the only remnants of the original quartz. Vesicles in Qtz-C are lined up along these unmelted relics. We observed traces of turbulent movement, such as schlieren of silica glass in the upper part of Qtz-C. The small sinuous silica glass between Qtz-A and Qtz-C also indicates movements in the sandstone melt. The alignment of vesicles in Qtz-C indicates melting and healing along a former crack. Fig. 2.4b shows further sets of PDF in quartz as well as the formation of glass along a fracture. The density contrast between crystalline and amorphous SiO_2 is clearly visible in this back-scattered electron (BSE) image with amorphous parts of lower density (PDF lamellae and fused silica glass) displaying a darker gray in the BSE-mode.

The gray parts of the highly shocked ejecta fragments are caused by finely disseminated projectile matter mixed with partially molten sandstone (Fig. 2.3, Fig. 2.5). Projectile material is mechanically injected into the sandstone to various amounts. During the impact, the Campo del Cielo projectile was transformed into different states, comprising (i) partly fused fragments containing shocked schreibersite, melt pockets and molten margins and, (ii) projectile droplets. (i) Partly fused fragments (150 - 500 μm) usually have molten margins, which are generally rich in vesicles (Fig. 2.5c). Small melt pockets (10 - 40 μm) occur within these projectile fragments (Fig. 2.5d). (ii) The melt pockets consist of two coexisting melts of different composition. One melt is situated at the rim of the melt pocket and appears brighter in the BSE image due to higher mean atomic number. The other melt of lower mean atomic number is located in the center of the melt pocket. Projectile fragments that show such melt pockets and molten margins are named "partly fused projectile fragments" in this study. In addition, a metallic melt forms immiscible droplets (spherical and spheroidal shape) in the sandstone melt. Fig. 2.4a and Fig. 2.5b demonstrate that metallic droplets have entered the low-viscosity sandstone melt but not the fused silica glass. The size of the metallic droplets ranges from a few nanometers up to 50 μm . The spheroidal shape is caused by surface tension at the contact with quartz. Mineralogical and geochemical features in the highly shocked ejecta fragments are the most interesting results of this study, and they are described in more detail in the following sections.

2.4.3 Chemical modification of the sandstone

As described above, the sandstone melt is produced by preferential melting and mixing of the phyllosilicate-bearing sandstone matrix and quartz. In rare cases, rutile is involved. Melting of the sandstone resulted in melts of quite different compositions with SiO_2 contents of 50.6 to 89.1 wt.%, Al_2O_3 of 2.51 to 16.4 wt.%, FeO of 5.78 to 32.3 wt.%, and NiO of 0.01 to 0.33 wt.% (Table 2.3). The chemical composition of the sandstone melt is variable at the scale of micrometers. Especially remarkable is the highly variable FeO content in the sandstone melt (Fig. 2.6). Fig. 2.6 and Fig. 2.7 show metal contents instead of metal oxides allowing inclusion of Campo del Cielo meteorite data (non-oxide) into the diagrams. Although a certain fraction of iron in the sandstone melt obviously originated from the phyllosilicate-matrix, the amount of iron-oxides/hydroxides (forming the occasional staining of the sandstone) is simply too low to contribute to the Fe budget of the melt (see Table 2.2; 0.45 % Fe_2O_3 in Seeberger Sandstein). The FeO content in most of the analyzed sandstone melt patches is higher than the average FeO content of the phyllosilicate matrix (3.25 ± 2.60 wt.%; Table 2.2). The FeO concentration

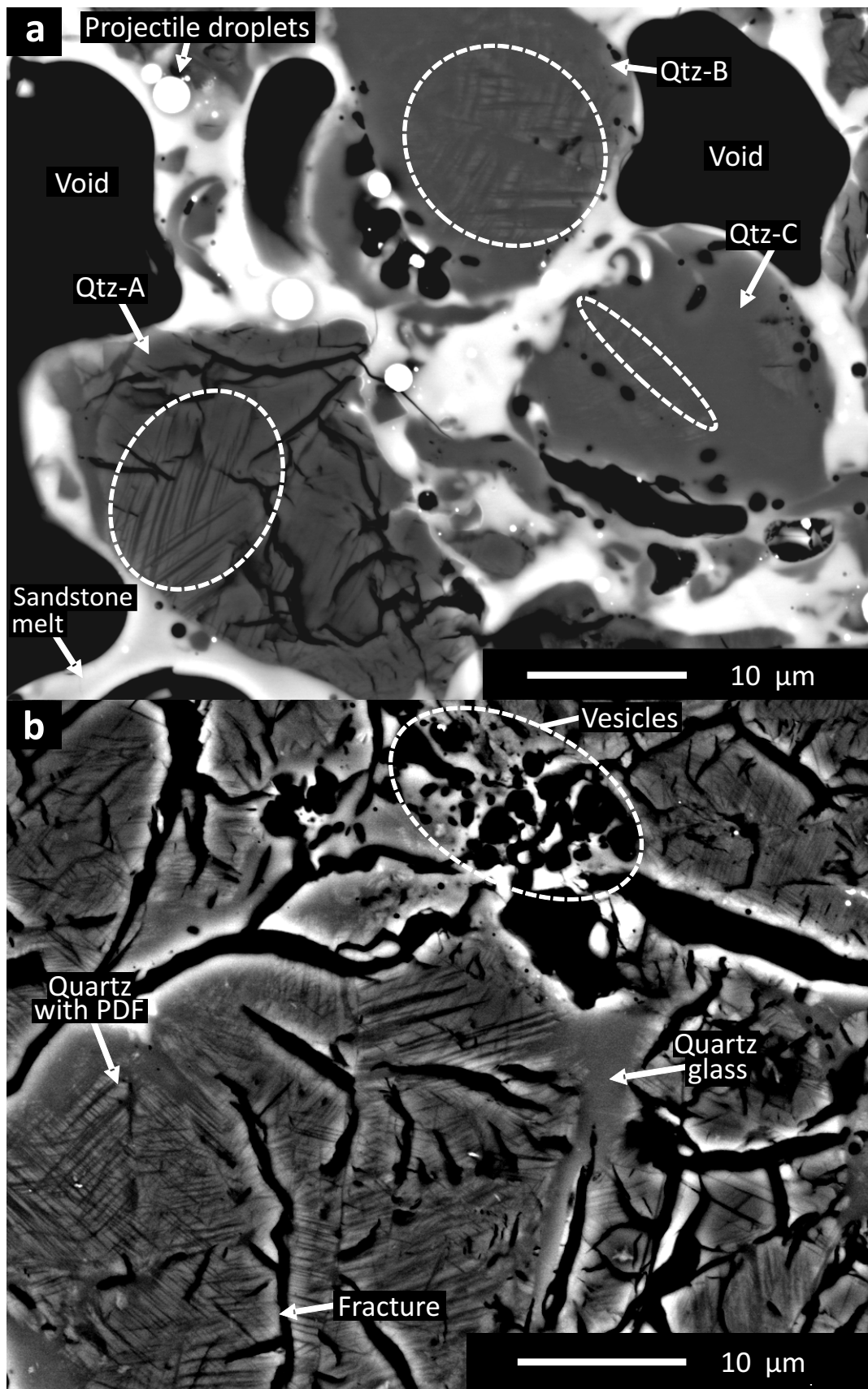


Figure 2.4: (a) Shock-metamorphic features of the sandstone and projectile droplets (BSE-image). (b) Different sets of PDF in quartz and produced silica glass (BSE-image); for detailed explanation see text.

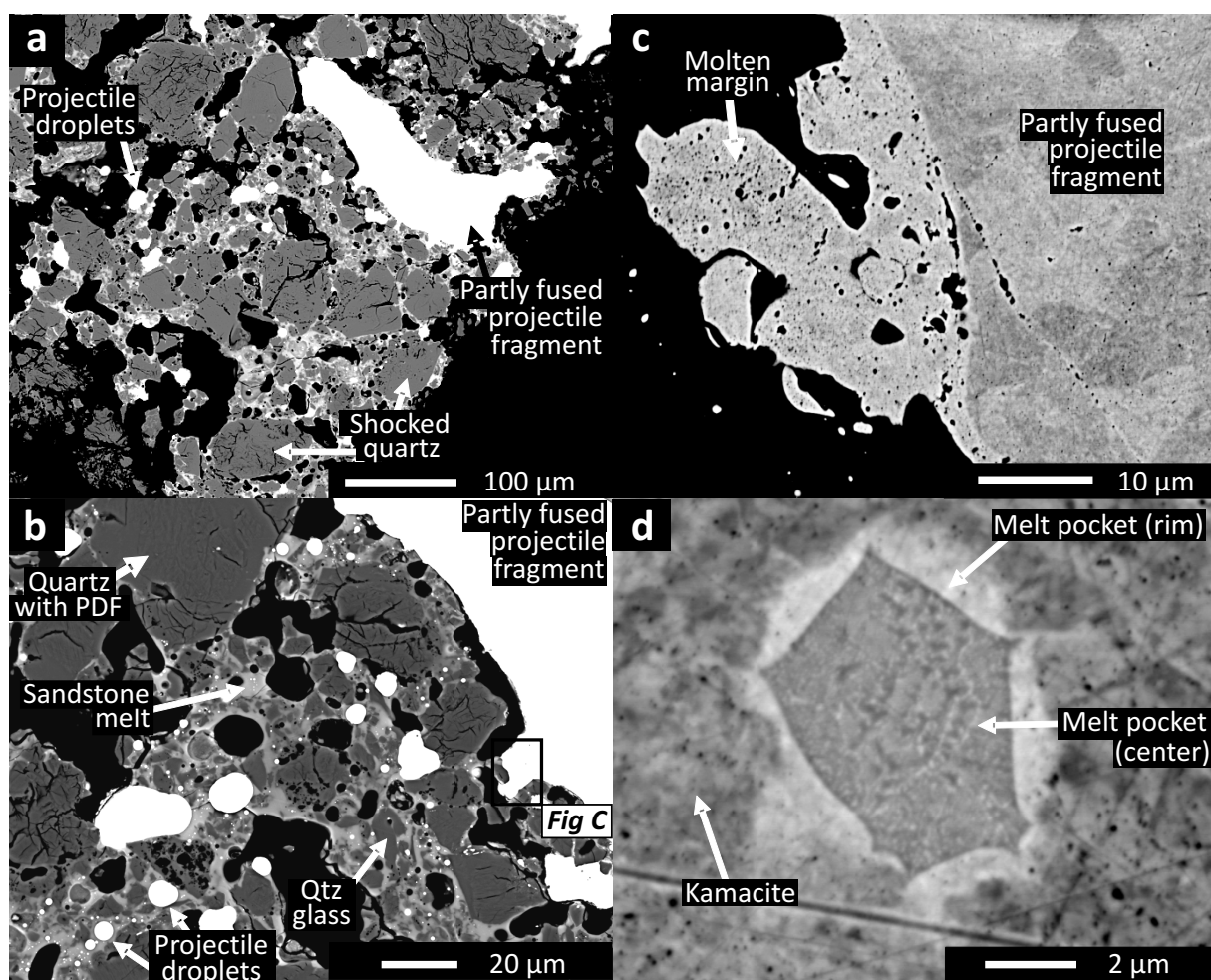


Figure 2.5: (a, b) BSE image of a highly shocked ejecta fragment showing typical textures and components. (c) Magnification of 2.5b shows a molten margin of a partly fused projectile fragment; due to the high contrast the silicate phases on the left side are not visible (BSE-image). (d) Typical melt pocket (center) with a rim in a partly fused projectile fragment; for detailed explanation see text.

roughly shows a positive correlation with the Al_2O_3 content of the sandstone melt. NiO is also slightly enriched in the sandstone melt compared to the bulk sandstone (Fig. 2.7). Within the sandstone melt, Fe/Ni remains generally one to two orders of magnitude below that ratio in the projectile; yet it is shifted in some cases to lower Fe/Ni (Fig. 2.7). The shocked quartz with PDF and silica glass also show FeO and NiO enrichment compared to unshocked Qtz grains (Fig. 2.7). Quartz with PDF, and silica glass both contain minor FeO (< 1.1 wt.%) and NiO (< 0.06 wt.%). The average FeO content of shocked Qtz is 0.48 wt.%. The average Fe/Ni of Qtz with PDF (~ 20) and of silica glass (~ 24) is in significant contrast to the average Fe/Ni in the sandstone (~ 422), but resembles Fe/Ni of the projectile (~ 14). Representative microprobe data are given in Table 2.3

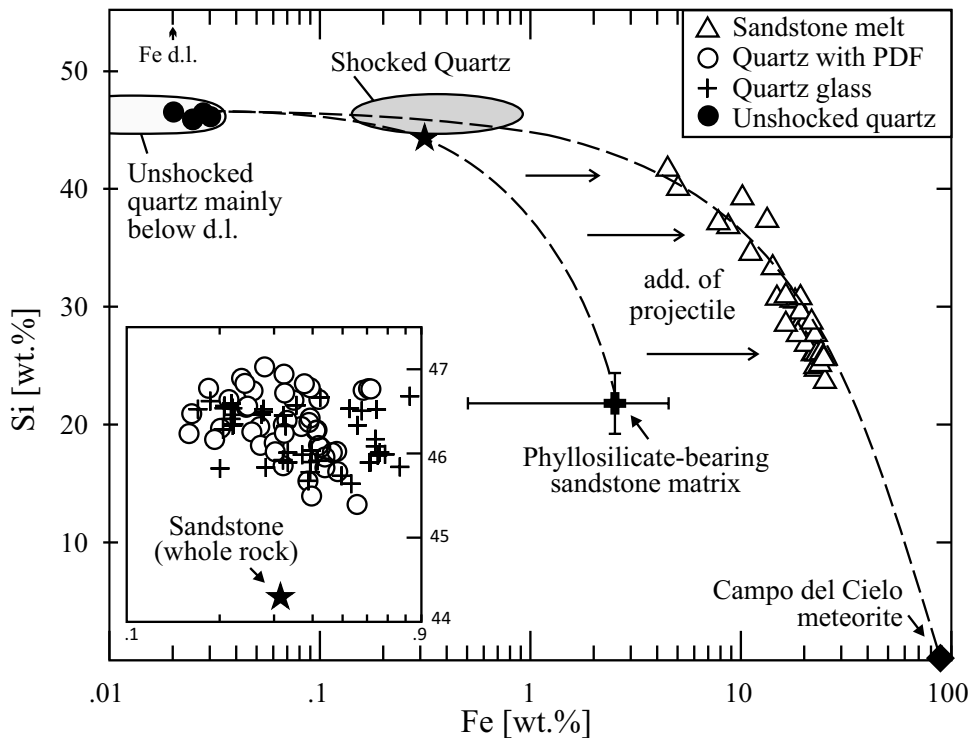


Figure 2.6: Fe vs. Si for various materials of the highly shocked ejecta fragments. The insert shows in detail the "shocked quartz"-field (Qtz with PDF, silica glass). d.l. = detection limit.

2.4.4 Chemical modification of the Fe-meteorite projectile

Microprobe analyses of each projectile material are compiled in Fig. 2.8, and Table 2.4 gives some representative analyses. The chemical modifications observed in shocked projectile material are discussed with respect to the unshocked CDC meteorite (Table 2.2). The matrix of partly fused projectile fragments is oxidized to some extent and shows slightly higher P and Si values, but in general, resembles the original kamacite matrix. Schreibersite areas in the matrix of the partly fused projectile fragments have higher Fe/Ni due to an increase of Fe and decrease of Ni but their P content remained unchanged. Shock metamorphism caused complete melting of the rhabdites and some melting of the kamacite host crystal producing melt pockets. The melt in the pocket shown in Fig. 2.5d is separated into a P-rich melt in the center, and a P-poor melt at the rim (Fig. 2.5d) that has a slightly higher Ni-content (Table 2.4). Microprobe line-scans through the

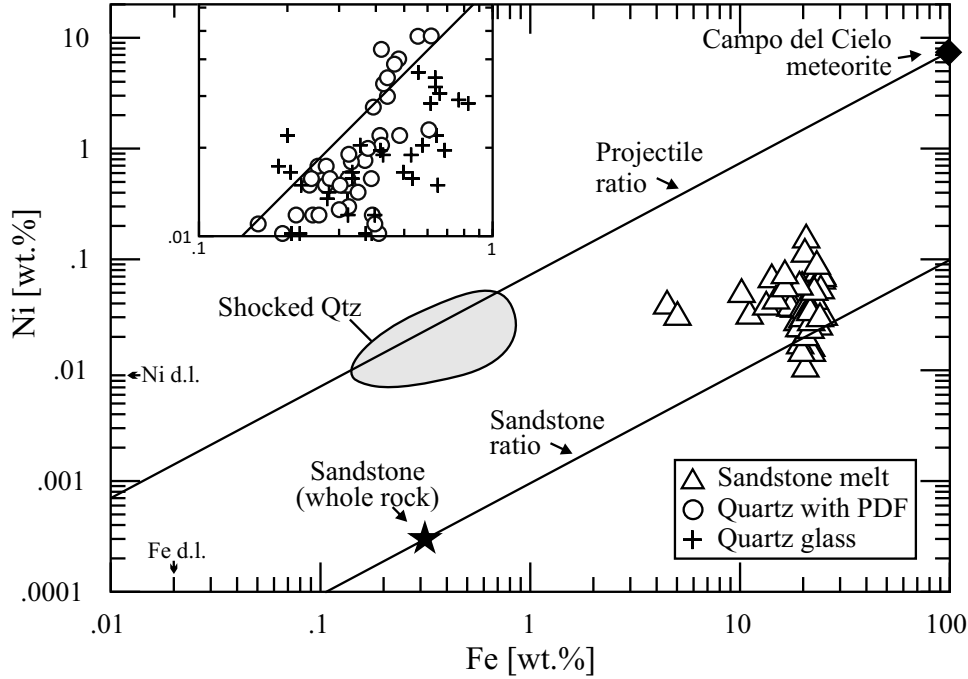


Figure 2.7: Fe vs. Ni for various materials of the highly shocked ejecta fragments. The inset represents the "shocked quartz"-field in detail (Qtz with PDF, silica glass). Unshocked quartzes are below the detection limits and not shown here.

melt pockets show Ni depletion in the surrounding kamacite. The plot in Fig. 2.8 represents the ideal mixing line between the rhabdite and kamacite matrix. The curved line lies above the chemical compositions of the average melt pocket rim and center. This is due to Ni-enrichment in the rim and the center of the melt pocket, which originates by diffusion from the kamacite matrix. Furthermore, the molten margins of partly fused fragments slightly differ in its chemical composition compared to the unshocked CDC meteorite. These melts have on average 0.4 wt.% more Ni, 400 ppm more Co and 1.7 wt.% less Fe than the CDC meteorite, yielding a decrease in Fe/Ni and Fe/Co. In addition, we observed P-values of the molten margins which are similar to that of the CDC meteorite, but the oxygen content is higher by ~ 0.6 wt.% suggesting some oxidation. These molten margins also contain up to 2300 ppm Si. Enrichment of Ni, Co, P and Si and depletion of Fe are most extensive for the projectile droplets that have entered the sandstone melt. These metallic droplets vary significantly in composition (cf. Table 2.4). The enrichment of Ni and Co over Fe correlates negatively with the size of the projectile droplets, and is most prominent in spheres with a diameter smaller than $3 \mu\text{m}$ (Fig. 2.9). For this correlation only metallic spheres (no spheroids) were analyzed. The chemical compositions of the molten margins of projectile fragments and the metallic droplets generally range between the CDC whole rock ratio and its kamacite ratio (Fig. 2.8 and Fig. 2.10).

2.5 Discussion

2.5.1 Chemical interaction between projectile and sandstone target

As mentioned above, the partly fused projectile fragments contain metallic melts at their margins (Fig. 2.5c). Microprobe analyses indicate that these melts represent a mixture of the CDC

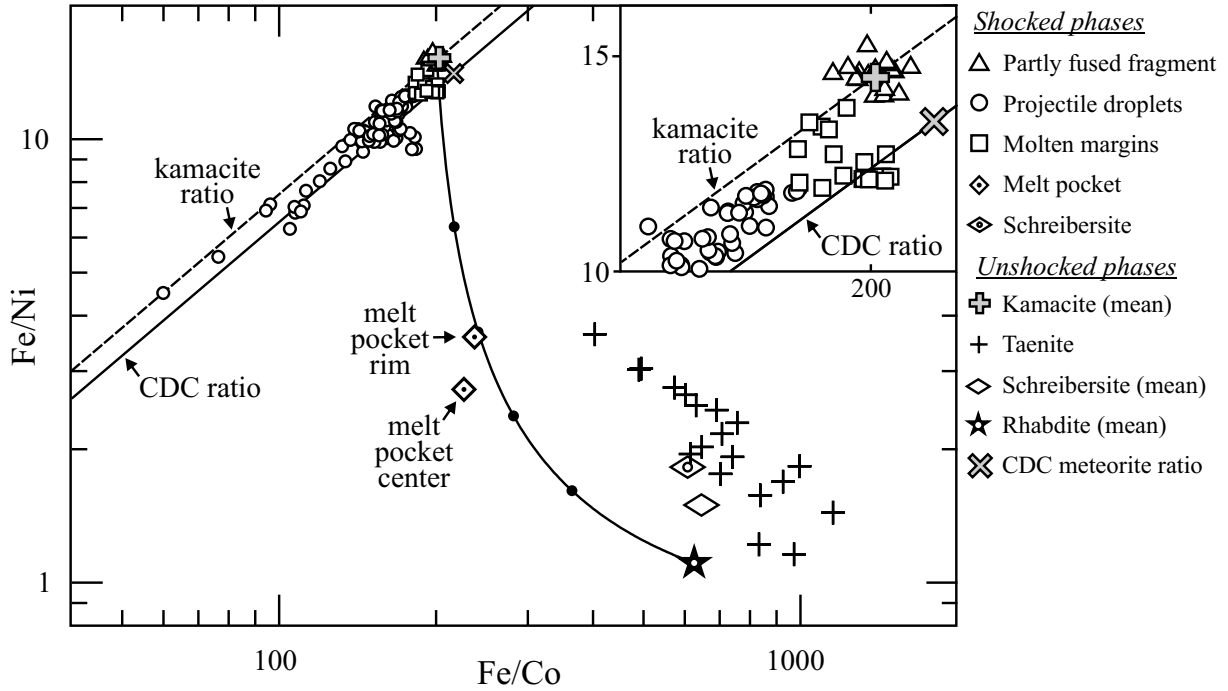


Figure 2.8: Fe/Ni and Fe/Co for different phases of the projectile before and after the impact. The curved line represents the mixing line between unshocked kamacite and rhabdite. The dots on the mixing line are a subdivision in 20% steps. The insert shows in detail the data array close to the CDC meteorite ratio.

meteorite components. The dominant contribution is from the kamacite matrix, with an admixture of P-rich phases. We assume that the rhabdites are the main P-donators as they are more homogeneously distributed than schreibersite. The dissemination of projectile material in the sandstone is a highly dynamic and turbulent process. It appears that some portion of the molten rims were separated from the projectile fragments, injected into the low viscosity sandstone melt and disseminated as small metallic droplets. In these projectile droplets Ni and Co are enriched to a greater degree than Fe, compared to the molten margins of partly fused projectile fragments and the CDC meteorite composition. The positive slope of this trend, shown in Fig. 2.8, is a result of the removal of Fe (see above). The range of projectile material compositions observed in the ejecta cannot be explained as simple mixtures of taenite and kamacite (Fig. 2.8). The Fe/Ni and Fe/Co decrease, due to loss of iron, but Ni/Co remains nearly constant. Obviously the Fe depletion in the molten margins of projectile fragments and the metallic droplets is associated with the enrichment of Fe and to a lesser degree of other siderophile elements in the sandstone melt and in shocked quartz.

Summarizing these petrographic and geochemical observations, two coexisting but largely immiscible melts (projectile melt and sandstone melt) exist in the highly shocked ejecta fragments. Several studies of Meteor crater (e.g., Hörz *et al.*, 2002; Kearsley *et al.*, 2004; Mittlefehldt *et al.*, 2005), Wabar crater (e.g., Gibbons *et al.*, 1976; Hörz *et al.*, 1989), Monturaqui crater (e.g., Bunch & Cassidy, 1972; Kearsley *et al.*, 2004) and Kamil crater (D’Orazio *et al.*, 2011) described similar petrographic features in siliceous impactite material. The authors observed numerous metallic droplets with meteoritic origin in vesicular glasses, comparable to our observations shown in Fig. 2.4a, Fig. 2.5b. In impact melts of Meteor Crater (Arizona, USA), Hörz

et al. (2002) and Kearsley *et al.* (2004) described a decrease of Fe/Ni in meteoritic droplets compared to the composition of the Canyon Diablo meteorite, and a complementary increase of this ratio in the surrounding target melt. Based on microprobe data, Hörz *et al.* (1989) and Mittelfehldt *et al.* (1992) demonstrated that impact melt material from Wabar crater are generally enriched in Fe over Ni compared to the iron meteorite impactor. The results of our study (Fig. 2.7 and Table 2.4) are consistent with these data. In our study the average Fe/Ni in sandstone melt of highly shocked ejecta fragments is generally above the Fe/Ni in the bulk Campo del Cielo. The Fe/Ni also varies strongly in the sandstone melt between 120 and 1406. Thus, during the formation of Meteor crater, Wabar crater, and the laboratory impacts of the MEMIN research unit, comparable selective element partitioning processes between the projectile and target occurred.

In order to quantify such fractionation processes it is important to understand the behavior of the moderate siderophile elements Fe, Co, and Ni. Partitioning of these elements between silicate and metallic melts has been studied extensively in laboratory experiments at varying conditions of pressure (P), temperature (T), oxygen fugacity (f_{O_2}), as well as metal and silicate composition. All experimental data demonstrated that independent of P, T, f_{O_2} and compositional variations the sequence is always $D_{met/sil}^{Ni} \gg D_{met/sil}^{Co} \succ D_{met/sil}^{Fe}$ (e.g., Hiligren *et al.*, 1994, 1996; Ohtani *et al.*, 1997; Righter *et al.*, 1997; Schmitt *et al.*, 1989; Walker *et al.*, 1993), where $D_{met/sil}^X$ is the metal/silicate partitioning coefficient of element x. The experimental results clearly indicate that the partitioning coefficient of Fe is always lower than the coefficient for Ni. Therefore, iron partitions preferentially into the silicate melt compared to Ni and Co. The siderophile character of Fe, Ni, and Co is linked to the selective oxidation behavior of these elements (White, 2011) which is based on differences in the affinity to form an oxide. The Gibbs free energies (ΔG) for oxidation of pure Fe, Ni, and Co are: $\Delta G^\circ_{Fe/FeO} \ll \Delta G^\circ_{Co/CoO} \prec \Delta G^\circ_{Ni/NiO}$ for all temperatures. Thus, Fe oxidizes preferentially over Co and Ni. An iron meteorite can be considered as a metallic alloy whose oxidation is more complex than oxidation of pure metals. When oxidation of alloys (e.g., Fe-Ni-Co) proceeds with selective oxidation of a less noble metal like Fe, a depletion zone of this less noble metal is formed in the underlying alloy (Seo & Sato, 1983). In our experiment, the molten margins of larger projectile fragments, which are enriched in Ni, could be considered as such a depletion zone, caused by an oxidation process. We suggest that the projectile material, especially the material that later forms droplets is injected into the sandstone melt and immediately reacts as described above. During this process the projectile material was slightly oxidized (cf. Table 2.2 and 2.1). We consider gas trapped / originally present in the pore space of the sandstone, and the dissociation of H_2O (Brett, 1967) originating from the phyllosilicate-bearing matrix as potential sources for oxygen. This view is supported by the highly vesicular sandstone melt (Fig. 2.4 and Fig. 2.5) which implies vaporization of certain amounts of H_2O , which in turn, may have been dissociated. Brett (1967), Gibbons *et al.* (1976), Kearsley *et al.* (2004), Kelly *et al.* (1974) and Mittelfehldt *et al.* (2005) considered selective oxidation as the main reason for enrichment of Ni (and Co) observed in metallic droplets in impactites from the Wabar, Monturaqui, Henbury, and Meteor craters. D’Orazio *et al.* (2011) described similar reaction margins in the ablation crust of Gebel Kamil, the iron meteorite that formed the Kamil crater in Egypt.

Brett (1967) suggested that a combined oxidation-fractionation process occurred in a very short time interval prior to the projectile melt injecting into the target melt. This implicates formation of an iron-oxide layer in the projectile prior to the incorporation of FeO into the sandstone melt. In this model, an FeO "skin" around each metallic droplet partitions into the target glass, enriching it in iron, and causing an FeO-free surface of the droplet. In our samples, we did not observe a distinct oxide-layer on projectile material. Small droplets have relatively greater surface areas for oxidation, thus possibly explaining the Ni- (and Co-) enrichment with decreasing size (Gibbons *et al.*, 1976), as shown in Fig. 2.9.

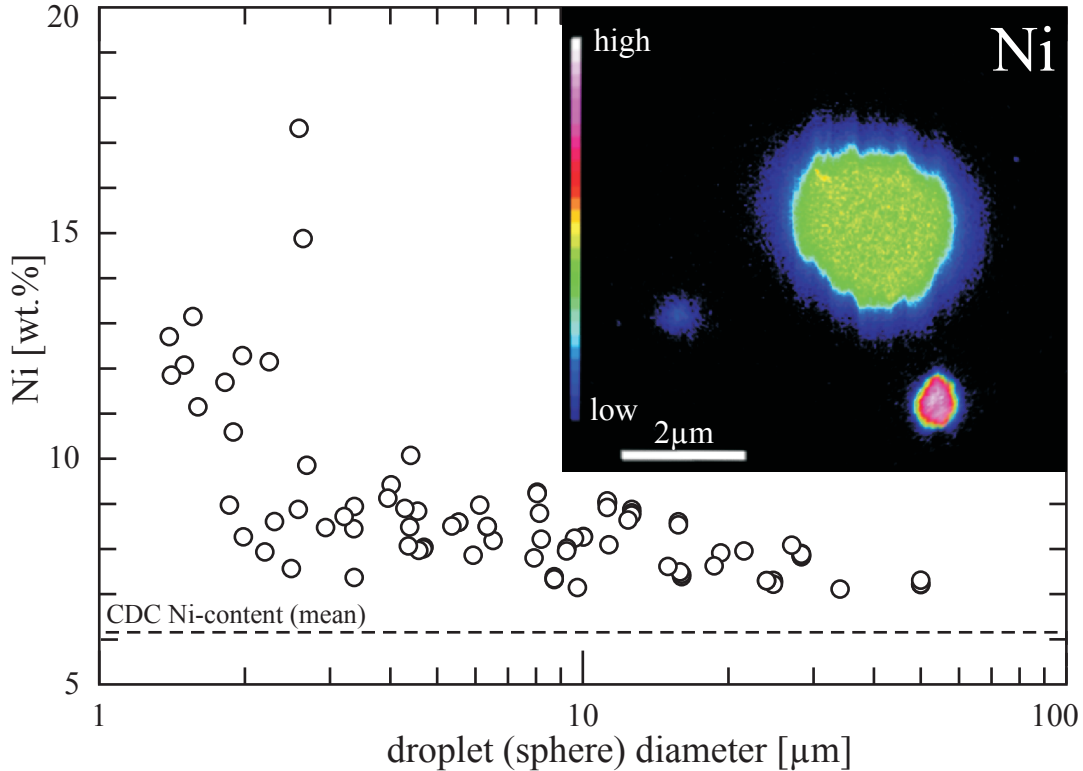


Figure 2.9: Ni content versus grain size of projectile droplets.

It is apparent from Fig. 2.10 that projectile droplets at terrestrial craters differ from the respective original meteorite composition. For example, some spheres of meteoritic origin from the Wabar crater have Ni contents of about 90 wt.% (e.g., Gibbons *et al.*, 1976). As previously mentioned, Fe oxidizes more preferentially than Co, which in turn oxidizes more preferentially than Ni. We did not observe this chemical behavior in the projectile material of our study. For most droplets Ni/Co ranges between the ratios for the bulk CDC and kamacite. Only the most fractionated (Fe-poor) meteoritic droplets show some Ni/Co fractionation (Bunch & Cassidy, 1972; Gibbons *et al.*, 1976; Kearsley *et al.*, 2004). At Fe/Co < 15 it is clearly shown that the Ni/Co-ratio of Wabar, Monturaqui and Meteor crater spheres differ significantly from their initial meteorite ratio (Fig. 2.10). In these cases Ni is on average more enriched than Co resulting in a higher Ni/Co. Another process causing selective oxidation of iron meteorite material occurs by interaction of the incoming projectile with air (Mittlefehldt *et al.*, 2005). These authors show that ballistically dispersed metallic spherules from Meteor crater are generally enriched in Ni and Co over Fe. Projectile droplets from the Meteor crater that directly interacted with molten

target material, however, show a much more pronounced fractionation between Fe and Ni+Co (Kearsley *et al.*, 2004) than the spheres selectively oxidized in air (Fig. 2.10). Although the projectile droplets in our experiment are surrounded by a sandstone melt, we do not observe such an extreme inter-element fractionation as recorded in samples from Meteor crater (Kearsley *et al.*, 2004). We suggest that the difference in the intensity of inter-element fractionation between nature and experiment is due to differences in physical conditions like maximum pressure, temperature, and time. Especially differences in cooling rates may influence the intensity of chemical interactions between projectile and target. In the case of the MEMIN experiments, composition and thus structure of the siliceous sandstone melt affect the amount of projectile elements dissolved. This melt varies considerably in Al content as a result of different proportions of molten quartz and Al silicates (e.g. phyllosilicates). The Al-rich melts are considerably more depolymerized than Si-rich and Al-poor melts (Mysen & Richet, 2005). The relative enrichment of Fe in Al-rich melts is facilitated by the charge compensation of Al^{3+} by divalent cations.

We have documented in our highly shocked ejecta fragments a slight enrichment of meteoritic Fe and Ni in quartz with PDF and silica glass (Fig. 2.7, Table 2.3). This corresponds to an addition of 0.1 to 0.7 % meteorite component to shocked quartz. In contrast to Fe/Ni in sandstone melts, the average Fe/Ni of these shocked SiO_2 phases lies close to the ratio for the original Campo del Cielo (Table 2.3 and 4). This result is unusual, and rather unexpected. Superficial contamination of the quartz by matter from adjacent projectile droplets as well as partly fused projectile fragments during polishing of the thin sections cannot be completely excluded. We intend to apply other sensitive preparation and analytical methods to test whether this observation can be confirmed.

2.5.2 P-T-conditions during the impact

Poelchau *et al.* (2011, 2013) calculated a maximum shock pressure of 55 GPa for our experiment using the planar impact approximation and material parameters for Coconino sandstone and steel. Such a maximum shock pressure, however, is insufficient to cause melting let alone vaporization of the meteoritic projectile. Therefore it is necessary to consider spatially localized factors that may boost local heating beyond the bulk temperatures calculated here to levels sufficient to melt projectile and target material. For instance, the melting point of an iron meteorite is approximately 1497 °C, its boiling point is 3235 °C (Remo, 1994), which is similar to pure iron with melting and boiling points of 1536 °C and 2860 °C, respectively. Several observations which are at odds with the calculated peak pressures need to be explained. Highly shocked ejecta fragments such as illustrated in Fig. 2.4a display different shock-metamorphic features on a very small scale: Melting of quartz seems to start at the quartz grain rims and along the PDF. Hence, it is possible that a transformation from diaplectic quartz to fused quartz (silica glass) has occurred within the PDF. This ongoing transformation is well illustrated in Qtz-B and Qtz-C (Fig. 2.4a). Vesicles within the Qtz-C and the schlieren-like rims indicate a predominantly molten state of this grain (fused Qtz). The PDF are isotropic glass lamellae along defined crystallographic planes in crystalline quartz; these PDF form by the transformation of quartz in the solid state in the shock pressure interval of 13 - 35 GPa. The width of the amorphous lamellae increases with pressure to finally merge at a shock pressure > 35 GPa into

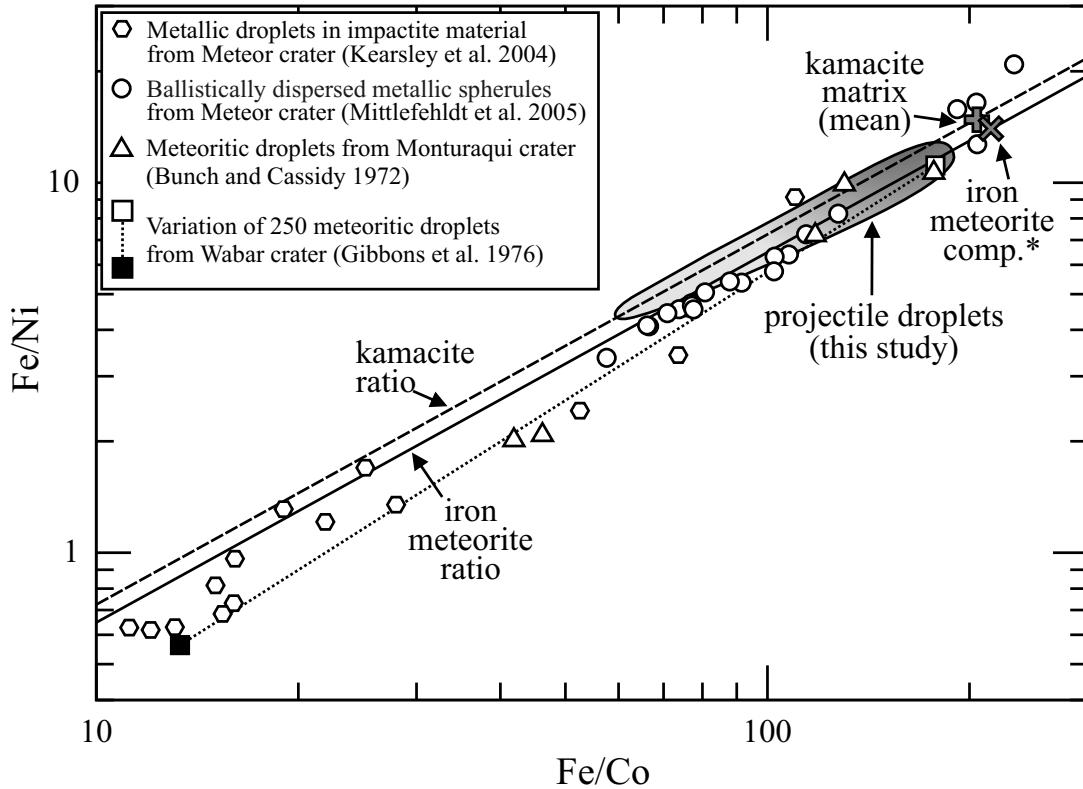


Figure 2.10: Fe/Ni and Fe/Co for different metallic spheres from natural craters compared with results of this study. Iron meteorite composition and ratio include Campo del Cielo and Canyon Diablo. The gray-scale gradient in the "projectile droplets"-field reflects the numbers of measurements - with a high number at dark gray and low number at light gray (cp. Fig. 2.8).

patches of diaplectic glass that finally replace the entire Qtz grain in a pseudomorphic manner (e.g., Langenhorst & Deutsch, 1994; Langenhorst, 2002). All these shock-features occur at a distance of $\sim 20 \mu\text{m}$ (Fig. 2.4) next to fused silica glass, substantiating a very heterogeneous P-T history. Concerning the projectile fragments, tiny vesicles in the molten rim of a partly fused projectile fragment (Fig. 2.5c) may indicate boiling of the projectile. This finding concurs with data by Kenkmann *et al.* (2007, 2013) for the MEMIN pilot study (P1-2808) with a steel projectile and a target of Seeberger Sandstein (impact velocity $5.3 \text{ km} \times \text{s}^{-1}$; calculated peak shock pressure of 50 - 60 GPa). These authors report droplets with vesicles on the surface of recovered pieces of the projectile and foamy textures of projectile spheroids, indicative of temperatures near the liquid-vapor transition of steel. In the numerical modeling of the formation of Meteor crater, Artemieva & Pierazzo (2011) used the ANEOS for pure Fe as equation of state for the Canyon Diablo IAB iron meteorite projectile. They report an onset of melting at 162 GPa, and of vaporization at 320 GPa. The peak pressure of 55 GPa as calculated for our experiment is obviously far too low to explain the observed phase changes in the CDC projectile. To overcome this problem, we suggest the formation of locally restricted areas/volumes of significantly enhanced pressure and/or temperature conditions; such areas may be at or near the contact between projectile and sandstone target. Three principal mechanisms are envisaged. (i) As suggested by Kenkmann *et al.* (2007, 2013) friction and deformation (i.e., plastic work) of the projectile may play an important role in the increase of temperature. (ii) The effect of

shock heating in porous material may be the other process for substantial temperature increase on a macroscopic and microscopic level. Macroscopically, in porous targets, the kinetic energy of the projectile is transferred more effectively into target heating (Ahrens & Gregson, 1964). The amount of plastic work during compaction and compression of a porous material is large compared to processes in a shock front passing through non-porous material, leading to higher temperatures after the shock-wave has passed (Wünnemann *et al.*, 2006). On the microscopic scale, "pore collapse" results in local pressure and temperature peaks. Recent developments of new material models for use in hydrocodes treat the collapse of pore space during the impact process (Güldemeister *et al.*, 2013). These models provide a good approximation to understand the P-T differences documented by mineralogical changes. Güldemeister *et al.* (2011, 2013) showed that despite a general decrease of the average shock pressure due to porosity, a significant local increase of shock pressure (up to four times of the initial pressure) occurs in the vicinity of pores. Therefore, we suggest enhanced post-shock temperatures (cp. eg. Stöffler & Langenhorst, 1994). This pore collapse mechanism can explain our observations in the highly shocked ejecta fragments, with low and high shock-metamorphic features occurring very close to each other. (iii) The target chamber was evacuated to 0.3 bar during the impact experiment. The residual atmosphere of the chamber is shocked and compressed in front of the accelerated projectile. The shock compression leads to heating of the air and consequently also of the projectile surface. Berry *et al.* (2007) measured surface temperatures of up to 1800 °C during a free flight experiment of a hemispherical graphite projectile, accelerated to $4.5 \text{ km} \times \text{s}^{-1}$ at 0.32 bar experimental gas pressure. Since the experimental conditions of Berry *et al.* (2007) are similar to our experiments we also expect some heating and maybe melting of the projectile front prior to impact.

2.6 Conclusions

We have observed complex mixing and shock features in ejecta fragments collected from a MEMIN experiment with a 1-cm-sized projectile of Campo del Cielo iron meteorite and a sandstone target. These features include the occurrence of PDF in quartz, transformation of quartz into diaplectic glass, as well as the formation of fused vesicular silica glass. For the first time meteoritic Fe and Ni were detected in shocked quartz. Regarding the projectile, various amounts of material are mechanically injected (as partly fused fragments) into the sandstone. Heterogeneous melting of sandstone and projectile occurred, followed by mixing of both melts. This process is connected with significant inter-element fractionation. In sandstone melt, meteoritic Fe is selectively enriched over Ni and Co, whereas in coexisting meteoritic droplets and molten margins of projectile fragments, Ni and Co are enriched over Fe. This fractionation most likely results from differences in the siderophile character, or in other words, from differences in the reactivity of the three elements with oxygen. Data from the Meteor and Wabar craters show trends similar to those observed in the mesoscale laboratory craters of the MEMIN project. The variability and strong deviation of Fe/Ni, and Fe/Co in the impact melts from the respective ratios in the meteorite causes a severe problem for identification of the projectile types in impact craters as already noted by Attrep *et al.* (1991) and Mittlefehldt *et al.* (1992). In accordance with these authors we recommend caution in assigning specific projectile types without detailed

knowledge of projectile-target mixing and inter-element fractionation processes involved.

2.A Tables of chapter 2.

Table 2.1: Measurements of the NIST glass standards

<i>NIST SRM 610</i>	MfN [*] (this study)	sigma	Literature ¹	sigma	NIST ²	sigma
Ni [ppm]	431	33	458.7	4	485	4
Fe [ppm]	429	45	458	9	458	9
<i>NIST SRM 612</i>	MfN [*] (this study)	sigma	Literature ¹	sigma	NIST ²	sigma
Ni [ppm]	43	17	38.8	3.7	38.8	0.2
Fe [ppm]	57	19	51	2	51	2

* Electron microprobe data

¹ Jochum et al. 2011; preferred average values of the authors.

² Reference value determined by the National Institute of Standards and Technology (from Jochum et al. 2011)

Table 2.2: Chemical composition of the Campo del Cielo (CDC) meteorite, Seeberger Sandstein and the phyllosilicate-bearing sandstone matrix.

wt.% ± 2σ	Kamacite [*]	Taenite [*]	Schreibersite [*]	Rhabdite [*]	¹ CDC (whole rock)
Fe	92.93 ± 0.52	67.09 ± 6.77	51.23 ± 0.26	45.03 ± 3.09	92.6
Ni	6.25 ± 0.39	32.95 ± 6.60	34.24 ± 0.22	41.18 ± 3.15	6.62
Co	0.45 ± 0.03	0.02 ± 0.01	0.08 ± 0.01	0.07 ± 0.02	0.43
P	0.07 ± 0.02	0.10 ± 0.04	15.02 ± 0.08	14.03 ± 0.62	0.25
Si	0.01 ± 0.006	b.d.l.	b.d.l.	b.d.l.	n.a.
² modal	88	1.2	3.2	3.5	
Fe/Ni	14.6	2	1.5	1.1	13.9
wt.% ± 2σ	Seeberger Sandstein ⁺	Phyllosilicate-matrix [*]			
SiO ₂	94.77 ± 0.90	46.60 ± 5.52			
Al ₂ O ₃	3.11 ± 0.10	25.86 ± 9.50			
Fe ₂ O ₃	0.45 ± 0.09	3.25 ± 2.60 (FeO)			
CaO	0.05 ± 0.01	0.23 ± 0.12			
MgO	0.12 ± 0.02	1.13 ± 0.79			
Na ₂ O	0.15 ± 0.05	0.1 ± 0.18			
K ₂ O	0.23 ± 0.01	2.93 ± 2.10			
TiO ₂	0.31 ± 0.04	0.16 ± 0.26			
MnO	< 0.01	b.d.l.			
P ₂ O ₃	0.02 ± 0.01	0.08 ± 0.07			
ppm					
Ni	3.33 ± 0.41	b.d.l.			
Co	0.96 ± 0.04	b.d.l.			
Cr	63.33 ± 21.01	b.d.l.			
Fe/Ni	945	-			

b.d.l. - below detection limit; n.a. - not analyzed

* Electron microprobe data

+ XRF data; Ni, Co, Cr were measured with ICP-MS

¹ Buchwald (1975)

² Bunch and Cassidy (1968)

Table 2.3: Electron-microprobe data for various phases in the highly shocked ejecta fragments.

Element [wt.%]	SiO ₂	TiO ₂	Al ₂ O ₃	FeO	NiO	MgO	CaO	Na ₂ O	K ₂ O	Fe/Ni	Total
<i>Sandstone melt</i>											
SM.01	85.59	1.02	4.61	6.48	0.04	0.14	0.07	0.04	0.79	170	98.78
SM.02	78.65	0.38	6.41	11.22	0.02	0.31	0.08	0.03	0.89	488	98.07
SM.03	73.81	0.77	8.4	14.3	0.04	0.27	0.08	0.04	0.58	367	98.34
SM.04	60.17	0.87	12.62	25.59	0.05	0.41	0.14	0.04	0.63	569	100.61
SM.05	57.3	0.7	13.76	26.2	0.14	0.31	0.1	0.04	0.39	186	99.05
SM.06	59.26	0.68	12.24	26.31	0.03	0.4	0.11	0.04	0.53	1052	99.67
SM.07	57	1.1	9.91	30.23	0.1	0.43	0.11	0.06	0.58	318	99.7
mean (n = 55)	61.85	0.92	11.12	24.94	0.05	0.38	0.12	0.03	0.55	500	
2 σ	17.18	1	5.6	12.54	0.06	0.2	0.06	0.04	0.32		
<i>Silica glass</i>											
Silica-gl.01	98.03	b.d.l.	0.07	0.26	0.03	b.d.l.	b.d.l.	b.d.l.	b.d.l.	9	98.44
Silica-gl.02	99.41	n.a.	0.03	0.35	0.02	n.a.	n.a.	n.a.	n.a.	21	99.81
Silica-gl.03	98.19	b.d.l.	0.04	0.43	0.02	b.d.l.	b.d.l.	b.d.l.	b.d.l.	20	98.73
Silica-gl.04	99.84	n.a.	0.03	0.55	0.02	n.a.	n.a.	n.a.	n.a.	23	100.44
Silica-gl.05	98.6	b.d.l.	0.05	0.82	0.04	b.d.l.	b.d.l.	b.d.l.	b.d.l.	19	99.58
Silica-gl.06	98.78	b.d.l.	0.07	0.82	0.04	b.d.l.	b.d.l.	b.d.l.	b.d.l.	20	99.81
Silica-gl.07	98.07	n.a.	0.02	0.99	0.04	n.a.	n.a.	n.a.	n.a.	27	99.11
Mean (n = 44)	98.87		0.04	0.52	0.02					24	
2 σ	1.36		0.08	0.46	0.02						
<i>Quartz with PDF</i>											
Qtz-pdf.01	98.77	n.a.	0.01	0.25	0.01	n.a.	n.a.	n.a.	n.a.	19	99.04
Qtz-pdf.02	99.78	n.a.	0.02	0.28	0.02	n.a.	n.a.	n.a.	n.a.	18	100.09
Qtz-pdf.03	99.59	n.a.	0.02	0.31	0.02	n.a.	n.a.	n.a.	n.a.	21	99.93
Qtz-pdf.04	98.62	n.a.	0.02	0.35	0.02	n.a.	n.a.	n.a.	n.a.	16	99.01
Qtz-pdf.05	99.31	b.d.l.	0.03	0.51	0.04	b.d.l.	b.d.l.	b.d.l.	b.d.l.	14	99.94
Qtz-pdf.06	99	n.a.	0.05	0.53	0.01	n.a.	n.a.	n.a.	n.a.	41	99.58
Qtz-pdf.07	97.95	n.a.	0.12	0.62	0.03	n.a.	n.a.	n.a.	n.a.	22	98.72
mean (n = 47)	99.07		0.05	0.44	0.02					20	
2 σ	1.86		0.2	0.3	0.04						
<i>Unshocked quartz</i>											
Qtz.01	98.86	n.a.	b.d.l.	b.d.l.	b.d.l.	n.a.	n.a.	n.a.	n.a.		98.86
Qtz.02	98.74	n.a.	b.d.l.	b.d.l.	b.d.l.	n.a.	n.a.	n.a.	n.a.		98.74
Qtz.03	98.73	n.a.	b.d.l.	b.d.l.	b.d.l.	n.a.	n.a.	n.a.	n.a.		98.73
Qtz.04	99.09	n.a.	b.d.l.	b.d.l.	b.d.l.	n.a.	n.a.	n.a.	n.a.		99.09
mean (n = 25)	98.57										
2 σ	0.88										

b.d.l. - below detection limit; n.a. - not analyzed

Table 2.4: Electron-microprobe data for various projectile residues (after impact)

Element [wt.%]	Co	Fe	Ni	O	P	Si	Total	Fe/Ni	sphere \emptyset [μm]
<i>Partly fused projectile fragment</i>									
P.1	0.44	91.49	6.55	0.51	0.04	0.19	99.21	14	
P.2	0.46	92.75	6.36	0.33	0.1	0.03	100.02	14.6	
P.3	0.48	92.92	6.11	0.35	0.1	0.1	100.05	15.2	
P.4	0.46	92.87	6.08	0.37	0.09	0.1	99.96	15.3	
P.5	0.45	92.28	6.02	0.55	0.1	0.11	99.51	15.3	
P.6	0.47	92.61	5.88	0.65	0.09	0.17	99.87	15.7	
mean (n=63)	0.46	92.78	6.21	0.44	0.1	0.08	100.07	14.9	
2σ	0.02	1.04	0.38	0.18	0.04	0.12			
<i>Schreibersite (shocked)</i>									
S.1	0.09	53.23	29.23	1.02	14.98	0.09	98.64	1.8	
S.2	0.09	53.22	29.54	0.89	15.06	0.12	98.91	1.8	
S.3	0.08	53.26	29.53	0.8	14.98	0.13	98.78	1.8	
S.4	0.09	53.15	29.44	0.97	15.01	0.11	98.76	1.8	
S.5	0.09	53.14	29.44	0.97	15.04	0.13	98.81	1.8	
S.6	0.1	54.89	28.3	0.93	14.78	0.13	99.14	1.9	
mean (n=8)	0.09	53.35	29.28	0.9	14.99	0.12	98.73	1.8	
2σ	0.02	1.28	0.82	0.18	0.18	0.04			
<i>Melt pocket (r=rिम; c=center)</i>									
MP.r.1	0.32	77.13	20.88	0.29	1.17	0.02	99.82	3.7	
MP.r.2	0.33	76.14	21.98	0.32	0.99	0.02	99.79	3.5	
MP.r.3	0.31	76.56	21.48	0.29	1.06	0.03	99.73	3.6	
mean (n=7)	0.32	76.67	21.44	0.32	1.11	0.03	99.89	3.5	
2σ	0.02	0.74	0.78	0.1	0.18	0.02			
MP.c.1	0.29	65.08	24.01	0.2	10.39	0.01	99.98	2.7	
MP.c.2	0.29	64.99	23.96	0.28	10.5	0.02	100.03	2.7	
MP.c.3	0.29	65.1	24.15	0.26	10.21	0.02	100.02	2.7	
mean (n=4)	0.29	64.98	23.86	0.27	10.59	0.02	100	2.7	
2σ	0.02	0.3	0.4	0.06	0.46	0.02			
<i>Molten margins of partly fused projectile fragments</i>									
P2.1	0.49	91.66	6.62	0.59	0.08	0.21	99.65	13.9	
P2.2	0.48	92.05	6.67	0.63	0.11	0.22	100.17	13.8	
P2.3	0.49	90.83	6.79	0.81	0.21	0.23	99.36	13.4	
P2.4	0.48	91.41	6.89	0.58	0.28	0.17	99.81	13.3	
P2.5	0.45	91.79	6.92	0.44	0.19	0.19	99.99	13.3	
P2.6	0.48	90.4	7.19	0.59	0.29	0.19	99.13	12.6	
mean (n=28)	0.46	91.09	6.98	0.6	0.2	0.23	99.58	13.1	
2σ	0.04	1.06	0.42	0.16	0.12	0.12			
<i>Projectile droplets</i>									
PS.1	0.51	90.52	7.22	0.98	0.24	0.3	99.77	12.5	50
PS.2	0.56	90.65	7.85	0.56	0.3	0.21	100.13	11.5	28
PS.3	0.54	89.89	7.91	0.26	0.23	n.a.	98.92	11.4	19
PS.4	0.6	89.2	8.6	0.32	0.34	0.35	99.42	10.4	15
PS.5	0.68	86.26	10.07	0.55	0.3	0.35	98.2	8.6	5
PS.6	1.04	80.59	14.88	0.38	0.45	0.52	97.86	5.4	3
mean (n=92)	0.59	88.73	8.73	0.39	0.4	0.39	99.14	10.2	12
2σ	0.24	4.88	2.44	0.46	0.66	0.26			

n.a. - not analyzed

3 Geochemical processes between steel and silica-rich targets in hypervelocity cratering experiments

Matthias Ebert^{1,2,*}, Lutz Hecht^{1,2}, Alexander Deutsch³, Thomas Kenkmann⁴,
Richard Wirth⁵, Jasper Berndt³

(published 2014 in *Geochimica et Cosmochimica Acta* **133**, 257-279; DOI: 10.1016/j.gca.2014.02.034)

⁽¹⁾Museum für Berlin - Leibniz-Institut für Evolutions- und Biodiversitätsforschung, Invalidenstr. 43, D-10115 Berlin, Germany; Freie Universität Berlin, Institut für Geowissenschaften, Malteserstr. 74-100, D-12249 Berlin, Germany; ⁽³⁾Westfälische Wilhelms-Universität, Institut für Planetologie, Wilhelm-Klemm-Str. 10, D-48149 Münster, Germany; ⁽³⁾Albert-Ludwigs-Universität Freiburg, Institut für Geowissenschaften, Albertstr. 23-B, D-79104 Freiburg, Germany; ⁽⁵⁾Helmholtz-Zentrum Potsdam, Deutsches GeoForschungsZentrum, 3.3, Telegrafenberg, D-14473 Potsdam, Germany; ^(*)Correspondence author's e-mail address: matthias.ebert@mfn-berlin.de

3.1 Abstract

The possibility of fractionation processes between projectile and target matter is critical with regard to the classification of the impactor type from geochemical analysis of impactites from natural craters. Here we present results of five hypervelocity MEMIN impact experiments (Poelchau et al., 2013) using the Cr-V-Co-Mo-W-rich steel D290-1 as projectile and two different silica-rich lithologies (Seeberger sandstone and Taunus quartzite) as target materials. Our study is focused on geochemical target-projectile interaction occurring in highly shocked and projectile-rich ejecta fragments. In all of the investigated impact experiments, whether sandstone or quartzite targets, the ejecta fragments show (i) shock-metamorphic features e.g., planar-deformation features (PDF) and the formation of silica glasses, (ii) partially melting of projectile and target, and (iii) significant mechanical and chemical mixing of the target rock with projectile material. The silica-rich target melts are strongly enriched in the "projectile tracer element" Cr, V, and Fe, but have just minor enrichments of Co, W, and Mo. Inter-element ratios of these tracer elements within the contaminated target melts differ strongly from the original ratios in the steel. The fractionation results from differences in the reactivity of the respective elements with oxygen during interaction of the metal melt with silicate melt. Our results indicate that the principles of projectile-target interaction and associated fractionation do not depend on impact energies (at least for the selected experimental conditions) and water-saturation of the target. Partitioning of projectile tracer elements into the silicate target melt is much more enhanced in experiments with a non-porous quartzite target compared with the porous sandstone target. This is mainly the result of higher impact pressures, consequently higher temperatures and longer reaction times at high temperatures in the experiments with quartzite as target material.

3.2 Introduction

During an impact process a certain amount of projectile (< 1 wt.%) can be incorporated into impact melt rocks and breccias, fractures in the crater floor, or the ejecta (e.g. Goderis *et al.*, 2012; Koeberl *et al.*, 2012). The chemical composition of these materials is dominated by the composition of the target rocks. The identification of meteoritic matter in impact melt rocks

relies predominantly on the study of siderophile elements and, specifically, platinum group elements (PGE - e.g., Pt, Pd, Os, Ru, Rh, Ir) in impactites (e.g., Morgan *et al.*, 1975; Palme *et al.*, 1981; Evans *et al.*, 1993; McDonald *et al.*, 2001), which are fingerprints reflecting the composition of the impacted bolides. Siderophile elements e.g., Co, Ni, (Cr) and PGE are enriched by several orders of magnitude in meteorites compared to crustal target rocks (Rudnick and Gao, 2003). This allows a clear distinction between the terrestrial and the meteoritic components. Furthermore, isotope ratios have been shown to complement the identification of projectile matter (e.g., Koeberl, 1998; Tagle and Hecht, 2006; Goderis *et al.*, 2012; Koeberl *et al.*, 2012). The most suitable isotope ratios for determining projectile components in impactites are $^{187}\text{Os}/^{188}\text{Os}$ and $^{54}\text{Cr}/^{52}\text{Cr}$ (Goderis *et al.*, 2012). During the formation of impact derived materials, several factors, i.e., the physical impact and post-impact conditions, as well as element characteristics, may lead to fractionation of the siderophile elements, causing problems in the identification of projectile matter: (i) partitioning and diffusion processes of meteoritic matter within the impact melt (Koeberl, 1998), (ii) hydrothermal processes related to the impact melt (Wallace *et al.*, 1990), and (iii) different vaporization (and condensation) temperatures of the siderophile elements (Gibbons *et al.*, 1976). Little is known about chemical processes during mixing of projectile melts and target melts, although melt mixing is a common feature in several natural impactites; e.g. from the Henbury craters in Australia (Gibbons *et al.*, 1976), Wabar craters in Saudi Arabia (Gibbons *et al.*, 1976; Kearsley *et al.*, 2004; Hamann *et al.*, 2013), Meteor crater in Arizona (Mittlefehldt *et al.*, 2005) or the Kamil crater in Egypt (Dâ€™Orazio *et al.*, 2011). In all these craters an iron meteorite impacted into a silica-rich sedimentary target, metallic and silicate melts were produced and significantly mixed. Geochemical studies have clearly shown that during the mixing process projectile droplets and target melts underwent chemical changes compared to the original composition of the target and the projectile. Iron and nickel from the impactor were partitioned in, and became structural part of the silicate melts, or of minerals that crystallize from this melt (e.g., Mittlefehldt *et al.*, 1992; Hörz *et al.*, 2002; Hamann *et al.*, 2013; Ebert *et al.*, 2013). In their recent study of the Wabar impact melt, Hamann *et al.* (2013) report on small scale partitioning processes which occur during formation of the projectile-target mixture. Cooling of this mixture has induced liquid immiscibility and caused phase-separation and formation of an emulsion of different silicate melts. Along with the exploration of terrestrial craters, laboratory experiments are important tools to study impact processes. Wozniakiewicz *et al.* 2011 performed hypervelocity cratering experiments with pyrrhotite as well as pentlandite projectiles and Al foils targets, as analogue to the Stardust mission. Their SEM and TEM study clearly show that fractionation processes occur during melting and mixing of molten projectile and target material. The sulfur of the projectiles was partially separated from the Fe and Ni, leaving nearly the original Ni to Fe ratio (Wozniakiewicz *et al.* 2011).

Thus, the question arises what controls the element partitioning during these highly dynamic processes. From all these observations it follows that inter-element fractionation of siderophile elements between projectile and target matter cause problems in the chemical classification of projectile traces in natural impactites. Quantification of the projectile partitioning into ejecta requires sophisticated experiments using meteorite analogues (e.g., steels), and well-defined target materials. Here, we present results of five MEMIN (Multidisciplinary Experimental and

Numerical Impact research Network) hypervelocity cratering experiments using steel spheres as projectile and two different silica-rich lithologies (sandstone and quartzite) as target. The steel D290-1 has high amounts of Cr, Co, V, Mo, and W - elements that are nearly absent in the targets allowing the tracing of projectile matter in detail. The quartzite and sandstone targets were used in order to determine effects of different porosities (0 vs. 23 vol.%) and water-saturation (dry or 50 %) on cratering efficiency (Poelchau *et al.*, 2013). Moreover, these petrophysical properties, as well as the variation of the projectile size at constant velocity, enables further insights in the effect of impact energies. All these factors of the parameter study may influence origin and mixing of target and projectile melts too. This will be discussed in detail in this work.

3.3 Experimental and analytical methods

The hypervelocity cratering experiments were carried out with two different light-gas accelerators at the Fraunhofer Ernst-Mach-Institute (EMI) in Freiburg (caliber 8.5 mm) and Efringen-Kirchen (caliber 38.7 mm), Germany. For details of the accelerators and the exact experimental assembly we refer to Lexow *et al.* (2013). The experimental conditions of the discussed experiments (A6-5126, E1-3382, E2-3383, A20-5339 and E6-3452) are listed in Table 3.1, and discussed in Poelchau *et al.* (2013). Material ejected from the laboratory craters was collected with a capture system, in which bricks of phenolic foam were assembled in a modular arrangement (Fig. 1; Sommer *et al.*, 2013). The catcher was mounted parallel to the target surface at a distance of about 50 cm and had an entry hole for the projectile. The samples (highly shocked and projectile rich ejecta fragments, cf. section 3.2.1) analyzed in this study were recovered from the inner zone of the green phenolic foam plates (Fig. 3.1) with tweezers and brushes. Ejecta fragments were mounted in 1 inch epoxy cylinders, polished and (semi-) quantitatively analyzed with the JEOL JXA-8500F field-emission electron microprobe (EMP at MfN) and the JEOL JSM-6610LV scanning electron microscope (SEM at MfN). Individual analytical conditions were applied to determine small concentrations of projectile matter within the target melt: We used two measurement programs, 'M' for the silicate phases and 'P' for projectile material. The EMP measurement conditions are listed in Table 3.2. Semi-quantitative SEM analyses were performed at 15 kV acceleration voltage and 60 nA beam current. Each SEM measurement lasted until 50k net counts were reached (approximately 3 to 4 minutes per analysis). Focused ion beam milling (FIB) was applied to cut site-specific TEM-foils from the area of interest using the FEI FIB200TEM device at the Deutsches GeoForschungsZentrum, Potsdam (GFZ). Transmission electron microscopy (TEM) was carried out at the TEM laboratory of the GFZ, using the FEI Tecnai G2 F20 X-Twin electron microscope operated at 200 kV. The TEM is equipped with a high-angle annular dark-field detector (HAADF). Trace element analysis of the steel projectile was performed on a LA-ICP-MS (Element 2, ThermoFisher; WWU) using a 193 nm ArF excimer laser (UP193HE, New Wave Research). Laser repetition rates were 5 Hz using an energy density of ~ 9 J/cm². Laser-spot diameters varied between 25 - 235 μ m; for analytical details see Berndt *et al.* (2011).

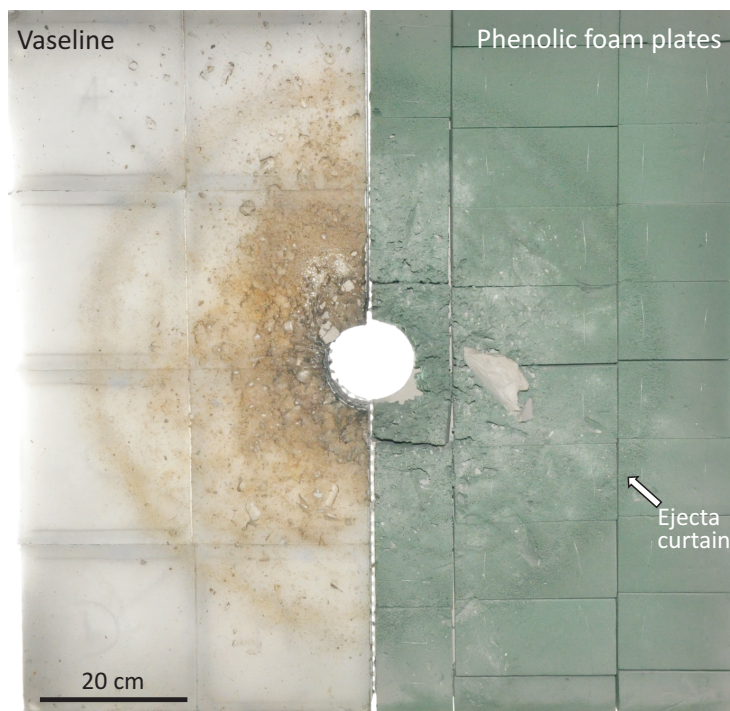


Figure 3.1: Photograph of the ejecta catcher system; consisting of tiles covered with Vaseline (left) and phenolic foam plates (right). Note the remarkable imprint of the ejecta curtain and the main mass of the ejecta in the middle of the catcher surrounding the entrance hole for the projectile. The highly shocked and projectile-rich ejecta fragments originate from the inner part of the catcher (Experiment E1-3382).

3.4 Results

3.4.1 Composition and microstructure of projectile and target

3.4.1.1 Seeberger Sandstein (target lithology)

The Seeberger Sandstein quarried by the TRACO company in Germany is of uppermost Triassic age (209 - 200 Ma; Stück *et al.*, 2011) and was deposited as fluvial sediment within the Thuringian basin. The sandstone comprises of ~ 89 vol.% quartz, ~ 10 vol.% phyllosilicates and accessory minerals (rutile, altered ilmenite, zircon, rare iron-oxides/hydroxides). The phyllosilicates, mostly clay minerals ($< 10 \mu\text{m}$) and subordinate micas ($< 100 \mu\text{m}$), account for the main part of the sandstone matrix forming coatings around quartz grains and aggregates of fine material within the pore space (Fig. 3.2a). The sandstone has an overall porosity of 23 ± 1 vol.%. Exact knowledge of the amount of siderophile elements in the sandstone target is mandatory for identification of projectile matter in the ejecta. The indigenous concentrations of Co, Cr, W, Mo, and V in the sandstone are low, at the ppm level, compared to the one at percent level measured in the steel projectile. The bulk composition of the Seeberger Sandstein and its phyllosilicate bearing matrix are given in Table 3.3.

3.4.1.2 Taunus quartzite (target lithology)

The Taunus quartzite was formed during the Variscan orogeny (Lower Devonian age, Siegen stage, ~ 405 Ma; Mittmeyer, 1980). The quartzite is characterized by fine-grain sizes of 75 - 125 μm , high-quartz content (~ 91 vol.%) and virtually no porosity (Fig. 3.2b). Besides the major

quartz component, the quartzite comprises also a fine-grained phyllosilicate-bearing matrix (~ 8 vol.%) and very small amounts of rutile, chromite, zircon, monazite, and iron oxides. The modal composition, i.e., amount of the phyllosilicate matrix in quartzite and sandstone, was determined with quantitative image analysis of EDX aluminium element maps; using the open source image software JMicroVision (www.jmicrovision.com). The chemical composition of the quartzite and its phyllosilicate bearing matrix is listed in Table 3.3.

3.4.1.3 D290-1 steel (projectile material)

D290-1 is the internal designation used by the Federal Institute for Materials Research and Testing (BAM- Berlin, Germany; for more details about the high speed steel see www.bam.de/de/_rm-certificatesmedia/rm_cert_iron_steel/rm_cert_highly_alloy_steel/d290_1.pdf). Further metallurgical designations of this steel are AISI M35, DIN S6-5-2-5 or Material No 1.3243. Steel D290-1 was chosen as the projectile material due to its high content of the tracer elements: Cr, V, Co, Mo, and W. Iron can also be considered as a tracer element because of the high amounts in the steel and the low amounts in the silicate targets. D290-1 belongs to the group of high speed steels with about 22 % alloying elements. The chemical composition of the D290-1 steel is listed in Table 3.3. The steel has a homogeneous microstructure with a ferrous (austenite) matrix and conspicuous finely dispersed blocky carbides (Fig. 3.2c), mainly Mo-W-rich and V-Cr-rich carbides with a mean grain size of about $< 5 \mu\text{m}$. They are mainly distributed along grain boundaries of the austenite matrix. The steel was produced by hot isostatic pressing of gas atomized steel powder. This production method is causing a certain micro-porosity of the steel with pores smaller 100 nm.

3.4.2 Impact-induced features and modes of projectile-target mixing

3.4.2.1 Highly shocked and projectile rich ejecta

The hypervelocity impacts result in the ejection of various materials from the growing crater. The materials, which were extracted after the experiment from the ejecta catcher system, are mainly represented by weakly deformed, highly deformed, and highly shocked fragments as well as projectile relicts (Ebert *et al.*, 2013; Kenkmann *et al.*, 2013). Only the highly shocked ejecta fragments contain projectile material. The following sections contain general macroscopic and microscopic observations of the highly shocked projectile rich ejecta fragments, collected from experiments with both sandstone and quartzite targets. Due to the similar observations in the ejecta of A6-5126, E1-3382, E2-3383, they are summarized as sandstone experiments, and A20-3359 and E6-3452 as quartzite experiments, respectively. The highly shocked ejecta is represented by white to dark gray variegated clusters of fragments that appear darker than less shocked ejecta (Fig. 3.2d). The conspicuous dark color indicates the presence of projectile matter. Intense fracturing and pulverization, however, increases the surface of quartz grains so that these parts of the highly shocked ejecta appear macroscopically white. The highly shocked and projectile rich ejecta occur as μm - to mm-sized (up to 5 mm) fragments; on average the fragments of the dry sandstone experiments are larger than the corresponding material from the water saturated sandstone and dry quartzite experiments. This ejecta type represents the most strongly shocked part of the target and quartz shows various shock features (Fig. 3.3

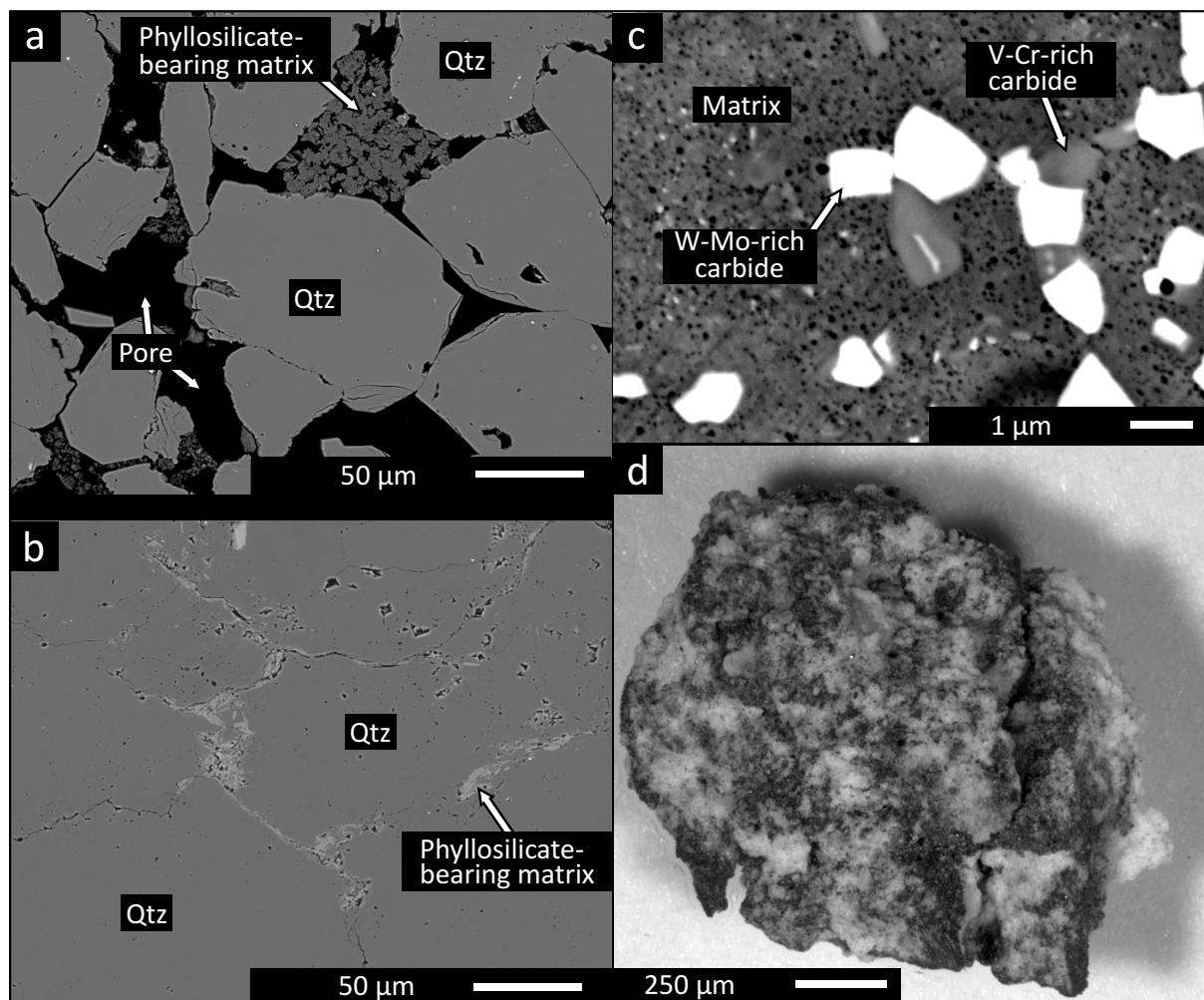


Figure 3.2: Back-scattered electron (BSE) image of (a) the original Seeberger sandstone, (b) the Taunus quartzite, and (c) steel D290-1. Black dots are pores. (d) Photomicrograph of a highly shocked (and projectile rich) ejecta fragment of the sandstone experiment E1-3382. Fragments from quartzite experiments look very similar.

and Fig. 3.4), including intense fracturing, formation of planar deformation features (PDF), and onset to complete transformation of quartz to fused silica glass (lechatelierite). Strongly fractured quartz grains always show multiple sets (2 or 3) of PDF (Fig. 3.3b). Melting of quartz starts at the grain margins, propagates along fractures and/or PDF, and ends in a completely transformation into silica glass (Fig. 3.3b, c and Fig. 3.4b, c). The alignment of vesicles within silica glasses indicates melting along a former fracture (Fig. 3.3c). The highly shocked quartzite ejecta (A20-3359, E6-3452) show enhanced formation of silica glass, compared to the experiments with sandstone targets. The shock features vary on very narrow distances within a single fragment ($< 20 \mu\text{m}$). In the electron back-scattered (BSE) mode of the microprobe it is easy to distinguish between still crystalline quartz, the amorphous PDF, and silica glasses which both have a lower density, hence, displaying a darker shade of gray. In addition to the shock-metamorphism of quartz, we have observed in experiment E6-3452 with quartzite, the marginal decomposition of zircon to baddeleyite (ZrO_2) with a grain size of up to $0.5 \mu\text{m}$ (Fig. 3.4f). This decomposition reaction indicates post-shock temperatures in excess of 1676°C , and a rapid quenching of the shocked material (Wittmann *et al.*, 2006). Zircon, which is

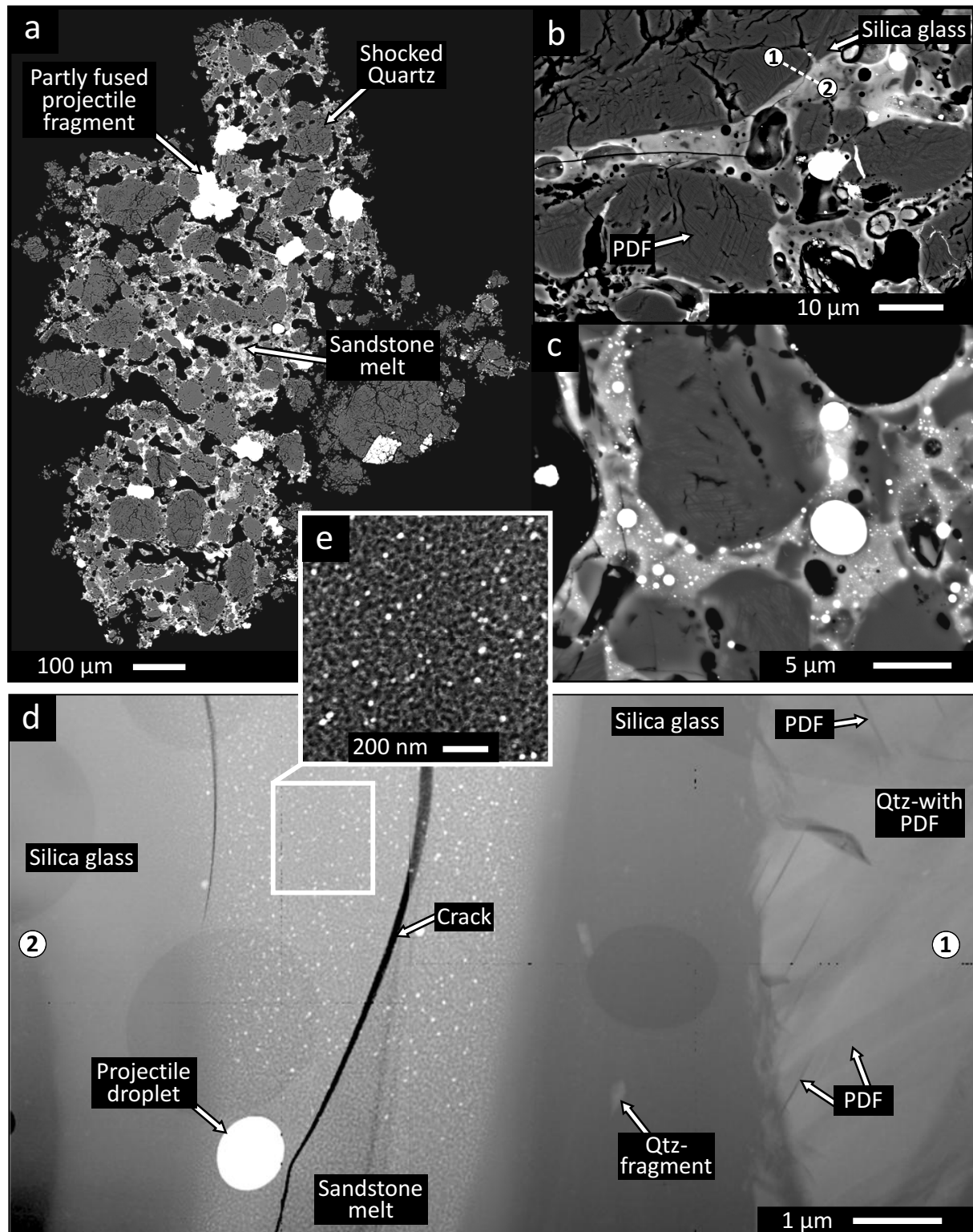


Figure 3.3: (a-c) BSE images of highly shocked sandstone ejecta with shocked quartz (dark gray), sandstone target melt (light gray) and different projectile material (white); (b) The white dashed line between point 1 and 2 marks the position of the TEM foil; (d) HAADF image of the marked TEM foil (in Fig. 3.3b) with sandstone melt, silica glass, Qtz with three different sets of PDF and projectile droplets; (e) Magnification of Fig. 3.3d shows liquid immiscibility textures of silica rich liquid (*L_{Si}*, dark gray), iron-rich liquid (*L_{Fe}*, light gray) and projectile droplets (HAADF image) - (a,b,e,d: E1-3382; c:A6-5126).

very rare in the target materials, has not been observed in the highly shocked ejecta fragments from sandstone experiments. Partial melting of the target rock is a conspicuous feature in the highly shocked ejecta (Fig. 3.3 and Fig. 3.4). The sandstone and quartzite melts form a more or less interconnected network ($< 100 \mu\text{m}$) between the shocked quartz grains. Partial melting of sandstone and quartzite mainly comprises the phyllosilicate-bearing matrices but involves quartz, too. Quartz fragments were partially mingled into the target melts as small fragments as well as individual schlieren of silica glass (both $< 10 \mu\text{m}$) and may form an intimate mixture (Fig. 3.3b, Fig. 3.4b). Silica glass schlieren indicate some localized melt flow. The TEM analyses provided further details of the small scale heterogeneity within the shocked target (Fig. 3.3d, e). The TEM investigations were only carried out with samples from the sandstone experiments. Figure 3.3b shows the location of the FIB prepared TEM foil (between point 1 and 2), which comprise the transformation from PDF bearing quartz to silica glass and the sandstone melt. The density contrast between crystalline and amorphous SiO_2 is clearly visible in the Z -contrast sensitive HAADF-image with amorphous parts of lower density (PDF lamellae and fused silica glass) displaying a darker gray color. Different sets of PDF are shown in Fig. 3.3d with a width of individual lamellae of $\sim 10 \text{ nm}$. Due to a small angle between the FIB cut and PDF they appear wider in the HAADF image. The small quartz grains within the silica glass are unmelted fragments of the original unshocked quartz. The Z -contrast reflecting HAADF images of Fig. 3.3d, e clearly show that the sandstone melt is not homogenous, but a heterogeneous multicomponent silicate glass. In detail the sandstone melt is composed of an emulsion of two compositionally different melts that quenched to a phase-separated glass. It is dominated by a highly siliceous glassy matrix (termed *Lsi* for silica-rich liquid) that contains homogeneously dispersed Fe-rich glass droplets (termed *Lfe* for Fe-rich liquid). The amorphous high absorption phase is *Lfe* (light gray in Fig. 3.3e), while the low absorption phase is *Lsi* (dark gray in Fig. 3.3e). Figure 3.3e reveals emulsion textures with the droplet sizes in the range of 10 to 30 nm. These silicate melt droplets are partially interconnected into small clusters, by which they lose their spherical shape. This is an impressive example of liquid-phase separation in glass-forming systems with strong chemical differences (see discussion). In addition, we observed numerous small metallic projectile droplets and columnar Cr-V-rich minerals within the sandstone melt. Due to the extremely small sizes the phase separation feature of the sandstone melt is rarely visible with standard electron beam techniques.

In contrast, the emulsion textures of the impact-induced quartzite melt are observable with the high-resolution field-emission microprobe (Fig. 3.4c-e). With increasing distance from the metallic projectile droplet in the highly shocked quartzite ejecta, a compositional gradient forms a zone of iron enrichment. This zone shows three different emulsion textures (Fig. 3.4c, d), marked as 1, 2, and 3 in Fig. 3.4c. Part 1 predominately consists of *Lfe* with minor amounts of *Lsi* droplets. Part 2 has more or less equal proportions of irregular shaped *Lfe* and *Lsi* droplets; whereas part 3 is dominated by *Lsi* containing low amount of *Lfe* droplets. Individual silica melt droplets reach sizes up to 250 nm. Many droplets are interconnected, and most of them are non-spherical in shape. Thus, most of the emulsion domains are associated with/or in direct vicinity of *Lfe*, which forms this conspicuous rim or irregular shaped patches around certain projectile droplets (Fig. 3.4b-e). Within the iron enrichment zone further geochemical processes

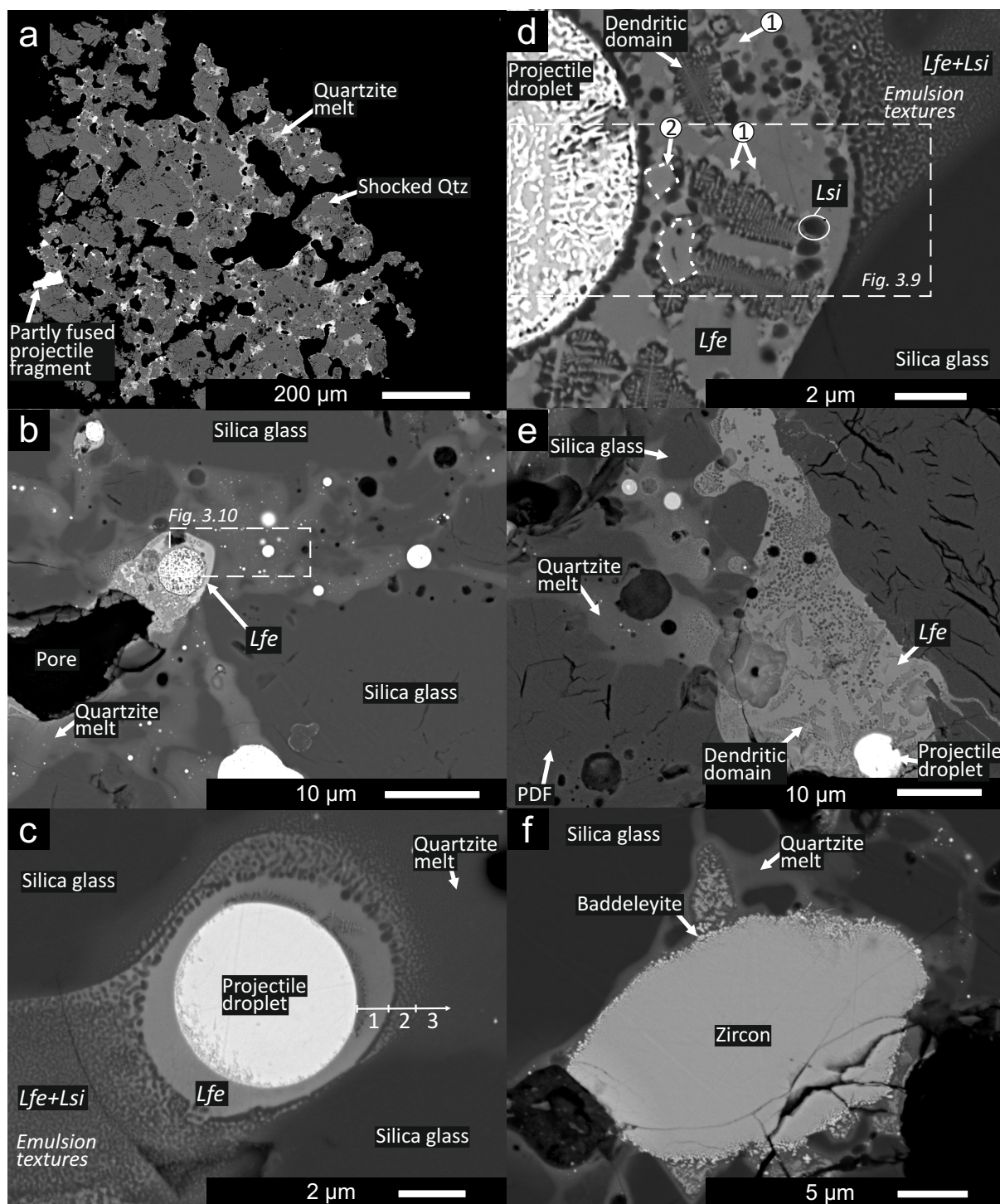


Figure 3.4: (a) BSE image of highly shocked quartzite ejecta with shocked quartz (dark gray), quartzite target melt (light gray) and steel projectile material (white); (b) typical projectile-target mixing and unmixing textures, *Lfe* surrounding projectile droplets as well as silica glass; (c) iron enrichment zone around steel projectile droplet with subsequent unmixing into Fe-rich (*Lfe*) and Si-rich (*Lsi*) silicate melts (d) projectile droplet and iron enrichment zone; including dendritic domains of Cr-V-rich minerals and (1) Fe-rich minerals, (2) Cr-V-rich minerals (A20-5339); (e) typical projectile-target mixing and unmixing textures, *Lfe* surrounding projectile droplets and quartzite melt; silica glass and PDF-bearing Qtz; (f) Marginal decomposition of zircon to baddeleyite. (a-e: A20-5339; e: E6-3452).

occurred: (i) crystallization of dendritic domains associated with small Cr-V-rich and Fe-rich minerals (probably spinels), and (ii) secondary phase separation of *Lsi* as irregularly shaped patches ($< 1 \mu\text{m}$; Fig. 3.4d). The interstitial material of the dendrites is also rich in silica. The iron enrichment zones mainly occur around projectile droplets larger $\geq 4 \mu\text{m}$ and are in most cases ($> 95 \%$) in the direct vicinity of a pore. The remaining 5 % may also have contacts to pores, which are not visible due to cutting effects. These iron enrichment zones are frequently present in the quartzite experiment A20-3359 but are completely lacking within the ejecta of the impact experiments with sandstone as target material.

3.4.2.2 Projectile within the highly shocked ejecta

Projectile material occurs as partly fused projectile fragments and finely disseminated projectile droplets within the highly shocked ejecta. The interior of projectile fragments (100 μm - 1 mm) may display the original steel texture (cf. Fig. 3.2c); in a few cases the Mo-W-rich carbides were re-orientated near the projectile fragment margins, due to shearing and deformation. Projectile fragments without evidence of melting can also show a preferred orientation of the Mo-W-rich carbides along parallel zones again indicating a strong deformation during compression and fragmentation of the projectile sphere. The partly fused projectile fragments have molten margins, which show variable states of homogenization of the steel (Fig. 3.5a). Figure 3.5a gives a detailed insight into the successive melting of projectile fragments. The right side of the fragment is clearly unaltered; whereas towards the left side the textures indicate increasing melting and homogenization of the steel matrix; the steel D290-1, however, rarely shows complete homogenization. Even within single melt droplets separation of Mo-W-rich carbides from the rest of the melt is common (white phase in BSE images Fig. 3.5a-c, e). The formation of such Mo-W-rich carbides with fish-bone-structures (Fig. 3.5e) is well known in metallurgical processes; the textures represent eutectic carbides (e.g., Weber *et al.*, 2009). The conspicuous Mo-W-rich carbides may also occur within very small metallic projectile droplet (Fig. 3.5c). The projectile melt droplets (few nm up to 100 μm in size) were mechanically separated from the molten margins of the partly fused projectile fragments (left side in Fig. 3.5a, Fig. 3.5b-d) during the impact process. Projectile droplets without eutectic Mo-W-rich carbides are also common (Fig. 3.5d). Note that all these metallic droplets have mingled with low-viscosity target melts but not with pure silica melt (fused silica).

3.4.3 Chemical modification of projectile and target material

3.4.3.1 Chemical modification of the sandstone targets

The chemical composition of the produced target melts in the three different sandstone experiments are very similar (cf. Table 3.4, Fig. 3.6). Therefore we summarize the microprobe data of the sandstone experiments at this point; explicit differences between experiments A6-5126, E1-3382 and E2-3383 are accordingly explained. Heterogeneities in the matrix and different ratios of molten matrix and partially molten quartz cause stark compositional variations in the target melt (Table 3.4): SiO_2 (51.70 - 84.43 wt.%), Al_2O_3 (3.77 - 25.93 wt.%), K_2O (0.11 - 2.05 wt.%), MgO (0.11 - 1.65 wt.%), FeO (4.37 - 24.89 wt.%) and TiO_2 (0.12 - 2.43 wt.%). Most remarkable is the highly variable FeO content and in addition a significant enrichment of

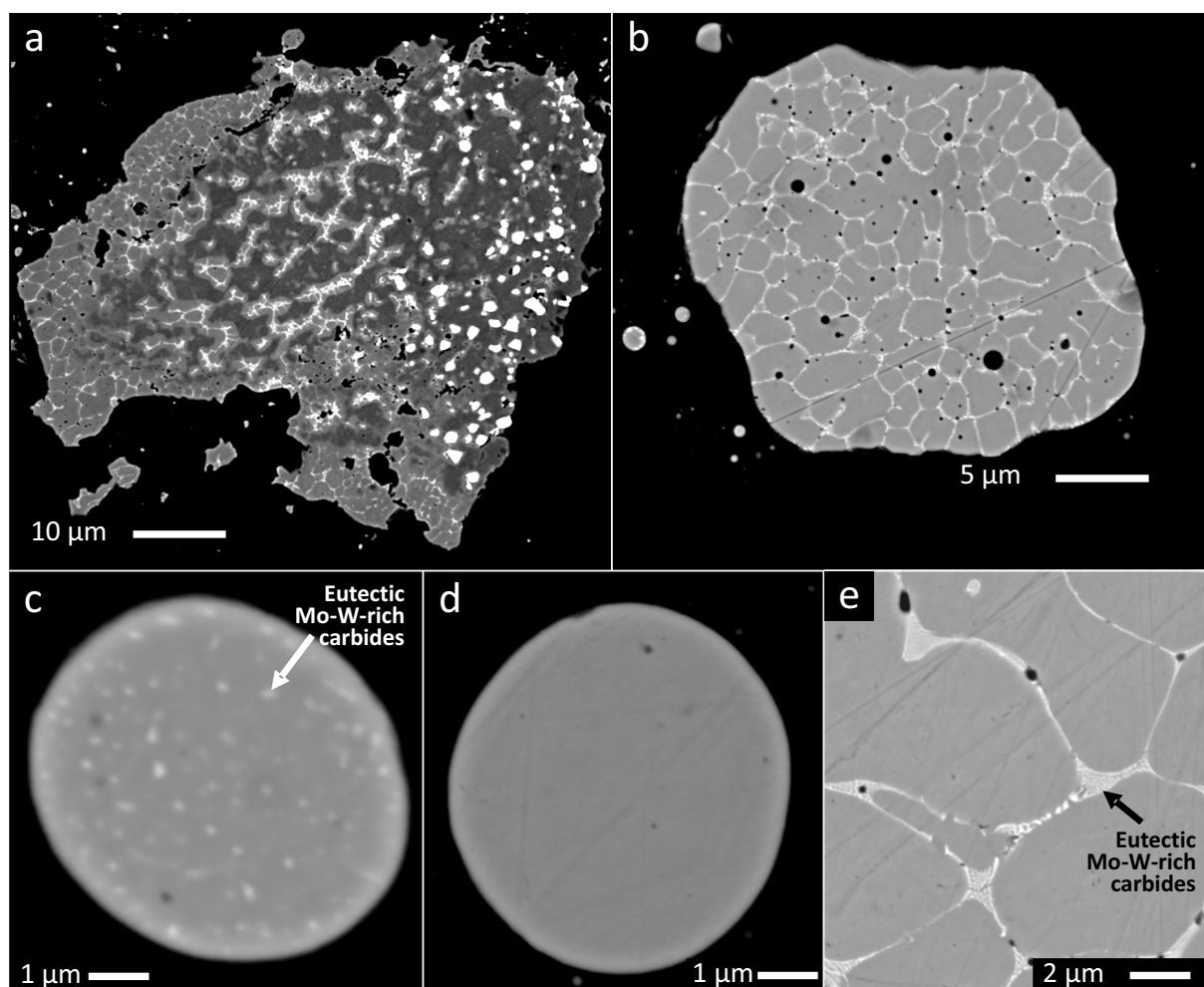


Figure 3.5: BSE images of shocked projectile material. In order to show the internal structure of the material, the BSE images were taken with low-brightness conditions; thus the surrounded, low-dense target material is not visible (black areas); (a) Partly fused projectile fragment with gradual melting and homogenization textures (roughly from right to left); (b,c) Molten projectile droplets with Mo-W-rich zones, partly crystallized to Mo-W-rich carbides; (d) homogenous projectile droplet; (e) high magnification of a projectile droplet with eutectic Mo-W-rich carbide-fishbone-structure. (a-c: E1-3382; d: E6-3452, e: A20-5339).

Cr_2O_3 (0.31 - 11.75 wt.%) and V_2O_3 (0.23 - 7.32 wt.%). It is assumed that a certain fraction of Fe, Cr, and V in the sandstone melt may originate from the matrix. The amounts of minerals containing these elements (e.g., iron oxides or chromites) are much too low to contribute to the high amounts of these elements in the melt (Table 3.4). Therefore the relatively high contents of FeO, Cr_2O_3 and V_2O_3 in melts resulted from projectile addition. Figure 3.6 shows metal contents instead of metal oxides in order to include steel D290-1 data (non-oxide) as ratio lines or data points for comparison with the produced target melts. There is a strong scatter in Fe/Cr of the sandstone melt (1.2 to 40.1) but Fig. 3.6a-c clearly shows that its average Fe/Cr (~ 6.4) is lower than Fe/Cr in the projectile (~ 18.9). The same applies for Fe/V with an average of about 7.4 for the sandstone melt. The Cr/V of the sandstone target melt (~ 1.7) approximates to Cr/V in the projectile (~ 2.2). The element maps shown in Fig. 3.7 provide a detailed view into the partitioning processes. Note that the chemical composition of the sandstone melts is

quite variable even on the micrometer scale. Figure 3.7 shows that nearly the entire Cr and V budget of the projectile droplets partition into surrounding sandstone melt. Co is also slightly enriched in the sandstone target melt compared to the bulk sandstone (Table 3.3 and Table 3.4, Fig. 3.6d-f). Within the sandstone melts, the average Fe/Co (~ 328) is one order of magnitude above that ratio in the target (Fe/Co ~ 15.1); yet it is shifted in some cases to lower Fe/Co (Fig. 3.6d-f). Unfortunately most of the WO_3 and MoO_3 measurements are below the respective detection limit of the EMP. According to TEM analyses the sandstone melt is composed of a mixture of two melts (*Lsi* and *Lfe*) and small Cr-V-rich minerals (cf. Fig. 3.3d, e). In addition, we consider gas trapped / originally present in the pore space of the sandstone, and the dissociation of H_2O (Brett, 1967) originating from the phyllosilicate-bearing matrix of the quartzite and sandstone as potential sources for oxygen. This view is supported by the vesicular target melts (cp. Fig. 3.3c and Fig. 3.4b), which implies vaporization of certain amounts of H_2O , which in turn, may have been dissociated. It follows that the microprobe data of the sandstone melt (and probably also the quartzite melt) provide mostly a mixture of these four components in various proportions.

3.4.3.2 Chemical modifications of the quartzite targets

The composition of the impact-generated melts in the quartzite experiments E6-3452 and A20-5339 are quite identical (cf. Table 3.5, Fig. 3.8). The quartzite melt show large compositional variation, i.e., SiO_2 contents ranging from 48.74 to 87.1 wt.%, Al_2O_3 0.42 to 32.19 wt.%, FeO 4.18 to 38.23 wt.%, MgO 0.27 to 1.23 wt.%, K_2O 0.05 to 2.16 wt.% and TiO_2 0.19 to 5.35 wt.% (Table 3.5). The average FeO content of the quartzite melt patches (18.49 ± 7.91 wt.%) is significantly higher than the average FeO of its phyllosilicate-bearing matrix (2.46 ± 1.70 wt.%; Table 3.3). The quartzite melt shows a distinct enrichment of Cr_2O_3 (0.12 to 7.66 wt.%) and V_2O_5 (0.09 to 5.37 wt.%). Two different data sets exist (i) data points with Fe/Cr (and Fe/V) plotting above the projectile ratio line in Fig. 3.8, and (ii) data plotting below this ratio line. The projectile tracer elements Co, W, and Mo also partition preferentially into the quartzite melt (enrichment: $\text{Co} \sim \text{W} \succ \text{Mo}$), but to a considerably lower degree compared to Cr and V (Table 3.5). Within the quartzite melt, the average Fe/Co (~ 139.2) is mainly one order of magnitude above that ratio in the projectile (Fig. 3.8b). Within the highly shocked ejecta of the quartzite experiments Fe-rich silicate melt (*Lfe*) occurs as conspicuous rim around certain projectile droplets (Figs. 3.4, 3.9 and 3.10) and as part of melt emulsions. This *Lfe* is defined by high FeO contents with an average of 53.8 wt.% (calculated by using A20-5339 and E6-3452 data) which allows a good distinction to the other target melts even in the BSE mode. The *Lfe* has variable amounts of SiO_2 (23.53-43.93 wt.%), Al_2O_3 (0.65-5.96 wt.%), WO_3 (1.4-9.97 wt.%) and minor fractions of Cr_2O_3 ($\prec 1.43$ wt.%), V_2O_5 ($\prec 1.01$ wt.%), CoO ($\prec 3.14$ wt.%), and MoO_3 ($\prec 1.9$ wt.%). The high Fe and W contents and the low Co of *Lfe* are illustrated in the element distribution maps of Fig. 3.9 and Fig. 3.10. Iron oxide is nearly homogeneously distributed in the *Lfe*; WO_3 , however, shows a diffuse distribution. The *Lsi* droplets within the rim of *Lfe* indicate liquid-liquid unmixing. The high Si content of *Lsi* droplets is clearly visible in the Si element map of Fig. 3.9. Additional phase separations occurred within the iron enrichment zone, resulting inter alia in the formation of sub- μm sized minerals and dendritic domains rich in Cr and V (cf. Fig. 3.4, distribution maps in Fig. 3.9). Due to their small sizes

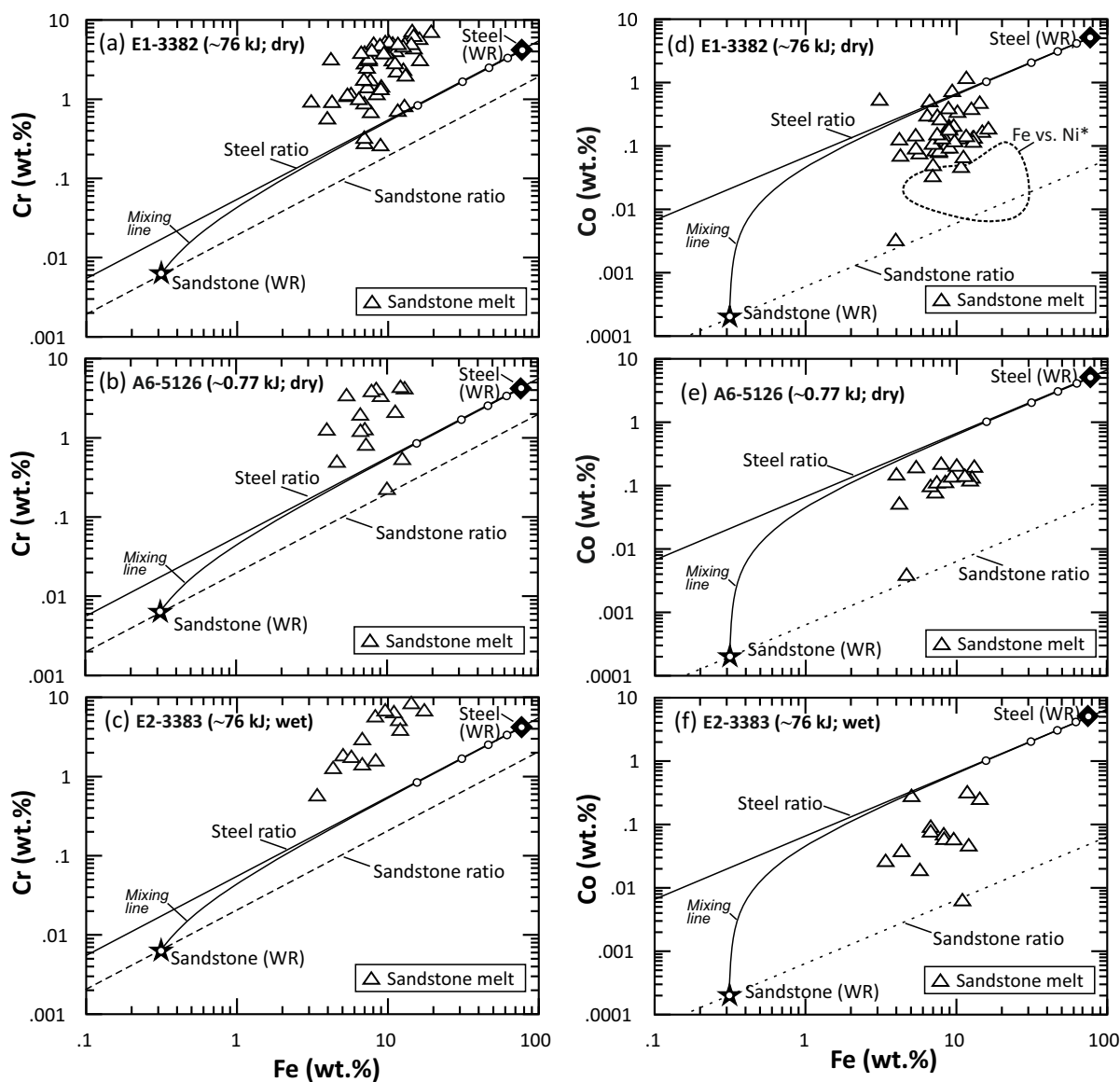


Figure 3.6: (a-c) Fe vs. Cr microprobe data for sandstone melts; Cr preferentially partitioned into the sandstone melt, resulting in an average Cr/Fe above the steel ratio line; (d-f) Fe vs. Co microprobe data for sandstone melt; minor amounts of Co partitioned into the sandstone melt, resulting in an average Co/Fe ratio below the steel ratio; (d) includes Fe vs. Ni* data field of an equivalent experiment with an iron meteorite projectile from Ebert *et al.* (2013); data from hypervelocity impact experiment E1-3382, A6-5126 and E3-3383; impact energies in kilojoules (kJ); WR=whole rock composition; dry=dry target, wet=water saturated target. The dots on the mixing line are subdivisions in 20% steps.

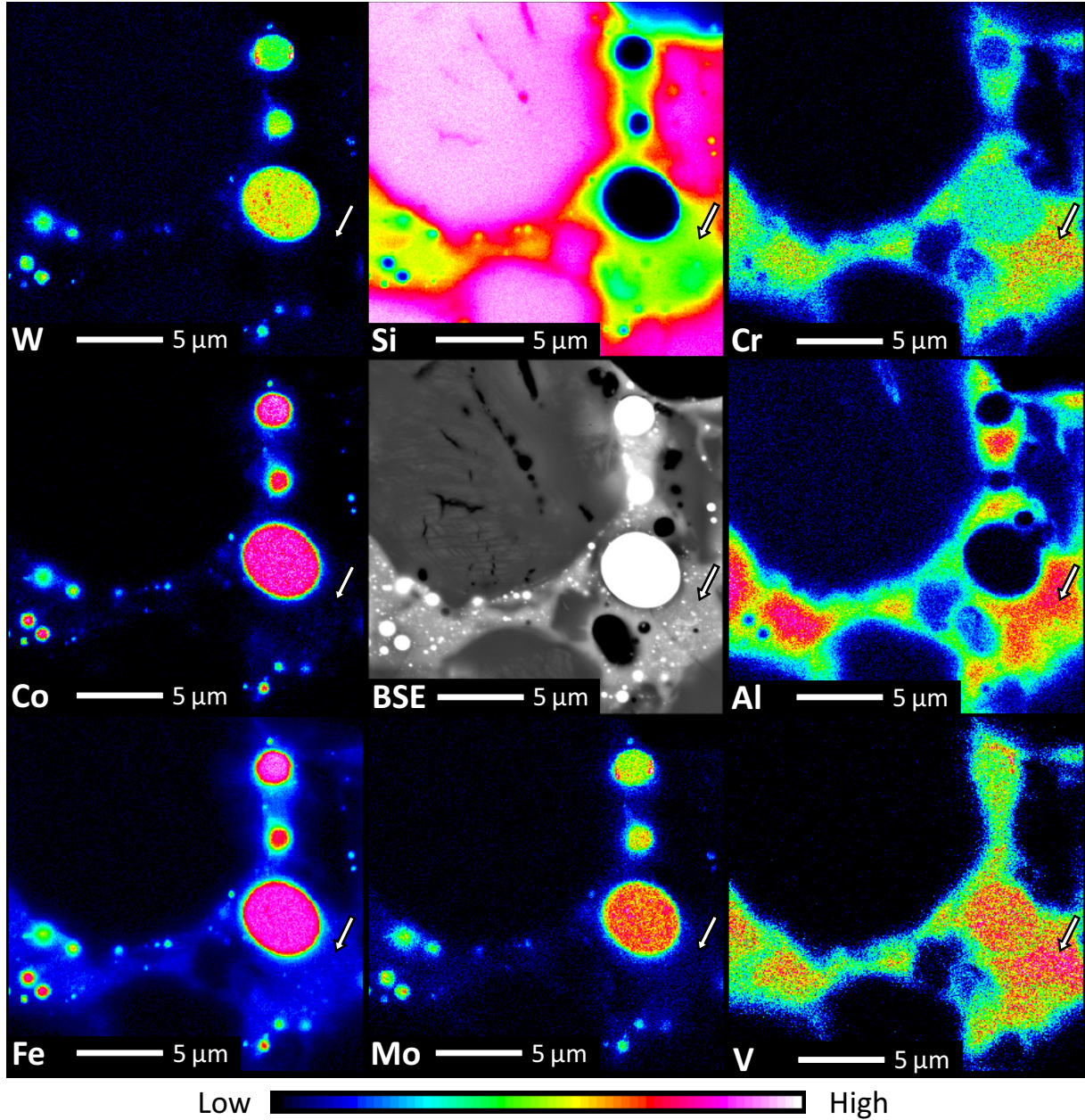


Figure 3.7: Qualitative element maps of a highly shocked ejecta fragment with shocked Qtz grains (BSE - dark gray), sandstone melt (light gray), projectile droplets (light spheres of D290-1 steel) and pores (black spaces). Note the strong partitioning of Cr and V into the Al-rich silicate melt near the largest projectile droplet (highlighted by the white arrow). W, Co and Mo mainly remain in the projectile droplets and partially form discrete phases (Experiment A6-5126).

an exact determination of their chemical composition is complicated and our data probably reflect mixed analyses. The Cr-V-rich minerals and dendritic domains give a good estimate of the major element composition; e.g., the Cr-V-rich minerals have Cr_2O_3 and V_2O_3 amounts up to 27.77 wt.% and 11.92 wt.%, respectively (FeO 61.24 wt.%; SiO_2 27.39 wt.%, Al_2O_3 3.21 wt.% maximum values). The interstitial material of the dendritic domains is rich in silica. The Cr_2O_3 and V_2O_3 contents are consequently on average lower (13.13 wt.% and 5.99 wt.%, respectively) than the element contents of the Cr-V-rich minerals (element maps in Fig. 3.9). We suggest that the Cr-V-rich minerals belong to the spinel group and are probably a variation of chromite, but due to the small sizes high resolution TEM analyses are needed to confirm this suggestion. In addition, the dendritic domains are partially surrounded by small Fe-rich minerals (probably magnetite; cf. Fig. 3.4d and Fe element map in Fig. 3.9) with up to 75 wt.% FeO. Again an exact composition is difficult to determine given the very small size of the phase. We assume that the SiO_2 and Al_2O_3 signal that we have detected together with iron, reflect some mixture analyses with the components that surround the Fe-rich phase. Table 3.5 gives some representative microprobe data of the quartzite melt and the Fe-rich silicate melt.

3.4.3.3 Chemical modifications of the steel projectile

Accompanied by chemical alterations during melting and mixing, three different modification states (a-c, see below) of the projectile material that occur in the highly shocked ejecta fragments of all of the five impact experiments can be distinguished. The projectile material can reach these states by two ways: "directly" due to the heterogeneous distribution of energy in form of heat within the crater, or "successively" during a time-depending movement of the projectile material through the target melts. The time-depending movement and contemporaneously chemical modification play a minor role, since the conditions for these geochemical processes are only present for an ultra-short time interval during the impact experiment. The "direct" way, driven by energy partitioning during the impact, seems to be the most likely modification for the projectile material. The intensity of the modification increases from (a) to (c); intermediate states between them also occur. Figure 3.5a gives the best example for the first state (a): partially homogenization of the projectile during melting. The dark gray color of the projectile melt within the partly fused projectile fragment (BSE image - Fig. 3.5a) indicates only a minor enrichment of W and Mo, compared to the matrix of the original D290-1 steel. At higher temperatures and progressive melting of the Mo-W-rich carbides, the projectile melt is significantly enriched in W and Mo (light gray melt in Fig. 3.5a); but this successive homogenization also leads to decrease of Fe and Co compared to the matrix of the original steel. Table 3.6 gives some representative EMP analyses and the data are compiled in Fig. 3.11. The distribution of the data points that represent various projectile melts is outlined by a solid line in Fig. 3.11. This projectile melt represents more or less the source material of the projectile droplets, which were separated from the molten margin of the partly fused projectile fragments and incorporated into the impact-induced targets melts. During movement through the targets melt further chemical changes occur. In state (b) projectile material also undergoes a loss of Cr and V. As described above, these elements were partitioned into the surrounding silicate melts and silicate phases. Due to the release of Cr and V the projectile droplet have consequently slightly higher Fe values (Fig. 3.11). In state (c) a significantly loss of iron leads to a relative enrichment of

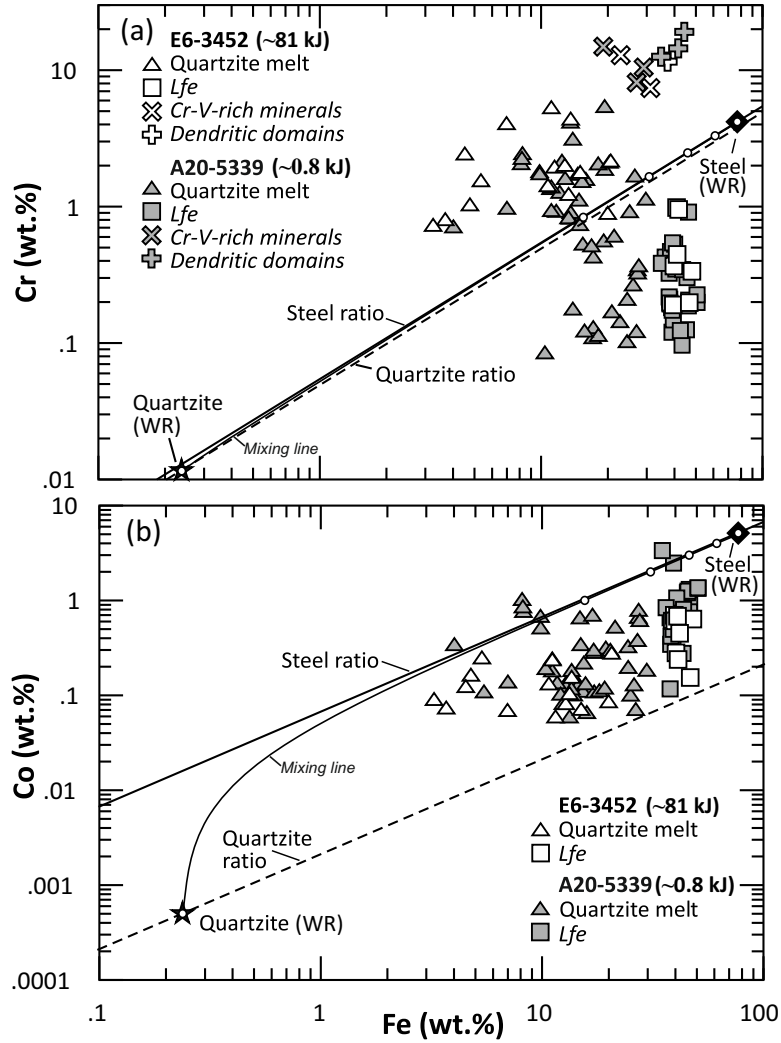


Figure 3.8: (a) Fe vs. Cr and (b) Fe vs. Co microprobe data for quartzite melt, *Lfe*, Cr-V-rich minerals and dendritic domains; data from hypervelocity impact experiment E6-3452 and A20-5339; WR=whole rock, impact energies in kilojoule (kJ). The dots on the mixing line are subdivisions in 20% steps.

the other remaining tracer elements (Fig. 3.11). We found three different types of projectile droplets (PD). Type 1 (PD1) are apparently homogeneous droplets without eutectic Mo-W-rich carbides (Fig. 3.5d). PD1 of highly shocked quartzite ejecta have on average higher Mo, W, and Co amounts compared to the first developed projectile melt and to similar droplets from the sandstone experiment (Fig. 3.11 and Table 3.6). Type 2 (PD2) occurs only in quartzite target melt and comprises homogeneous droplets surrounded by a conspicuous iron enrichment zone (Fig. 3.4c). The PD2 droplets contain high amounts of Co (mean 11.0 wt.%), Mo (11.2 wt.%), and W (12.8 wt.%) and relatively low amounts of Fe (64.2 wt.%) compared to the source projectile melt or the D290-1 steel values. Type 3 (PD3) are heterogeneous metallic spheroids surrounded by an iron enrichment zone, e.g., the droplets in Fig. 3.4b and d, and Figs. 3.9 and 3.10. The EMP data are mixture analyses of Mo-W-rich carbides (light dendritic-like phases in Fig. 3.4) and matrix melt of the corresponding projectile droplets. Cobalt has an average abundance of 5.94 ± 0.13 wt.% in the original steel matrix; changes in the Co content, therefore,

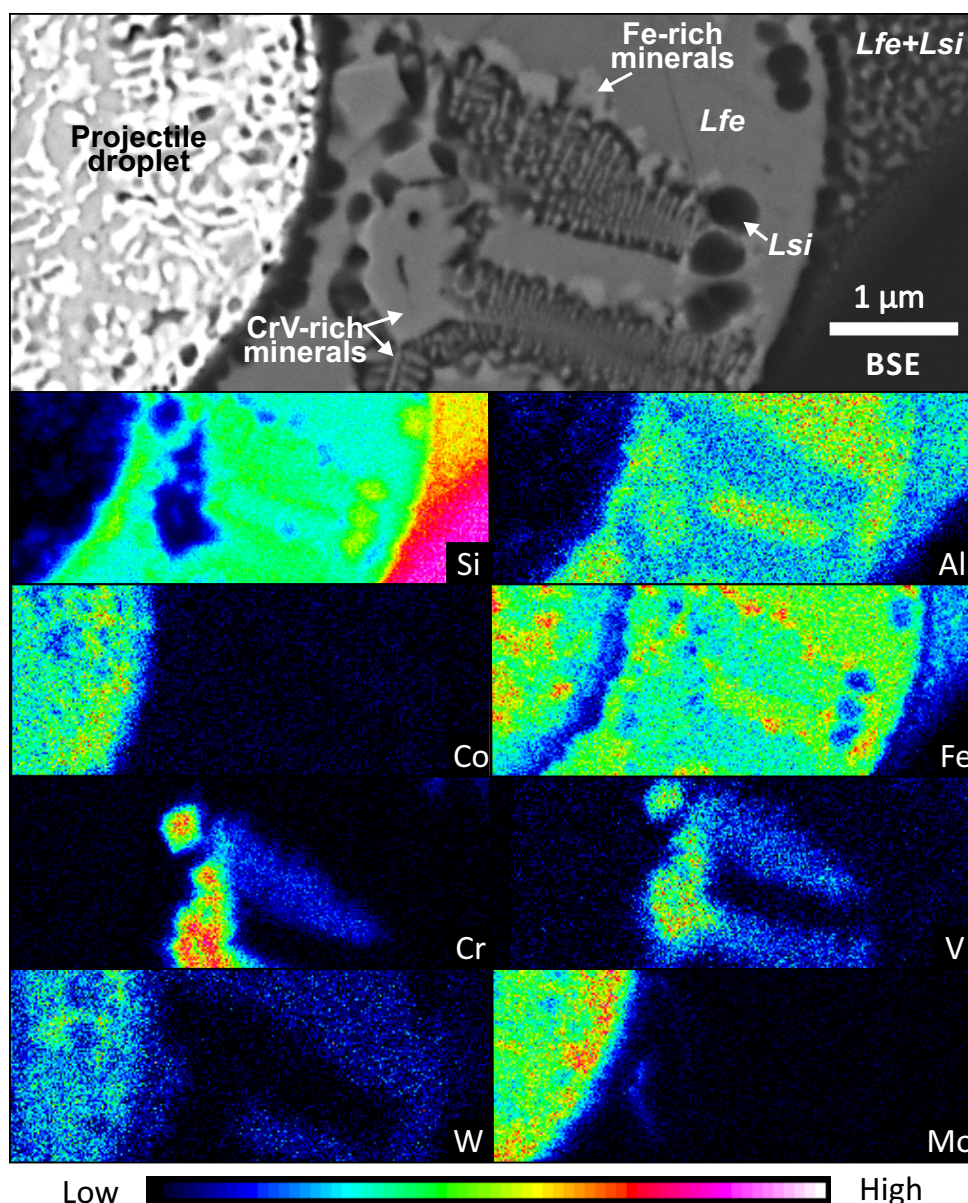


Figure 3.9: Qualitative element maps (exact position is shown as rectangle in Fig. 3.4d) of a highly shocked ejecta fragment with projectile droplet; (Experiment A20-5339).

provide the best information about the chemical modification of the steel during melting and the formation of droplets. The maximum observed Co content in PD3 droplets is 38.6 wt.%. This enormous enrichment is caused by the strong depletion of Fe; in some cases PD3 lost nearly their entire Fe (Table 3.6, Fig. 3.10).

3.5 Discussion

3.5.1 Origin of the highly shocked and projectile rich ejecta

Shock metamorphism, melting of target and projectile, and mixing among both entities may occur at several stages at the impact process, finally resulting in projectile bearing ejecta. This section discusses the modification of projectile material and the development of the highly shocked ejecta (Fig. 3.12, modified from Melosh, 1989, and French, 1998). Stage I (Fig. 3.12a) comprises

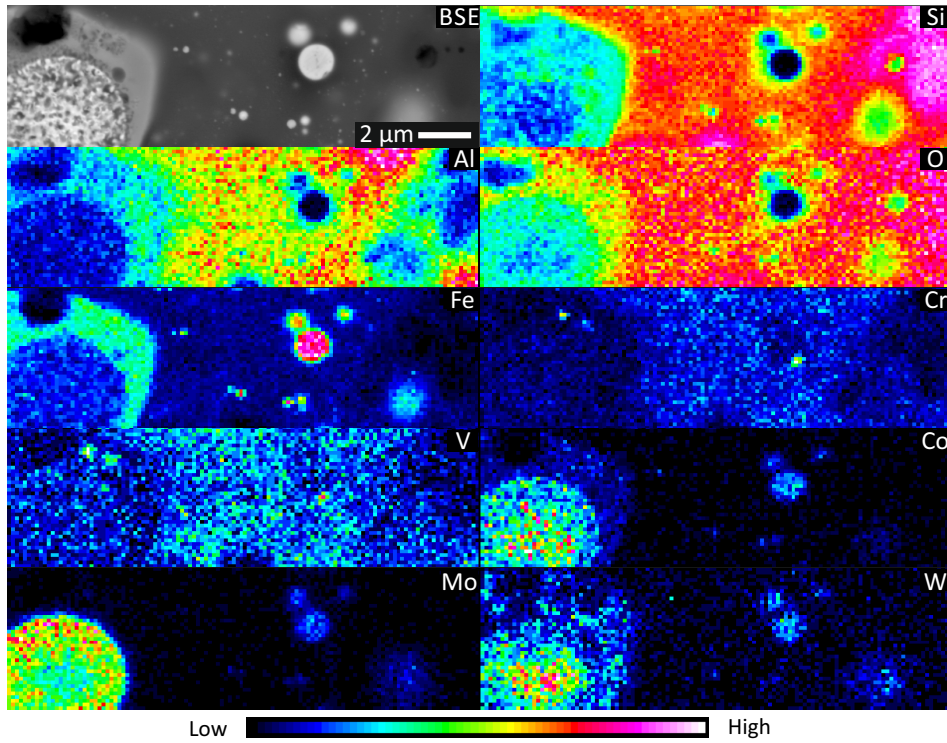


Figure 3.10: Qualitative element maps (outlined rectangle of Fig. 3.4b) of a highly shocked ejecta fragment with *Lfe* (light gray surrounding the large droplet), projectile droplets (light projectile melt droplets of D290-1 steel) and quartzite melt (dark gray); note the enrichment of Mo in the margins of the large projectile droplet (left side of the image), on the other hand W and Co are enriched in center - (Experiment A20-5339).

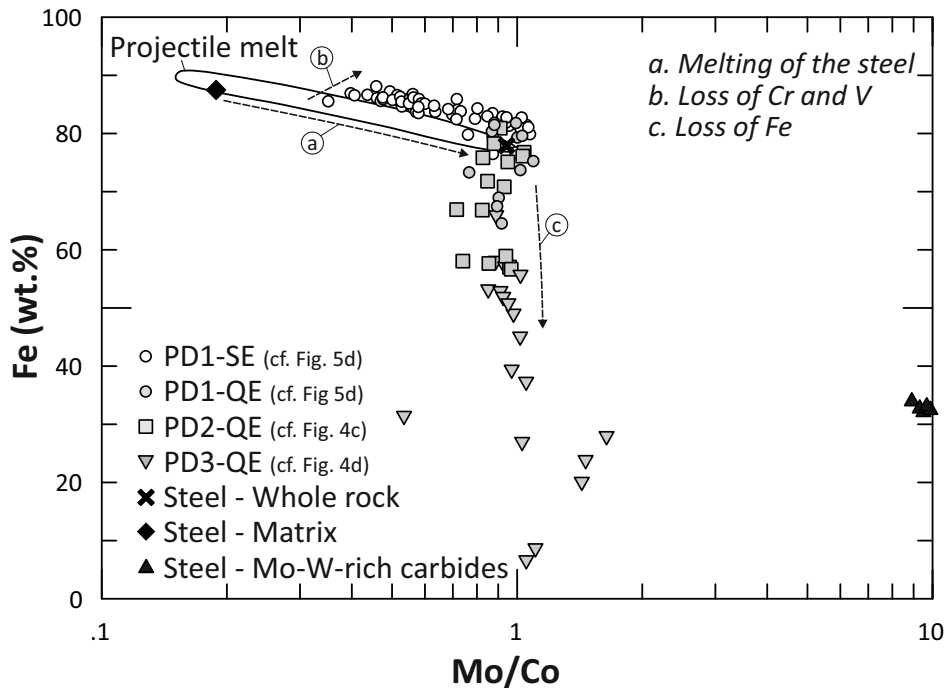


Figure 3.11: Fe vs. Mo/Co for various projectile material (EMP and SEM data), Point a,b and c represent different chemical states of projectile melts, which result from a modification of the projectile material during melting and mixing with the target melts; PD1 to PD3 - projectile droplet types (explanation see text); SE - experiments with sandstone targets; QE - experiments with quartzite targets.

heating of the projectile before penetrating the target. The residual nitrogen-air gas mixture in the accelerator blast tank and the target chamber (0.1 - 0.3 bar) is significantly compressed in the front of the accelerated projectile. This shock compression causes heating of both, the atmosphere and the projectile's surface. Berry *et al.* (2007) measured projectile surface temperatures of up to 1800 °C during a free flight experiment of a hemispherical graphite projectile, accelerated to $4.5 \text{ km} \times \text{s}^{-1}$ at 0.32 bar residual gas pressure. These experimental conditions are similar to our MEMIN experiments; hence, we expect certain heating and occasionally melting of the projectile in the flight phase as already suggested by Ebert *et al.* (2013) for another MEMIN experiment. Stage II (Fig. 3.12b) encompasses the end of the contact/compression stage of the impact. The leading edge of the projectile had penetrated the target. The projectile was intensely plastically deformed (flattening and expansion) and its high kinetic energy was converted into a shock wave at the projectile target interface, which expands hemispherical within the target and the projectile causing there compression and significant heating. The release wave (reflection of the shock wave at the rear of the projectile) propagates through the projectile from the back to the front. This unloads the projectile and results in fragmentation and consequently heating of the steel interior. Kenkmann *et al.* (2013, 2007) have observed friction controlled melting and probably vaporization features on projectile residue surface other MEMIN hypervelocity experiments (D2-3299, E1-3382, E2-3383, E3-3384). Frictional shearing and heating predominantly affected the surface of the projectile and shear bands in the projectile leading to melting and even localized boiling of steel and the target at the immediate projectile-target interface. This contact zone is pointed out as projectile droplet-rich zone in Fig. 3.12c of this study. Due to the highly turbulent and dynamic impact process this projectile melt is injected into the shocked and partly molten target melts. These small amounts of the steel (< 5 vol.%) are distributed as projectile droplets and few partly fused projectile fragments. With increasing distance from the direct contact zone, the degree of shock overprint of the target gradually becomes lower. Therefore, we consider the small volume at the interface between projectile and target as the origin of the highly shocked and projectile rich ejecta. This zone also contains the highest degree of shock features, i.e., PDF in quartz, formation of lechatelierite and partly melting of the target. Stage III (Fig. 3.12d) covers the ongoing deformation of the projectile. Some of the recovered projectile relics have the shape of a deformed bowl with a convex outer and concave inner side, a serrated, sometimes fragmented brim, and a central knobby region in the center of the inner side (Kenkmann *et al.*, 2013). At higher impact velocities, the projectiles were also crushed to smaller unshaped fragments. Approximately 58 - 92 % of the projectile material survived as such relatively large fragments (Kenkmann *et al.*, 2013). The contact/compression phase grades into the excavation of the crater. At this point the highly shocked and projectile rich material was completely ejected from the crater, which is supported by Buhl *et al.* (2013), who observed no evidences of projectile material or target melts within the corresponding crater floors. The ejected bowl shaped projectile relicts have a discontinuous coating of the highly shocked target material on their outer convex side (Kenkmann *et al.*, 2013). A similar feature was observed on an iron meteorite fragment at the Kamil impact site (D'Orazio *et al.*, 2011). These authors reported target rock material stuck onto the surfaces of some meteorite shrapnel specimen. They suggested a swarm of iron meteorite fragments was associated with a dense,

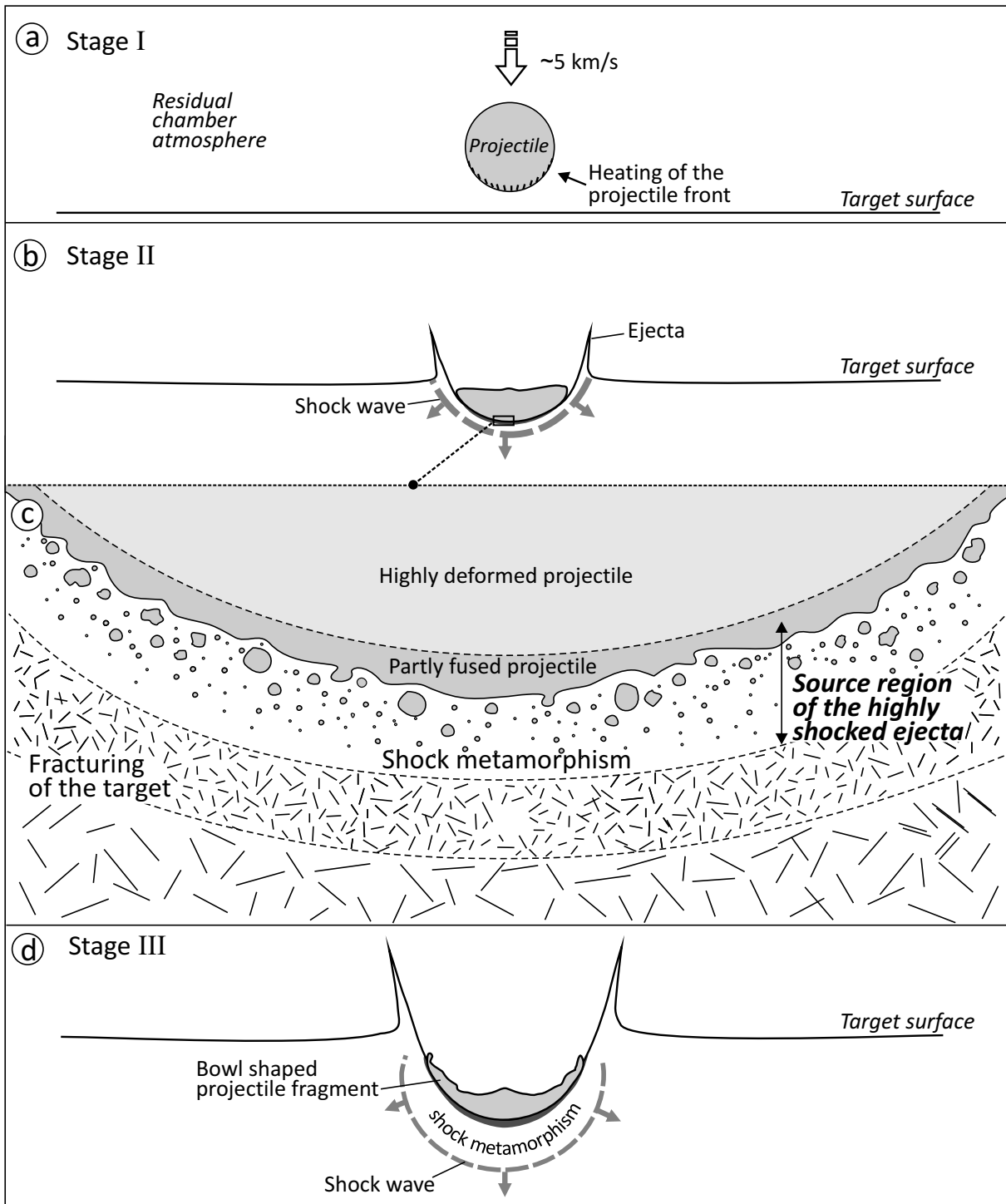


Figure 3.12: Series of schematic cross-section diagrams showing the development of the highly shocked ejecta (modified from Melosh, 1989 and French, 1998).

hot spray of molten projectile that interact with target material. An alternative explanation may be that these fragments derive from the projectile-target contact zone, similar to those observed in our experiments. The higher degree of melting of target material attached to these Gebil Kamil fragments is consistent with either higher impact velocities and/or larger volume of interaction zone at peak shock conditions in nature. In addition, the highly shocked ejecta of our study show many similarities to the impact glass of the Kamil crater (Folco *et al.*, 2011). These authors described a pumiceous impact glass found scattered in the ejecta blanket. The Kamil glasses consist of siliceous (white) and Fe-Ni-rich (dark) glasses deriving from melting of target and projectile, which strongly resembles our recovered highly shocked and projectile rich ejecta (cf. Fig. 3.2d this study).

3.5.2 Inter-element fractionation processes

During the cratering process a high number of molten projectile droplets were incorporated into the target melts. Thus, in general, two immiscible melts coexist in the highly shocked ejecta. Due to the low concentration of tracer elements (e.g., Fe, Cr, V) in the target rocks (Table 3.3), any higher concentration of these elements in sandstone and quartzite ejecta could only be derived from the steel projectile. Complementary to the Cr, V, and Fe depletions of the metallic projectile droplets and target-derived melts show enrichment of these elements and to a much lesser degree of Co, W, and Mo. The loss of Cr, V, and especially Fe yield a relative enrichment in Co, Mo, and W in the projectile droplets (e.g., Fig. 3.11). Within these droplets, Mo and W form separate phases with a heterogeneous distribution (e.g., large projectile droplet in Fig. 3.7). The details of the element partitioning of Fe and Cr (equivalent for V) within the quartzite ejecta are described in three steps in Fig. 3.13: (i) At the onset of projectile-target interaction Cr (and V) of the projectile droplets are preferentially partitioned into the silicate melt with respect to Fe, yielding Cr/Fe well above the target and projectile ratios. (ii) At the margins of PD2 and PD3 iron may be enriched even further in the adjacent silicate melt. This is not the case for Cr (and V) because almost all the Cr and V of these droplets has been partitioned. We propose the development of a temporary silicate melt composition (gray field in Fig. 3.13) which is dominated by the ongoing Fe partitioning. With increasing distance from the projectile droplet (PD2, PD3) Fe is relatively more enriched than Cr as indicated by the variable Cr concentrations of the gray field in Fig. 3.13. (iii) During quenching of the ejecta further processes occur resulting in a chemical modification of the “proposed silicate melt composition”; whereby it is not quite clear whether there was a certain chronological order or whether the processes occurred simultaneously. This step (iii) itself comprises three different processes: (a) the melt within the proposed silicate melt composition field is unmixed due to liquid immiscibility resulting in separated iron-rich (*Lfe*) and silica-rich (*Lsi*) melts.

Phase separation, or liquid immiscibility, is a common process in glass forming multicomponent silicate-dominated systems (e.g., James, 1975; Roedder, 1978; Veksler *et al.*, 2008). Immiscibility is a result of a three-dimensional low compatibility between the network-formers (in this case mainly Si^{4+}) and network-modifiers (e.g., Fe^{2+}) of silicate melts (Hudon & Baker, 2002). Whether silicate melt shows phase separation or not is based on thermodynamics and the behavior of the system’s Gibbs free energy ΔG (Shelby, 2005). In case the silicate melt splits

into two coexisting liquids during quenching, its free energy of mixing ΔG_m was lower than the ΔG_m of a homogenous mixture of the two components (for more detailed explanations, see, e.g., James, 1975; Hamann *et al.*, 2013; Shelby, 2005). (b) As we observe Cr-V-spinels in *Lfe*, it must be assumed that *Lfe* melt had originally a different composition, shifted by the crystallization of the spinels shifts to various but lower Cr/Fe ratios. (c) Along with Cr-V-spinel formation Fe-rich-spinels (probably magnetite) crystallized within pre-*Lfe*. Yet as only a low amount of Fe-rich-spinels is present, their formation yielded much less chemical modification on *Lfe* than crystallization of the Cr-V-spinels. These observations clearly show partitioning of projectile tracer elements into silicate melts is intensified in experiments with a quartzite target compared to the porous sandstone target.

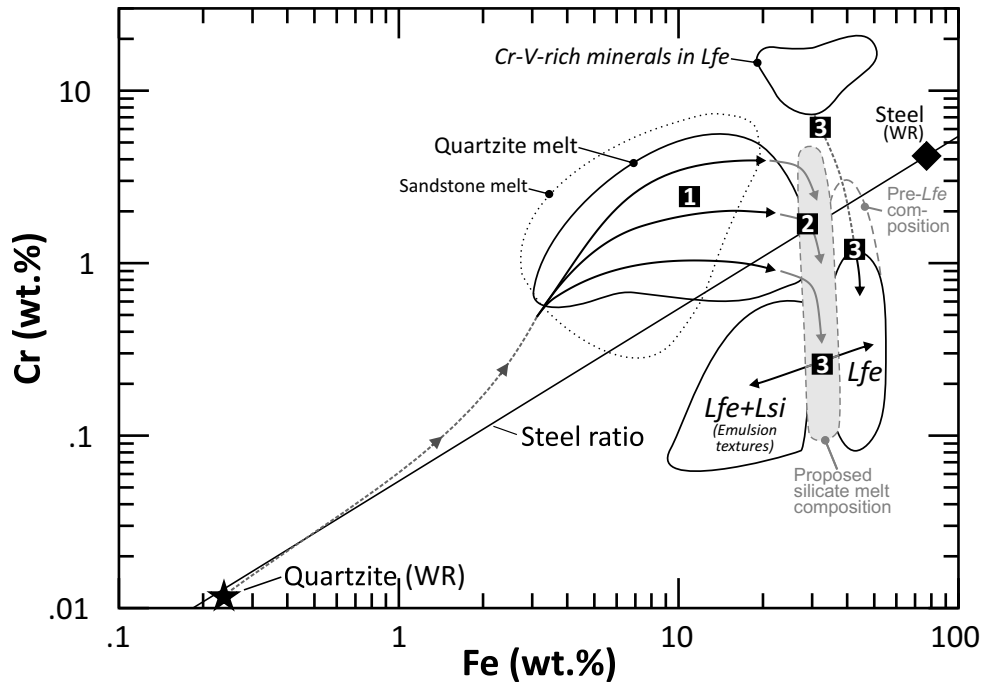


Figure 3.13: Schematic illustration of the chemical modification of the quartzite target for Fe and Cr (V gives similar results as Cr); indicating 3 steps of element fractionation involved in the formation of coexisting liquids and associated mineral phases (see text for more details).

We recently observed similar liquid immiscibility processes between ultrabasic melts and highly polymerized high-silica melts at the margins of iron meteorite spheres within the impact melts of the Wabar craters (Hamann *et al.*, 2013). In order to quantify the observed inter-element fractionation processes within the highly shocked ejecta fragments it is important to understand the chemical behavior of our projectile tracer elements. After the classical work of Goldschmidt (1937) Co and Mo belong to the moderately siderophile, while Cr and V are lithophile elements. Fe and W show affinities to more than one phase (see below). In the geochemical system of coexisting silicate and metallic melts Fe and W have also moderately siderophile character (Hiligren *et al.*, 1994).

Partitioning of these elements between silicate and metallic liquids has been studied extensively in laboratory experiments (e.g., Righter *et al.*, 2010 and references in there). The partitioning behavior is expressed as distribution coefficient $D_{met/sil}^X$, which gives the ratio of

the concentration of element X in metallic melt (met) and the silicate melt (sil). In most studies the partitioning experiments were performed to reach equilibrium conditions. Our experiments, however, are snapshots of an ongoing fractionation due to the extreme short term dynamics of an impact. The parameters which were varied in common partitioning experiments are oxygen fugacity (f_{O_2}), pressure (P), temperature (T) as well as metal and silicate composition. The $D_{met/sil}^X$ values significantly increase with decreasing f_{O_2} . The strong effect of the oxygen fugacity on the partitioning coefficients clearly indicate that Fe, Cr, V, Mo and W are dissolved as oxides (FeO, Cr₂O₃, V₂O₃, MoO₃, WO₃) in the silicate melts (Schmitt *et al.*, 1989; Holzheid & Palme, 1996; Corgne *et al.*, 2008). All these elements, however, become more siderophile with decreasing f_{O_2} . Comparing different experimental data sets (Hiligren *et al.*, 1994; Holzheid *et al.*, 1994; Ohtani *et al.*, 1997; Righter *et al.*, 1997; Righter & Drake, 1999; Righter *et al.*, 2010) demonstrated that on a wide range of P, T, f_{O_2} , and melt compositions the $D_{met/sil}^X$ sequence is mainly: Mo (› Ni) » Co ~ W » Fe › Cr ~ V, corresponding to the decreasing siderophile behavior of these elements. The experimental results, Cr, V, and Fe partition preferentially into the silicate melt compared to Mo, W, Co explain our observations within the highly shocked sandstone and quartzite ejecta (Table 3.4 - Table 3.6). Some projectile droplets (PD3; Fig. 3.4b-e) of the quartzite ejecta, however, are surrounded by *Lfe* which demonstrates enhanced partitioning, compared to the sandstone experiments. Conspicuous is the high amount of WO₃ within the *Lfe* rim, compared to CoO concentrations. Although Co and W have a similar siderophile character and similar contents in the steel projectile, W partitioned preferentially into the *Lfe* rim compared to Co. Partitioning experiments by Righter & Drake (1997) and Righter *et al.* (2010) have shown that Co and Mo become less siderophile with increasing temperature, whereas, W exhibits the opposite behavior. That implies the W enrichment around PD3; could probably occur during cooling. Jaeger & Drake (2000), however, found that the partition coefficients of Co and W respond differently to variations in the silicate melt composition: Cobalt seems almost unaffected by changes in the degree of polymerization; whereas, $D_{met/sil}^W$ decreases with increasing basicity of the silicate melt. The authors emphasize cations with higher oxidation states (W⁴⁺) can be better incorporated in basic (higher NBO/T - non-bridging oxygen per tetrahedral-coordinated cation, see Mysen *et al.*, 1982) melts than cations with lower oxidation states (Co²⁺). The *Lfe* rims have a high NBO/T average value of 1.4; this may explain further the enhanced W enrichment compared to the Co enrichment.

3.5.3 Effects of experimental conditions

The MEMIN cratering experiments comprise a parametric study of the role of porosity, water saturation of the pores, target layering, projectile size, and impact velocity on cratering mechanics, shock effects, and projectile distribution during cratering (Poelchau *et al.*, 2013).

3.5.3.1 Impact energy

Projectiles of 2.5 and 12 mm in diameter were used in our cratering experiments. At impact velocities of approximately $5 \text{ km} \times \text{s}^{-1}$, these projectile with a mass of $\sim 0.067 \text{ g}$ and 7.3 g , respectively, result in impact energies of $\sim 0.7 \text{ kJ}$, and $\sim 81 \text{ kJ}$. Despite three orders of magnitude difference in impact energy, no systematic relation between energy and inter-element fractiona-

tion processes were observed within the highly-shocked projectile-rich ejecta fragments (Figs. 3.6 and 3.7). This suggests that our experimental results are applicable to natural impact crater formation. The impact energies of small and young terrestrial craters like Wabar, Kamil and Meteor clearly exceed the impact energies of our laboratory experiments (e.g., Meteor crater impact energy: $\sim 1.05 \times 10^7$ kJ; Melosh & Collins, 2005). Nevertheless, experiments and nature reveal macroscopic, microscopical and geochemical similarities (Mittelfehldt *et al.*, 1992; Mittelfehldt *et al.*, 2005; D’Orazio *et al.*, 2011; Ebert *et al.*, 2013; Hamann *et al.*, 2013). Hamann *et al.* (2013) and D’Orazio *et al.* (2011) demonstrated that impact melt material from Wabar and Kamil, respectively, are generally enriched in Fe over Ni compared to the Fe/Ni in the iron meteorite projectiles. If we use Co as comparative element for Ni (both moderately siderophile) the results of our study (Table 3.4, Fig. 3.6) show a comparable trend. Especially, the strong iron transfer from the projectile melts into the target melts, which partly leads to liquid immiscibility features (see Hamann *et al.*, 2013, and Fig. 3.4 of this study), seems to be a fundamental process which occur both in natural impactites and experimental ejecta.

3.5.3.2 Water-saturation of the sandstone targets

We did not see any differences in the element partitioning behavior between the dry and wet sandstone experiments (cf. Fig. 3.6). Thus, at least at the scale of laboratory experiments, the presence of water in the target does not influence the partitioning of the tracer elements between target and projectile melts; which is a further major outcome of this study. Of course, this only applies for the experimental conditions that we have used in our experiments. However, Righter & Drake (1999) carried out a series of piston cylinder experiments at 1 GPa and 1300 °C, aimed to isolate the effect of water on the partitioning of e.g., Co, Mo, W, and Ni between metal and hydrous silicate liquid. Their experimental results show that the distribution coefficients of Co, W, Mo, and Ni remain unchanged up to 3.5 wt.% (up to 2.8 wt.% for Mo) water dissolved in the silicate melt. Since we observed more or less identical partitioning processes in experiments with dry and wet sandstone targets (e.g. Fig. 3.6) we assume that only little or no water was involved in these geochemical processes, which is in accordance with the results of Righter & Drake (1999). Most of the pore water in the highly shocked zone of the target obviously have been evaporated during the hypervelocity impact and did not react with the melts.

3.5.3.3 Porosity of the target

The MEMIN experiments A20-5339 and E6-3452 were carried out with quartzite targets devoid of porosity. Microchemical and SEM investigations (Fig. 3.8 and Table 3.5) of the highly shocked ejecta material from these experiments show three main differences compared to experiments with porous sandstone (~ 23 % porosity): The highly-shocked quartzite ejecta (i) has a higher content of silica glasses and consequently less quartz grains with planar-deformation features, (ii) contains far fewer projectile melt droplets, and (iii) displays enhanced inter-element fractionation compared to the sandstone ejecta (e.g., Fig. 3.6 and Table 3.4). Poelchau *et al.* (2013) calculated a maximum shock pressure of 59 and 63 GPa for the dry sandstone experiments A6-5126 and E1-3382, respectively, using the planar impact approximation and material parameters for Coconino sandstone and steel compiled in Melosh (1989). Using corresponding material parameters for quartzite, the calculated maximum shock pressure for the quartzite experiments

A20-5339 and E6-3452 yields a maximum shock pressure of ~ 80 GPa. We suggest that this higher initial pressure is the reason why the highly shocked quartzite ejecta contains a higher amount of silica glasses compared to the sandstone ejecta. Melting of the steel projectile, in particular the formation of melt droplets, cannot be exclusively explained by the (calculated) initial shock pressure and high post-shock temperatures (e.g., Shoemaker *et al.*, 1963; Ebert *et al.*, 2013). Causes for this melting most likely are friction and shearing at the direct interface between projectile and target (Kenkmann *et al.*, 2013). Projectile droplets of type 2 and type 3 in the highly shocked quartzite ejecta display enhanced inter-element fractionation (Tables 5 and 6) which suggests (i) higher temperatures of the droplets and (ii) longer reaction times between projectile droplet and surrounding silicate melt at high temperatures. In other words projectile melt droplets in the quartzite ejecta had stayed for a longer time at higher temperatures compared to those within the sandstone ejecta. The temperature difference between the experiments with 0 and 23 % porosity may explain the drastic Fe partitioning into the *Lfe* rims of projectile droplets, which only occur in the experiments with quartzite as target (e.g., 3.4e). Partitioning experiments were conducted under defined conditions (T, P, f_{O_2} , duration of the experiments) in order to reach equilibrium conditions, which clearly differ from the non-equilibrium conditions of the hypervelocity impact experiments. Nevertheless, the partitioning experiments may give some general indications to support our observation and assumptions. For example, Hiligren *et al.* (1994) and Holzheid & Palme (1996) have shown that the partitioning coefficient of Fe between silicate melt and metallic melt decreases slightly with increasing temperature. Thus, in their experiments the formation of FeO in the silicate melts is supported by higher temperatures, compared to lower temperatures. Therefore a change in temperature (higher T in the quartzite experiments) could result in the formation of the Fe-rich silicate melt rims.

3.6 Conclusions

Our study has documented in detail the complex process of mechanical and chemical mixing of projectile and target materials during hypervelocity impacts. Most prominent is the injection of projectile melt droplets into target melts. Two coexisting but largely immiscible melts exist in the highly shocked sandstone and quartzite ejecta fragments. The ejecta contains various shock features including multiple sets of PDF in quartz, the onset to complete transformation of quartz to silica glass, and partial melting of the targets. The melting is concentrated in the phyllosilicate-bearing matrix of the sandstone and quartzite, but involves quartz grains, too. Significant inter-element fractionation occurs during mixing of projectile and target material, and some projectile tracer elements partition preferentially into the target melts. The degree of this element enrichment is mainly controlled by the lithophile or siderophile character of the respective tracer element. The different geochemical behavior of the tracer elements leads to element ratios in the target melts, which differ strongly from the respective element ratios of the projectile. Thus, determination of the projectile type via trace element ratios in terrestrial impactites would cause problems and lead to erroneous results. Our study emphasize the importance of H₂O bearing phases during impact melting, or in more general terms, the significant influence of minor components in silicate rich targets on geochemical exchange processes. The laboratory experiments yield results very similar to observations in nature, e.g., at Meteor crater

and the Wabar craters (Kearsley *et al.*, 2004; Mittlefehldt *et al.*, 2005; Hamann *et al.*, 2013). From our perspective, small scale geochemical processes, like (i) partitioning of projectile elements into target melts, (ii) the associated phase separation into Fe-rich and Si-rich melts, and (iii) the strong modification of the ratio of projectile tracer elements in the impact-generated silica melts, seem to be common features during mixing of projectile and target melts. Our results are similar for experiments at low impact energy and with a dry target as well as at high impact energy and with a water-saturated target. It follows that the degree of water-saturation in the target materials and impact energy obviously do not affect the described geochemical processes, at least at the scale of our hypervelocity impact experiments. On the other hand, projectile tracer elements Cr, V, Fe, Co, Mo, and W are more strongly partitioned into the silicate target melt in experiments with a non-porous quartzite compared to the porous sandstone target. This is mainly the result of higher shock pressure and the related higher shock and post-shock temperatures yielding a longer time-span with physical conditions more favorable to partition of elements between projectile and target melt.

3.A Tables of chapter 3.

Table 3.1: Conditions of the hypervelocity cratering experiments

MEMIN experiment No.	Target lithology	Target dimensions [cm]	Projectile diameter [mm]	Projectile weight [g]	Velocity [km×s ⁻¹]	Impact energy [J]	Impact peak pressure [GPa]	Crater depth [cm]
A6-5126	Sandstone dry	20x20x20	2.5	0.067	4.8	773	63 ^a	1.1
E1-3382	Sandstone dry	80x80x50	12	7.323	4.6	76032	59 ^a	6.8
E2-3383	Sandstone (50 % wet)*	80x80x50	12	7.313	4.6	76805	-	5.96
A20-5339	Quartzite	20x20x20	2.5	0.067	5.0	834	81	1.06
E6-3452	Quartzite	80x80x40	12	7.311	4.7	81060	74	5.5

^a Data from Poelchau *et al.*, (2013)

* Sandstone target with 50% water-saturation

Table 3.2: EMP measurement conditions for various phases

Element	Standard	X-ray	Crystal	Peak Pos. [mm]	Peak		Background		D.L.		Diameter		Acc. Voltage		Probe current	
					[s]	[s]	[ppm]	[μm]	[kV]	[nA]						
<i>Same conditions for M, P</i>																
Si	Quartz	Ka	TAP	77.33	M	P	M	P	M	P	M	P	M	P	M	P
Al	Albite	Ka	TAP	90.627	40	40	20	20	220	100	3	1	10	15	60	30
Fe	elem. Fe	Ka	LIF	134.597	40	40	20	20	960	500	3	1	10	15	60	30
Mg	Augite	Ka	TAP	107.506	40	-	20	-	220	-	1	-	10	-	60	-
K	Sanidine	Ka	PETJ	119.785	40	-	20	-	250	-	1	-	10	-	60	-
Ti	Titanite	Ka	PETJ	87.866	40	-	20	-	260	-	1	-	10	-	60	-
V	elem. V	Ka	LIFH	174.102	60	40	30	20	450	250	3	1	10	15	60	30
Co	elem. Co	Ka	LIFH	124.547	60	40	30	20	600	500	3	1	10	15	60	30
Cr	elem. Cr	Ka	PETJ	73.273	40	40	20	20	580	240	3	1	10	15	60	30
Mo	elem. Mo	La	PETH	173.092	60	40	20	20	550	230	3	1	10	15	60	30
W	elem. W	La	LIFH	102.133	60	40	20	20	860	280	3	1	10	15	60	30

elem. - elemental; D.L. - detection limit; Pos. - position; Acc. - acceleration; M - silicate phases; P - projectile material

Table 3.3: Chemical composition of the targets and the projectile

(wt.% $\pm 2\sigma$)	Seeberger Sandstein ^a	Phyllosilicate-matrix	Taunus Quartzite	Phyllosilicate-matrix	Steel D290-1(DIN 1.3243)			
					(wt.% $\pm 2\sigma$)	Matrix	BAM whole rock*	W/Mo-rich phases
SiO ₂	94.77 \pm 0.90	46.60 \pm 5.52	95	47.70 \pm 2.71	O	0.54 \pm 0.18	-	0.12 \pm 0.03
Al ₂ O ₃	3.11 \pm 0.10	25.86 \pm 9.50	2.8	32.25 \pm 3.68	Si	0.07 \pm 0.01	0.072 \pm 0.007	0.21 \pm 0.01
Fe ₂ O ₃	0.45 \pm 0.09	3.25 \pm 2.6 ^o	0.34	2.46 \pm 1.70 ^o	P	0.02 \pm 0.01	0.016 \pm 0.0015	0.01 \pm 0.005
CaO	0.05 \pm 0.01	0.23 \pm 0.12	0.04		S	0.03 \pm 0.01	0.016 \pm 0.0008	0.52 \pm 0.02
MgO	0.12 \pm 0.02	1.13 \pm 0.79	<0.01	1.24 \pm 0.57	V	2.12 \pm 0.23	1.91 \pm 0.04	1.92 \pm 0.35
Na ₂ O	0.15 \pm 0.05	0.1 \pm 0.18	<0.01	0.69 \pm 0.68	Cr	3.56 \pm 0.42	4.18 \pm 0.06	4.51 \pm 0.11
K ₂ O	0.23 \pm 0.01	2.93 \pm 2.10	1.15	10.39 \pm 0.81	Mn	0.22 \pm 0.04	0.244 \pm 0.010	0.09 \pm 0.04
TiO ₂	0.31 \pm 0.04	0.16 \pm 0.26	0.3	0.55 \pm 0.28	Fe	87.46 \pm 2.96	77.92*	32.5 \pm 0.26
MnO	<0.01	b.d.l.	<0.01		Co	5.94 \pm 0.13	5.12 \pm 0.12	2.3 \pm 0.06
P ₂ O ₅	0.02 \pm 0.01	0.08 \pm 0.07	<0.01		Ni	0.34 \pm 0.02	0.329 \pm 0.018	0.14 \pm 0.06
					Mo	1.12 \pm 0.35	4.83 \pm 0.09	22.8 \pm 0.30
					W	1.20 \pm 0.49	6.27 \pm 0.14	36.4 \pm 0.26
(ppm $\pm 2\sigma$)					(ppm $\pm 2\sigma$) ^b			
Ni	3.33 \pm 0.41	b.d.l.	5	n.a.	Si	822 \pm 177	822 \pm 177	
Co	0.96 \pm 0.04	b.d.l.	<5	n.a.	Mn	3338 \pm 162	3338 \pm 162	
Cr	63.33 \pm 21.01	b.d.l.	116	n.a.	Co	52281 \pm 958	52281 \pm 958	
Mo	b.d.l.	n.a.	<10	n.a.	Cu	910 \pm 24	910 \pm 24	
V	11.67 \pm 0.47	n.a.	18	n.a.	Ga	25.8 \pm 1.1	25.8 \pm 1.1	
W	4.00 \pm 0.50	n.a.		n.a.	Ge	6.6 \pm 0.5	6.6 \pm 0.5	
Zr	b.d.l.	n.a.	145	n.a.	As	83.7 \pm 5.6	83.7 \pm 5.6	
Ce	b.d.l.	n.a.	29	n.a.	Sb	19 \pm 1.8	19 \pm 1.8	

* Data from Federal Institute for Materials Research and Testing (BAM - Germany)

^a Calculated from BAM data sheet

^o Value as FeO

b.d.l. - below detection limit; n.a. - not analyzed

^a XRF data

^b LA-ICP-MS data (WWU Münster)

Table 3.4: EMP data for the sandstone melt of the highly shocked sandstone ejecta (E1-3382, E2-3383 and A6-5126)

Oxide	SiO ₂	Al ₂ O ₃	FeO	MgO	K ₂ O	TiO ₂	V ₂ O ₃	Cr ₂ O ₃	CoO	MoO ₃	WO ₃	Totals
<i>Sandstone melt</i>												
3382-SM_01	67.345	13.123	16.52	0.565	0.321	0.637	1.118	1.14	0.163	b.d.l.	b.d.l.	100.97
3382-SM_02	62.37	8.761	19.1	0.677	0.371	0.518	3.284	6.13	0.201	b.d.l.	b.d.l.	101.51
3382-SM_03	63.331	20.866	9.844	0.521	0.372	1.059	1.604	2.419	0.096	b.d.l.	b.d.l.	100.11
3382-SM_04	78.58	9.559	8.95	1.171	0.336	0.631	0.798	1.232	0.13	b.d.l.	b.d.l.	101.5
3382-SM mean (32)	67.454	11.964	12.5	0.556	0.438	0.901	2.224	3.561	0.1			99.769
3382-SM 2σ	7.445	6.887	4.86	0.392	0.327	0.489	1.8	2.773	0.095			1.37
3383-SM_01	66.086	23.35	5.375	1.212	0.313	0.308	0.256	0.433	0.067	b.d.l.	b.d.l.	97.461
3383-SM_02	69.042	18.545	8.575	0.336	0.284	0.839	1.151	2.915	0	b.d.l.	b.d.l.	101.78
3383-SM_03	54.075	22.776	10.92	0.786	0.365	0.87	3.104	6.127	0.155	b.d.l.	b.d.l.	99.488
3383-SM_04	52.43	15.336	16.87	0.458	1.192	0.839	4.642	6.241	0.259	b.d.l.	b.d.l.	98.687
3383-SM mean (20)	68.51	9.492	11.29	0.552	0.541	0.727	3.126	4.985	0.172			99.761
3383-SM 2σ	9.295	4.698	4.953	0.372	0.249	0.421	2.158	3.323	0.166			1.998
5126-SM_01	51.701	5.257	18.41	0.876	0.268	1.771	6.594	11.757	0.304	b.d.l.	b.d.l.	97.321
5126-SM_02	83.155	4.384	6.504	0.167	0.897	0.409	1.305	2.575	0.337	b.d.l.	b.d.l.	100.13
5126-SM_03	62.678	11.209	10.62	0.848	0.406	0.927	4.923	7.984	0.084	b.d.l.	b.d.l.	99.796
5126-SM_04	71.639	11.974	7.379	0.993	0.792	0.267	1.945	2.466	0.023	b.d.l.	b.d.l.	97.484
5126-SM mean (16)	66.142	15.49	10.53	0.585	0.541	0.802	1.861	3.119	0.159			99.473
5126-SM 2σ	8.911	6.574	3.867	0.333	0.258	0.331	1.421	2.304	0.086			1.671

All data in weight percent (wt.%); b.d.l. - below detection limit

Table 3.5: EMP data for the quartzite melt and the Fe-rich silicate melt (Lfe) of the highly shocked quartzite ejecta (A20-5339, E6-3452)

Oxide	SiO ₂	Al ₂ O ₃	FeO	MgO	K ₂ O	TiO ₂	V ₂ O ₃	Cr ₂ O ₃	CoO	MoO ₃	WO ₃	Totals
<i>Quartzite melt</i>												
3452-QM_01	61.544	12.687	19.31	0.704	0.393	0.609	1.293	2.526	0.087	b.d.l.	b.d.l.	99.169
3452-QM_02	68.63	5.314	17.523	0.687	0.369	0.691	2.541	6.203	0.188	b.d.l.	0.554	102.731
3452-QM_03	61.002	9.164	14.33	0.486	0.465	0.62	5.374	7.528	0.288	b.d.l.	1.091	100.394
3452-QM_04	64.962	3.995	25.737	0.783	0.341	0.486	1.369	1.263	0.104	b.d.l.	0.144	99.201
3452-QM mean (16)	63.01	9.001	18.417	0.696	0.381	0.65	1.917	4.364	0.168		0.281	98.778
3452-QM 2σ	5.621	5.213	1.264	0.012	0.017	0.058	0.883	2.6	0.09		0.386	1.994
5339-QM_01	17.272	19.863	0.574	0.346	1.237	1.131	17.272	0.751	0.266	0.121	0.153	101.944
5339-QM_02	6.208	15.991	0.433	0.258	0.238	2.467	6.208	3.044	0.1	b.d.l.	b.d.l.	99.483
5339-QM_03	7.201	38.236	0.298	1.39	0.298	1.774	7.201	1.606	0.223	0.062	0.965	101.61
5339-QM_04	7.101	34.087	0.634	0.3	0.634	2.067	7.101	2.378	0.086	0.044	0.196	99.017
5339-QM mean (20)	9.163	20.967	0.388	0.318	0.408	1.304	9.163	1.846	0.171	0.052	0.23	100.667
5339-QM 2σ	3.92	7.223	0.397	0.376	0.435	0.81	3.92	1.679	0.095	0.083	0.397	1.959
<i>Lfe (Fe-rich silicate melt)</i>												
3452-Lfe_01	33.125	4.774	51.956	0.496	0.369	0.711	0.329	0.355	0.541	0.091	6.614	99.362
3452-Lfe_02	32.257	0.964	60.13	0.757	0.307	0.48	0.189	0.195	0.289	0.21	3.133	98.909
3452-Lfe_03	30.527	1.103	61.831	0.205	0.465	0.248	0.299	0.807	0.489	0.164	2.828	98.965
3452-Lfe_04	30.961	3.357	53.899	0.397	0.191	0.298	0.854	0.571	1.39	0.471	7.169	99.557
3452-Lfe mean (8)	30.887	3.033	54.486	0.444	0.321	0.434	0.444	0.595	0.701	0.5	6.456	98.301
3452-Lfe 2σ	2.153	1.447	4.142	0.157	0.115	0.182	0.289	0.277	0.457	0.451	2.438	1.296
5339-Lfe_01	42.025	4.509	49.037	0.492	0.049	0.492	0.306	0.438	0.306	0.088	3.265	101.007
5339-Lfe_02	35.077	2.25	54.77	0.126	0.047	0.126	0.094	1.064	0.18	0.128	6.489	100.351
5339-Lfe_03	39.362	3.953	50.302	0.509	0.052	0.509	0.604	0.63	0.254	0.215	4.289	100.679
5339-Lfe_04	38.474	2.886	48.751	0.5	0.037	0.5	0.455	0.835	0.318	0.186	6.9	99.842
5339-Lfe mean (26)	37.221	3.231	53.273	0.487	0.109	0.446	0.423	1.179	0.426	0.406	4.561	101.041
5339-Lfe 2σ	4.876	1.647	5.475	0.287	0.095	0.236	0.238	0.871	0.263	0.596	2.439	2.208

All data in weight percent (wt.%); b.d.l. - below detection limit

Table 3.6: EMP and SEM data for projectile residues

Element	Si	Al	V	Cr	Fe	Co	Mo	W	O	Total
<i>Projectile melt</i>										
PM_1*	0.22	0.01	0.4	3.4	86.6	5.79	1.12	1.08	0.36	99.02
PM_2*	0.16	0.01	0.6	4.1	86.9	5.71	1.3	1.49	0.24	100.5
PM_3*	0.2	0.01	1	4	86	5.73	1.68	1.41	0.24	100.3
PM_4*	0.29	0.02	0.7	4.3	85.3	5.57	1.95	1.87	0.41	100.3
PM_5*	0.25	0.01	1.5	4.1	84.4	5.52	2.32	1.97	0.31	100.4
PM_1*	0.55	0.03	0.9	2.9	81.9	5.38	2.81	4.35	0.51	99.36
PM_2*	0.27	0.01	1.3	3.5	82.1	5.48	3.08	4.88	0.4	101
PM_3*	0.59	0.02	1.3	3.1	79.6	5.39	3.79	5.32	0.82	99.97
PM_4*	0.3	0.01	1.5	4	79.8	5.41	4.33	5.26	0.4	100.9
PM_5*	0.32	0.01	2	4.5	76.3	5.15	5.63	6.29	0.31	100.5
PM mean (n=58)	0.33	0.01	0.98	3.74	83.82	5.55	2.62	3.33	0.35	100.73
2 σ	0.15	0.01	0.37	0.49	3.09	0.19	1.173	1.78	0.10	0.73
<i>Type 1 projectile droplet (sandstone experiment)</i>										
PD1-SE_1*	1.53	0.07	0.2	0.4	85.3	6.54	2.31	3.76	1.25	101.5
PD1-SE_2*	b.d.l.	b.d.l.	0.8	2.3	83.1	5.3	3.7	4.8	b.d.l.	100
PD1-SE_3*	0.71	0.03	0.8	1.6	79.6	6.43	4.93	6.36	0.25	100.7
PD1-SE_4*	0.7	0.05	1	1.7	76.3	6.41	5.64	6.88	0.36	99.01
PD1-SE_5*	b.d.l.	0.28	0.3	0.6	80.9	5.67	6.07	6.3	b.d.l.	100
PD1-SE mean (n=40)	0.1	0.16	0.3	1	83.5	5.88	4.18	4.88	0.82	100
PD1-SE 2 σ	0.33	0.09	0.3	0.5	2.81	0.43	1.27	1.09	0.6	0.31
<i>Type 1 projectile droplet (quartzite experiment)</i>										
PD1-QE_1*	b.d.l.	b.d.l.	0.8	0.4	79.4	6.43	5.65	7.32	b.d.l.	100
PD1-QE_2*	b.d.l.	b.d.l.	0.5	0.5	80.2	6.49	5.68	5.56	1.06	100
PD1-QE_3*	b.d.l.	0.3	0.2	0.7	81.6	5.9	5.9	5.4	b.d.l.	100
PD1-QE_4*	b.d.l.	b.d.l.	b.d.l.	b.d.l.	79.4	7.07	7.32	6.22	b.d.l.	100
PD1-QE_5*	b.d.l.	b.d.l.	b.d.l.	b.d.l.	64.3	12.9	11.9	10.8	b.d.l.	100
PD1-QE mean (n=12)	0.2	0.5	0.5	75	8.4	7.84	7.81	1.59		
PD1-QE 2 σ	0.1	0.2	0.2	5.7	2.3	2.02	1.85	0.72		
<i>Type 2 projectile droplet surrounded by Lfe (quartzite experiment)</i>										
PD2-QE_1*	0.39	0.07	0.2	0.6	66.9	12.5	8.92	12.1	0.79	102.5
PD2-QE_2*	0.34	0.07	0.2	0.2	66.8	11.4	9.39	12.4	0.94	101.7
PD2-QE_3*	0.55	0.09	0.3	0.1	58.1	14.8	10.9	15.7	1.43	101.8
PD2-QE_4*	0.56	0.07	0.2	0.4	57.7	14	12	13.4	0.49	98.81
PD2-QE_5*	0.45	0.01	0	0.1	57	13.8	13.3	15.2	0.1	99.92
PD2-QE mean (n=17)	0.46	0.07	0.3	0.5	64.2	11	11.2	12.8	0.84	100.3
PD2-QE 2 σ	0.1	0.03	0.1	0.2	14.5	2.68	5.24	7.7	0.41	0.91
<i>Type 3 projectile droplet matrix + W/Mo phase surrounded by Lfe (quartzite experiment)</i>										
PD3-QE_1*	0.76	0.06	0.3	0.5	65.9	11.2	9.98	8.97	2.43	100.1
PD3-QE_2*	1.62	0.2	0.2	0.3	57.1	13.5	12.6	11.2	3.64	100.3
PD3-QE_3*	b.d.l.	b.d.l.	b.d.l.	b.d.l.	50.8	19.1	18.2	10.9	1.1	100
PD3-QE_4*	b.d.l.	b.d.l.	b.d.l.	b.d.l.	6.6	38.6	40.6	13.5	0.8	100
PD3-QE_5*	b.d.l.	b.d.l.	b.d.l.	b.d.l.	8.7	36.7	40.6	13.1	0.9	100
PD3-QE mean (n=17)	0.54	0.32	0.7	0.8	39.8	21.3	21.8	15.5	1.22	99.83
PD3-QE 2 σ	0.22	0.23	0.9	1.3	17.7	8.92	9.7	6.8	0.95	0.77

All data in weight percent (wt.%); b.d.l. - below detection limit

* EMP data

* SEM data

4 Distribution of the highly shocked and projectile rich ejecta

During a hypervelocity impact, the asteroid can completely destroyed. Parts of the impactor are either melted or vaporized and often mixed with a much larger volume of target material Pierazzo & Melosh (2000). Although the projectile material can partly survive the formation of a small (or even a mid-sized) crater, erosion processes over long periods of time leading to loss most or even all of this material. Consequently, it is very difficult to find parts of the projectile, or even its geochemical signature, on terrestrial surfaces after an impact. Due to this, little is known about distribution of projectile material at natural impact structures. Hypervelocity cratering experiments give important information on the fate of the projectile, i.e., its dissemination in the target and partitioning into ejected material.

The experimental setup of the MEMIN hypervelocity impact experiments provides that a large part of the ejecta will be collected with a new designed ejecta catcher; consisting inter alia of phenolic foam plates (cf. Fig. 4.1 and Sommer *et al.*, 2013). The ejecta catcher was placed inside the target chamber parallel to the target surface at a distance of 50-53 cm (in HIE with the extra large two-stage light gas gun (XLLGG)). The projectile impacted perpendicular to the target surface, thus leading to a radial-symmetric ejecta distribution pattern in the catcher (Fig. 4.1).

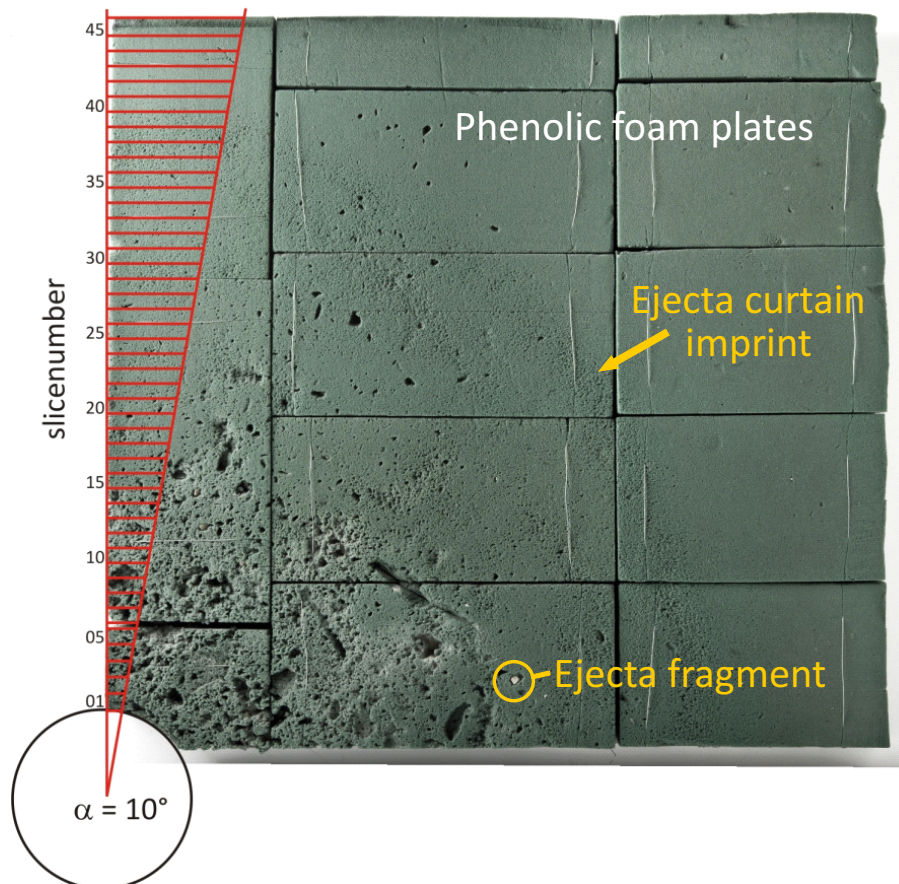


Figure 4.1: Quarter part of the ejecta catcher system; consisting of phenolic foam plates (from MEMIM experiment D3-3298). The red-lined radial cutout marked the foam slices (1 cm width), which were used for ejecta separation.

A certain amount of the ejecta was not collected in the catcher; instead is located on the sample chamber floor after the experiment. Projectile remnants were separated from the floor with magnetic devices before collecting the complete ejecta. In order to avoid contamination a protective case was constructed for experiments with the XLLGG. In a next step, ejecta particles had to be removed from the catcher for further analyses. For this, a narrow strip was cut from the center to the edge of the phenolic foam. This strip of 45 cm length (XLLGG experiments) was again cut in 1 cm width pieces. The ejecta fragments were carefully recovered from these small foam pieces with tweezers and brushes. The position of single ejecta pieces was recorded for determination of the ejecta angle. Thus, the ejecta catcher systems were used to collect material of the evolving ejecta curtain at different ejection angles. The three different ejecta types (see Fig. 4.2b), type I: weakly deformed ejecta, type II: highly deformed ejecta, and type III: highly shocked ejecta fragments (cp. chapter 2.2.2) can be assigned to a certain ejection angle. Most important for this study are especially the highly shocked ejecta fragments which contain 10 - 30 % projectile material in each fragment. It must be expected that only ~ 1 % of the original projectile is included in the highly shocked ejecta. The rest of the projectile is represented as mm-sized, irregular formed fragments (HIE with velocities of $\sim 4.56 \text{ km}\times\text{s}^{-1}$) or as bowl shaped fragments (HIE with lower velocities: $\sim 2.5 \text{ km}\times\text{s}^{-1}$; cp. chapter 6 and Fig. 6.1a). These projectile fragments were predominantly found within the ejecta which was deposited on the floor of the experiment chamber. Projectile distribution of two hypervelocity impact experiments (D3-3298 and E1-3382) could be investigated in detail. The experiments D3-3298 and E1-3382 were performed at the XLLGG using dry sandstone as target and Campo del Cielo meteorite or steel D290-1 as projectile. Unfortunately, the phenolic foam plates of the other experiments with water-saturated sandstone targets and quartzite target were strongly damaged. Thus, in these cases an analysis of the ejecta distribution was not possible. The distribution diagrams in Fig. 4.3 and Fig. 4.4 clearly show that the highly shocked and projectile-rich ejecta is mainly distributed between angles of 71° and 81° in D3-3298 and between of 69° and 82° in experiment E1-3382. Within these ranges a certain scatter of the type III masses is visible; a maximum at 76° is indicated. D3-3298 partly contains two times the amount of type III at an individual angle compared to E1-3382. At lower angles $< 50^\circ$ our catching setup is insufficient to reveal very small amounts of projectile-rich material, which could occur in this area of the catcher. Summarizing it can be said that during the cratering process ejecta fragments with a heterogeneous mixing of projectile and target material will be ejected in a steep angle with regard to the impact angle. As mentioned in chapter 3.3.1 the ejecta type III originates from a small zone at the interface between projectile and target (see Fig. 3.12b,c). It is assumed that the highly shocked and projectile-rich ejecta is excavated during an early phase of the impact, before the drastic hemispherical growing of the main part of the crater. The projectile penetrates the target, it intensely plastically deformed and probably forms a penetration hole, which is only a bit broader than the projectile itself (indicated in stage II and III in Fig. 3.12). Due to the rather elongated shape of the penetration path the projectile-rich ejecta have to be ejected in a steep angle. The observed projectile distribution is evidenced by previous hypervelocity impact experiments. Evans *et al.* (1994) impacted an Fe-Ni-PGE alloy projectile ($6.4 \text{ km}\times\text{s}^{-1}$) into a Mo target. Their results indicate that high angle (55° up to 75°), high velocity ($> 6 \text{ km}\times\text{s}^{-1}$)

melted ejecta is projectile rich. In contrast the low angle (10° up to 40°), low velocity ($< 1 \text{ km} \times \text{s}^{-1}$) contains only a very small portion of projectile matter. This is in accordance with predictions from modeling and observations in nature (O'Keefe & Ahrens, 1977; Grieve, 1982). Furthermore, our results may be helpful for testing the applicability of new numerical models which simulate impact processes. Ejecta type I and II show no preferred distribution within the ejecta pattern of the catcher (Fig. 4.3 and Fig. 4.4). At first view two main regions of ejecta material are visible, an inner region with the main mass of the ejecta and an outer region with low amount of ejected material. This result is mainly consistent with the imprints of the phenolic foam plates (Fig. 4.1). In addition, Sommer *et al.* (2013) distinguishes three ejection zones with different characteristic properties (same MEMIN experiments), which should be mentioned at this point: an "inner zone" carrying projectile material, spall fragments and fine-grained ejecta; a "mixed zone" containing a mixture of fine particles and spall fragments (low ejecta imprint density) and an "outer zone" composed of very fine-grained ejecta fragments forming a prominent outer ring in phenolic foam.

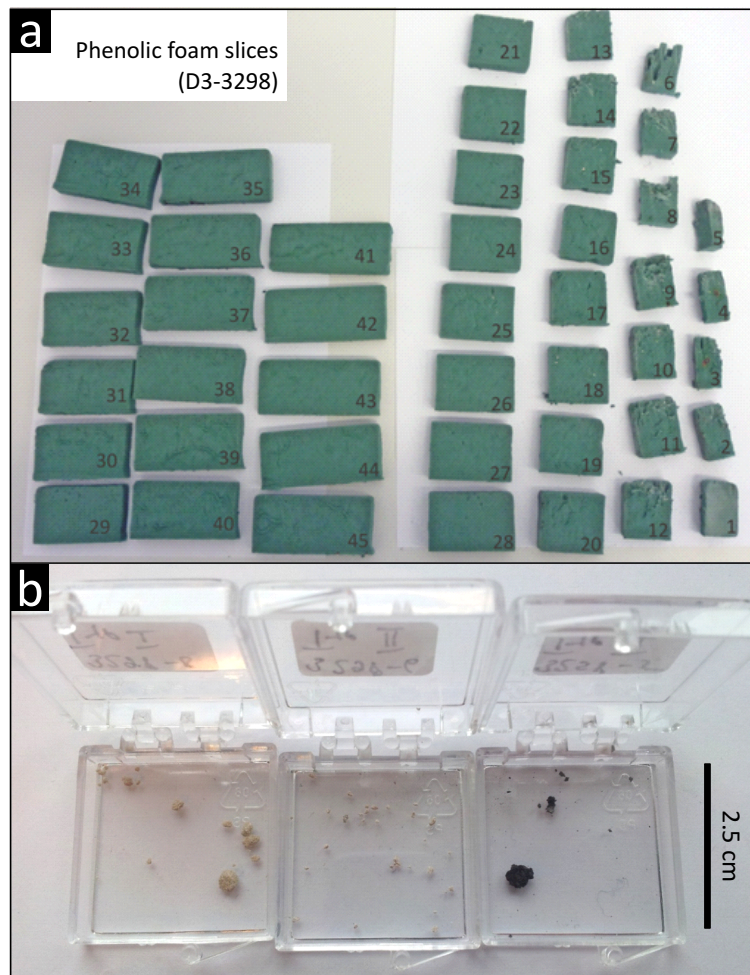


Figure 4.2: (a) Phenolic foam slices of experiment D3-3298; (b) the three ejecta types which were separated from the foam slices: type I: weakly deformed ejecta, type II highly deformed ejecta, and type III: highly shocked ejecta fragments. For more details about the ejecta types see chapter "2.2.2 - Ejecta types"

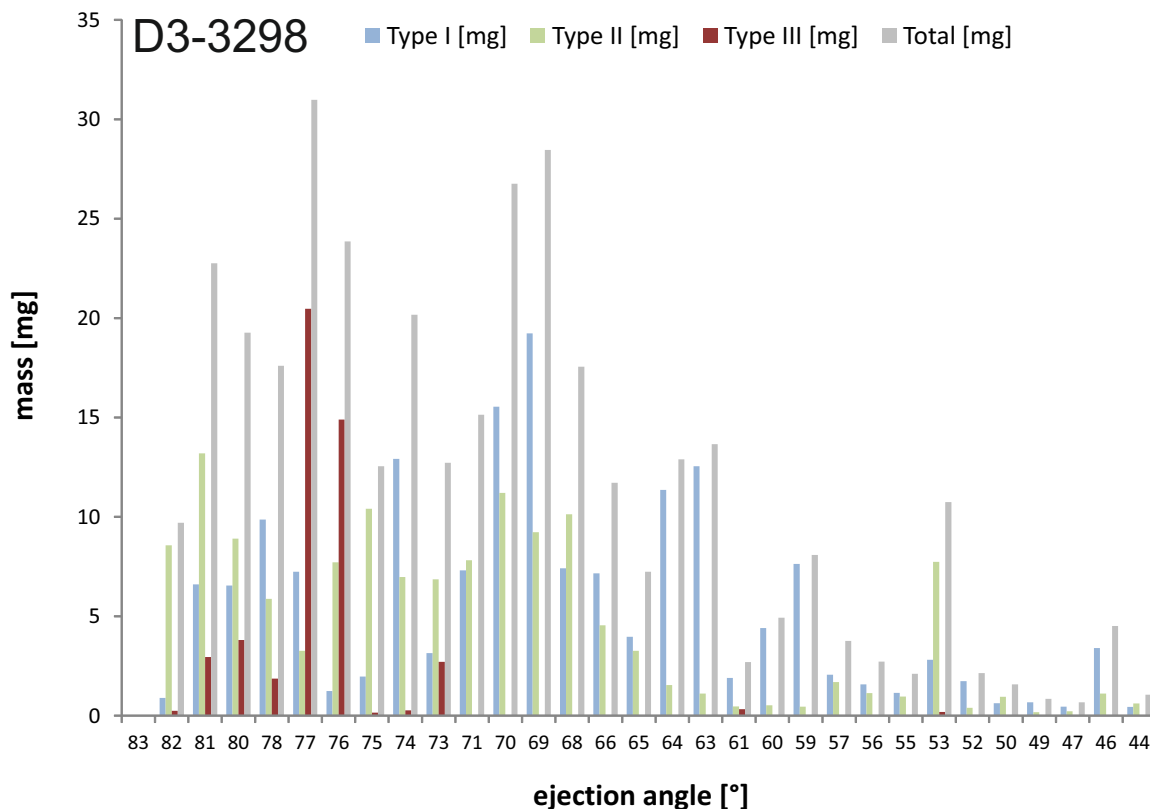


Figure 4.3: Ejection angle vs. mass of the three different ejecta types - D3-3298 (Sandstone/Iron meteorite)

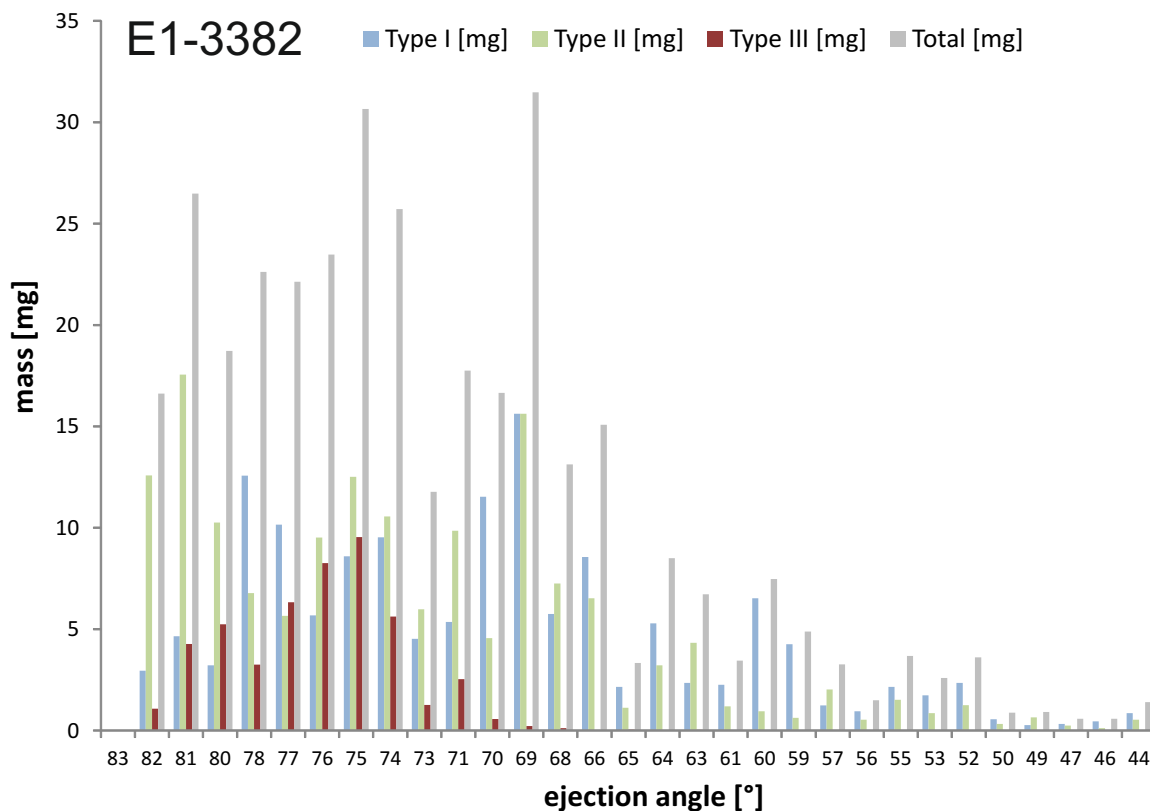


Figure 4.4: Ejection angle vs. mass of the three different ejecta types - E1-3382 (Sandstone/Steel D290-1).

5 Are laser-induced melting experiments suitable to simulate meteorite impact processes?

Matthias Ebert^{1,2,*}, Lutz Hecht^{1,2}

(almost ready for submission in *Meteoritics and Planetary Science*)

⁽¹⁾Museum für Berlin - Leibniz-Institut für Evolutions- und Biodiversitätsforschung, Invalidenstr. 43, D-10115 Berlin, Germany; Freie Universität Berlin, Institut für Geowissenschaften, Malteserstr. 74-100, D-12249 Berlin, Germany; ^(*)Correspondence author's e-mail address: *matthias.ebert@mfn-berlin.de*

5.1 Abstract

Projectile and target material may get completely molten and mixed during the highly dynamic hypervelocity impact process. This mixing is accompanied by significant element partition processes. Laser-induced melting experiments (LE) were conducted with the Trumpf Haas HL 3006D welding facility at the Technical University of Berlin in order to produce and analyze target and projectile melts and their mixtures under more idealized conditions. The LE were able to produce features very similar to those of impactites from impact craters and cratering experiments: formation of lechatelierite, partially to completely molten sandstone and injection of projectile droplets into the target melts. The target and projectile melts have experienced significant chemical modifications during the impact. Inter-element ratios of the projectile tracers Cr, V, Co, Ni, Mo, and W within the contaminated target melts are strongly modified from the original ratios in the projectile. This fractionation process is most likely the result of differences in the lithophile or siderophile character of the projectile tracer elements, or more precisely, of differences in their reactivity with oxygen during interaction of metal melt with silicate melt. Fe, Cr and V of the projectile droplets nearly totally partition into the sandstone melt, whereas the siderophile Co, Ni, Mo and W almost entirely remain in the projectile droplets. In addition, emulsion textures, observed within the contaminated target melts, indicates phase separation into Fe-rich and Si-rich silicate melts during the quenching process. This liquid immiscibility phenomenon was recently described for the Wabar impact glasses. The laser technique does not reproduce typical high-pressure shock effects, e.g. PDF in quartz, but it can be definitely used to simulate high-temperature effects of an impact, mainly for the investigation of geochemical processes. This method allows (i) separate high-temperature (partial) melting of target and projectile material to better constrain primary melt heterogeneities before mixing and (ii) the quantification of element partitioning processes between coexisting projectile and target melts.

5.2 Introduction

There are several small and young craters, e.g., Meteor crater (USA), Kamil crater (Egypt), Wabar crater field (Saudi Arabia) and Henbury crater field (Australia), where intense mixing of target and projectile melts is a common feature. Impact melt rocks from these craters contain conspicuous metallic spheres, which originated from the impactor (iron meteorites in all the mentioned craters; e.g., Gibbons *et al.*, 1976; Hörz *et al.*, 2002; Mittlefehldt *et al.*, 2005; Hamann

et al., 2013). These impactites are rarely present in a fresh state; most of them show significant alterations, they are crystallized, hydrated, and oxidized (Hörz *et al.*, 2002). An exception is inter alia the Wabar impact melt which allowed geochemical analysis of very pristine material. Detailed electron microprobe studies of the Wabar glasses have shown that during the mixing process projectile melt spheres and target melts clearly reveal chemical changes compared to the target and the meteorite. Fe and Ni from the impactor were partitioned in, and became structural part of the silicate melts or of minerals that grew from this melt (Gibbons *et al.*, 1976; Hamann *et al.*, 2013). Especially, the strong iron transfer from the projectile melts spheres into the targets melts, which partly leads to phase separations of the silicate melts, developed as liquid immiscibility emulsions (Hamann *et al.*, 2013), seems to be a fundamental process occurring in natural impactites. Along with the petrological and mineralogical investigations of natural impactite material, laboratory experiments are the most important tool to study vaporization of projectile and target material, formation of impact melts and possible chemical modifications of projectile and target during these processes. Gerasimov *et al.* (2005) performed laser pulse vaporization experiments in order to simulate impact-induced vaporization. They showed that the vaporization of obsidian and augite (as analogues for Earth's crust chemical composition) starts with the loss of Si, Fe, and alkalis and consequently enrich in Mg, Ca, Al and Ti. The authors found a good possibility to recognize evaporative differentiation trends in natural impact glasses; based on the conservation of the initial Ca/Al ratio and the anti-correlation of Si and Al. However, the experiments of Gerasimov *et al.* (2005) are only focused on the chemical changes of the target and limited on analyses of condensed vapor. Our research group MEMIN (Multidisciplinary Experimental and Numerical Impact research Network) recently performed hypervelocity impact experiments using steel and Campo del Cielo iron meteorite as projectiles and two different silica-rich lithologies (sandstone and quartzite) as target (Ebert *et al.*, 2013; Ebert *et al.*, 2014). In all of the investigated impact experiments the ejecta fragments show (i) shock-metamorphic features like planar-deformation features and the formation of silica glasses (ii) partially melting of projectile and target, and (iii) significant mechanical and chemical mixing of the target rock with projectile material. The silica-rich target melts are strongly enriched in the projectile tracer elements Cr, V, and Fe but have just minor enrichments of Ni, Co, W, and Mo. The fractionation results from differences in their reactivity with oxygen during interaction of metal melt with silicate melt (Ebert *et al.*, 2013; Ebert *et al.*, 2014). Hypervelocity impact experiments are expensive and elaborate; only few shots are possible. Due to the small amount of usable material and the tiny phases within highly shocked ejecta produced in these experiments (Ebert *et al.*, 2013) electron microscopic analysis are challenges. For these reasons and the main result that predominantly high temperatures are required for melting, mixing and element partition processes we have looked for experiments in order to produce and analyze target and projectile melts and a mixture of them under more idealized conditions. Therefore we have performed laser-induced melting experiments (LE) at the laser welding facility of the Technical University of Berlin. This method allows (i) separate (partial) melting of target and projectile material to be produced to better constrain "primary" melt heterogeneities before mixing occurs, and (ii) mixing of larger amounts of projectile and target melts to receive better conditions for microanalytical studies (e.g. to allow larger spot sizes for trace element analysis of

glasses). The laser-induced melting technique generates high-temperature effects; shock effects (e.g. like planar deformation features in quartz) were not produced with this method.

5.3 Experimental and analytical methods

5.3.1 Laser-induced melting technique

The laser-induced melting experiments were conducted at the laser welding facility of the Technical University of Berlin. The Trumpf Haas HL 3006D facility is equipped with a Nd:YAG-Laser which operates in the infra-red spectra (wavelength 1064 nm) and has a maximum output power of 3 kW. Laser point irradiation was carried out in an experiment with a $2 \times 2 \times 2$ cm cube of sandstone (LE-F in Table 5.1, Fig. 5.1). For the other laser experiments centimeter-sized pieces of Seeberger sandstone were fixed either separately or laterally together with a piece of Campo del Cielo meteorite or D290-1 steel (Fig. 5.2) on an aluminium bottom plate (4×4 cm in size). In order to capture ejected melts and to protect the laser facility against these melt droplets, the experimental setup has also 3 aluminium side-walls (4×2 cm), one glass wall and a top plate with a slit for the laser beam.

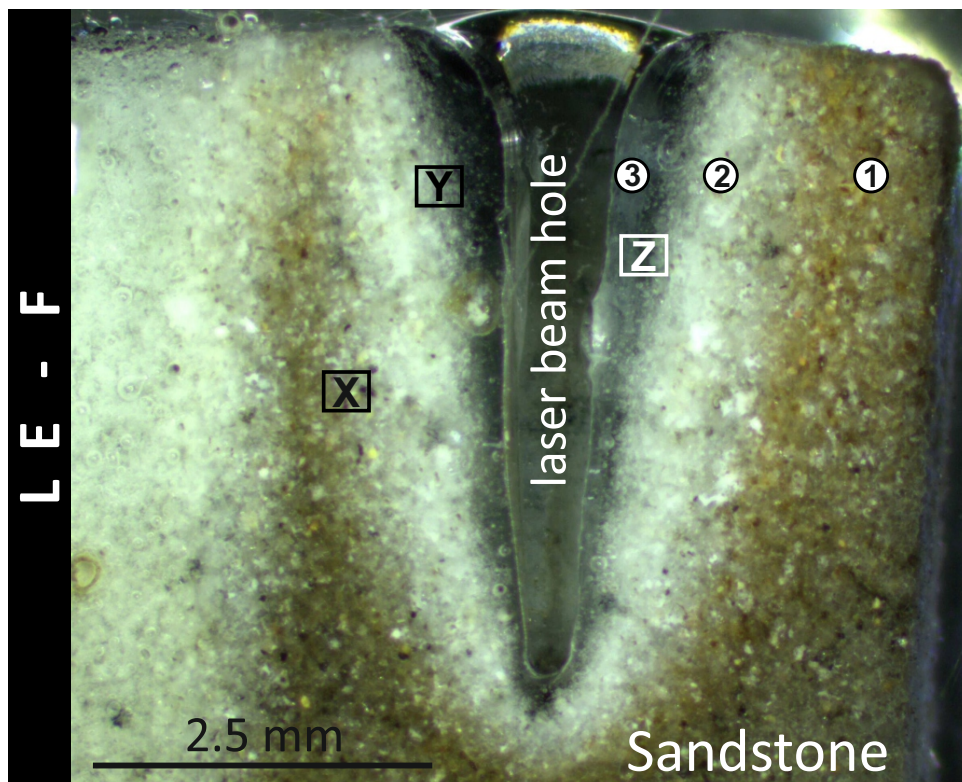


Figure 5.1: Cross section of the laser beam key hole of experiment LE-F; Point 1: unaltered sandstone, 2: partial melting of the sandstone, 3: complete melting and mixing of all sandstone components. Rectangle X marks: Fig. 5.3, Y: Fig. 5.4a, Z: Fig. 5.4b.

The different walls of this assemblage were changed for each laser experiment. The laser beam was automatically conducted along 1 cm lines across the two materials with robotic machinery. The laser was continuously irradiated (no pulsing mode) through air on the samples with a focal point position of 0 mm. The experimental conditions of each experiment are compiled in Table 5.1.

5.3.2 Samples and analytical methods

In order to analyze the molten areas of the sandstone or the molten contact zone between sandstone and iron meteorite (or sandstone and steel) small pieces were cut out along the melt track parallel to the laser beam trajectory (cp. Fig. 5.1 and Fig. 5.2c,f). The exact positions of the thick sections are marked as solid line in Fig. 5.2b and Fig. 5.2e. The separated samples were embedded into 1 inch epoxy cylinders, polished and coated with carbon. Quantitative analyses were carried out with the JEOL JXA-8500F electron microprobe (EMP) equipped with a field emission cathode, five wavelength-dispersive spectrometers, and an energy-dispersive spectrometer. Measurement conditions for wavelength-dispersive X-ray spectrometry varied depending on properties and compositions of analyzed materials (Table 5.2). Two different measurement programs were defined for the silicate and metallic phases. Raw data were processed for matrix effects using a conventional ZAF routine in the JEOL series operating system.

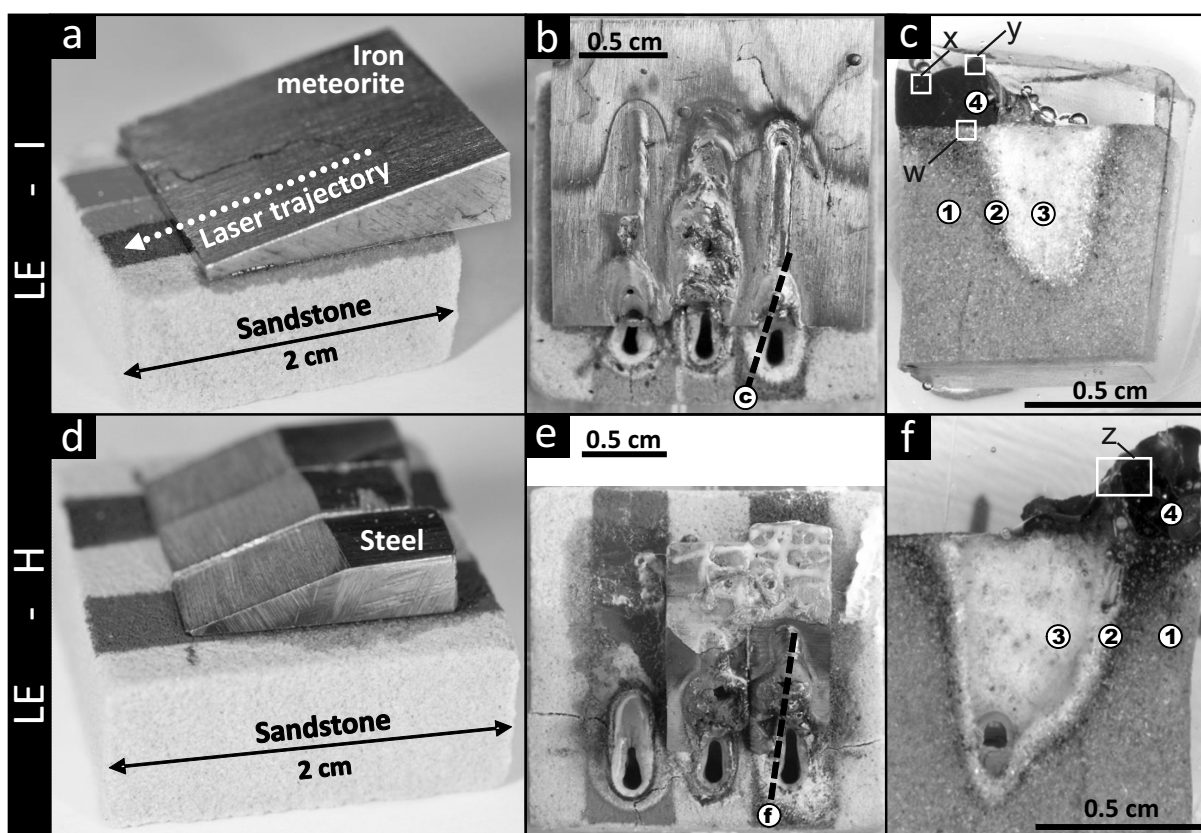


Figure 5.2: (a,d) Photograph of the experimental setup (LE-I, LE-H) before laser beam irradiation; (b,e) after laser beam irradiation; (c,f) sections used for geochemical analyses (exact position marked in Fig. 5.2e and f); Point 1: unaltered sandstone, 2: partial melting of the sandstone, 3: complete melting of the sandstone, 4: projectile melt; w - Fig. 5.8; x - Fig. 5.7a, y - Fig. 5.7b, z - Fig. 5.5a.

5.4 Results

5.4.1 Target and projectile material

The original manuscript contains a detailed geochemical and petrographic description of the target (Seeberger sandstone) and projectile (Campo del Cielo meteorite and D290-1 steel) materials. In order to avoid repetitions in this thesis the reader is referred to the respective sections of the other chapters. The chemical composition of the sandstone target and Campo del Cielo projectile is listed in Table 2.2 on page 29. The composition of the D290-1 steel and its phases is compiled in Table 3.3 on page 58. Back-scattered electron images of the meteorite including the main phases and textures are shown in Fig. 2.1 on page 14; the Seeberger sandstone in Fig. 2.2b on page 16; the D290-1 steel in Fig. 3.2c on page 37.

5.4.2 Modes of melting and mixing

5.4.2.1 Pure sandstone

The following results are based on experiment LE-F for which only a piece of Seeberger sandstone were used; no projectile. This allows the observation of gradually melt formation and the generation of chemical data without projectile contamination (pure sandstone melt). In LE-F the short laser pulse (0.5 s) produced a ~ 0.6 cm depth laser beam hole (Fig. 5.1), which is surrounded by a small (~ 0.4 cm in diameter from the focal point of the laser beam) heat affected area. Three different laser-sandstone interaction zones (Points 1 to 3 in Fig. 5.1) are defined by regions of similar physical reactions observed in the sandstone from no modification to intense melting. This range is the consequence of a strongly developed temperature gradient.

Zone 1 (Point 1 in Fig. 5.1) shows no thermal modification of the sandstone minerals. Accordingly, the texture of this zone corresponds to that of the original sandstone (cp. Fig. 3.2a). Only few long fractures are present, which have their origin in zone 2 and 3.

Zone 2 (Point 2 in Fig. 5.1) contains a wide range of thermal reactions of the sandstone minerals (Fig. 5.3). Contrary to the unmodified sandstone matrix of zone 1, here the phyllosilicates show evidences of dehydroxylation (loss of constitutional OH) together with partial melting. Dehydroxylation is indicated by a broadening of the distances of the individual clay flakes probably due to the escaping water vapor (Fig. 5.3b). The dehydroxylation temperature of inter alia kaolinite (majority of the phyllosilicates in the Seeberger sandstone after Stück, 2013) starts at 550°C - 600°C (Yeskis *et al.*, 1985). At this temperature kaolinite is transformed into amorphous metakaolin (Redfern, 1987). On the other hand, the elongated cavities between the phyllosilicates partially skip into an irregular rounded form (framed with white dashed circle in Fig. 5.3b); thus partial melting of the phyllosilicates is assumed. At approximately 600°C quartz grains expand by 1.75 % of the original size (Salehi *et al.*, 2007). In the case of full grain contact (low void space), grains have less space to expand and fractures develop (Fig. 5.3a). The release of gases during the dehydration of the phyllosilicates can also produce stress and subsequent fractures. With progressive melting the fused phyllosilicates formed melt accumulations. Small bubbles occur in this melt with sizes ranging between few nanometer to tenth of micrometers. Partially large bubbles are developed in the center of a melt accumulation (marked as "3" in Fig. 5.3a and as "bubble" in Fig. 5.3b). With decreasing distance to the laser beam penetration

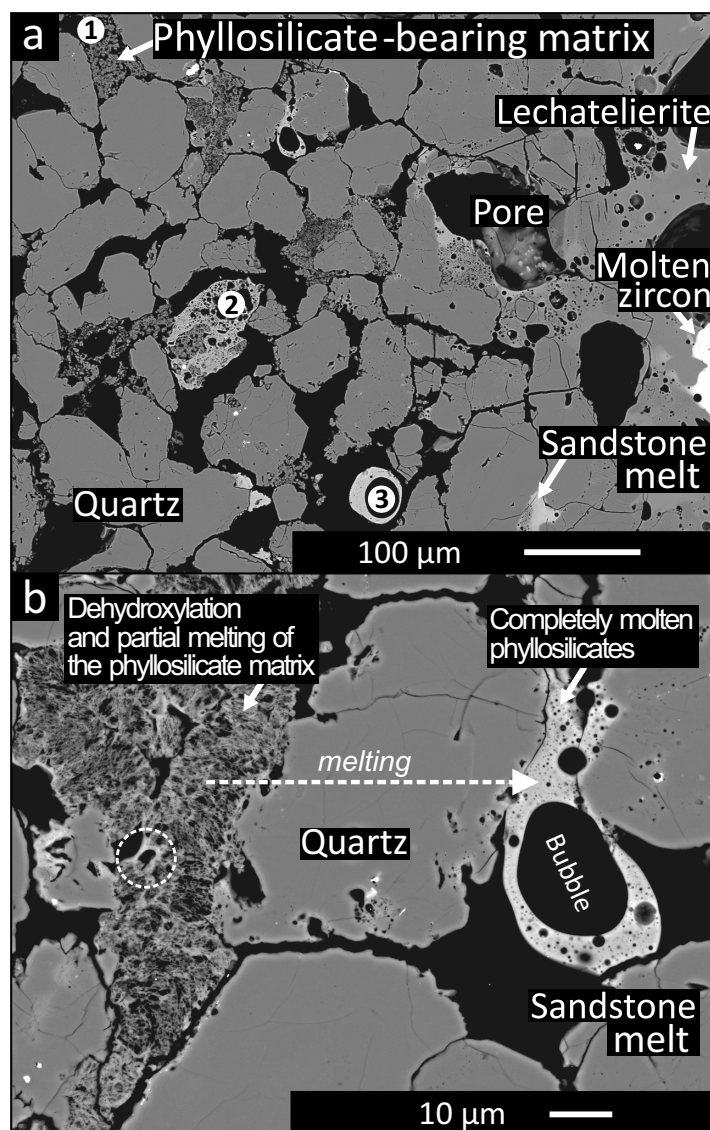


Figure 5.3: (a,b) Different stages of dehydration and melting processes in the sandstone (BSE images; LE-F). Exact position is shown as rectangle X in Fig. 5.1. (a) Point 1: unaltered phyllosilicate-bearing matrix, 2: dehydration and initial melting of the phyllosilicates, 3: completely molten phyllosilicates. (b) Dehydration and initial melting of the phyllosilicates on the left side (cp. with pristine matrix in Fig. 3.2a); completely molten phyllosilicates on the right side (see text for more details).

point the temperature increases and the quartz margins begin to melt (exemplary marked as white star in Fig. 5.4a), thus approximately 1600°C - 1700°C were reached. Lechatelierite (fused quartz) has a lesser density than crystalline quartz. Therefore with the material contrast of the microprobe BSE mode it is possible to distinguish between these two silica states. Lechatelierite shows a darker shade of gray than the unaltered quartz. This is best demonstrated in the higher contrast strip at the top of Fig. 5.4a. Melting of the quartz starts at the margins and propagates inwards along irregular tracks and form a network of lechatelierite. With ongoing melting these silica glass tracks enlarge until successively small quartz islands completely disappear, and the whole quartz grain is completely transformed into lechatelierite. Whereby, at this melting stage (zone 2) the original form of the quartz is more or less preserved. Quartz fracturing mainly occurs

in an area where the quartz grains are not yet completely molten (cp. right side of Fig. 5.4). In a completely molten stage the cracks were healed due to the viscous melt (cp. left side of Fig. 5.4).

Zone 3: Complete melting and mixing of all sandstone components occur in the direct vicinity of the laser beam penetration point (see left side in Fig. 5.4b), which define **zone 3** (Point 3 in Fig. 5.1). Here often schlieren of mixed lechatelierite and molten matrix minerals occur which indicate melt pool movements induced by the laser beam. Chemical signatures of molten rutile in the sandstone melt indicate minimum temperatures of 1842°C (Rosenqvist, 2004) at zone 3 (more details about chemical composition see below).

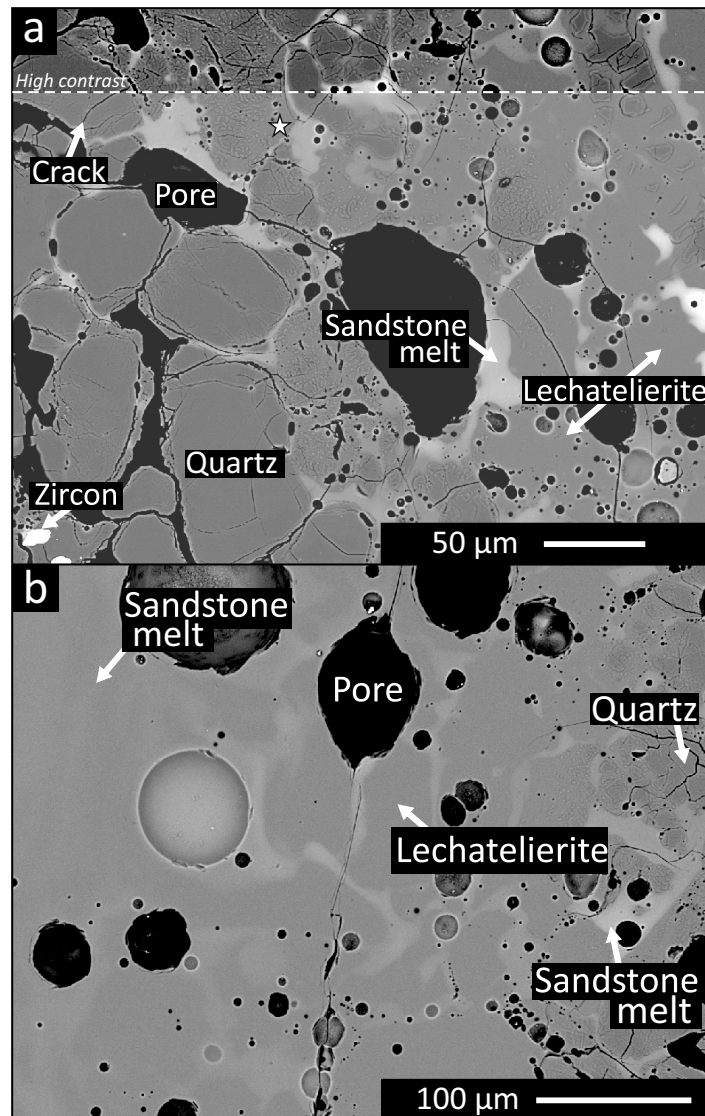


Figure 5.4: (a,b) BSE images of different melt textures in the sandstone target (LE-F). (a) Note the "high contrast" area in the upper part of the image, which allows a good distinction between lechatelierite and crystalline quartz (light gray 'islands'). Laser beam heat gradient extends from the right to the left side (high T to low T). (b) Laser beam heat gradient extends from the left to the right side (high T to low T). Exact position is shown as rectangle Z in Fig. 5.1.

5.4.2.2 Projectile

Steel (LE-G, LE-H): The textures shown in Fig. 5.5c indicate melting and homogenization of the steel matrix (cp. Fig. 3.2c on page 37). The steel D290-1, however, rarely shows complete homogenization. Conspicuous feature are Mo-W-rich carbides with fish-bone structures (Fig. 5.5c) which are well known in metallurgical processes and represent eutectic carbides (e.g., Weber *et al.*, 2009). These textures are completely identical with the textures of the projectile droplets observed in the highly shocked ejecta (cp. Fig. 3.5 on page 42). During the irradiation process steel melt spheres ($< 1 \mu\text{m}$ in diameter) were separated from the steel piece and mechanically injected into the high viscous sandstone melt (Fig. 5.5b,d and Fig. 5.6b-d). The Mo-W-rich carbides may also occur within very metallic projectile droplet, as indicated by very tiny spots of Mo (and W) in the corresponding element map in Fig. 5.10 (best visible in the upper and lower droplet of this figure).

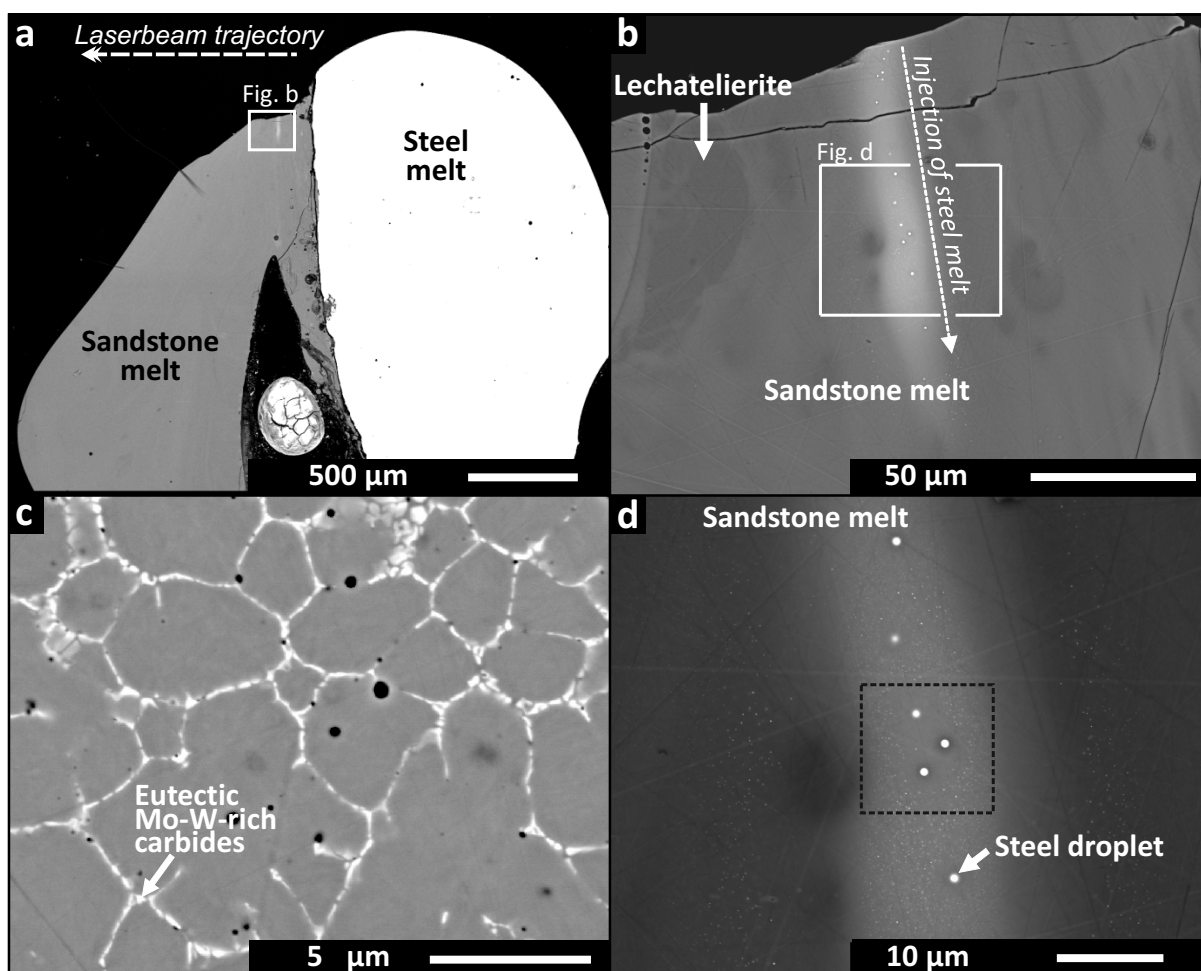


Figure 5.5: (a-d) BSE images of LE-H; (a) Molten contact between steel and sandstone; (b) Completely molten sandstone with injection path of projectile melt; (c) Low brightness magnification of the steel melt; typical textures of the molten steel with fish-bone structures of Mo-W-rich carbides (d) Magnification of Fig. 5.5b at high contrast; dash lined rectangle marked the element maps of Fig. 5.10.

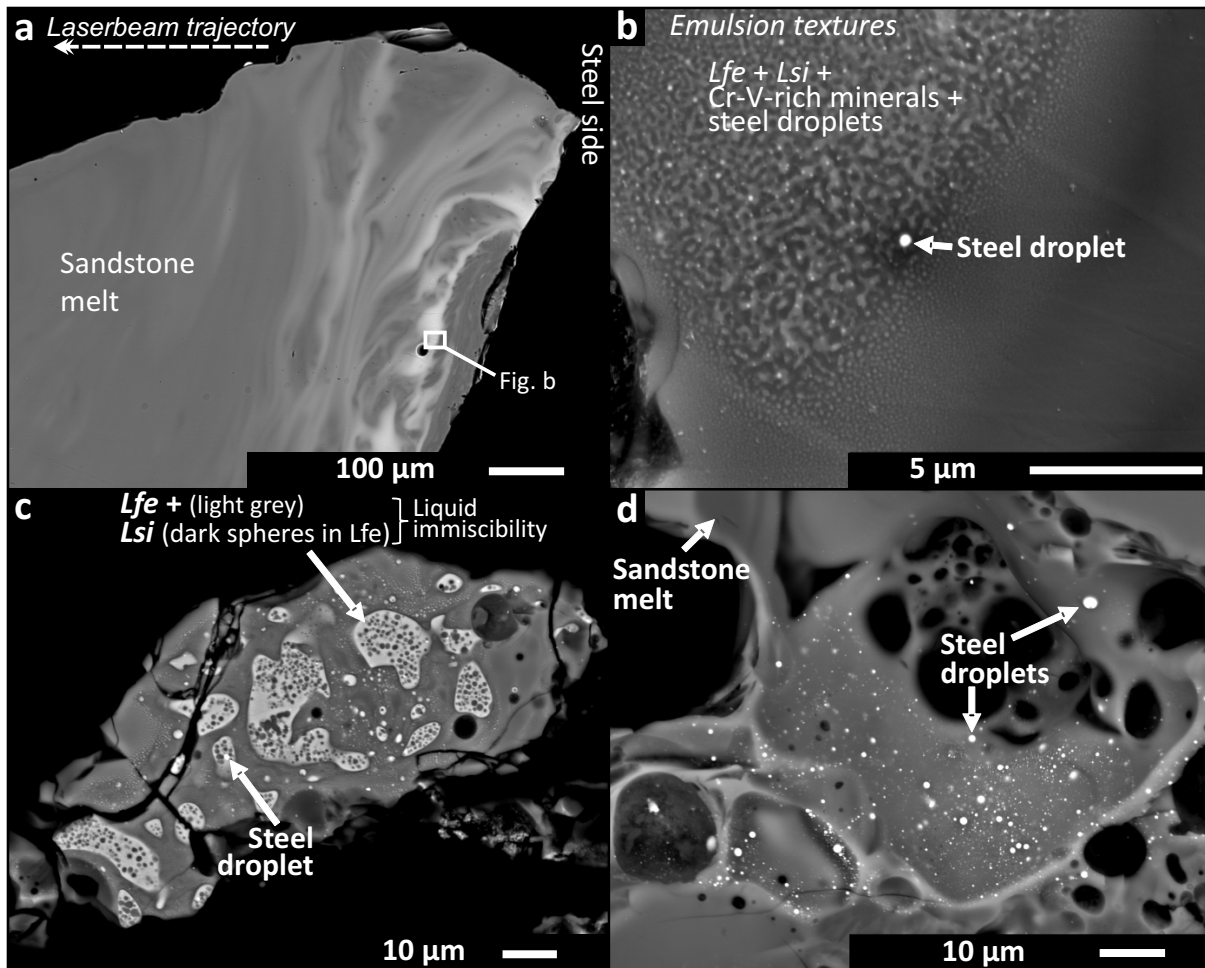


Figure 5.6: (a-d) BSE images of LE-G; (a) Molten contact between steel and sandstone; (b) Typical unmixing features within the contaminated sandstone melt; see text for more explanations; (c) Emulsion textures of Lfe and Lsi ; (d) Significant mixing of steel melt droplets (white) and sandstone melt, note that this is a three dimensional view into the melt.

Campo del Cielo meteorite: The cut section of LE-I (Fig. 5.2) provides two regions within the meteorite which are showing partial and complete melting. Small melt pockets (10 - 120 μm) only occur within the partly fused region of the Campo del Cielo meteorite piece (Fig. 5.7a). The melt pockets consist of two coexisting melts of different composition. One melt is situated at the rim of the melt pocket and appears brighter in the BSE image due to higher mean atomic number. The other melt of lower mean atomic number is located in the center of the melt pocket. The complete molten region of the meteorite (Fig. 5.7b) shows no melt pockets, which is an evidence of significant homogenization of its minerals. Furthermore, tiny pores ($< 5 \mu\text{m}$) indicate intense melting, probably vaporization. The homogenized meteorite solidified as kamacite, partially as crystals with different orientations; see parallel bands in Fig. 5.7b. Molten spheres of the Campo del Cielo meteorite are very rare and have sizes $< 1 \mu\text{m}$; too small for quantitative microprobe measurements. The spheres are only located in the sandstone melt which is in the near vicinity (distance $< 75 \mu\text{m}$) of the completely molten Campo del Cielo (Fig. 5.8).

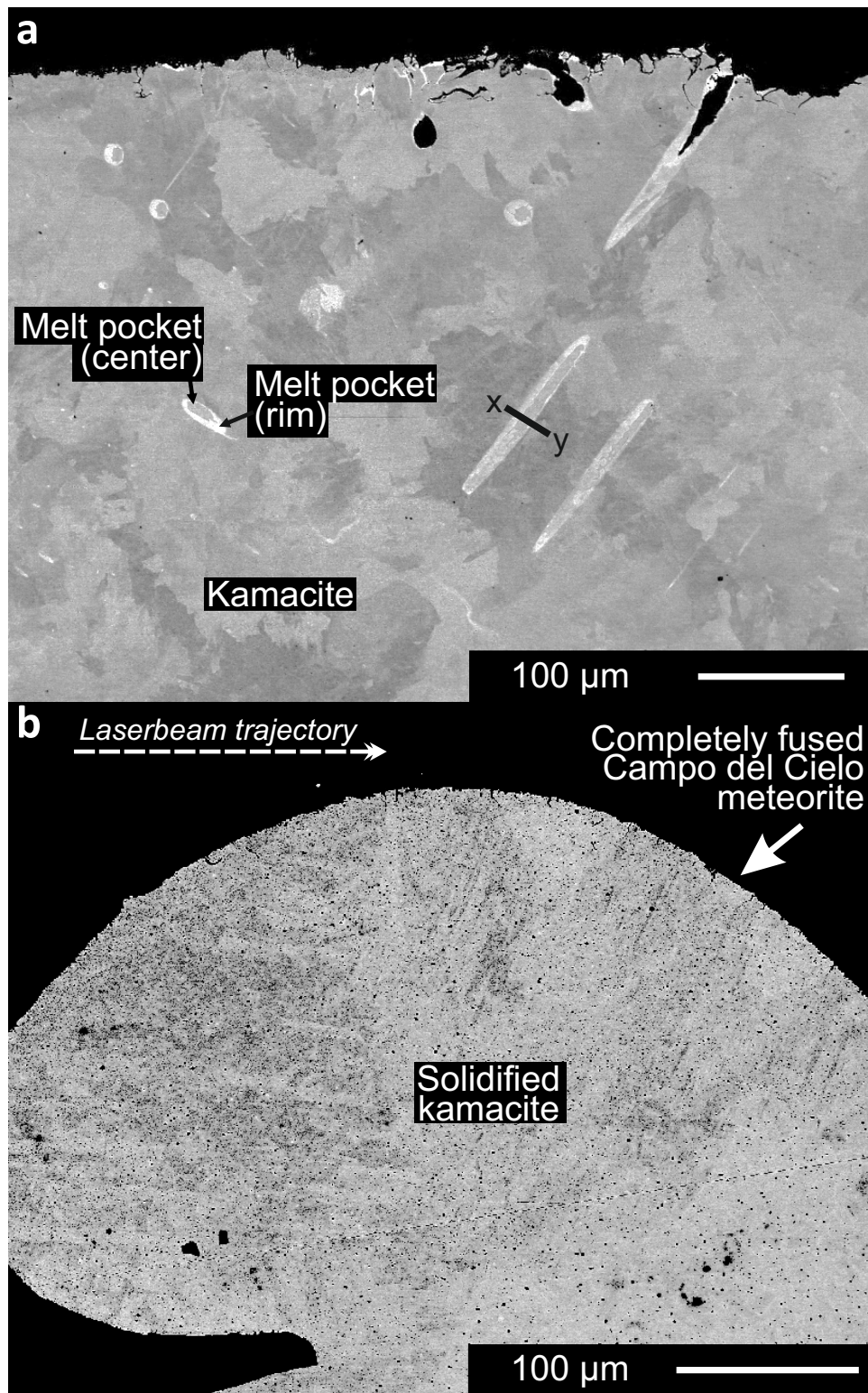


Figure 5.7: (a) BSE image of typical melt pockets with rim and center part in a partly fused Campo del Cielo meteorite; exact position of this image is marked as rectangle "X" in Fig. 5.2c; line x-y marked a chemical profile shown in Fig. 5.13. (b) BSE image of the completely fused Campo del Cielo meteorite; exact position of this image is marked as rectangle "Y" in Fig. 5.2c.

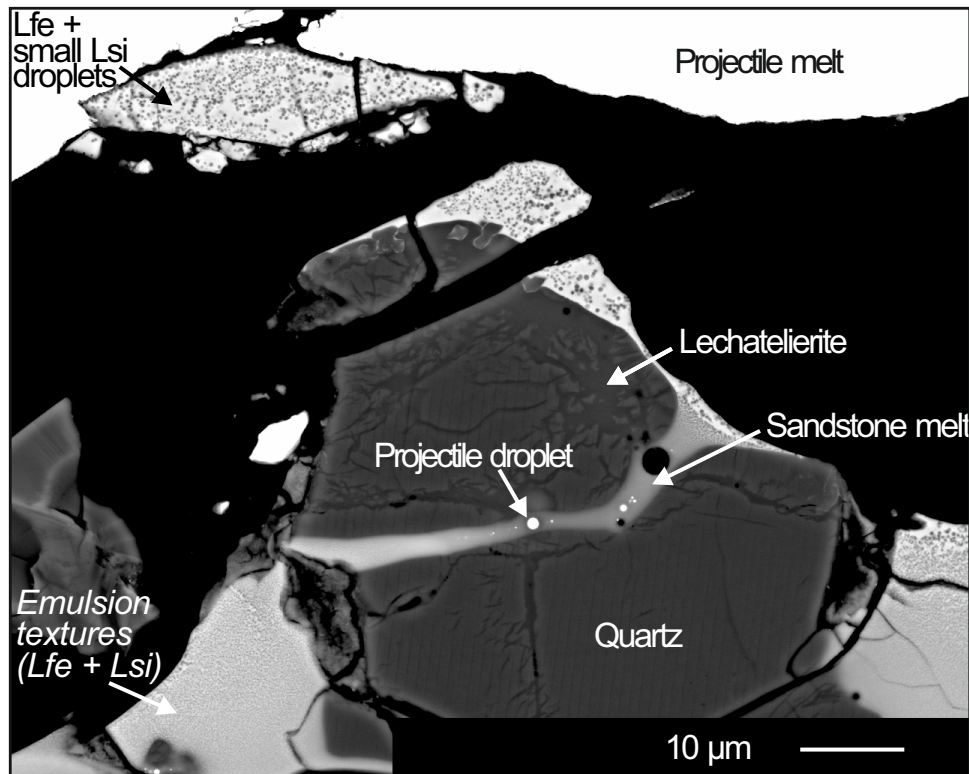


Figure 5.8: BSE image of the molten contact between Campo del Cielo meteorite and sandstone. Please note that the projectile melt is only the large white curved part at the top of the image, which is separated from the whitish emulsion textures below it (LE-I). Exact position of this image is marked as "W" in Fig. 5.2c

5.4.2.3 Mixing of target and projectile melts

Steel matter occurs within schlieren of the sandstone melt at the contact to the projectile (Fig. 5.5b and Fig. 5.6a; LE-H, LE-G), suggesting heterogeneous chemical mixing between projectile and target melts. BSE images provided further details of the small scale heterogeneity within the contaminated sandstone melt (e.g. Fig. 5.6b). Characteristic features are the emulsion textures of the sandstone target melt (e.g. Fig. 5.6b,c). This emulsion contains at least three almost immiscible melts. It is dominated by a highly siliceous glassy matrix (termed *Lsi*) that contains ubiquitously and dispersed droplets of iron-rich glass (termed *Lfe*), and less abundant, metallic steel spheres. *Lfe* and *Lsi* droplets are partially interconnected into small cluster, by which they lose their spherical shape (Fig. 5.6b, BSE image of Fig. 5.9). Due to Cr and V element maps the formation of very tiny Cr-V-rich minerals is assumed which occur as irregular distributed clusters in the direct vicinity of the *Lfe* glass (Fig. 5.9 and Fig. 5.10). A further type of emulsion texture (in this case double emulsion) is shown in Fig. 5.6c, which represents an impressive example for the immiscibility of melts with strong chemical differences. Irregular shaped *Lfe* bodies (5 - 30 μm) occur in the silica-rich sandstone target melt; this represents the first emulsion. The *Lfe* bodies contain a number of small ($< 1 \mu\text{m}$) *Lsi* droplets that are rarely interconnected; which is the second emulsion. Note the remarkable sharp boundaries between *Lfe* and *Lsi* in Fig. 5.6c and the dimly transitions between both melts in Fig. 5.6b and Fig. 5.9. Only in a very few cases a high abundance of steel spheres occurs in the sandstone

melt (Fig. 5.6d).

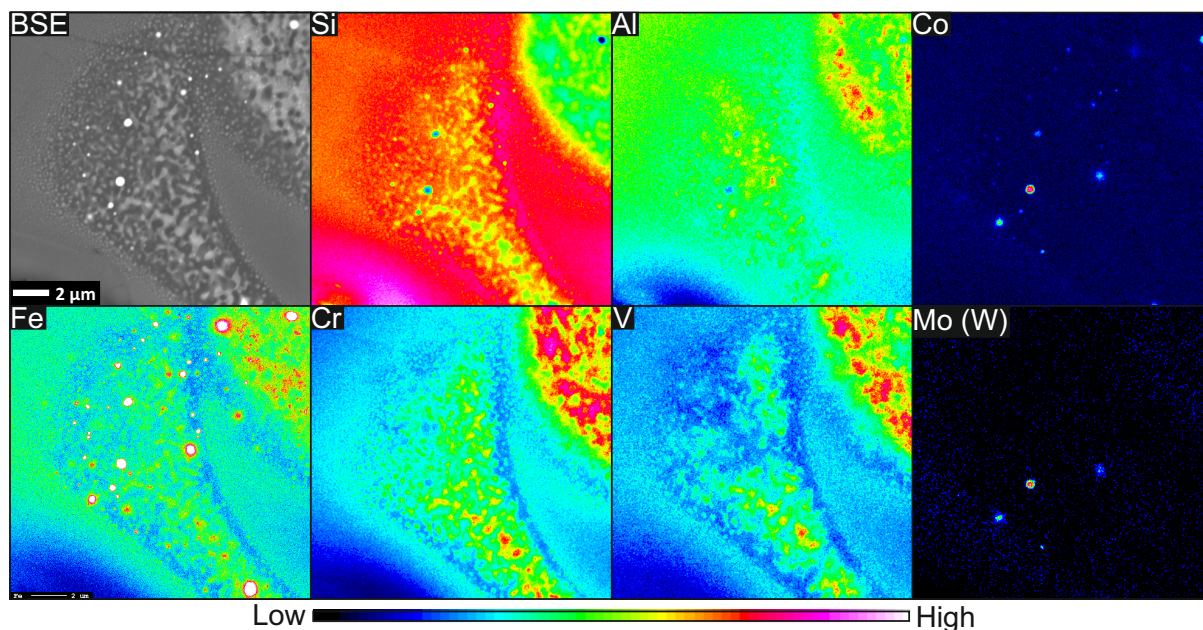


Figure 5.9: Qualitative element maps of sandstone melt mixed with light projectile melt droplets of D290-1 steel (LE-G).

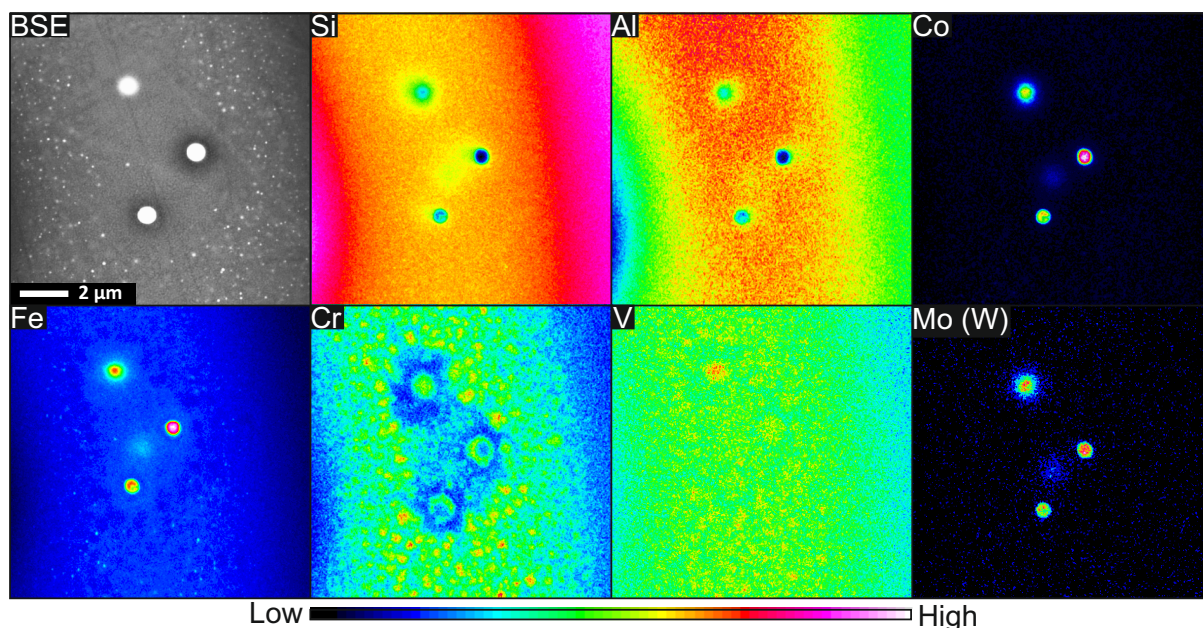


Figure 5.10: Qualitative element maps (outlined rectangle of Fig. 5.5d) of sandstone melt mixed with light projectile melt droplets of D290-1 steel (LE-H).

In experiment LE-I projectile matter is transferred from completely fused Campo del Cielo meteorite (cp. Fig. 5.7b) into the sandstone target melt, especially at the interface between the two source materials. The transition between molten projectile and molten sandstone target is defined by a compositional gradient which clearly show unmixing of melts (Fig. 5.8 and Fig. 5.11a). This spatial and chemical transition is named "*zone of iron enrichment*". This zone, which is approximately 50 μm in diameter, can be divided into three parts of different

textures (explanation adopted from Ebert *et al.*, 2014). Part 1 predominately consists of *Lfe* with minor amounts of well rounded *Lsi* droplets (see BSE image of Fig. 5.11b). Part 2 has more or less equal proportions of irregular shaped *Lfe* and *Lsi* droplets. Many droplets are interconnected, and most of them are non-spherical in shape. Part 1 and part 2 are sharply disconnected from each other by a silica-rich meniscus (see BSE image of Fig. 5.11b); a smoothed transition rarely occurred. Part 3 is dominated by *Lsi* containing low amounts of *Lfe* droplets. Individual silica melt droplets reach sizes from a few tenth of nanometer up to 250 nm. Under rare circumstance, this chemical process was accompanied by a mechanical mixing of projectile droplets into the sandstone melt (small projectile droplets in Fig. 5.8).

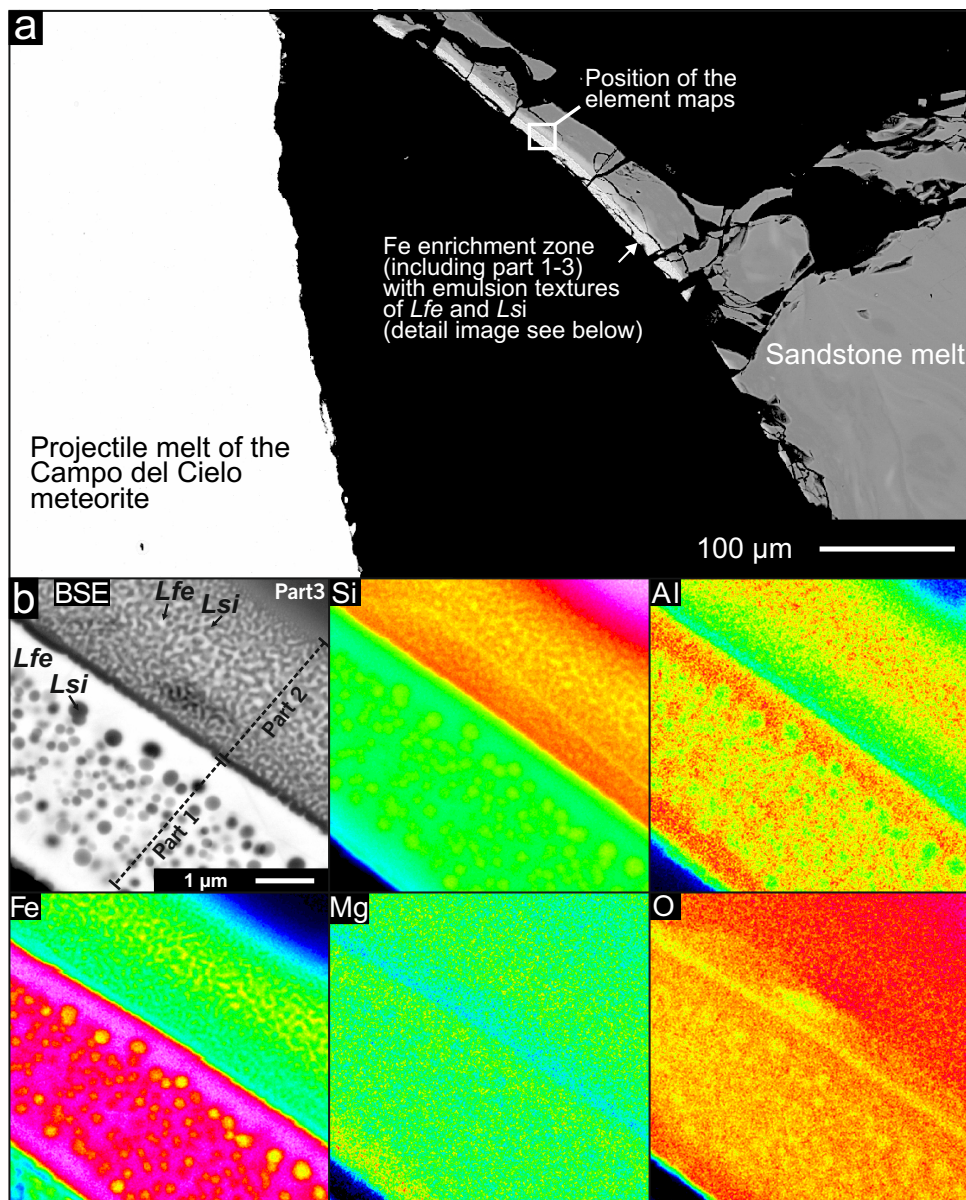


Figure 5.11: (a) BSE image of the interface between projectile melt, Fe enrichment zone and sandstone target melt (experiment LE-I). The space between projectile melt and silicate melts is probably caused by the preparation of the section (see text for more details). (b) Microprobe element maps of the Fe enrichment zone and its conspicuous emulsion textures of *Lfe* and *Lsi*.

5.4.3 Compositional variations of pure sandstone melt and projectile melts

5.4.3.1 Sandstone melt

The experiment LE-F provides chemical data of pure sandstone melt, not contaminated with projectile matter. The produced sandstone melt shows significant compositional variations (Fig. 5.12): SiO₂ (73.96 ± 14.35 wt.%), Al₂O₃ (18.26 ± 10.39 wt.%), K₂O (2.21 ± 1.75 wt.%), FeO (2.69 ± 2.11 wt.%), MgO (1.25 ± 0.98 wt.%), and TiO₂ (0.68 ± 0.42 wt.%). Table 5.3 gives some representative microprobe analyses of this sandstone melt. The phyllosilicate-bearing matrix provides only a small amount of TiO₂ (\bar{O} = 0.16 ± 0.26 wt.%, see also Table 2.2 on page 29). Nevertheless, the sandstone melt can locally reach high TiO₂ content (7.85 ± 5.30 wt.%). In this case it is suggested that a supply of TiO₂ by molten rutile took place (named as "Sandstone melt with Ti supply"). The other oxides show a compositional variation, which is more or less comparable to the chemistry of the melt describe above: SiO₂ (71.02 ± 8.74 wt.%), Al₂O₃ (15.71 ± 8.21 wt.%), K₂O (2.21 ± 1.75 wt.%), FeO (2.67 ± 1.31 wt.%) and MgO (0.88 ± 0.38 wt.%). In order to distinguish the sandstone between "with" and "without" Ti supply, an upper limit of about 1 wt.% TiO₂ for the sandstone melt without TiO₂ supply is assumed. This assumption is based on the fact that all oxide contents of the phyllosilicates increase during melting, due to the dehydration of these minerals. An increase of about one order of magnitude for the TiO₂ content seems to be a realistic value within the range of the phyllosilicates values. An important observation is the linear dependence of FeO and MgO. With increasing FeO content MgO also increases (cp. Mg vs Fe in Fig. 5.12). A deviation from this linear dependence, for instance by an enrichment of Fe, can be used to identify an addition of projectile matter within the sandstone melts of the other laser experiments (see below). The stark compositional variations of the sandstone melts reflect different ratios of molten matrix (especially phyllosilicates and rutile) and molten quartz but also heterogeneities in the phyllosilicate-bearing matrix. The Al vs. Ti diagram of Fig. 5.12 clearly shows that the sandstone melt plot within the triangle of the chemical end-member phyllosilicates, rutile and quartz. In the same plot the sandstone melts with TiO₂ partially lies directly on the mixing line between rutile and phyllosilicate (ideal rutile composition is used). Deviations from this mixing line are due to incorporation of SiO₂ from molten quartz grains. Fig. 5.12 shows metal contents instead of metal oxides allowing comparisons with diagrams where projectile data (non-oxide) is included.

5.4.3.2 D290-1 steel

At high temperatures and progressive melting of the original Mo-W-rich carbides, the projectile melt is enriched in W and Mo; this leads to decrease of Fe and Co compared to the matrix of the original steel. The steel melt slightly varies in its chemical compositions, i.e., Fe contents with 81.02 ± 1.45 wt.%, Co 5.41 ± 0.10 wt.%, Mo 3.69 ± 0.72 wt.%, W 5.00 ± 0.76 wt.%, Cr 3.35 ± 0.49 wt.%, V 1.16 ± 0.22 wt.% and O 0.40 ± 0.07 wt.% (LE-G; mean of 18 measurements). In comparison with the steel melt which was produced in hypervelocity impact experiments, the steel melt of the laser experiments has slightly higher Mo and W values. This probably indicates higher melting temperatures and consequently better conditions for the mixing of the molten Mo-W-rich carbides and steel matrix. Unfortunately, in LE-G and LE-H the molten metallic spheres which were mixed into the sandstone melt are too small (< 1 μm) for quantitative micro-

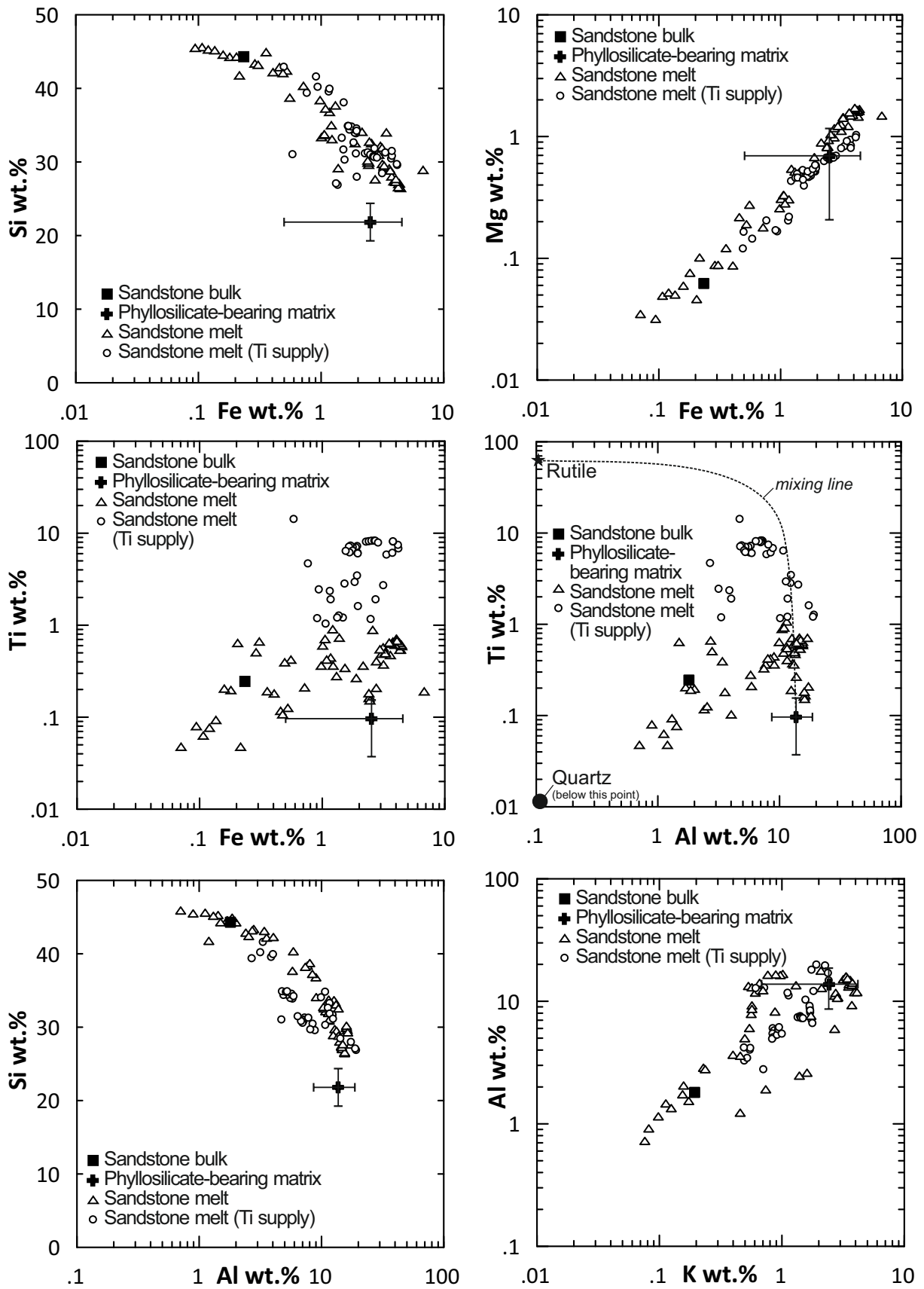


Figure 5.12: Chemical variation of the produced sandstone melt from LE-F.

probe analyses. Qualitative element maps clearly show high Fe, Co, Mo and W contents (Fig. 5.10); which can be used as evidence that these sphere are steel melt. The Mo-W-rich carbides may also occur within very small metallic projectile droplet, indicated by the really tiny "red" spots (high values) of Mo and W, especially in the upper and lower sphere of the Mo-W element map in Fig. 5.10. Furthermore, note that the 3 "largest" spheres in Fig. 5.10 have only small Cr and V contents which partly occur in rim region of the sphere.

5.4.3.3 Campo del Cielo Meteorite

Laser-induced melting of the schreibersites, rhabdites and melting of the kamacite host crystal produces conspicuous melt pockets within the partly fused Campo del Cielo meteorite (Fig. 5.7a). The melt of the pocket shown in is separated into a P-rich melt in the center, and a P-poor melt at the rim that has a slightly higher Ni-content. Microprobe analyses through the melt pockets show Ni depletion in the surrounding kamacite (Fig. 5.13). In the impact experiments with Campo del Cielo meteorite as projectile material, melting of rhabdites leads to the formation of comparable melt pockets (cp. Fig. 2.5 on page 19). The solidified kamacite of the completely molten meteorite piece (Fig. 5.7b) shows no significant difference to the original kamacite and is in the range of the bulk meteorite. Its mean composition (mean of 41 measurements) is Fe 91.79 ± 0.73 wt.%, Ni 6.23 ± 0.50 wt.%, Co 0.47 ± 0.02 wt.%, P 0.16 ± 0.10 , O 0.46 ± 0.10 wt.% and Si 0.02 ± 0.01 wt.%. Especially the phosphorus value indicates that the kamacite is nominally enriched by the completely solved taenite, schreibersite and rhabdite.

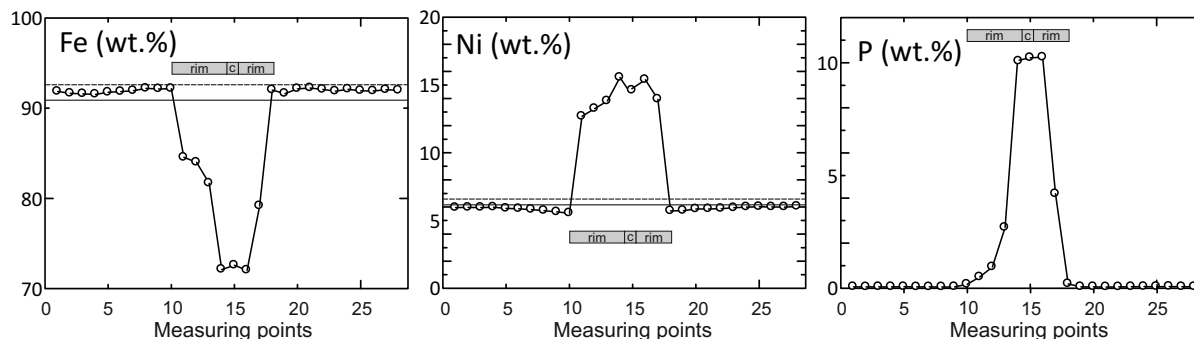


Figure 5.13: Electron microprobe profile for Fe, Ni and P through a melt pocket; exact position marked as line between x and y in Fig. 5.7a; "c" center of the melt pocket. 1 point $\sim 1 \mu\text{m}$. Solid line represents the bulk Campo del Cielo; dashed line represents the partially molten Campo del Cielo.

5.4.4 Element partitioning between projectile and target melt

5.4.4.1 Iron

Element partitioning can be studied by comparing data of pure (LE-F) and contaminated (LE-I, LE-G and LE-H) sandstone melts. The pure sandstone melt shows a more or less linear dependence with increasing FeO and MgO values (cp. Fe vs Mg in Fig. 5.12 and Fig. 5.14). A deviation from this Mg/Fe ratio can be used to identify an addition of Fe which originates from the molten projectile. Figure 5.14 clearly shows an enrichment of Fe (as oxide) within the sandstone melt of the steel and meteorite experiments. Some data points of the LE-H sandstone melt plot in the compositional range of the phyllosilicate-bearing matrix. However, since most of these data points are right to the LE-F sandstone slope, an iron enrichment from the projectile has to be assumed. Different ratios of molten matrix, molten quartz and projectile matter, but also heterogeneities in the phyllosilicate-bearing matrix cause very strong variations of the contaminated sandstone melts (LE-I in Fig. 5.15). The average FeO content of the sandstone melt patches of LE-I (8.95 ± 2.87 wt.%) are slightly higher than the average FeO of LE-H (4.68 ± 4.18 wt.%) and also higher than the FeO in the pure sandstone melt of LE-F (2.67 ± 2.11 wt.%). In case of experiment LE-I, emulsions of *Lfe* and *Lsi* become visible in the BSE mode of the electron microprobe when the FeO contents exceeds ~ 10 wt.% (cp. Fig. 5.8 and Fig. 5.15). More details about the chemistry of *Lfe* and *Lsi* see below.

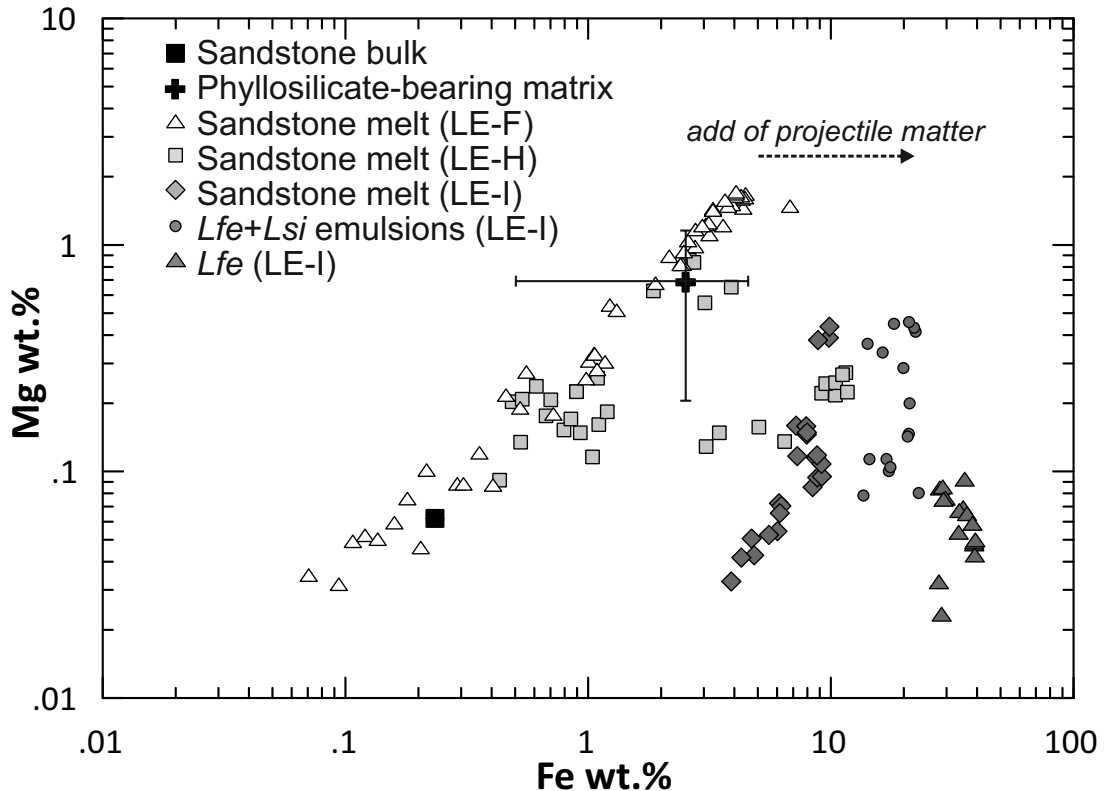


Figure 5.14: Fe vs. Mg for sandstone melts from different laser-induced melting experiments.

5.4.4.2 Chromium and vanadium

The sandstone melt of LE-G and LE-H shows a distinct enrichment of Cr_2O_3 (0.06 to 4.15 wt.% and 0.03 to 1.05 wt.%, respectively) and V_2O_3 (0.03 to 3.47 wt.% and 0.03 to 1.08 wt.%), which

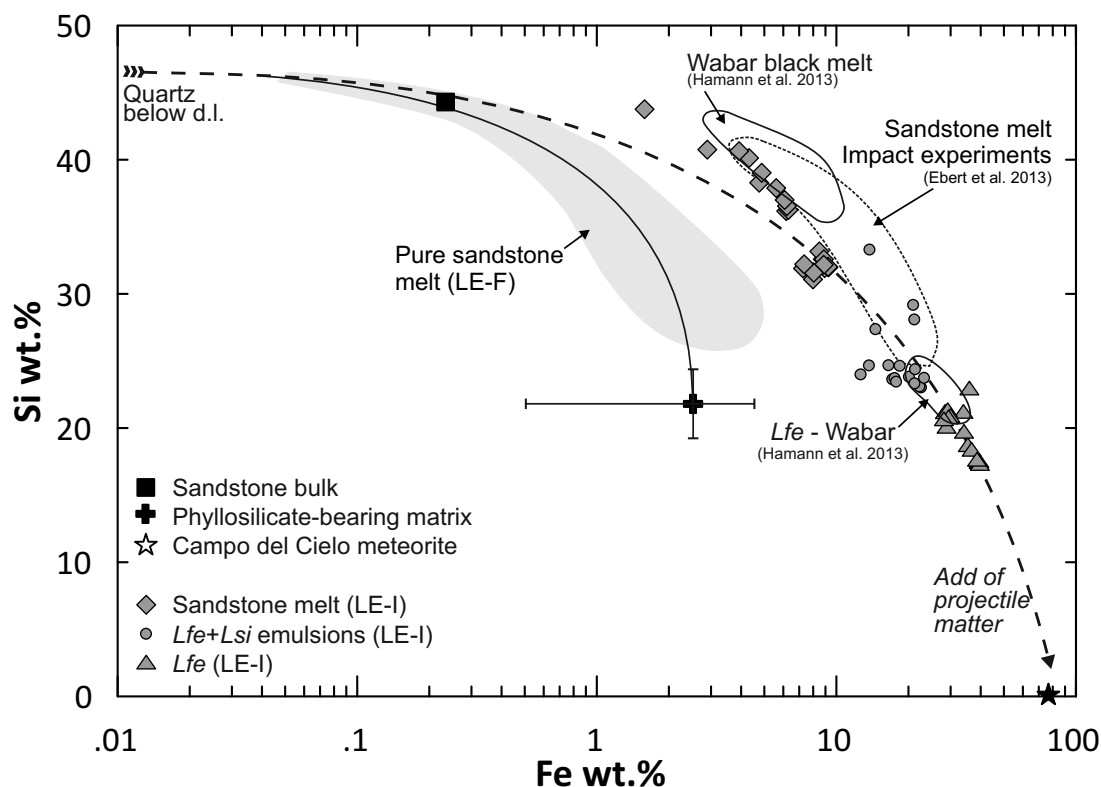


Figure 5.15: Fe vs. Si for sandstone melts from laser-induced melting experiments LE-I. Dashed line field contains Fe vs. Si data from a hypervelocity impact experiments carried out with the same sandstone (target) and a Campo del Cielo meteorite sphere (see Ebert *et al.*, 2013); Solid lined field marked the black impact glass of the Wabar crater (Hamann *et al.*, 2013)

only occur in the lower ppm range within the original sandstone (cp. Table 2.2 on page 29 and Table 5.4). This result is a further evidence of mixing steel matter into sandstone melt. Fig. 5.16 shows Fe vs. Cr data; here both LE-G and LE-H data plot above the projectile ratio line. Thus, Cr (and V) is more able to produce an oxide in the sandstone melt than Fe. By comparing both steel experiments it should be mentioned, although the sandstone melt of LE-G has a stronger Fe enrichment compared to LE-H, the sandstone melt of LE-H incorporated more Cr and V. Thus, there is no link between the enrichment of these three elements.

5.4.4.3 Cobalt, nickel, molybdenum and tungsten

Co is also partitioned into the sandstone melt, but to a considerably lower degree compared to Cr and V. The CoO content in the produced sandstone melt of the steel experiments varies between 0.014 and 0.5 wt.% (LE-G) as well as between 0.02 and 0.57 wt.% (LE-H). The average Fe/Co is mainly one order of magnitude above that ratio in the steel projectile (Fig. 5.16). Thus, Fe is more able to produce an oxide in the sandstone melt than Co. In the experiment with the Campo del Cielo meteorite as projectile the CoO content of the sandstone melt was generally below the detection limit of the microprobe. The reason for this is probably the low Co content (0.43 wt.%) of the meteorite itself. However, Ni is transferred from the molten meteorite into the adjacent sandstone melt. The NiO values are between ~ 200 ppm and ~ 0.1 wt.% (Table 5.5). Highest Ni enrichments occur in the emulsions of Lfe and Lsi (Fig. 5.17). Same as in the case with Fe and Co (steel experiments), the Fe/Ni of the sandstone melt (LE-I) lies also one

order of magnitude above the projectile ratio (plots are below the projectile ratio line Fig. 5.17). The steel tracer Mo and W could not be identified in the sandstone melt of LE-G and LE-H; an exception represents *Lfe* (see below).

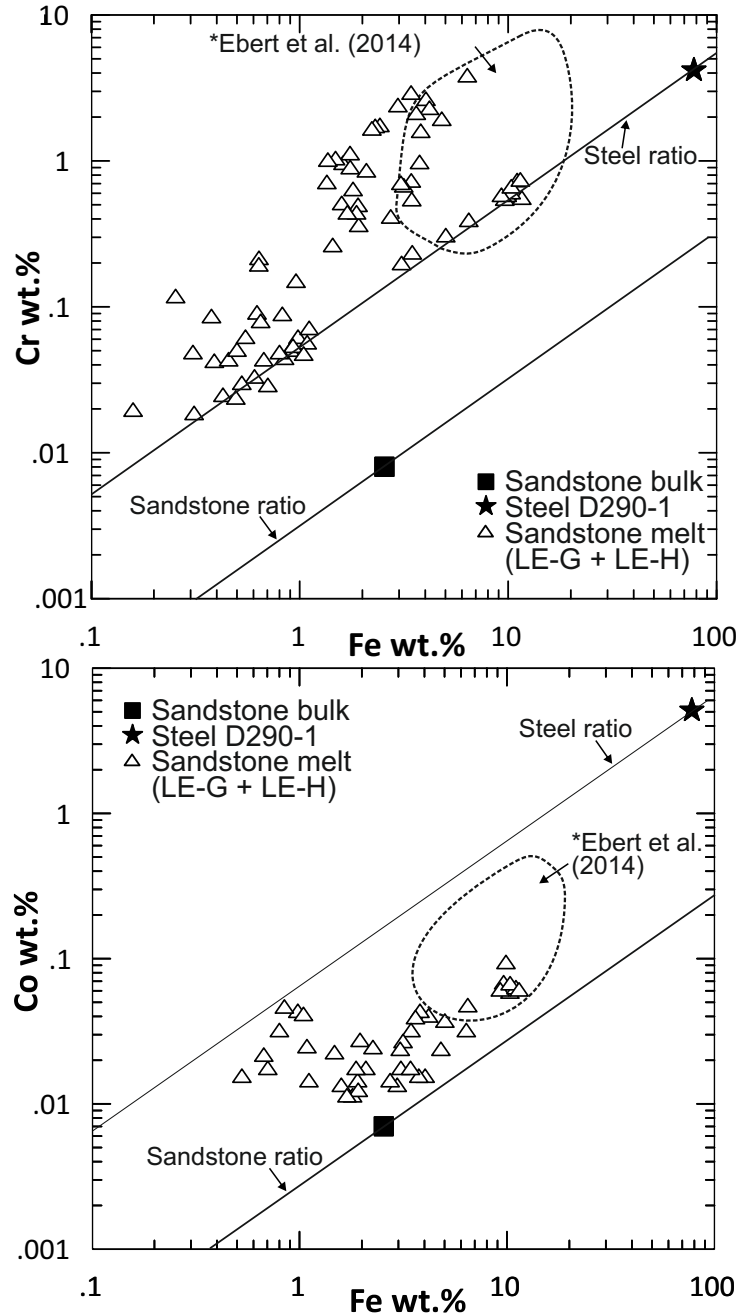


Figure 5.16: Fe vs. Cr and Fe vs. Co for sandstone melt of experiment LE-F and LE-G. Dashed line fields contain Fe vs. Cr (and Fe vs. Co) data from hypervelocity impact experiments carried out with the same sandstone (target) and steel D290-1 spheres (see Ebert *et al.*, 2014).

5.4.4.4 *Lfe* and *Lsi*

Lfe and *Lsi* are represented as a separate section, since they strongly differ from the sandstone melt (see above), in its compositions and textures (see chapter 3.2.3). The two melts were observed in experiment LE-G and LE-I, in the molten contact zone between steel (or iron

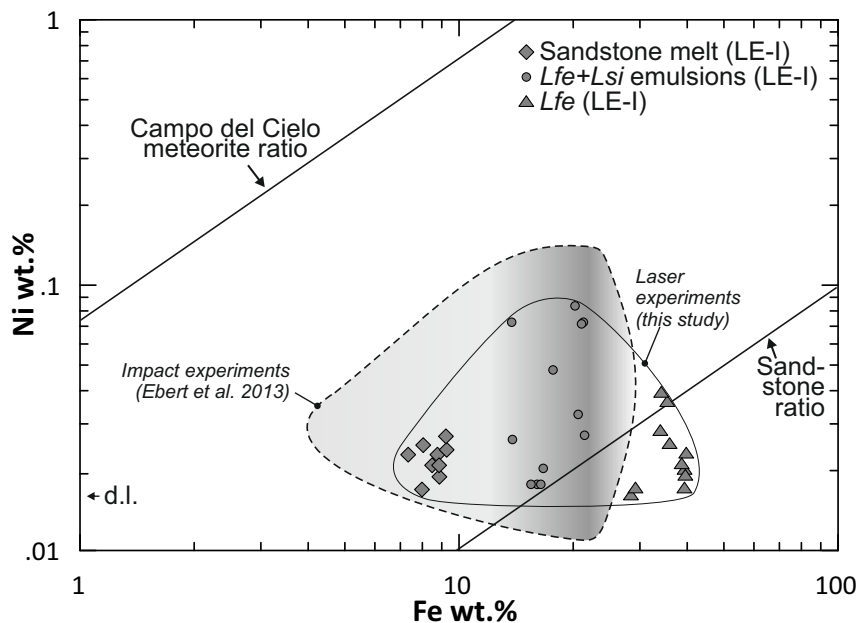


Figure 5.17: Fe vs. Ni for sandstone melt of experiment LE-I. For comparison the dashed line and gray shaded field indicates the data range from a hypervelocity impact experiments carried out with the same sandstone (target) and a Campo del Cielo iron meteorite sphere (see Ebert *et al.*, 2013); whereby the darkest gray shade contain most of the data points.

meteorite) and sandstone (Fig. 5.6c and Fig. 5.8). *Lfe* shows remarkable high amounts of FeO; LE-G slightly higher values compared to LE-I (LE-G: 52.76 ± 1.24 wt%; LE-I: 44.74 ± 5.56 wt%; see also Fig. 5.15). Besides the FeO content, conspicuous feature are the oxide values of the highly siderophile elements Ni, Co, Mo and W. In case of the experiment with steel the *Lfe* phase contains minor amounts of CoO (0.64 ± 0.07 wt%), MoO₃ (0.15 ± 0.06 wt%) and WO₃ (4.79 ± 0.53 wt%). Microprobe measurements of *Lfe* in LE-I shows NiO values of approximately 0.03 ± 0.01 wt%. The chemical data of the *Lfe* phase is listed in Table 5.4 and Table 5.5. *Lfe* differs drastically from the average *Lsi* phase that shows very high amounts of SiO₂ (92.5 ± 0.88 wt%) and minor amounts of Al₂O₃ (3.81 ± 0.33 wt%), K₂O (0.39 ± 0.07 wt%), MgO (0.27 ± 0.08 wt%), TiO₂ (0.22 ± 0.05), FeO ($1.63 \pm .57$ wt%) and Cr₂O₃ (0.03 ± 0.01 wt%). Unfortunately, due to the extreme small droplet sizes, Lsi could only measured in experiment LE-G.

5.5 Discussion

5.5.1 Partitioning behavior of projectile tracer elements

The projectile tracer elements Fe, Co, Ni, Cr, V, Mo and W are enriched to various extents in the sandstone melts as well as in *Lfe* and *Lsi* (Fig. 5.14 - Fig. 5.17; Table 5.4 and Table 5.5). Thus, mixing of coexisting projectile melts and target melts is connected with element partitioning processes. As already described by Gibbons *et al.* (1976), Mittlefehldt *et al.* (2005) and Ebert *et al.* (2013, 2014) the partitioning behavior of each tracer element depends on their oxidation ability. Co, Ni, Fe, and Mo belong to the moderately siderophile, while Cr, V, and W are lithophile elements (Goldschmidt, 1937), yet Fe and W show affinities to more than one phase. Partitioning of these elements between silicate and metallic melts has been studied extensively in

laboratory experiments (e.g., Righter *et al.*, 2010 and references in there). The strong effect of the oxygen fugacity on the partitioning coefficients clearly indicate that Fe, Cr, V, Mo, Ni, Co and W are dissolved as oxides (FeO, Cr₂O₃, V₂O₃, MoO₃, CoO, NiO and WO₃) in the silicate melts (e.g., Schmitt *et al.*, 1989; Holzheid *et al.*, 1994). Comparing different experimental data sets Hiligren *et al.* (1994); Holzheid *et al.* (1994); Ohtani *et al.* (1997); Righter & Drake (1997, 1999); Righter *et al.* (2010) demonstrated that on a wide range of P, T, fO₂, and melt compositions the ability to form an oxide in the silicate melts is mainly: Cr ~ V > Fe >> W ~ Co >> Ni ~ Mo (from able to almost unable), corresponding to the increasing siderophile behavior of these elements. The experimental results, that Cr, V, and Fe partition preferentially into the silicate melt compared to Mo, W, Co, Ni, explain our observations within the sandstone melts.

5.5.2 Comparison with impactites from nature and impact experiments

5.5.2.1 Melting, mixing and phase formation processes

Before melting starts dehydration of the phyllosilicate-bearing matrix is the main modification of the sandstone target in our laser experiments (cp. Fig. 5.3 and Fig. 5.4). To our best knowledge, this low temperature effect was not described in detail in the context of low grade shock effects of natural impact events so far. However, post-shock temperatures are hemispherical distributed in an impact crater; from high temperatures at the direct point of the impact to low temperatures farther inside the crater. Therefore, it must be assumed that such a modification of phyllosilicates also occur in the low temperature zone of a natural impact crater. In the laser-induced melting experiments melting textures are revealed very similar to those of highly shocked targets: partly to completely fused quartz, partially to completely molten sandstone and mechanical injection of projectile matter (cp. Fig. 5.4 - Fig. 5.6). Impactites from the Kamil crater in Egypt, the Wabar craters in Saudi Arabia or the Meteor crater in Arizona show mixing of molten projectile spheres or schlieren of projectile matter (an iron meteorite in all cases) with shocked sedimentary target (Gibbons *et al.*, 1976; See *et al.*, 1998; Hörz *et al.*, 2002; Mittlefehldt *et al.*, 2005; Folco *et al.*, 2011; Hamann *et al.*, 2013), comparable to this study. See *et al.* (1998) investigated a dumbbell-shaped melt from the Wabar impact site. The glass derived from relatively homogenous dune sand target (Wynn & Shoemaker, 1998). See *et al.* (1998) clearly demonstrated via electron microprobe maps that the impact glass contains Fe and Ni of the projectile. Fe and Ni are heterogeneous distributed as schlieren in this melt. These schlieren are comparable with the schlieren of experiment LE-G and LE-H containing projectile-matter (Fig. 5.5b and Fig. 5.6a). In the thumb-bell-shaped Wabar melt no projectile droplets were observed, assuming that the metallic spheres were completely dissolved in the silicate melt. Hamann *et al.* (2013) observed complex mixing of IIIAB iron meteorite matter and highly siliceous target rocks in a sample of pristine Wabar impact glass. In contrary to the dumbbell-shaped melt from See *et al.* (1998), this impactite also contains target material in crystalline and glassy form. Hamann *et al.* (2013) showed that melting of the quartz starts at the margins and propagates inwards, which is in agreement to our laser-experiments, especially the quartz grains in zone 2 of LE-F (cp. chapter 5.2.2.1). In LE-G, LE-H and LE-I a small number of very tiny (< 2 μm) projectile droplets occur, which were injected into the target melt (Fig. 5.5b). High abundance of steel droplets as shown in Fig. 5.6d is very rare in the sandstone melt and limited to the near interface between steel

and sandstone. There can be two reasons for the less abundance of projectile droplets within the sandstone melt of the laser experiments: (i) lack of dynamic during irradiation and/or (ii) the droplets are mainly dissolved in the silicate melt due to very high temperatures (at least up to 1842°C, melting point of rutile). As mentioned before, characteristic features are the emulsions textures of the sandstone target melt in LE-G, LE-H and LE-I (cp. Fig. 5.6c and Fig. 5.11b). The emulsions contain at least three almost immiscible melts; *Lfe*, *Lsi* and metallic projectile droplets. In hypervelocity impact experiments with steel D290-1 and quartzite as target material exactly the same impressive examples for immiscibility of melts with strong chemical differences is observed (Ebert *et al.*, 2014). In this case liquid immiscibility domains are associated with/or in direct vicinity of *Lfe*, which forms a conspicuous rim or irregular shaped patches around certain projectile droplets. The completely fused Campo del Cielo meteorite (LE-I; Fig. 5.7b) can be considered as a huge projectile droplet which was in direct contact with the sandstone melt. At their interface an Fe enrichment zone was formed, in accordance with the observation from the impact experiments. Furthermore the *Lfe* of the highly shocked ejecta shows crystallization of dendritic domains associated with small Cr-V-rich and Fe-rich minerals (probably spinels). It is assumed that the tiny Cr-V-rich minerals which occur in the direct vicinity of the *Lfe* glass of our laser-experiments (cp. Fig. 5.9 and Fig. 5.10) are similar spinels. In comparison to these experimental data, the Wabar black melt is an emulsion of a Fe- and Ca-rich, poorly polymerized melt (*Lfe*) and a highly siliceous, highly polymerized melt (*Lsi*) plus occasionally dispersed FeNi spheres that resemble remnants of the projectile (Hamann *et al.*, 2013). These FeNi spheres are the system's Fe supply, which corresponds to the Fe supply from the molten steel and meteorite in the laser experiments. Folco *et al.* (2011) analyzed a pumiceous, siliceous glass derived from the impact melting of the target, which were associated with an Fe-Ni-rich glass, containing metallic droplets from the impactor. Unmixing of different silicate melts as described in our study, seems to be also a common phenomenon within the Fe-Ni-rich glass of Kamil crater, as recognizable in one of the figures of (Folco *et al.*, 2011). Thus, phase separation during quenching could play a major role in the formation of impactites that are the result of mixing iron meteorite matter with highly siliceous target rocks (Hamann *et al.*, 2013). The melt pockets shown in Fig. 5.7a seem to be a typical melting feature within partly fused iron meteorites. The same feature is observed in projectile fragments which are located in highly shocked ejecta fragments derived from impact experiments (Ebert *et al.*, 2013). Shock metamorphism caused complete melting of the rhabdites, schreibersites and some melting of the kamacite host crystal producing melt pockets. In this hypervelocity impact experiments, too, the melt in the pocket is separated into a P-rich melt in the center, and a P-poor melt at the rim. With regard to all these results, the laser induced melting experiments are a possibility to simulate the melting and quenching processes of impactites.

5.5.2.2 Chemical signature of the projectile

Hypervelocity impact experiments and natural impactites reveal several geochemical similarities with this study (Mittelfehldt *et al.*, 1992; Mittelfehldt *et al.*, 2005; D'Orazio *et al.*, 2011; Ebert *et al.*, 2013; Hamann *et al.*, 2013; Ebert *et al.*, 2014). Hamann *et al.* (2013) and D'Orazio *et al.* (2011) found out that impact melt material from Wabar and Kamil, respectively, are generally enriched in Fe over Ni compared to the Fe/Ni in the iron meteorite projectiles. Identical

chemical processes were observed in the highly shocked ejecta fragments from hypervelocity impact experiments using iron meteorite as projectile and sandstone as target (Ebert *et al.*, 2013). Figure 5.17 contains a comparison of Fe vs. Ni data from LE-I and the mentioned impact experiment of Ebert *et al.* (2013). In both cases Fe and Ni show more or less the same amounts of enrichment within the sandstone melt. Whereby the *Lfe-Lsi* emulsion composition mostly corresponds to the chemical signature of most of the sandstone data points Fig. 5.17. Pure *Lfe* (LE-I) clearly exceeds the Fe content of the impact produced target melt; Ni values are in the same range. Here again, the Fe/Ni completely differ from the Fe/Ni of the Campo del Cielo iron meteorite. Cr and Co enrichments within the produced silicate melts (LE-G and LE-H) show the same trends (Fig. 5.16) compared with the data set of impact experiments with steel D290-1 and Seeberger sandstone (Ebert *et al.*, 2013, 2014). The impact experiments reveal higher enrichments of Co and Cr, due to the fact that these elements are stronger "diluted" within sandstone melt of the laser experiments. Thus, the steel matter in LE-G and LE-H is effectively more mixed with molten silica and molten sandstone matrix. However in both experiment types, the Fe/Cr lies above the projectile ratio line due to the lithophile character of chromium and Fe/Co lies below the projectile ratio line due to the strong siderophile character of cobalt.

From Fig. 5.15 it is obvious that SiO₂ and FeO contents of Wabar black melt (Hamann *et al.*, 2013) and contaminated sandstone melt of LE-I are highly variable, but more or less in comparable ranges. The Wabar black melt values plots somewhat above the LE-I sandstone melt, shown as solid lined field in the same figure. The SiO₂ values of the Wabar black melt are slightly higher compared to LE-I Fig. 5.15; this is probably due to differing bulk composition of the two targets. Furthermore, due to a low melting grade of the sandstone below the molten Campo del Cielo meteorite piece in LE-I (see Fig. 5.8), only a small number of quartz grains provide SiO₂ for the sandstone melt. Consequently, the meteoritic Fe is only slightly mingled within this silicate melt; this explained the high FeO values of *Lfe* in LE-I (Fig. 5.5), which are partially higher than the *Lfe* values from the Wabar impactite.

5.6 Conclusions

With regard to the title of this work "Are laser-induced melting experiments suitable to simulate meteorite impact processes?" it should be mentioned that the laser-induced melting experiments do not reproduce hypervelocity impact process phenomena like shock effects (e.g., PDF in quartz), but they can be definitely used to simulate high-temperature effects of an impact mainly for the investigations of geochemical processes. The method was able to produce characteristic temperatures of impact-induced melting, which can reach several thousand degrees Celsius (1842 °C indicated by molten rutile). The laser experiments produce melting textures very similar to those of impactites from impact craters and impact experiments: formation of lechatelierite, partially to completely molten sandstone and incorporation of projectile matter. Thus, experimental can be used to analyze the melting phenomena of a target material. The associated dynamic mixing of large projectile melt droplets, which we know from natural impactites, is partly missing. A modification of the experimental setup, for example by putting the projectile and sandstone on top of each other and reducing the thickness of the projectile may fix this problem. However, element partitioning processes, which are well known from hypervelocity

impacts, could observe in our laser experiments. This includes incorporation of projectile tracer elements into the sandstone melts and the phase separation of silicate melts (liquid immiscibility) during quenching. The degree of this element enrichment is mainly controlled by the lithophile or siderophile character of the respective tracer element. The different geochemical behavior of the tracer elements leads to element ratios in the target melts, which differ strongly from the respective element ratios of the projectile.

5.A Tables of chapter 5.

Table 5.1: Experimental conditions

Name	Target material	Projectile material	Laser power	Duration of irradiation	Laser point diameter
<i>LE-F</i>	Seeberger sandstone	No projectile	2.5 kW	0.5 s (point)	5 mm
<i>LE-G</i>	Seeberger sandstone	D290-1 (Steel)	2 kW	1 cm*s ⁻¹ (line)	1 mm
<i>LE-H</i>	Seeberger sandstone	D290-1 (Steel)	2 kW	1 cm*s ⁻¹ (line)	1 mm
<i>LE-I</i>	Seeberger sandstone	Campo del Cielo (Iron meteorite)	2 kW	1 cm*s ⁻¹ (line)	1 mm

Table 5.2: EMP measurement conditions for various phases

Element	Standard	X-ray	Crystal	Peak P.	Peak (s)		BG (s)		D.L. (ppm)		Dia. (μ m)		Acc. Vol. (kV)		Pr. current (nA)	
					S	M	S	M	S	M	S	M	S	M		
	Same conditions for S, M				S	M	S	M	S	M	S	M	S	M	S	M
Si	Quartz	K α	TAP	77.33	40	40	20	20	290	100	5	1	20	15	60	30
Al	Albite	K α	TAP	90.627	40	-	20	-	250	-	5	-	20	-	60	-
Fe	elem. Fe	K α	LIF	134.6	40	40	20	20	260	500	5	1	20	15	60	30
Mg	Augite	K α	TAP	107.51	40	-	20	-	240	-	5	-	20	-	60	-
K	Sanidine	K α	PETJ	119.79	40	-	20	-	350	-	5	-	20	-	60	-
Ti	Titanite	K α	PETJ	87.866	40	-	20	-	600	-	5	-	20	-	60	-
V	elem. V	K α	LIFH	174.1	40	40	20	20	250	250	5	1	20	15	60	30
Co	elem. Co	K α	LIFH	124.55	60	40	30	20	140	450	5	1	20	15	60	30
Ni	Elem. Ni	K α	LIFH	115.23	60	40	30	20	180	350	5	1	20	15	60	30
Cr	elem. Cr	K α	PETJ	73.273	60	40	30	20	200	240	5	1	20	15	60	30
Mo	elem. Mo	L α	PETH	173.09	60	40	30	20	300	230	5	1	20	15	60	30
W	elem. W	L α	LIFH	102.13	60	40	30	20	770	280	5	1	20	15	60	30

P₂O₅, SO₂ are generally below the detection limit; S - silicate phases, M - metallic phases. elem. - elemental; D.L. - detection limit; Pos. - position; Acc. - acceleration.

Table 5.3: Microprobe data (selection) of the pure sandstone melts

Oxide in wt.%	Al ₂ O ₃	FeO	K ₂ O	MgO	SiO ₂	TiO ₂	Total
<i>Sandstone melt (LE-F)</i>							
LE-F-SM-01	29.26	5.49	4.04	2.672	56.48	1.04	98.99
LE-F-SM-02	32.68	3.55	2.51	1.591	58.72	0.34	99.4
LE-F-SM-03	23.64	8.75	2.54	2.4	61.48	0.31	99.13
LE-F-SM-04	30.29	3.09	0.92	1.33	64.22	0.29	100.2
LE-F-SM-05	25.99	2.44	0.79	1.09	69.27	0.42	100
LE-F-SM-06	21.66	1.37	0.73	0.53	71.82	1.73	97.85
LE-F-SM-07	15.17	0.71	1.06	0.44	82.48	0.68	100.6
LE-F-SM-08	5.27	0.37	0.27	0.14	92.39	0.81	99.28
LE-F-SM-09	2.47	0.17	0.15	0.08	96.27	0.15	99.3
LE-F-SM-10	1.33	0.09	0.09	0.06	97.81	0.08	99.46
<i>Sandstone melt with Ti supply (LE-F)</i>							
LE-F-SM-Ti-01	36.33	1.74	2.77	0.75	57.68	1.97	101.22
LE-F-SM-Ti-02	31.57	1.81	2.92	0.75	62.09	1.16	100.29
LE-F-SM-Ti-03	9.063	0.77	0.61	0.24	66.15	23.12	100.03
LE-F-SM-Ti-04	23.94	2.52	0.88	0.95	66.35	5.62	100.27
LE-F-SM-Ti-05	22.39	1.94	0.79	0.84	70.91	1.96	98.82
LE-F-SM-Ti-06	10.12	2.33	1.03	0.77	73.32	11.48	99.06
LE-F-SM-Ti-07	20.63	1.59	0.83	0.7	74.21	1.43	99.41
LE-F-SM-Ti-08	9.15	2.17	1.02	0.77	74.34	11.6	99.05
LE-F-SM-Ti-09	7.47	1.52	0.67	0.33	84.35	3.83	98.17
LE-F-SM-Ti-10	6.39	1.19	0.64	0.28	88.72	1.93	99.15

Na₂O, MnO, P₂O₅, SO₂ are below the detection limit

Table 5.4: Microprobe data of the contaminated sandstone melt, *Lfe* and *Lsi* (LE-G, LE-H)

Oxide in wt.%	SiO ₂	Al ₂ O ₃	TiO ₂	MgO	K ₂ O	FeO	Cr ₂ O ₃	V ₂ O ₃	CoO	MoO ₃	WO ₃	Total
LE-G-SM-01	91.62	5.77	0.61	n.a.	0.21	0.59	0.06	b.d.l	b.d.l	b.d.l	b.d.l	98.86
LE-G-SM-02	89.43	6.48	0.37	n.a.	0.5	0.82	0.3	0.12	b.d.l	b.d.l	b.d.l	98.02
LE-G-SM-03	87.21	4.96	1.26	n.a.	0.25	2.32	0.9	0.49	0.01	b.d.l	b.d.l	97.41
LE-G-SM-04	88.55	3.53	0.88	n.a.	0.18	2.69	1.21	0.85	0.02	b.d.l	b.d.l	97.92
LE-G-SM-05	90.53	2.72	0.53	n.a.	0.22	1.91	1.47	1.16	b.d.l	b.d.l	b.d.l	98.54
LE-G-SM-06	86.28	4.01	0.61	n.a.	0.27	2.86	2.35	1.73	b.d.l	b.d.l	b.d.l	98.1
LE-G-SM-07*	84.13	2.61	0.6	n.a.	0.24	3.81	3.39	2.72	0.02	b.d.l	b.d.l	97.51
LE-G-SM-08*	80.82	4.26	0.63	n.a.	0.22	4.41	4.13	3.47	b.d.l	b.d.l	b.d.l	97.92
LE-G- <i>Lfe</i> -01	32.9	4.23	0.48	0.71	0.44	52.23	0.28	0.21	0.71	0.21	5.23	97.63
LE-G- <i>Lfe</i> -02	35.23	3.89	0.51	0.43	0.37	51.88	0.13	0.08	0.65	0.16	4.93	98.26
LE-G- <i>Lfe</i> -03	33.71	2.56	0.12	0.39	0.22	54.18	0.24	0.13	0.57	0.08	4.21	96.41
LE-G- <i>Lsi</i> -01	91.88	4.04	0.18	0.21	0.34	1.23	0.04	0.03	b.d.l	b.d.l	b.d.l	97.95
LE-G- <i>Lsi</i> -02	93.12	3.57	0.25	0.32	0.44	2.03	0.02	b.d.l	b.d.l	b.d.l	b.d.l	99.75
LE-H-SM-01	95.47	1.16	0.24	0.01	0.45	1.26	0.09	0.08	0.05	b.d.l	b.d.l	98.82
LE-H-SM-02	72.03	9.13	0.83	0.37	0.22	14.97	0.79	0.87	0.57	b.d.l	b.d.l	99.78
LE-H-SM-03	86.5	9.57	1.03	0.34	0.39	0.91	0.04	0.07	0.02	b.d.l	b.d.l	98.84
LE-H-SM-04	81.41	8.24	1.13	0.26	0.36	6.46	0.44	0.4	0.05	b.d.l	b.d.l	98.74
LE-H-SM-05	74.69	9.26	1.17	0.37	0.3	11.96	0.82	0.85	0.07	b.d.l	b.d.l	99.32
LE-H-SM-06	85.96	7.71	0.45	0.22	0.36	3.97	0.28	0.16	0.02	b.d.l	b.d.l	99.12
LE-H-SM-07	73.37	9.53	1.08	0.41	0.21	13.33	0.94	1.02	0.08	b.d.l	b.d.l	99.88
LE-H-SM-08	83.12	8.45	1.11	0.24	0.37	4.47	0.33	0.24	0.02	b.d.l	b.d.l	98.35

CaO generally below detection limit; n.a. - not analyzed; b.d.l. - below detection limit

Table 5.5: Microprobe data (selection) of the contaminated silicate melts (LE-I)

Oxide in wt.%	SiO ₂	Al ₂ O ₃	TiO ₂	MgO	K ₂ O	FeO	NiO	Total
<i>Sandstone melt</i>								
LE-I-SM-1	69.798	9.896	5.309	0.193	0.266	11.295	0.029	96.786
LE-I-SM-2	68.384	15.672	2.428	0.636	0.886	11.508	0.016	99.530
LE-I-SM-3	83.621	4.546	2.397	0.072	0.196	6.275	0.013	97.110
LE-I-SM-4	87.062	3.310	1.949	0.055	0.183	5.048	0.012	97.619
LE-I-SM-5	93.766	1.275	0.913	0.013	0.122	2.035	b.d.l.	98.127
<i>Lfe+Lsi emulsions</i>								
LE-I-Emuls-1	54.442	13.557	2.376	0.187	0.250	26.349	0.016	97.177
LE-I-Emuls-2	58.635	12.931	1.370	0.166	0.278	23.838	0.016	97.234
LE-I-Emuls-3	49.289	11.659	4.674	0.933	0.425	29.028	0.014	96.022
LE-I-Emuls-4	59.973	7.667	2.106	0.242	0.412	27.596	0.092	98.088
LE-I-Emuls-5	62.301	8.197	2.029	0.235	0.410	27.284	0.090	100.546
<i>Lfe</i>								
LE-I- <i>Lfe</i> -1	45.094	8.438	1.939	0.088	0.331	43.777	0.035	99.702
LE-I- <i>Lfe</i> -2	43.227	8.406	1.156	0.110	0.198	45.032	0.050	98.179
LE-I- <i>Lfe</i> -3	38.239	7.168	1.383	0.070	0.063	50.971	0.024	97.918
LE-I- <i>Lfe</i> -4	38.781	6.099	1.415	0.082	0.065	51.236	0.029	97.707
LE-I- <i>Lfe</i> -5	49.821	4.055	0.887	0.151	0.045	46.300	0.032	101.291
LE-I- <i>Lfe</i> -6	42.415	8.438	0.519	0.125	0.094	48.577	0.016	100.184

P₂O₅, SO₂ are generally below the detection limit; b.d.l. - below detection limit

6 Application to natural impactites

6.1 Projectile-target interaction

Kenkmann *et al.* (2013) investigated deformation and melting features on steel projectile in different MEMIN hypervelocity impact experiments. In contrast to the highly-shocked and projectile rich ejecta which was described in detail in chapter 2 and 3, in Kenkmann *et al.* (2013) the analyses was concentrated on the main masses of projectile relics. The masses of these recovered relics (found on the chamber floor, not in the ejecta catcher) ranged between 58 % and 92 % of their initial projectile weight. A significant trend between impact energy, water saturation of the sandstone target and the mass of projectile relics could not be found. Intensified fragmentation is suggested in the experiments with wet targets. The projectile relics have the shape of a deformed bowl with a convex outer an irregularly formed concave inner side, and a knobby region in the inner side (cp. Fig. 6.1a-c). The intense deformation of the projectiles during the impact process is already described in Fig. 3.12 on page 51. The projectile relict of experiment 3232 (MEMIN pilot study) was centered cut in two pieces, in order to investigate its cross-section by means of SEM (Fig. 6.1c). Besides the bowl shaped geometry, most conspicuous are the shocked sandstone material which occurs on the front and rear side of the fragment (white material in Fig. 6.1a and gray material in BSE image Fig. 6.1c). Especially, the thin silicate layer on the front side shows the formation of PDF in quartz, partial melting of the sandstone, and melting and mixing of projectile droplets. As mention before, the area at the direct interface between projectile and target can be considered as source region of the highly-shocked an projectile-rich ejecta. This composite of projectile and target material is known from natural impact crater. In 2008 D’Orazio *et al.* (2011) discovered the relatively young (< 5000 a) and small (~45 m) Kamil meteorite crater in South Egypt. The Kamil crater was formed by impacting of the Gebil Kamil iron meteorite into a mainly quartz-arenite (sandstone) target, which clearly allows a direct comparison with the present study. Some of the meteorite shrapnels, which D’Orazio *et al.* (2011) found in the crater area, had a peculiar lithic material stuck to the surfaces (Fig. 6.1d, e). The material on the Kamil shrapnels is composed of an aggregate of quartz-arenite clasts, loose quartz crystals, and Fe-Ni metal spherules set in a heterogeneous matrix of very fine-grained quartz, vesicular brown to colorless glass. Thus, the MEMIN experiments show exactly the same feature on the recovered projectiles. D’Orazio *et al.* (2011) suggested a swarm of Gebil Kamil fragments was associated with a dense, hot spray of molten projectile and target material. A further explanation, can be assumed from our laboratory experiments that the coatings on the Kamil meteorite debris may also represent the direct contact zone during the impact. D’Orazio *et al.* (2011) indicates higher Ni/Fe of projectile droplets within the produced glass coating compared to the Ni/Fe of the bulk Gebil Kamil. The results of the MEMIN hypervelocity impact experiments (chapter 2 and 3) have shown that such a modification of the bulk projectile chemistry is linked to a selective Fe partitioning process, which occurs from the molten droplet into the silicate target melt. This clearly explains the relatively high FeO content (approximately 29 wt.%) of the brownish Kamil glass (D’Orazio *et al.*, 2011) and is additionally more or less in the same range of FeO values (mean 24.94 wt.% FeO, cp. Table 2.3 on page 30), which was observed in the MEMIN experiments

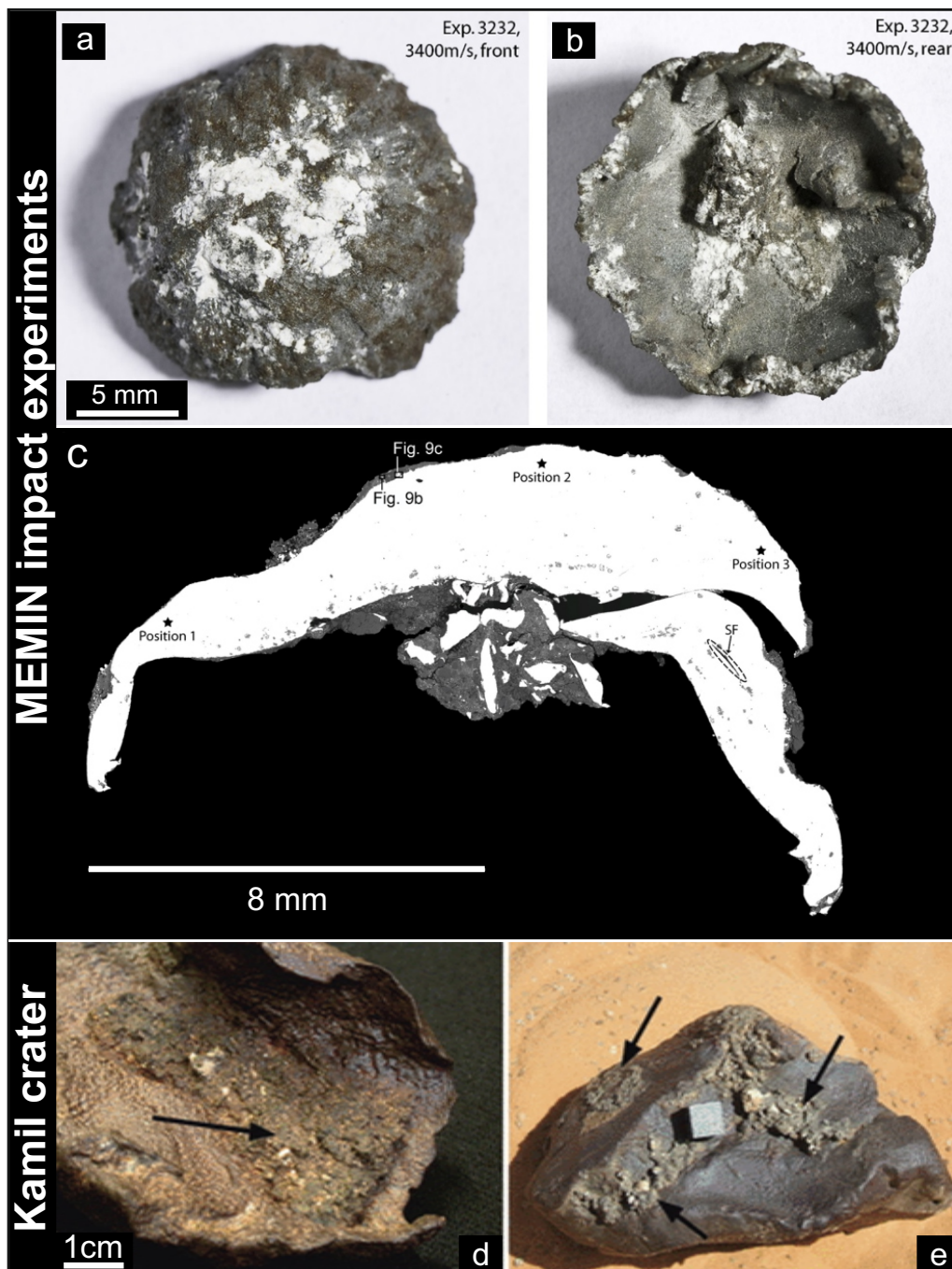


Figure 6.1: (a) Front and (b) rear of the steel projectile relic of MEMIN experiment 3232 (from Kenkmann *et al.*, 2013); (c) 172 stitched BSE images display a cross-section of the projectile relict 3232. Note the thin shocked sandstone layer at the outer rim and inner rim of the sample (from Kenkmann *et al.*, 2013); the labeling of (c) refers to the original paper and is not relevant for this chapter; (d) and (e) photographs of Kamil target rock material stuck onto the surfaces of some Gebil Kamil shrapnels (modified from Fig. 12 in Folco *et al.*, 2011)

with the Campo del Cielo iron meteorite as projectile. Besides the mentioned shrapnels of the Kamil crater Folco *et al.* (2011) collected ejected impact glass samples in the vicinity of the crater. These impactites are defined by a heterogeneous mixing of siliceous (white) and Fe-Ni-rich (dark) glasses, deriving from melting of target and projectile (Fig. 6.2a). The mm- to decimeter-sized Kamil impact glasses looks identical compared to the mm-sized highly-shocked

and projectile-rich ejecta fragments of the MEMIN study (cp. Fig. 6.2a and Fig. 2.3a). BSE images of the Kamil glass show textural relations between melt with very different chemical composition (see Fig. 6.2b modified from Folco *et al.*, 2011). Although the authors distinguished between Fe-Ni-droplets, Fe-rich silicate melt and Si-rich silicate melt; unfortunately they represent no further detailed chemical analyses of the melts. However, the experiences with the small scale geochemical processes of the MEMIN experiments allow further interpretation of the BSE image in Fig. 6.2b and the unmixing/ mixing process during impact of the Kamil crater.

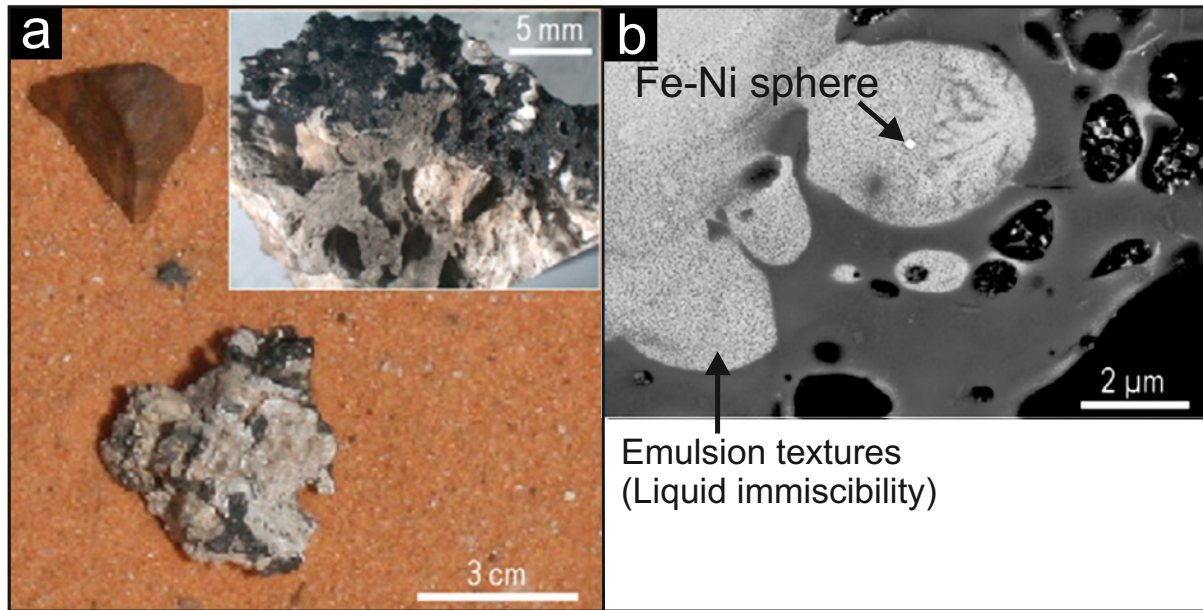


Figure 6.2: (a) Pumiceous impact glass found scattered in ejecta blanket of the Kamil crater (modified from Folco *et al.*, 2011); (b) Textural relationships between siliceous (dark) and Fe-rich (bright) impact glass (modified from Folco *et al.*, 2011), note the emulsion textures which indicate liquid immiscibility of Si-rich and Fe-rich melts.

During cooling the of Kamil impact melt, which were enriched in meteoritic iron from the projectile droplets, the melt separated into two melts with strong compositional differences by immiscibility. That's why the light gray melt in Fig. 6.2b shows emulsion textures. The phenomenon of liquid immiscibility was described in detail within the Wabar impactite (Hamann *et al.*, 2013). The study included petrography and microchemistry of impact glasses from the Wabar impact craters (Saudi Arabia) that are amongst the youngest terrestrial impact craters (290 ± 38 a Prescott *et al.*, 2004); thus pristine material is available. Like the Kamil crater, the Wabar craters enable direct comparisons with the MEMIN experiments, since an iron meteorite penetrated into a quartz-rich target (dune sand). Electron microprobe investigations of the Wabar glass showed complex mixing of IIIAB iron meteorite matter and highly siliceous target rocks. It is suggested that during the cratering process of the Wabar craters, metallic projectile melt has mechanically entered the target melt at various proportions, thereby preferentially partitioning meteoritic iron into the highly siliceous target melt, through the mechanism of selective oxidation (Gibbons *et al.*, 1976; Hamann *et al.*, 2013; Ebert *et al.*, 2013). Quenching of the projectile-target mixture induced silicate liquid immiscibility and caused phase-separation and formation of an emulsion of a poorly polymerized, ultrabasic melt (*Lfe*) rich in divalent cations

like Fe^{2+} , Ca^{2+} , or Mg^{2+} , that is dispersed in a compositionally dominant, highly polymerized, high-silica melt (*Lsi*) matrix (Hamann *et al.*, 2013). The typical Wabar melt emulsion displays a spheres-in-a-matrix texture of $\sim 10\text{-}20\%$ *Lfe* homogeneously dispersed in the form of two sets of spheres and droplets (10-30 nm and 0.1-0.4 μm in diameter) in $\sim 80\text{-}90\%$ *Lsi* matrix, plus occasionally disseminated FeNi spheres (cp. Fig. 6.3a). This change of texture can be interpreted as evidence of the transfer process of meteoritic iron from the meteoritic FeNi spheres into the target melt.

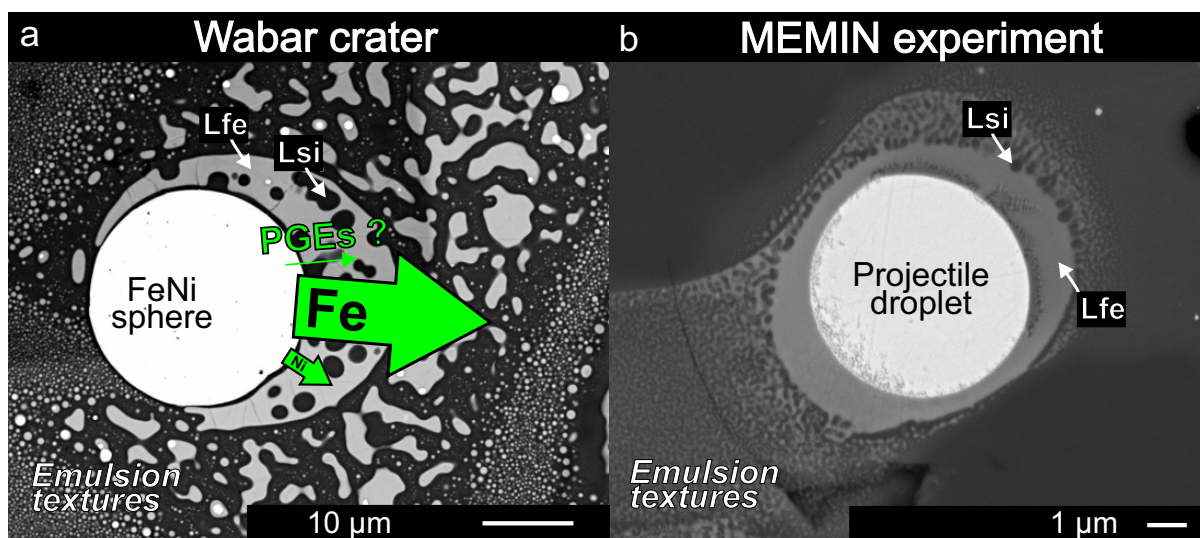


Figure 6.3: Comparison of unmixing features between experiment and nature. (a) BSE images of typical features in Wabar impact melt. Emulsion structure (corona) around large FeNi sphere. Note the gradual coarsening of *Lfe* spheres in direction to the large FeNi sphere (modified from Hamann *et al.*, 2013). The meaning of the green arrows is discussed in the text of this chapter; (b) BSE image of a highly shocked ejecta from a MEMIN experiments (A20-5339) with iron enrichment zone around steel projectile droplet with subsequent unmixing into Fe-rich (*Lfe*) and Si-rich (*Lsi*) silicate melts.

The same intense transfer of Fe from the projectile into the silicate target and the quench-induced phase separation could be observed in the present study (e.g., Fig. 6.3). Liquid immiscibility emphasized by emulsion textures occur on the nano-meter scale in the hypervelocity impact experiments with sandstone targets (Fig. 3.3 on page 38) and on the micrometer scale in the experiments with quartzite targets (Fig. 3.4 on page 40). Single phase liquids rapidly cooled from a stable two-liquid field showed liquid immiscibility which is interpreted to be metastable because the droplet size is quench-rate dependent (Freestone & Powell, 1983). Consequently different quenching times can be estimated qualitatively by comparing the individual liquid sizes within respective impact material; from short to "long" time: impact experiments with sandstone < impact experiments with quartzite < Kamil impact glass < Wabar impact glass.

6.2 Application of experimental results to nature

The MEMIN experiments and the analyses of the Wabar impact glass (Hamann *et al.*, 2013), clearly showed that the projectile droplets lose iron and size (cp. Fig. 2.9) during their movement

through the silicate target melt. These spheres became more and more enriched in Ni and Co (as well as enriched in Mo and W in the experiment with steel) in accordance to previous studies by Gibbons *et al.* (1976). This inter-element fractionation can be explained by differing siderophile characters or different reactivity of these elements with oxygen. However, as indicated by electron microprobe analyses of the Wabar glass (Hamann *et al.*, 2013) or the ejecta of this study (chapter 2 and 3) the target melts are also slightly enriched by siderophile elements. Figure 6.4 shows the chemical data of six projectile droplets (projectile type 2, cp. Fig. 6.3b, quartzite experiments) normalized to the steel D290-1 bulk composition and plotted against the lithophile (Cr, V) and increasing siderophile (Fe, W, Co, Mo; adopted from Hiligren *et al.*, 1994) character of the projectile tracer elements. The lithophile elements Cr and V are preferentially partitioned from the projectile melt droplets into the surrounding silicate melt, resulting in a spherule/D290-1 ratio which is below 1 (Fig. 6.4). As mentioned before the ability of the siderophile elements to form oxides in the silicate target melts is a function of its siderophile character. It can be said that the spherule/D290-1 ratio of a specific tracer element increases with increasing siderophile behavior. E.g., Mo has the most siderophile behavior and thus shows the most obvious enrichment in the projectile droplets (Fig. 6.4). Metallic spherules from the Meteor crater allows a direct comparison with the experimental data of the MEMIN experiment. Mittlefehldt *et al.* (2005) determined trace element concentration of ballistically dispersed metallic spherules from Meteor crater (USA, Arizona) by the mean of instrumental neutron activation analysis (INAA). Figure 6.5 shows the ratios between the chemical data of the original Canyon Diablo meteorite (data taken from Wasson & Kallemeyn, 2002) and Ni, Co, Ir (PGE) and Fe data of six metallic impact spherules from the Meteor crater (Mittlefehldt *et al.*, 2005). As indicated by Fig. 6.5 all elements are enriched over Fe in the spherules compared to the original bulk Canyon Diablo meteorite. In comparison Co has a weaker siderophile character than Ni, explaining the lower enrichment of Co in the Meteor crater droplets. This is in agreement with the different enrichment of these elements in the experimental droplets, emphasized as dotted and dashed line with positive slope in Fig. 6.5. These regression lines, named "Spherules/D290-2" and "Spherules/Campo del Cielo", are calculated from the droplet data of Table 2.4 and Table 2.6. However, what happened with the strongly siderophile platinum group elements? This question is indicated by the green arrows in Fig. 6.3a. Besides the inter-

element ratios of moderately siderophile elements (Ni, Co; see Fig. 6.4), the ratios of the PGE may have been also modified during projectile-target interaction. Mittlefehldt *et al.* (2005) assumed selective oxidation as mechanism for the chemical modification of the projectile melt droplets from the Meteor crater, which occurs during flight through air. As already mentioned the intensity of the respective element enrichment depends the reactivity with oxygen. Therefore Ir, which is the most siderophile element compared to the other elements, shows the strongest enrichment; especially in spherule 5 (Fig. 6.5). In order to emphasize this dependency the regression line of the Meteor crater projectile droplets is shown in Fig. 6.5, which clearly has a positive correlation. Unfortunately no other PGE data is given for the metallic spherules from the Meteor crater. However, it must be assumed that selective oxidation also changes the inter-element ratios of all PGE in the metallic spherules compared to the iron meteorite bulk. In case of a large meteorite impact such modification of the element ratios may distort the originally

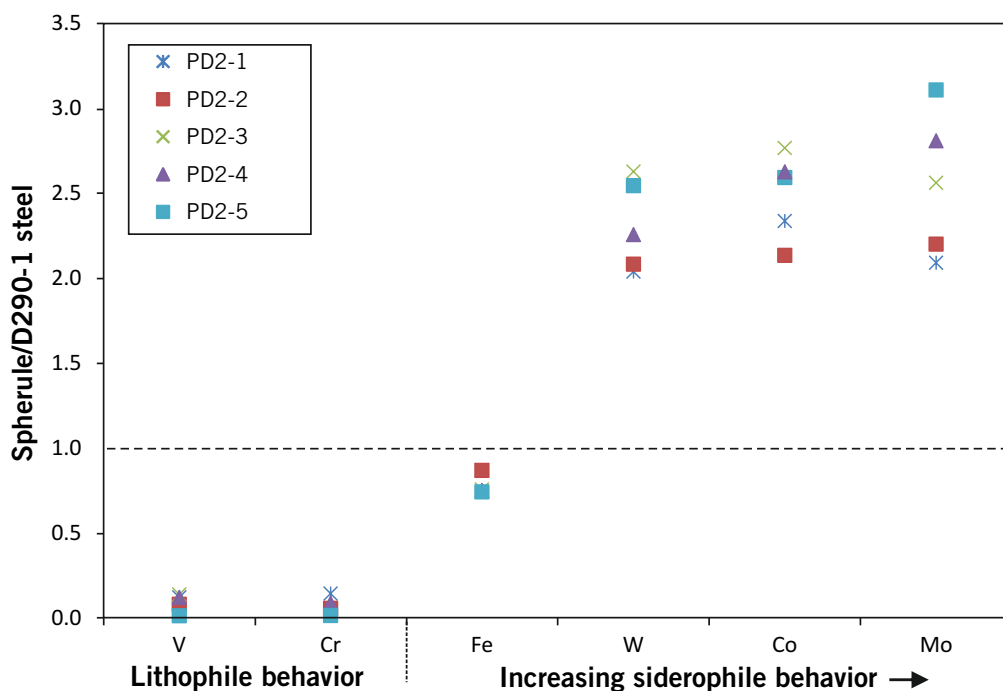


Figure 6.4: Chemical data of projectile droplets (projectile type 2; quartzite experiments) normalized to the steel D290-1 bulk composition plotted against the lithophile (Cr,V) and increasing siderophile (Fe, W, Co, Mo) character of the projectile tracer elements.

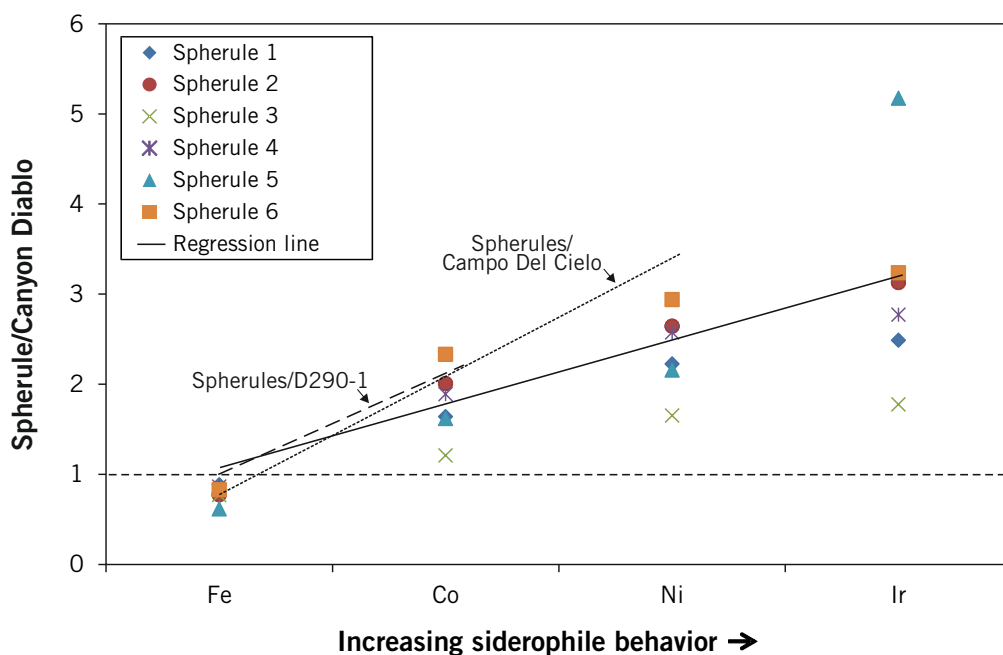


Figure 6.5: Plot shows a comparison between the chemical data of the original Canyon Diablo meteorite (data taken from Wasson & Kallemeyn, 2002) and Fe, Ni, Co, and Ir (PGE) data of six impact spherules from the Meteor crater (Mittlefehldt *et al.*, 2005) depending on the increasing siderophile character of the elements; for detailed explanation see text.

signature of the impactor. This is important to understand impact-related fractionation of PGE which are commonly used to identify the projectile in terrestrial craters. There are no investigations which deals with the PGE analyses of incorporated projectile droplets.

7 Summary and general conclusions

In the following chapter, the key results are briefly summarized with regard to the 3 main objectives (cp. chapter 1) of this experimental work.

1. Small scale mechanical and geochemical mixing processes of projectile matter and target melts in impactites:

- The performed hypervelocity impact experiments enabled a simulation of natural meteorite impact processes. As evidence for this, the sandstone and quartzite ejecta show various shock-metamorphic features including multiple sets of PDF in quartz, the onset to complete transformation of Qtz to silica glass, and partial melting of the targets. The melting is concentrated in the phyllosilicate-bearing matrix of the sandstone and quartzite, but involves quartz grains, too.
- This work has documented in detail the complex process of mechanical and chemical mixing of projectile and target materials during hypervelocity impacts. Most prominent is the injection of projectile melt droplets into target melts. In general two coexisting but largely immiscible melts exist in the highly shocked sandstone and quartzite ejecta fragments. During the impact process projectile droplets were only incorporated into the sandstone and quartzite target melts; and not into molten silica glasses. The sandstone (quartzite) melt was formed due to melting of the phyllosilicate-bearing matrix. Thus, this study emphasize the importance of H₂O bearing phases (phyllosilicate-bearing matrix in both sandstone and quartzite) during impact melting, or in more general terms, the significant influence of minor components in silicate rich targets on geochemical exchange processes.
- Hypervelocity impact experiments are expensive and elaborate; only few shots are possible. Due to the small amount of usable material and the tiny phases within highly shocked ejecta produced in these experiments, electron microscopic analysis are challenges. High temperatures are required for melting, mixing and element partition processes. Thus, the laser experiments are ideally suited in order to produce and analyze target and projectile melts and a mixture of them under more idealized conditions. The laser-induced melting experiments can be used to simulate low- to high-temperature effects of an impact. Melting textures were produced very similar to those of impactites from impact craters and impact experiments: e.g., formation of lechatelierite, partially to completely molten sandstone. Due to the high energetic laser beam several thousand degrees Celsius were reached; indicated by molten rutile ~ 1842 °C. Most interesting were the dehydration of the phyllosilicates within the sandstone matrix, which was the precursor of melting. Low temperature dehydration could not be observed in the impact experiments.
- Projectile matter were also incorporated as chemical signature and very tiny droplets into the sandstone target melt of the laser experiments. Nevertheless, the associated dynamic

mixing of *large* projectile melt droplets, which is known from natural impactites, is partly missing. A modification of the experimental setup, for example by putting the projectile and sandstone on top of each other and reducing the thickness of the projectile may fix this problem.

- Significant inter-element fractionation occurs during mixing of projectile and target material (in both experiment types). The silica-rich target melts are strongly enriched in the projectile tracer elements Cr, V, and Fe but have just minor enrichment of Co, Ni, W, and Mo. The degree of this element enrichment is mainly controlled by the lithophile or siderophile character of the respective tracer element. Thus, the fractionation results from differences in the reactivity of the respective elements with oxygen during interaction of metal melt with silicate melt. The different geochemical behavior of the tracer elements leads to element ratios in the target melts, which differ strongly from the respective element ratios of the projectile. In this situation a determination of the projectile type via trace element ratios in terrestrial impactites would cause problems and lead to erroneous results, if inter-element fractionation occurred, as already noted by Attrep *et al.* (1991) and Mittelfehldt *et al.* (1992). In accordance with these authors caution is recommended in assigning specific projectile types without detailed knowledge about these fractionation processes.

2. Parameters that control inter-element fractionation between siderophile elements of the impactor during penetrating silicate-dominated targets:

- The geochemical results are similar for hypervelocity impact experiments at low impact energy and with dry target as well as at high impact energy and with water-saturated target. It follows that the degree of water-saturation in the target materials and impact energy obviously do not affect the described geochemical processes, at least at the scale of our hypervelocity impact experiments. On the other hand, partitioning of the projectile tracer elements Cr, V, Fe, Co, Mo, and W into the silicate target melt is intensified in experiments with a non-porous quartzite compared the porous sandstone target. This is mainly the result of higher shock pressure and the related higher shock and post-shock temperatures.
- The intensified partitioning processes in impact experiments with quartzite as target material lead to the formation of an Fe enrichment zone surrounding projectile droplets. During quenching further phase formation processes occurred within the iron enrichment zone : (i) crystallization of dendritic domains associated with small Cr-V-rich and Fe-rich minerals, and (ii) unmixing of the target melt. This liquid immiscibility occurs between melts with strong chemical differences and forms conspicuous emulsion textures. The incorporation of steel and iron meteorite matter into sandstone melt in LE-G, LE-H and LE-I is also accompanied by phase separation of iron rich and silica rich melts. In addition, we recently described this feature in the impact glass of the Wabar crater (Hamann *et al.*, 2013). Thus, partitioning of projectile elements into target melts and associated liquid immiscibility seem to be common features during mixing of projectile and target melts.

- The laser experiments easily reach several thousand degree Celsius in the target, which initiates melting of the projectile and target. In contrast, melting of the projectile, in particular the formation of melt droplets, cannot be exclusively explained by the (calculated) initial shock pressure and high post-shock temperatures in the discussed impact experiments. Therefore, as result of the cooperation with other MEMIN group researcher three mechanisms for enhanced thermal input are suggested: 1) friction and deformation (i.e., plastic work) of the projectile, 2) more effective transfer of kinetic energy to porous material (in case of the sandstone) including the local increase of shock pressure due to pore collapse, and 3) heat transfer from shock compressed air during projectile flight (projectile pre-heating). This conclusions included results from different members and sub-projects of the MEMIN group (Kenkmann *et al.*, 2007; Gldemeister *et al.*, 2013; Ebert *et al.*, 2013).

3. Spatial dissemination of projectile material in the ejecta curtain during the excavation of the crater:

- The technical setup of the hypervelocity impact experiments, especially the new designed ejecta catcher, has provided that the main part of the ejected material could be collected and used for detailed distribution analyses.
- The ejecta distribution clearly showed that the highly shocked and projectile-rich ejecta is mainly distributed between angles of 70° and 80° in the impact experiments with dry sandstone targets and steel as well as iron meteorite as projectile.
- The projectile-rich ejecta is mainly ejected in a steep angel compared to the impact angle. This result is important for two reasons: (i) During a terrestrial impact the projectile can partly survive the formation of a small (or even a mid-sized) crater, but erosion processes over long periods of time leading to loss most or even all of this material. Thus, impact experiments provide information about the projectile distribution during the crater formation, an information which is no longer present in nature. (ii) Furthermore, this result may can be helpful for testing the applicability of new numerical models, which include simulating the fate of the projectile during an impact process.

8 Outlook and open questions

- Traces of "projectile elements" have been detected with EMP in thin sections of ejecta fragments in shocked quartz (silica glass and Qtz with PDF; cp. chapter 2.2.3 on page 20). The average projectile element ratio of these shocked SiO_2 phases lies close to the ratio for the original projectile. This result is unusual, and rather unexpected. In order to excluded superficial contamination of the quartz by matter from adjacent projectile droplets as well as partly fused projectile fragments during, 2 silica glasses and one PDF-bearing Qtz were prepared with FIB. On an area of $\sim 40 \mu\text{m}^2$ these shocked quartz grains were "polished" with the ion beam over ~ 24 hours. $1.5 \mu\text{m}$ of the surface were ablated (Fig. 8.1). Microprobe measurements before and after the FIB preparation show more or less identical element enrichment. However, to fully exclude surficial contamination processes femto-second LA-ICP-MS measurements should be planned for the future. In case that these enrichment are actually present, it would be a highly interesting topic to find a comparable chemical signature in naturally shocked quartz grains. If shocked quartz grains really incorporate meteoritic elements in the same element ratio as the projectile, they could provide information about the impactor type. Impactites from the Wabar craters, Kamil crater or Meteor crater would be good candidates to test this observation.

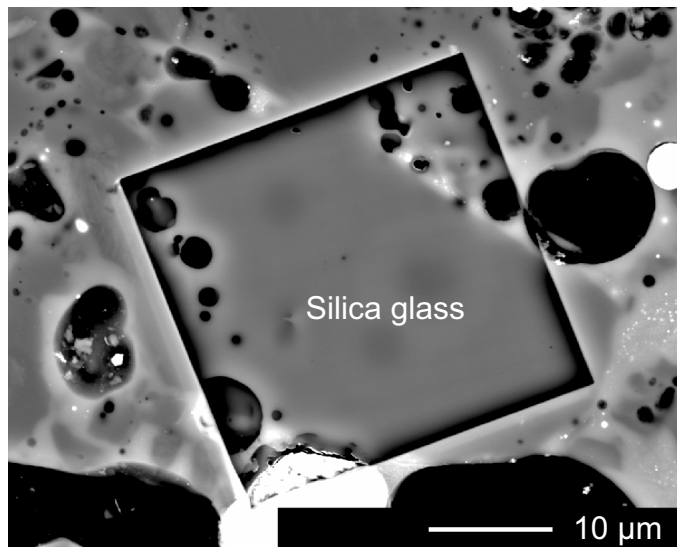


Figure 8.1: BSE image shows the via FIB ablated area of a silica glass within a highly-shocked and projectile-rich ejecta fragment (E1-3382).

- As already described in chapter 3.2.3.2 additional phase separations occurred within the Fe-enrichment zone, resulting inter alia in the formation of sub- μm sized minerals and dendritic domains rich in Cr and V or rich in Fe (cf. Fig. 3.4, distribution maps in Fig. 3.9). It is suggested that the Cr-V-rich minerals belong to the spinel group and are probably a variation of chromite. The minerals are too small for meaningful microprobe analyses. Therefore, TEM investigations are needed to confirm this assumption. In addition, detailed analyses of these minerals (and *Lfe* and *Lsi*) may give more insights into these complex small scale processes, which occur at the interface between projectile droplet and silicate melt (Fig. 3.4d). Perhaps quenching or cooling rates can be derived from this investigation.

- One major outcome of this thesis is the observation of significant element partitioning processes during mixing of projectile melts and targets melt, which occur both in impact and laser-induced melting experiments. Especially in case of the hypervelocity impact experiments the question arises "How long is the time interval of this geochemical process?". In general the partitioning process starts shortly after the contact of the projectile and ends with more or less quenching during penetrating the ejecta catcher. Based on high speed camera images (Hoerth *et al.*, 2013) it can be estimated that the highly shocked and projectile-rich ejecta reaches the catcher system approximately after 5-10 ms. In order to estimate times for this ultra-fast process it could be an approach to calculate diffusion coefficients for the partitioning of the projectile elements. EMP analyses provide the chemical changes of projectile and target melt; BSE images enable the estimation of diffusion lengths, e.g., at the Fe-enrichment zones of the projectile droplets.
- The laser-induced melting experiments turned out as an excellent method in order to investigate geochemical mixing processes between projectile melts and target melts. One problem during the electron microprobe analyses of the produced melts were the very small sizes of the projectile droplets (cp. Fig. 5.6). These droplets are too small for point measurements; mixing analyses must be expected. A modification of the experimental setup, for example by completely putting the projectile and sandstone on top of each other, reducing the thickness of the projectile and increasing the spot size of the laser beam may fix this problem.
- One additional observation of the laser-induced melting experiments is the formation of spherules, which were found on the top of the raw materials and on aluminium side-walls of the experimental setup (Fig. 8.2). No detailed investigation were performed in order to determine their chemical/mineral composition. These spherules may provide some new insights into the formation of impact spherules (e.g., impact spherule layers of the Barberton greenstone belt, Lowe *et al.*, 2003).

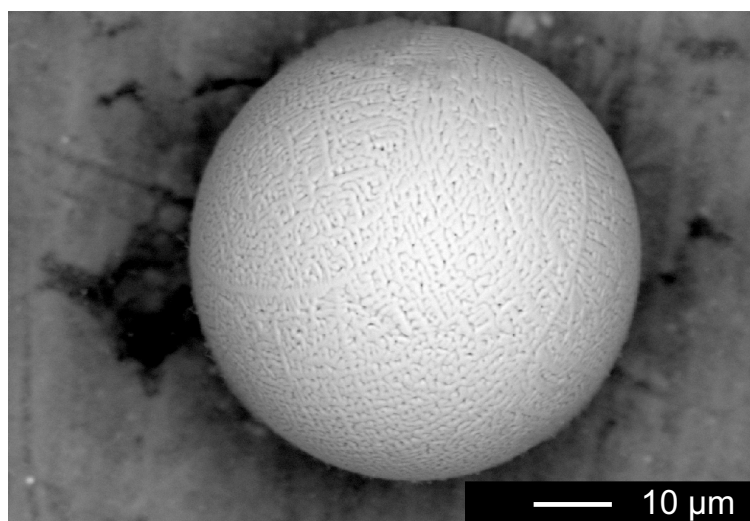


Figure 8.2: BSE image of a metallic spherules with conspicuous quenching textures, which were formed during the laser beam irradiation (LE-G).

- Projectile droplets in natural impactite show significant changes in the projectile element ratios compared to the element ratios of the original meteorite. As already asked in chapter 6.2 "What happened with the strongly siderophile platinum group elements during the impact?" In order to analyze the PGE concentrations of projectile droplets a analytical method with very low detection limits is needed. LA-ICP-MS would be applicable for PGE analyses in iron meteorite droplets. The spheres that were generated in the MEMIN experiments are too small for such a investigation because the laser beam needs sizes around 50 μm . The projectile droplets within the Wabar impact glass would be more suitable for LA-ICP-MS. There are no investigations which deals with the PGE analyses of incorporated projectile droplets.

References

- AHRENS, T. J., & GREGSON, V. G. 1964. Shock compression of crustal rocks: Data for quartz, calcite, and plagioclase rocks. *Journal of Geophysical Research*, **69**, 4839–4874.
- ALVAREZ, L. W., ALVAREZ, W., ASARO, F., & MICHEL, H. V. 1980. Extraterrestrial cause for the Cretaceous-Tertiary extinction. *Science*, **208**(4448), 1095–1108.
- ARTEMIEVA, N., & PIERAZZO, E. 2011. The Canyon Diablo impact event: 2. Projectile fate and target melting upon impact. *Meteoritics & Planetary Science*, **46**(6), 805–829.
- ATTREP, A., JR., ORTH, C. J., QUINTANA, L. R., SHOEMAKER, C. S., SHOEMAKER, E. M., & TAYLOR, S. R. 1991. *Chemical fractionation of siderophile elements in impactites from Australian meteorite craters*. 22th Lunar and Planetary Science Conference.
- BERNDT, J., DEUTSCH, A., SCHULTE, P., & MEZGER, K. 2011. The Chicxulub ejecta deposit at Demerara Rise (western Atlantic): Dissecting the geochemical anomaly using laser ablation–mass spectrometry. *Geology*, **39**(3), 279–282.
- BERRY, S. A., CHEN, F. J., WILDER, M. C., & REDA, D. C. 2007. Boundary layer transition experiments in support of the hypersonics program. *Reston, Virginia: The American Institute of Aeronautics and Astronautics*.
- BRETT, R. 1967. Metallic spherules in impactite and tektite glasses. *The American Mineralogist*, **52**, 721–733.
- BUCHWALD, V.F. 1975. *Handbook of iron meteorites, their history, distribution, composition, and structure*. Berkeley: University of California Press.
- BUHL, E., POELCHAU, M.H., DRESEN, G., & KENKMANN, T. 2013. Deformation of dry and wet sandstone targets during hypervelocity impact experiments, as revealed from the MEMIN Program. *Meteoritics & Planetary Science*, **48**(1), 71–86.
- BUNCH, T. E., & CASSIDY, W. A. 1968. Impact-induced deformation in the Campo del Cielo meteorite. *Pages 601–612 of: FRENCH, B.M., & SHORT, M. N. (eds), Shock metamorphism of natural materials*. Baltimore: Mono Book Corp.
- BUNCH, T. E., & CASSIDY, W. A. 1972. Petrographic and electron microprobe study of the Monturaqui impactite. *Contributions to Mineralogy and Petrology*, **36**(2), 95–112.
- CANUP, R.M., & ASPHAUG, E. 2001. Origin of the Moon in a giant impact near the end of the Earth's formation. *Nature*, **412**(6848), 708–712.
- CINTALA, M. J., & HÖRZ, F. 2008. Experimental impacts into chondritic targets, part I: Disruption of an L6 chondrite by multiple impacts. *Meteoritics & Planetary Science*, **43**(4), 771–803.
- CORGNE, A., KESHAV, S., WOOD, B. J., MCDONOUGH, W. F., & FEI, Y. 2008. Metal–silicate partitioning and constraints on core composition and oxygen fugacity during Earth accretion. *Geochimica et Cosmochimica Acta*, **72**(2), 574–589.

- D'ORAZIO, M., FOLCO, L., ZEOLI, A., & CORDIER, C. 2011. Gebel Kamil: The iron meteorite that formed the Kamil crater (Egypt). *Meteoritics & Planetary Science*, **46**(8), 1179–1196.
- DRESSLER, B. O., & REIMOLD, W. U. 2001. Terrestrial impact melt rocks and glasses. *Earth-Science Reviews*, **56**(1-4), 205–284.
- EBERT, M., HECHT, L., DEUTSCH, A., & KENKMANN, T. 2013. Chemical modification of projectile residues and target material in a MEMIN cratering experiment. *Meteoritics & Planetary Science*, **48**(1), 134–149.
- EBERT, M., HECHT, L., DEUTSCH, A., KENKMANN, T., WIRTH, R., & BERNDT, J. 2014. Geochemical processes between steel projectiles and silica-rich targets in hypervelocity impact experiments. *Geochemica et Cosmochemica Acta*.
- EVANS, N. J., SHAHINPOOR, M., & AHRENS, T. J. 1994. Hypervelocity impact: Ejecta velocity, angle, and composition. *Geological Society of America*, **293**, 93–101.
- FARROW, C.E.G., & WATKINSON, D. H. 1997. Diversity of precious-metal mineralization in footwall Cu-Ni-PGE deposits, Sudbury, Ontario: Implications for hydrothermal models of formation. *Canadian Mineralogist*, **35**, 817–840.
- FOLCO, L., DI MARTINO, M., EL BARKOOKY, A., D'ORAZIO, M., LETHY, A., URBINI, S., NICOLOSI, I., HAFEZ, M., CORDIER, C., VAN GINNEKEN, M., *et al.* 2011. Kamil Crater (Egypt): Ground truth for small-scale meteorite impacts on Earth. *Geology*, **39**(2), 179–182.
- FREESTONE, I. C., & POWELL, R. 1983. The low temperature field of liquid immiscibility in the system K₂O-Al₂O₃-FeO-SiO₂ with special reference to the join fayalite-leucite-silica. *Contributions to Mineralogy and Petrology*, **82**(2-3), 291–299.
- FRENCH, B. M. 1998. *Traces of catastrophe: A handbook of shock-metamorphic effects in terrestrial meteorite impact structures*. Lunar and Planetary Institute.
- GAULT, D. 1973. Displaced mass, depth, diameter, and effects of oblique trajectories for impact craters formed in dense crystalline rocks. *Earth, Moon, and Planets*, **6**(1), 32–44.
- GERASIMOV, M V, YAKOVLEV, O I, DIKOV, YU P, & WLOTZKA, F. 2005. Evaporative differentiation of impact-produced melts: Laser-simulation experiments and comparison with impact glasses from the Logoisk crater. *Geological Society of America Special Papers*, **384**, 351–366.
- GIBBONS, R. V., HÖRZ, F., THOMPSON, T. D., & BROWNLEE, D. E. 1976. Metal spherules in Wabar, Monturaqui, and Henbury impactites. *Pages 863–880 of: 7 th Lunar Science Conference*, vol. 1. Pergamon Press, Inc.
- GODERIS, S., PAQUAY, F., & CLAEYS, P. 2012. *Projectile Identification in Terrestrial Impact Structures and Ejecta Material*. John Wiley & Sons, Ltd. Pages 223–239.
- GOLDSCHMIDT, V.M. 1937. The principles of distribution of chemical elements in minerals and rocks. The seventh Hugo Müller Lecture, delivered before the Chemical Society on March 17th, 1937. *Journal of the Chemical Society (Resumed)*, 655–673.

- GREY, I. D. S., BURCHELL, M. J., & SHRINE, N. R. G. 2002. Scaling of hypervelocity impact craters in ice with impact angle. *Journal of Geophysical Research*, **107**(E10), 5076–5084.
- GRIEVE, R.A.F. 1980. Impact bombardment and its role in proto-continental growth on the early Earth. *Precambrian Research*, **10**(3), 217–247.
- GRIEVE, R.A.F. 1982. The record of impact on Earth: Implications for a major Cretaceous/Tertiary impact event. *Geological Society of America, Special Paper*, **190**, 25–37.
- GRIEVE, R.A.F. 1991. Terrestrial impact: The record in the rocks. *Meteoritics*, **26**(3), 175–194.
- GRIEVE, R.A.F. 2005. Economic natural resource deposits at terrestrial impact structures. *Special Publication Geological Society Of London*, **248**, 1.
- GRIEVE, R.A.F., & SHOEMAKER, E.M. 1994. The record of past impacts on Earth. *Page 417 of: Hazards due to comets and asteroids*, vol. 1. University of Arizona Press (Tucson).
- GÜLDEMEISTER, N., DURR, N., WÜNNEMANN, K., ELBESHAUSEN, D., & HIERMAIER, S. 2011. *Propagation of impact-induced shock waves in heterogenous rocks using mesoscale modeling (abstract)*. 44th Lunar and Planetary Science Conference.
- GÜLDEMEISTER, N., WÜNNEMANN, K., DURR, N., & HIERMAIER, S. 2013. Propagation of impact-induced shock waves in porous sandstone using mesoscale modeling. *Meteoritics & Planetary Science*, **48**(1), 115–133.
- HAMANN, C., HECHT, L., EBERT, M., & WIRTH, R. 2013. Chemical projectile-target interaction and liquid immiscibility in impact glass from the Wabar craters, Saudi Arabia. *Geochimica et Cosmochimica Acta*, **121**(0), 291 – 310.
- HILIGREN, V. J., DRAKE, M. J., & RUBIE, D. C. 1994. High-pressure and high-temperature experiments on core-mantle segregation in the accreting earth. *Science*, **264**(5164), 1442–1445.
- HILIGREN, V. J., DRAKE, M. J., & RUBIE, D. C. 1996. High pressure and high temperature metal-silicate partitioning of siderophile elements: The importance of silicate liquid composition. *Geochimica et Cosmochimica Acta*, **60**(12), 2257–2263.
- HOERTH, TOBIAS, SCHÄFER, FRANK, THOMA, KLAUS, KENKMANN, THOMAS, POELCHAU, MICHAEL H., LEXOW, BERND, & DEUTSCH, ALEXANDER. 2013. Hypervelocity impacts on dry and wet sandstone: Observations of ejecta dynamics and crater growth. *Meteoritics & Planetary Science*, **48**(1), 23–32.
- HOLZHEID, A, & PALME, H. 1996. The influence of FeO on the solubilities of cobalt and nickel in silicate melts. *Geochimica et cosmochimica acta*, **60**(7), 1181–1193.
- HOLZHEID, A, BORISOV, A, & PALME, H. 1994. The effect of oxygen fugacity and temperature on solubilities of nickel, cobalt, and molybdenum in silicate melts. *Geochimica et Cosmochimica Acta*, **58**(8), 1975–1981.
- HÖRZ, F. 1969. Structural and mineralogical evaluation of an experimentally produced impact crater in granite. *Contributions to Mineralogy and Petrology*, **21**(4), 365–377.

- HÖRZ, F. 2012. Cratering and penetration experiments in aluminum and teflon: Implications for space-exposed surfaces. *Meteoritics & Planetary Science*, **47**(4), 763–797.
- HÖRZ, F., FECHTIG, H., JANICKE, J., SCHNEIDER, E., & KUCZERA, H. 1983. *The chemistry of projectile residue in experimental microcraters (abstract)*. 14th Lunar and Planetary Science Conference.
- HÖRZ, F., BLANCHARD, D. P., SEE, T. H., & MURALI, A. V. 1989. *Heterogeneous dissemination of projectile materials in the impact melts from Wabar crater, Saudi Arabia*. 19th Lunar and Planetary Science Conference.
- HÖRZ, F., MITTFELDLT, D. W., SEE, T. H., & GALINDO, C. 2002. Petrographic studies of the impact melts from Meteor Crater, Arizona, USA. *Meteoritics & Planetary Science*, **37**(4), 501–531.
- HUDON, P., & BAKER, D. R. 2002. The nature of phase separation in binary oxide melts and glasses. I. Silicate systems. *Journal of Non-Crystalline Solids*, **303**, 299–345.
- JAEGER, W. L., & DRAKE, M. J. 2000. Metal–silicate partitioning of Co, Ga, and W: dependence on silicate melt composition. *Geochimica et Cosmochimica Acta*, **64**(22), 3887–3895.
- JAMES, P.F. 1975. Liquid-phase separation in glass-forming systems. *Journal of Materials Science*, **10**, 1802–1825.
- JAMMES, C., STÖFFLER, D., BISCHOFF, A., REIMOLD, W. U., & GAULT, D. E. 1983. *Reduction of SiO₂ and Si metallurgical transformations in al by hypervelocity impact of al-projectiles into quartz sand (abstract)*. 14th Lunar and Planetary Science Conference.
- JOCHUM, K. P., WEIS, U., STOLL, B., KUZMIN, D., YANG, Q., RACZEK, I., JACOB, D. E., STRACKE, A., BIRBAUM, K., FRICK, D. A., GÜNTHER, D., & ENZWEILER, J. 2011. Determination of Reference Values for NIST SRM 610-617 Glasses Following ISO Guidelines. *Geostandards and Geoanalytical Research*, **35**(4), 397–429.
- KEARSLEY, A., GRAHAM, G., MCDONNELL, T., BLAND, P., HOUGH, R., & HELPS, P. 2004. Early fracturing and impact residue emplacement: Can modelling help to predict their location in major craters? *Meteoritics & Planetary Science*, **39**(2), 247–265.
- KELLY, W. R., HOLDSWORTH, E., & MOORE, C. B. 1974. The chemical composition of metallic spheroids and metallic particles within impactite from Barringer Meteorite Crater, Arizona. *Geochimica et Cosmochimica Acta*, **38**(4), 533–534.
- KENKMANN, T., PATZSCHKE, M., THOMA, K., SCHÄFER, F., DEUTSCH, A., & HECHT, L. 2007. *Melting and vaporization of a steel projectile in meso-scale hypervelocity cratering experiments (abstract)*. 38th Lunar and Planetary Science Conference.
- KENKMANN, T., ARTEMIEVA, N. A., WÜNNEMANN, K., POELCHAU, M. H., ELBESHAUSEN, D., & PRADO, H. NUNEZ DEL. 2009. The Carancas meteorite impact crater, Peru: Geologic surveying and modeling of crater formation and atmospheric passage. *Meteoritics & Planetary Science*, **44**(7), 985–1000.

- KENKMANN, T., WÜNNEMANN, K., DEUTSCH, A., POELCHAU, M. H., SCHÄFER, F., & THOMA, K. 2011. Impact cratering in sandstone: The MEMIN pilot study on the effect of pore water. *Meteoritics & Planetary Science*, **46**(6), 890–902.
- KENKMANN, T., TRULLENQUE, G., DEUTSCH, A., HECHT, L., EBERT, M., SALGE, T., SCHÄFER, F., & THOMA, K. 2013. Deformation and melting of steel projectiles in hypervelocity cratering experiments. *Meteoritics & Planetary Science*, **48**(1), 150–164.
- KIEFER, S. W. 1971. *Shock metamorphism of the Coconino sandstone at Meteor crater*. Ph.D. thesis, California Institute for Technology.
- KOEBERL, C. 1998. Identification of meteoritic components in impactites. *Geological Society, London, Special Publications*, **140**, 133–153.
- KOEBERL, C., CLAEYS, P., HECHT, L., & McDONALD, I. 2012. Geochemistry of Impactites. *Elements*, **8**(1), 37–42.
- KRINOV, E. L., & FESENKOV, V. G. 1959. The Sikhote-Alin Iron Meteorite Shower. In Krinov, E. L. 1959. *Pages 99–156 of: The Main Conditions of the Fall of a Meteoritic Shower*. Russian Academy of Sciences.
- LANGENHORST, F. 2002. Shock metamorphism of some minerals: Basic introduction and microstructural observations. *Bulletin of the Czech Geological Survey*, **77**, 265–282.
- LANGENHORST, F., & DEUTSCH, A. 1994. Shock experiments on pre-heated α - and β -quartz: I. Optical and density data. *Earth and Planetary Science Letters*, **125**, 407–420.
- LEXOW, B., WICKERT, M., THOMA, K., SCHÄFER, F., POELCHAU, M. H., & KENKMANN, T. 2013. The extra-large light-gas gun of the Fraunhofer EMI: Applications for impact cratering research. *Meteoritics & Planetary Science*, **48**(1), 3–7.
- LOWE, D. R., BYERLY, G. R., KYTE, F. T., SHUKOLYUKOV, A., ASARO, F., & KRULL, A. 2003. Spherule beds 3.47-3.24 billion years old in the Barberton Greenstone Belt, South Africa: a record of large meteorite impacts and their influence on early crustal and biological evolution. *Astrobiology*, **3**(1), 7–48.
- LUCK, J.M., & TUREKIAN, K.K. 1983. Osmium-187/Osmium-186 in manganese nodules and the Cretaceous-Tertiary boundary. *Science*, **222**(4624), 613–615.
- MASAITIS, V.L. 1998. Popigai crater: Origin and distribution of diamond-bearing impactites. *Meteoritics & Planetary Science*, **33**(2), 349–359.
- MCDONALD, I., ANDREOLI, M. A. G., HART, R. J., & TREDoux, M. 2001. Platinum-group elements in the Morokweng impact structure, South Africa: Evidence for the impact of a large ordinary chondrite projectile at the Jurassic-Cretaceous boundary. *Geochimica et Cosmochimica Acta*, **65**, 299–309.
- MELOSH, H. J., & COLLINS, G. S. 2005. Planetary science: Meteor Crater formed by low-velocity impact. *Nature*, **434**(7030), 157–157.

- MELOSH, H.J. 1989. *Impact cratering: a geologic process*. Oxford monographs on geology and geophysics. Oxford University Press.
- MITTELFEHLDT, D. W., SEE, T. H., & HÖRZ, F. 1992. Dissemination and fractionation of projectile materials in the impact melts from Wabar Crater, Saudi Arabia. *Meteoritics*, **27**(4), 361–370.
- MITTELFEHLDT, D. W., HÖRZ, F., SEE, T. H., SCOTT, E. R. D., & MERTZMAN, S. A. 2005. Geochemistry of target rocks, impact-melt particles, and metallic spherules from Meteor Crater, Arizona: Empirical evidence on the impact process. *Geological Society of America Special Papers*, **384**, 367–390.
- MITTMEYER, H.G. 1980. Zur Geologie des Hunsrückschiefers. *Kleine Senckenberg Reihe*, **11**, 26–33.
- MOORE, H. J., GAULT, D. E., & LUGN, R. V. 1963. Experimental impact craters in basalt. *Transactions - Society of Mining Engineers*, **229**, 258–262.
- MORBIDELLI, A., CHAMBERS, J, LUNINE, J.I., PETIT, J.M., ROBERT, F., VALSECCHI, G.B., & CYR, K.E. 2000. Source regions and timescales for the delivery of water to the Earth. *Meteoritics & Planetary Science*, **35**(6), 1309–1320.
- MORGAN, J. W., HIGUCHI, H., GANAPATHY, R., & ANDERS, E. 1975. Meteoritic material in four terrestrial meteorite craters. *Pages 1609–1623 of: Lunar and Planetary Science Conference Proceedings*, vol. 6.
- MYSEN, B. O., VIRGO, D., & SEIFERT, F. A. 1982. The structure of silicate melts: implications for chemical and physical properties of natural magma. *Reviews of Geophysics*, **20**(3), 353–383.
- MYSEN, B.O., & RICHEL, P. 2005. *Silicate glasses and melts: properties and structure*. Elsevier.
- OHTANI, E., YURIMOTO, H., & SETO, S. 1997. Element partitioning between metallic liquid, silicate liquid, and lower-mantle minerals: implications for core formation of the Earth. *Physics of the Earth and Planetary Interiors*, **100**(1-4), 97–114.
- O'KEEFE, J. D, & AHRENS, T. J. 1977. Impact induced energy partitioning, melting and vaporisation on terrestrial planets. *Proceedings LPSC VIII*, 3357–3374.
- OSHTRAKH, M.I., LARIONOV, M.YU., GROKHOVSKY, V.I., & SEMIONKIN, V.A. 2011. An analysis of Fe and Ni distribution in M1, M2 and M3 sites of iron-nickel phosphides extracted from Sikhote-Alin meteorite using Mössbauer spectroscopy with a high velocity resolution. *Journal of Molecular Structure*, **993**, 38 – 42.
- PALME, H., GRIEVE, R. A. F., & WOLF, R. 1981. Identification of the projectile at the Brent crater, and further considerations of projectile types at terrestrial craters. *Geochimica et Cosmochimica Acta*, **45**(12), 2417–2424.

- PARK, F. R., BUNCH, T. E., & MASSALSKI, T. B. 1966. A study of the silicate inclusions and other phases in the Campo del Cielo meteorite. *Geochimica et Cosmochimica Acta*, **30**(4), 399–400.
- PIERAZZO, E., & MELOSH, H. J. 2000. Hydrocode modeling of oblique impacts: The fate of the projectile. *Meteoritics & Planetary Science*, **35**(1), 117–130.
- POELCHAU, M. H., DEUTSCH, A., KENKMANN, T., HOERTH, T., SCHÄFER, F., & THOMA, K. 2011. *Experimental impact cratering into sandstone: A MEMIN-progress report (abstract)*. 44th Lunar and Planetary Science Conference.
- POELCHAU, M. H., KENKMANN, T., THOMA, K., HOERTH, T., DUFRESNE, A., & SCHÄFER, F. 2013. The MEMIN research unit: Scaling impact cratering experiments in porous sandstones. *Meteoritics & Planetary Science*, **48**(1), 8–22.
- POLANSKEY, C. A., & AHRENS, T. J. 1990. Impact spallation experiments: Fracture patterns and spall velocities. *Icarus*, **87**(1), 140–155.
- PRESCOTT, J. R., ROBERTSON, G. B., SHOEMAKER, C., SHOEMAKER, E. M., & WYNN, J. 2004. Luminescence dating of the Wabar meteorite craters, Saudi Arabia. *Journal of Geophysical Research: Planets (1991-2012)*, **109**(E1).
- REDFERN, S. A. T. 1987. The Kinetics Of Dehydroxylation Of Kaolinite. *Clay Minerals*, **22**(4), 447–456.
- REISER, F., DUFRESNE, A., POELCHAU, M. H., DEUTSCH, A., & KENKMANN, T. 2011. *Catching as much information as possible: An efficient and easy-to-build ejecta catcher for high-velocity impact experiments (abstract)*. 44th Lunar and Planetary Science Conference.
- REMO, J. L. 1994. Classifying and modeling NEO material properties and interactions. *Pages 551–596 of: Hazards due to comets and asteroids*. Gehrels, T.
- RIGHTER, K., & DRAKE, M. J. 1997. Metal-silicate equilibrium in a homogeneously accreting earth: new results for Re. *Earth and Planetary Science Letters*, **146**(3), 541–553.
- RIGHTER, K., & DRAKE, M. J. 1999. Effect of water on metal-silicate partitioning of siderophile elements: a high pressure and temperature terrestrial magma ocean and core formation. *Earth and Planetary Science Letters*, **171**(3), 383–399.
- RIGHTER, K., DRAKE, M. J., & YAXLEY, G. 1997. Prediction of siderophile element metal-silicate partition coefficients to 20 GPa and 2800°C: The effects of pressure, temperature, oxygen fugacity, and silicate and metallic melt compositions. *Physics of the Earth and Planetary Interiors*, **100**(1-4), 115–134.
- RIGHTER, K., PANDO, K. M., DANIELSON, L., & LEE, C.-T. 2010. Partitioning of Mo, P and other siderophile elements (Cu, Ga, Sn, Ni, Co, Cr, Mn, V, and W) between metal and silicate melt as a function of temperature and silicate melt composition. *Earth and Planetary Science Letters*, **291**(1), 1–9.

- ROEDDER, E. 1978. Silicate liquid immiscibility in magmas and in the system K_2O - FeO - Al_2O_3 - SiO_2 . *Geochimica et Cosmochimica Acta*, **42**, 1597–1617.
- ROSENQVIST, T. 2004. *Principles of Extractive Metallurgy*. Tapir Academic Press.
- ROWAN, L. R., & HÖRZ, F. 1995. *Deciphering projectile compositions of impact craters via shock recovery experiments on simple metal-silicate systems*. 26th Lunar and Planetary Science Conference.
- SALEHI, I.A., GAHAN, B.C., & BATARSEH, S. 2007. *Laser drilling - Drilling with the power of light*. Tech. rept. Gas Technology Institute.
- SCHMITT, W., PALME, H., & WÄNKE, H. 1989. Experimental determination of metal/silicate partition coefficients for P, Co, Ni, Cu, Ga, Ge, Mo, and W and some implications for the early evolution of the Earth. *Geochimica et Cosmochimica Acta*, **53**(1), 173–185.
- SCHULTZ, P. H. 2003. *Transient crater growth in low density targets (abstract)*. 34th Lunar and Planetary Science Conference.
- SEE, T. H., WAGSTAFF, J., YANG, V., HÖRZ, F., & MCKAY, G. A. 1998. Compositional variation and mixing of impact melts on microscopic scales. *Meteoritics & Planetary Science*, **33**(4), 937–948.
- SEO, M., & SATO, N. 1983. Selective oxidation of Fe-30Ni alloy in a low-temperature range (433-473 K). *Oxidation of Metals*, **19**(3), 151–163.
- SHELBY, J. E. 2005. *Introduction to glass science and technology*. Royal Society of Chemistry.
- SHOEMAKER, E. M., GAULT, D. E., MOORE, H. J., & LUGN, R. V. 1963. Hypervelocity impact of steel into coconino sandstone. *American Journal of Science*, **261**, 668 – 682.
- SHOEMAKER, E.M. 1977. Why study impact craters. *Pages 1–10 of: Impact and explosion cratering: Planetary and terrestrial implications*, vol. 1.
- SOMMER, F., REISER, F., DUFRESNE, A., POELCHAU, M. H., HOERTH, T., DEUTSCH, A., KENKMANN, T., & THOMA, K. 2013. Ejection behavior characteristics in experimental cratering in sandstone targets. *Meteoritics & Planetary Science*, **48**(1), 33–49.
- STÖFFLER, D., & LANGENHORST, F. 1994. Shock metamorphism of quartz in nature and experiment: I. Basic observation and theory. *Meteoritics*, **29**, 155–181.
- STÜCK, H., SIEGESMUND, S., & RÜDRICH, J. 2011. Weathering behaviour and construction suitability of dimension stones from the Drei Gleichen area (Thuringia, Germany). *Environmental Earth Sciences*, **63**(7-8), 1763–1786.
- STÜCK, H. L. 2013. *Dimensional sandstones: Weathering phenomena, technical properties and numerical modeling of water migration*. Ph.D. thesis, Georg-August University School of Science.

- STUDIER, M. H., HAYATSU, R., & ANDERS, E. 1968. Origin of organic matter in early solar system - I. Hydrocarbons. *Geochimica et cosmochimica acta*, **32**(2), 151–173.
- TAGLE, R. 2005. LL-Ordinary chondrite impact on the Moon: Results from the 3.9 Ga impact melt at the landing site of Apollo 17. *Page 2008 of: 36th Annual Lunar and Planetary Science Conference*, vol. 36.
- TAGLE, R., & CLAEYS, P. 2005. An ordinary chondrite impactor for the Popigai crater, Siberia. *Geochimica et Cosmochimica Acta*, **69**(11), 2877–2889.
- TAGLE, R., & HECHT, L. 2006. Geochemical identification of projectiles in impact rocks. *Meteoritics & Planetary Science*, **41**(11), 1721–1735.
- VEKSLER, I. V., DORFMAN, A. M., RHEDE, D., WIRTH, R., BORISOV, A. A., & DINGWELL, D. B. 2008. Liquid unmixing kinetics and the extent of immiscibility in the system K_2O - CaO - FeO - Al_2O_3 - SiO_2 . *Chemical Geology*, **256**, 119–130.
- WALKER, D., NORBY, L., & JONES, J. H. 1993. Superheating effects on metal-silicate partitioning of siderophile elements. *Science*, **262**(5141), 1858–1861.
- WALLACE, M. W., GOSTIN, V. A., & KEAYS, R. R. 1990. Acraman impact ejecta and host shales: Evidence for low-temperature mobilization of iridium and other platinoids. *Geology*, **18**(2), 132–135.
- WASSON, J. T., & KALLEMEYN, G. W. 2002. The IAB iron-meteorite complex: A group, five subgroups, numerous grouplets, closely related, mainly formed by crystal segregation in rapidly cooling melts. *Geochimica et Cosmochimica Acta*, **66**(13), 2445–2473.
- WEAVER, H. A., A'HEARN, M. F., ARPIGNY, C., BOICE, D. C., FELDMAN, P. D., LARSON, S. M., LAMY, P., LEVY, D. H., MARSDEN, B. G., MEECH, K. J., & ET AL. 1995. The Hubble Space Telescope (HST) observing campaign on comet Shoemaker-Levy 9. *Science*, **267**(5202), 1282–1288.
- WEBER, S., THEISEN, W., CASTRO, F., & PYZALLA, A. 2009. Influence of gas atmosphere and hard particle addition on the sintering behavior of high alloyed PM cold work tool steels. *Materials Science and Engineering*, **A515**, 175–182.
- WHITE, W. 2011. *Geochemistry - Chapter 7*.
- WITTMANN, A., KENKMANN, T., SCHMITT, R.T., & STÖFFLER, D. 2006. Shock-metamorphosed zircon in terrestrial impact craters. *Meteoritics & Planetary Science*, **41**(3), 433–454.
- WOZNAKIEWICZ, P. J., ISHII, H. A., KEARSLEY, ANTON T., BURCHELL, MARK J., BLAND, PHILIP A., BRADLEY, JOHN P., DAI, ZURONG, TESLICH, NICK, COLLINS, GARETH S., COLE, MIKE J., & RUSSELL, SARA S. 2011. Investigation of iron sulfide impact crater residues: A combined analysis by scanning and transmission electron microscopy. *Meteoritics & Planetary Science*, **46**(7), 1007–1024.

- WÜNNEMANN, K., COLLINS, G. S., & MELOSH, H. J. 2006. A strain-based porosity model for use in hydrocode simulations of impacts and implications for transient crater growth in porous targets. *Icarus*, **180**(2), 514–527.
- WYNN, J.C., & SHOEMAKER, E.M. 1998. The day the sands caught fire. *Scientific American*, **279**, 36–45.
- YESKIS, D., VAN GROOS, A. K. F., & GUGGENHEIM, S. 1985. Dehydroxylation of kaolinite. *American Mineralogist*, **70**.

A List of figures

1.1	(a) Painting: "Fall of the Sikhote Alin meteorite" by A. A. Medvedev, who observed the impact from the roof of his house in February 1947; (b) Hubble image of the 21 fragments of the Shoemaker-Levy 9 comet prior impacting on Jupiter (May, 1994; source: www.hubblesite.org); (c) Jupiter's cloud-tops shortly after the impact of the first fragment-A of comet Shoemaker-Levy 9 (July 16, 1994; source: www.hubblesite.org); (d) Carancas crater, Peru (Kenkmann <i>et al.</i> , 2009). (e) A meteorite flashes across the sky over Chelyabinsk, Russia, image taken from a dashboard camera.	2
1.2	Comparison of the PGE projectile elemental ratios determined from the impact melt rocks of Popigai, Morokweng, and Serenitatis with elemental ratios of chondrites (Tagle & Hecht, 2006).	3
1.3	Backscattered electron image of emulsion features of Fe-rich (<i>Lfe</i>) and Si-rich (<i>Lsi</i>) silicate melts in the Wabar impactite. Adopted from Fig. 2d in Hamann <i>et al.</i> , 2013.	4
2.1	(a) Back-scattered electron image (BSE) of the Campo del Cielo meteorite with various phases. (b) Rhombohedral rhabdite in kamacite matrix of the Campo del Cielo meteorite projectile.	14
2.2	(a) Photomicrograph and (b) BSE image of a weakly deformed ejecta fragment; for detailed explanation see text. (c) Photomicrograph and (d) BSE image of a highly deformed ejecta fragment; for detailed explanation see text.	16
2.3	Photomicrograph (a) and scanning electron microscope image - BSE mode (b) of a highly shocked ejecta fragment; for detailed explanation see text.	16
2.4	(a) Shock-metamorphic features of the sandstone and projectile droplets (BSE-image). (b) Different sets of PDF in quartz and produced silica glass (BSE-image); for detailed explanation see text.	18
2.5	(a, b) BSE image of a highly shocked ejecta fragment showing typical textures and components. (c) Magnification of 2.5b shows a molten margin of a partly fused projectile fragment; due to the high contrast the silicate phases on the left side are not visible (BSE-image). (d) Typical melt pocket (center) with a rim in a partly fused projectile fragment; for detailed explanation see text.	19
2.6	Fe vs. Si for various materials of the highly shocked ejecta fragments. The insert shows in detail the "shocked quartz"-field (Qtz with PDF, silica glass). d.l. = detection limit.	20
2.7	Fe vs. Ni for various materials of the highly shocked ejecta fragments. The inset represents the "shocked quartz"-field in detail (Qtz with PDF, silica glass). Unshocked quartzes are below the detection limits and not shown here.	21

2.8	Fe/Ni and Fe/Co for different phases of the projectile before and after the impact. The curved line represents the mixing line between unshocked kamacite and rhadbite. The dots on the mixing line are a subdivision in 20% steps. The insert shows in detail the data array close to the CDC meteorite ratio.	22
2.9	Ni content versus grain size of projectile droplets.	24
2.10	Fe/Ni and Fe/Co for different metallic spheres from natural craters compared with results of this study. Iron meteorite composition and ratio include Campo del Cielo and Canyon Diablo. The gray-scale gradient in the "projectile droplets"-field reflects the numbers of measurements - with a high number at dark gray and low number at light gray (cp. Fig. 2.8).	26
3.1	Photograph of the ejecta catcher system; consisting of tiles covered with Vaseline (left) and phenolic foam plates (right). Note the remarkable imprint of the ejecta curtain and the main mass of the ejecta in the middle of the catcher surrounding the entrance hole for the projectile. The highly shocked and projectile-rich ejecta fragments originate from the inner part of the catcher (Experiment E1-3382). . .	35
3.2	Back-scattered electron (BSE) image of (a) the original Seeberger sandstone, (b) the Taunus quartzite, and (c) steel D290-1. Black dots are pores. (d) Photomicrograph of a highly shocked (and projectile rich) ejecta fragment of the sandstone experiment E1-3382. Fragments from quartzite experiments look very similar.	37
3.3	(a-c) BSE images of highly shocked sandstone ejecta with shocked quartz (dark gray), sandstone target melt (light gray) and different projectile material (white); (b) The white dashed line between point 1 and 2 marks the position of the TEM foil; (d) HAADF image of the marked TEM foil (in Fig. 3.3b) with sandstone melt, silica glass, Qtz with three different sets of PDF and projectile droplets; (e) Magnification of Fig. 3.3d shows liquid immiscibility textures of silica rich liquid (<i>Lsi</i> , dark gray), iron-rich liquid (<i>Lfe</i> , light gray) and projectile droplets (HAADF image) - (a,b,e,d: E1-3382; c:A6-5126).	38
3.4	(a) BSE image of highly shocked quartzite ejecta with shocked quartz (dark gray), quartzite target melt (light gray) and steel projectile material (white); (b) typical projectile-target mixing and unmixing textures, <i>Lfe</i> surrounding projectile droplets as well as silica glass; (c) iron enrichment zone around steel projectile droplet with subsequent unmixing into Fe-rich (<i>Lfe</i>) and Si-rich (<i>Lsi</i>) silicate melts (d) projectile droplet and iron enrichment zone; including dendritic domains of Cr-V-rich minerals and (1) Fe-rich minerals, (2) Cr-V-rich minerals (A20-5339); (e) typical projectile-target mixing and unmixing textures, <i>Lfe</i> surrounding projectile droplets and quartzite melt; silica glass and PDF-bearing Qtz; (f) Marginal decomposition of zircon to baddeleyite. (a-e: A20-5339; e: E6-3452).	40

3.5	BSE images of shocked projectile material. In order to show the internal structure of the material, the BSE images were taken with low-brightness conditions; thus the surrounded, low-dense target material is not visible (black areas); (a) Partly fused projectile fragment with gradual melting and homogenization textures (roughly from right to left); (b,c) Molten projectile droplets with Mo-W-rich zones, partly crystallized to Mo-W-rich carbides; (d) homogenous projectile droplet; (e) high magnification of a projectile droplet with eutectic Mo-W-rich carbide-fishbone-structure. (a-c: E1-3382; d: E6-3452, e: A20-5339).	42
3.6	(a-c) Fe vs. Cr microprobe data for sandstone melts; Cr preferentially partitioned into the sandstone melt, resulting in an average Cr/Fe above the steel ratio line; (d-f) Fe vs. Co microprobe data for sandstone melt; minor amounts of Co partitioned into the sandstone melt, resulting in an average Co/Fe ratio below the steel ratio; (d) includes Fe vs. Ni* data field of an equivalent experiment with an iron meteorite projectile from Ebert <i>et al.</i> (2013); data from hypervelocity impact experiment E1-3382, A6-5126 and E3-3383; impact energies in kilojoules (kJ); WR=whole rock composition; dry=dry target, wet=water saturated target. The dots on the mixing line are subdivisions in 20% steps.	44
3.7	Qualitative element maps of a highly shocked ejecta fragment with shocked Qtz grains (BSE - dark gray), sandstone melt (light gray), projectile droplets (light spheres of D290-1 steel) and pores (black spaces). Note the strong partitioning of Cr and V into the Al-rich silicate melt near the largest projectile droplet (highlighted by the white arrow). W, Co and Mo mainly remain in the projectile droplets and partially form discrete phases (Experiment A6-5126).	45
3.8	(a) Fe vs. Cr and (b) Fe vs. Co microprobe data for quartzite melt, <i>Lfe</i> , Cr-V-rich minerals and dendritic domains; data from hypervelocity impact experiment E6-3452 and A20-5339; WR=whole rock, impact energies in kilojoule (kJ). The dots on the mixing line are subdivisions in 20% steps.	47
3.9	Qualitative element maps (exact position is shown as rectangle in Fig. 3.4d) of a highly shocked ejecta fragment with projectile droplet; (Experiment A20-5339).	48
3.10	Qualitative element maps (outlined rectangle of Fig. 3.4b) of a highly shocked ejecta fragment with <i>Lfe</i> (light gray surrounding the large droplet), projectile droplets (light projectile melt droplets of D290-1 steel) and quartzite melt (dark gray); note the enrichment of Mo in the margins of the large projectile droplet (left side of the image), on the other hand W and Co are enriched in center - (Experiment A20-5339).	49
3.11	Fe vs. Mo/Co for various projectile material (EMP and SEM data), Point a,b and c represent different chemical states of projectile melts, which result from a modification of the projectile material during melting and mixing with the target melts; PD1 to PD3 - projectile droplet types (explanation see text); SE - experiments with sandstone targets; QE - experiments with quartzite targets.	49
3.12	Series of schematic cross-section diagrams showing the development of the highly shocked ejecta (modified from Melosh, 1989 and French, 1998).	51

3.13	Schematic illustration of the chemical modification of the quartzite target for Fe and Cr (V gives similar results as Cr); indicating 3 steps of element fractionation involved in the formation of coexisting liquids and associated mineral phases (see text for more details).	53
4.1	Quarter part of the ejecta catcher system; consisting of phenolic foam plates (from MEMIM experiment D3-3298). The red-lined radial cutout marked the foam slices (1 cm width), which were used for ejecta separation.	61
4.2	(a) Phenolic foam slices of experiment D3-3298; (b) the three ejecta types which were separated from the foam slices: type I: weakly deformed ejecta, type II highly deformed ejecta, and type III: highly shocked ejecta fragments. For more details about the ejecta types see chapter "2.2.2 - Ejecta types"	63
4.3	Ejection angle vs. mass of the three different ejecta types - D3-3298 (Sandstone/Iron meteorite)	64
4.4	Ejection angle vs. mass of the three different ejecta types - E1-3382 (Sandstone/Steel D290-1).	64
5.1	Cross section of the laser beam key hole of experiment LE-F; Point 1: unaltered sandstone, 2: partial melting of the sandstone, 3: complete melting and mixing of all sandstone components. Rectangle X marks: Fig. 5.3, Y: Fig. 5.4a, Z: Fig. 5.4b.	67
5.2	(a,d) Photograph of the experimental setup (LE-I, LE-H) before laser beam irradiation; (b,e) after laser beam irradiation; (c,f) sections used for geochemical analyses (exact position marked in Fig. 5.2e and f); Point 1: unaltered sandstone, 2: partial melting of the sandstone, 3: complete melting of the sandstone, 4: projectile melt; w - Fig. 5.8; x - Fig. 5.7a, y - Fig. 5.7b, z - Fig. 5.5a.	68
5.3	(a,b) Different stages of dehydration and melting processes in the sandstone (BSE images; LE-F). Exact position is shown as rectangle X in Fig. 5.1. (a) Point 1: unaltered phyllosilicate-bearing matrix, 2: dehydration and initial melting of the phyllosilicates, 3: completely molten phyllosilicates. (b) Dehydration and initial melting of the phyllosilicates on the left side (cp. with pristine matrix in Fig. 3.2a); completely molten phyllosilicates on the right side (see text for more details).	70
5.4	(a,b) BSE images of different melt textures in the sandstone target (LE-F). (a) Note the "high contrast" area in the upper part of the image, which allows a good distinction between lechatelierite and crystalline quartz (light gray "islands"). Laser beam heat gradient extends from the right to the left side (high T to low T). (b) Laser beam heat gradient extends from the left to the right side (high T to low T). Exact position is shown as rectangle Z in Fig. 5.1.	71
5.5	(a-d) BSE images of LE-H; (a) Molten contact between steel and sandstone; (b) Completely molten sandstone with injection path of projectile melt; (c) Low brightness magnification of the steel melt; typical textures of the molten steel with fish-bone structures of Mo-W-rich carbides (d) Magnification of Fig. 5.5b at high contrast; dash lined rectangle marked the element maps of Fig. 5.10.	72

5.6	(a-d) BSE images of LE-G; (a) Molten contact between steel and sandstone; (b) Typical unmixing features within the contaminated sandstone melt; see text for more explanations; (c) Emulsion textures of <i>Lfe</i> and <i>Lsi</i> ; (d) Significant mixing of steel melt droplets (white) and sandstone melt, note that this is a three dimensional view into the melt.	73
5.7	(a) BSE image of typical melt pockets with rim and center part in a partly fused Campo del Cielo meteorite; exact position of this image is marked as rectangle "X" in Fig. 5.2c; line x-y marked a chemical profile shown in Fig. 5.13. (b) BSE image of the completely fused Campo del Cielo meteorite; exact position of this image is marked as rectangle "Y" in Fig. 5.2c.	74
5.8	BSE image of the molten contact between Campo del Cielo meteorite and sandstone. Please note that the projectile melt is only the large white curved part at the top of the image, which is separated from the whitish emulsion textures below it (LE-I). Exact position of this image is marked as "W" in Fig. 5.2c . . .	75
5.9	Qualitative element maps of sandstone melt mixed with light projectile melt droplets of D290-1 steel (LE-G).	76
5.10	Qualitative element maps (outlined rectangle of Fig. 5.5d) of sandstone melt mixed with light projectile melt droplets of D290-1 steel (LE-H).	76
5.11	(a) BSE image of the interface between projectile melt, Fe enrichment zone and sandstone target melt (experiment LE-I). The space between projectile melt and silicate melts is probably caused by the preparation of the section (see text for more details). (b) Microprobe element maps of the Fe enrichment zone and its conspicuous emulsion textures of <i>Lfe</i> and <i>Lsi</i>	77
5.12	Chemical variation of the produced sandstone melt from LE-F.	79
5.13	Electron microprobe profile for Fe, Ni and P through a melt pocket; exact position marked as line between x and y in Fig. 5.7a; "c" center of the melt pocket. 1 point $\sim 1 \mu\text{m}$. Solid line represents the bulk Campo del Cielo; dashed line represents the partially molten Campo del Cielo.	80
5.14	Fe vs. Mg for sandstone melts from different laser-induced melting experiments. .	81
5.15	Fe vs. Si for sandstone melts from laser-induced melting experiments LE-I. Dashed line field contains Fe vs. Si data from a hypervelocity impact experiments carried out with the same sandstone (target) and a Campo del Cielo meteorite sphere (see Ebert <i>et al.</i> , 2013); Solid lined field marked the black impact glass of the Wabar crater (Hamann <i>et al.</i> , 2013)	82
5.16	Fe vs. Cr and Fe vs. Co for sandstone melt of experiment LE-F and LE-G. Dashed line fields contain Fe vs. Cr (and Fe vs. Co) data from hypervelocity impact experiments carried out with the same sandstone (target) and steel D290-1 spheres (see Ebert <i>et al.</i> , 2014).	83

5.17	Fe vs. Ni for sandstone melt of experiment LE-I. For comparison the dashed line and gray shaded field indicates the data range from a hypervelocity impact experiments carried out with the same sandstone (target) and a Campo del Cielo iron meteorite sphere (see Ebert <i>et al.</i> , 2013); whereby the darkest gray shade contain most of the data points.	84
6.1	(a) Front and (b) rear of the steel projectile relic of MEMIN experiment 3232 (from Kenkmann <i>et al.</i> , 2013); (c) 172 stitched BSE images display a cross-section of the projectile relict 3232. Note the thin shocked sandstone layer at the outer rim and inner rim of the sample (from Kenkmann <i>et al.</i> , 2013); the labeling of (c) refers to the original paper and is not relevant for this chapter; (d) and (e) photographs of Kamil target rock material stuck onto the surfaces of some Gebil Kamil shrapnels (modified from Fig. 12 in Folco <i>et al.</i> , 2011)	92
6.2	(a) Pumiceous impact glass found scattered in ejecta blanket of the Kamil crater (modified from Folco <i>et al.</i> , 2011); (b) Textural relationships between siliceous (dark) and Fe-rich (bright) impact glass (modified from Folco <i>et al.</i> , 2011), note the emulsion textures which indicate liquid immiscibility of Si-rich and Fe-rich melts.	93
6.3	Comparison of unmixing features between experiment and nature. (a) BSE images of typical features in Wabar impact melt. Emulsion structure (corona) around large FeNi sphere. Note the gradual coarsening of <i>Lfe</i> spheres in direction to the large FeNi sphere (modified from Hamann <i>et al.</i> , 2013). The meaning of the green arrows is discussed in the text of this chapter; (b) BSE image of a highly shocked ejecta from a MEMIN experiments (A20-5339) with iron enrichment zone around steel projectile droplet with subsequent unmixing into Fe-rich (<i>Lfe</i>) and Si-rich (<i>Lsi</i>) silicate melts.	94
6.4	Chemical data of projectile droplets (projectile type 2; quartzite experiments) normalized to the steel D290-1 bulk composition plotted against the lithophile (Cr,V) and increasing siderophile (Fe, W, Co, Mo) character of the projectile tracer elements.	96
6.5	Plot shows a comparison between the chemical data of the original Canyon Diablo meteorite (data taken from Wasson & Kallemeyn, 2002) and Fe, Ni, Co, and Ir (PGE) data of six impact spherules from the Meteor crater (Mittlefehldt <i>et al.</i> , 2005) depending on the increasing siderophile character of the elements; for detailed explanation see text.	96
8.1	BSE image shows the via FIB ablated area of a silica glass within a highly-shocked and projectile-rich ejecta fragment (E1-3382).	100
8.2	BSE image of a metallic spherules with conspicuous quenching textures, which were formed during the laser beam irradiation (LE-G).	101

B List of tables

2.1	Measurements of the NIST glass standards	29
2.2	Chemical composition of the Campo del Cielo (CDC) meteorite, Seeberger Sand- stein and the phyllosilicate-bearing sandstone matrix.	29
2.3	Electron-microprobe data for various phases in the highly shocked ejecta fragments.	30
2.4	Electron-microprobe data for various projectile residues (after impact)	31
3.1	Conditions of the hypervelocity cratering experiments	57
3.2	EMP measurement conditions for various phases	58
3.3	Chemical composition of the targets and the projectile	58
3.4	EMP data for the sandstone melt of the highly shocked sandstone ejecta (E1-3382, E2-3383 and A6-5126)	59
3.5	EMP data for the quartzite melt and the Fe-rich silicate melt (Lfe) of the highly shocked quartzite ejecta (A20-5339, E6-3452)	59
3.6	EMP and SEM data for projectile residues	60
5.1	Experimental conditions	88
5.2	EMP measurement conditions for various phases	88
5.3	Microprobe data (selection) of the pure sandstone melts	89
5.4	Microprobe data of the contaminated sandstone melt, <i>Lfe</i> and <i>Lsi</i> (LE-G, LE-H)	90
5.5	Microprobe data (selection) of the contaminated silicate melts (LE-I)	90

